Chloride induced corrosion and concrete carbonation of 3D printed concrete with reinforced connections

by

Jean De'M Malan

Thesis presented in fulfilment of the requirements for the degree of Master of Engineering in Civil Engineering in the Faculty of Engineering at Stellenbosch University

Supervisor: Prof. G.P.A.G. van Zijl
Co-supervisor: Dr A.S. van Rooyen

April 2022

Declaration

By submitting this thesis electronically, I declare that the entirety of the work contained therein is my own, original work, that I am the sole author thereof (save to the extent explicitly otherwise stated), that reproduction and publication thereof by Stellenbosch University will not infringe any third-party rights and that I have not previously in its entirety or in part submitted it to obtain any qualification.

April 2022

Acknowledgements

I would like to express my sincere gratitude to the following people for their assistance and support during the course of this study:

- Prof. G.P.A.G. van Zijl and Dr A.S. van Rooyen for being excellent supervisors and for their willingness to help during the course of this thesis.
- Dr Marchant van den Heever and Dr Jacques Kruger for the technical advice and help provided during the course of this thesis.
- The Civil Engineering laboratory and workshop: Lee-Roy Jones, Julian Thompson and Timothy Combrinck for assisting with my experimental work execution.
- The Geotechnical Engineering laboratory for allowing me to use their equipment for sample preparations.
- The University of Cape Town Concrete Material and Structural Engineering laboratory for the use of their equipment and testing assistance.
- PPC, FerroAtlantica, Ash Resources, Chryso, Sika, and SAPY for providing the materials used in this study.
- Stellenbosch University and the Civil Engineering Structures Department for their financial assistance during the study.
- Ricky Woods for proofreading this thesis.

Abstract

The durability of reinforced concrete structures is dependent on the ability of the concrete cover to combat the ingress of chlorides and carbon dioxide in marine and urban environments. The ingress of these contaminants reduces the pH of the concrete, breaks down the protective passive layer of the reinforcement and initiates the corrosion propagation stage. The high corrosion rates during the propagation stage result in fast degradation of the reinforcement, reducing the structural load-carrying ability and ultimately reducing the structural service life.

A vast amount of research has been conducted over the years regarding concrete carbonation and chloride-induced corrosion of cracked and uncracked cast structures. The presence of cracks has been shown to reduce the service life. Recently, automation has been introduced to the construction industry, specifically referring to additive manufacturing. Three-dimensional concrete printing is the most applied additive manufacturing technique in the construction industry and the lack of fusion at the interlayer region between subsequent printed layers is prominent, especially when a pass time is introduced between concrete layers. The pass time refers to the time between the printing of subsequent layers. As three-dimensional concrete printing is a newly implemented construction method, limited research is available regarding the durability of such three-dimensional concrete printing structures. This study investigates the durability of three-dimensional printed concrete with regard to concrete carbonation (accelerated concrete carbonation testing) and chloride-induced corrosion (via cyclic wetting and drying with a saline solution) to quantify the effect of the interlayer region. The effect of a pass time, varying from 0 to 30 min, is also considered and the results are compared to conventional cast concrete consisting of the same material. The durability performance is measured by conducting chloride-induced corrosion, accelerated concrete carbonation and durability index testing. Flexural strength tests are also conducted to quantify the lack of fusion present at the interlayer region.

The flexural strength and durability performance results show that the cast concrete outperforms three-dimensional concrete printing. The three-dimensional concrete printing samples resulted in higher corrosion rates, greater carbonation depths, lower quality durability index values and lower flexural strengths owing to the lack of fusion present at the interlayer region. The flexural strength and durability performance also decreases with an increase in pass time, which is attributed to the lack of fusion induced by the pass time. Two models for

predicting the concrete carbonation depth and chloride concentration profiles are adapted to incorporate the effect of the interlayer region and pass time present in three-dimensional concrete printing, using the durability index results as input parameters. These models can be used to predict the time to carbonation and chloride-induced corrosion initiation.

Opsomming

Die duursaamheid van gewapende betonstrukture word bepaal deur die betonbedekking se vermoë om die binnedring van chloriede en koolstofdioksied in mariene en stedelike omgewings te weerstaan. Die binnedring van hierdie kontaminante verlaag die pH van die beton, breek die beskermende passiewe laag van die staal af en inisieer die aktiewe korrosie-stadium. Die hoë korrosie-lesings tydens aktiewe korrosie lei tot vinnige vermindering van die staal, wat die kapasiteit van die struktuur verminder en uiteindelik die lewensduur van die struktuur verlaag.

Baie navorsing is al uitgevoer oor betonkarbonering en chloried-geïnduseerde korrosie van gekraakte en ongekraakte gegote strukture. Die teenwoordigheid van krake is bekend daarvoor om die lewensduur van strukture te verkort. Outomatisering is onlangs in die konstruksiebedryf bekendgestel, spesifiek met verwysing na additiewe vervaardiging. Drie-dimensionele betondruk is die mees toegepaste additiewe vervaardigingstegniek in die konstruksiebedryf en die gebrek aan samesmelting by die grensgebiede tussen opeenvolgende gedrukte lae is prominent, veral as 'n verloopstyd tussen betonlae toegepas word. Die verloopstyd verwys na die tyd tussen die druk van opeenvolgende lae. Aangesien drie-dimensionele betondruk 'n nuut geïmplimenteerde konstruksiemetode is, is beperkte navorsing oor die duursaamheid van drie-dimensionele betondruk-strukture beskikbaar. Hierdie studie ondersoek die duursaamheid van drie-dimensionele betondruk met betrekking tot betonkarbonasie (versnelde betonkarbonasie toets) en chloried-geïnduseerde (deur sikliese benatting en droging met ‘n soutoplossing) korrosie om die effek van die grensgebiede te kwantifiseer. Die effek van 'n verloopstyd, wat wissel van 0 tot 30 minute, word ook in ag geneem en die resultate word vergelyk met konvensionele gegote beton wat uit dieselfde materiaal bestaan. Die duursaamheid word gemeet deur chloried-geïnduseerde korrosie, versnelde betonkarbonasie en om duursaamheidsindekstoetse uit te voer. Buigsterkte-toetse word ook uitgevoer om die gebrek aan samesmelting se teenwoordigheid by die grensgebiede te kwantifiseer.

Die resultate van buigsterkte en duursaamheidstoetse toon dat die gegote beton beter as die drie-dimensionele betondruk presteer. Hoër korrosiesnelhede, groter karbonasie dieptes, laer kwaliteit duursaamheidsindeksresultate en laer buigsterkte, as gevolg van die gebrek aan samesmelting teenwoordig by die grensgebiede, is in drie-dimensionele betondrukproefstukke gemeet. Die buigsterkte en duursaamheidsprestasie neem ook af met 'n toename in verloopstyd

wat toegeskryf word aan die gebrek aan samesmelting wat deur die verloopstyd veroorsaak word. Twee voorspellingsmodelle van die beton karbonasie diepte en chloriede konsentrasieprofiele, met behulp van die duursaamheidsindeks-resultate as insetparameters, word aangepas om die effek van die grensgebiede en verloopstyd in drie-dimensionele betondruk in ag te neem. Hierdie modelle kan gebruik word om die tyd tot aktiewe karbonasie en chloried-geïnduseerde korrosie stadium te voorspel.

Table of Contents

List of Figures

Page

List of Tables

Page

Nomenclature

Abbreviations

3DCP	-	Three-dimensional concrete printing
AM	-	Additive manufacturing
CCI	-	Chloride conductivity index
CH	-	Calcium hydroxide
CSH	-	Calcium silicate hydrate
CV	-	Coefficient of variance
DI	-	Durability index
D/D_0	-	Ratio between the diffusion coefficients of cracked and uncracked concrete
FA	-	Fly ash
GGBS	-	Ground granulated blast-furnace slag
HCP	-	Half-cell potential
IR	-	Interlayer region
LPR	-	Linear polarisation resistance
MIP	-	Mercury intrusion porosimetry
MTM	-	Materials testing machine
OPC	-	Ordinary Portland cement
OPI	-	Oxygen permeability index
RC	-	Reinforced concrete
RH	-	Relative humidity

SCM - Supplementary cementitious materials

SEM - Scanning electron microscope

SF - Silica fume

SHCC - Strain-hardening cement-based composites

UCT - University of Cape Town

WSI - Water sorptivity index

w/b - Water to binder

XRF - X-ray fluorescence

µCT - X-ray micro-computed tomography

Terminology

A - Area

A_{28} - Carbonation coefficient based on the 28-day DI results

A_{CO2} - Carbonation coefficient

A_{pol} - Polarised steel surface area

$A_{SA,DI}$ - Carbonation coefficient based on 28-day OPI and exposure environment

A_{thix} - Structuration rate

B - Stern's content

b - Width

C - Concentration of fluid

C_s - Chloride concentration at the surface

$C_{x,t}$ - Chloride concentration at a depth x at time t

c - CO_2 surface concentration

c_x - CO_2 concentration at distance x

D - Diffusion coefficient

D_a - Apparent diffusion coefficient

$D_{a,r}$ - Apparent diffusion coefficient at a reference time

D_{dry} - Effective dry CO_2 diffusion coefficient

D_i - Short-term apparent diffusion confident

d - Concrete specimen's thickness

d_n - Particle diameter

ΔE - Change is potential

E_a - Activation energy (38.2 kJ/mol)

E_{corr} - Corrosion potential

erf - Mathematical error function

F - Faraday's constant (96 500 coulombs)

F_i - Degree of hydration

F_{load} - Failure load

F_{slope} - Slope of best fit

fnc - Calculated value

g - Gravitational acceleration (9.81 m/s^2)

h - Hydraulic head

ΔI - Change in current

I - Electrical current

I_{corr} - Corrosion intensity

$I_{corr,0}$ - Intercepted value of the linear line at the I_{corr} axis

i - Electric current

i_{corr} - Corrosion rate

J - Mass transport rate

$K_{H,i\ \&\ j}$ - Coefficient

k - Permeability coefficient

k_{cal} - Calibrated permeability coefficient

L - Length

l_{pol} - Polarised length

M_d - Dry sample mass

M_s - Vacuum saturated mass of the sample

M_{s0} - Sample mass at time 0 seconds

M_{sv} - Vacuum saturated mass of the sample

m - Amount of CO_2 diffusing though the diffusion area

n - Porosity of material

$n_{i\ \&j}$ - Coefficient

OPI_{28} - 28-day OPI

P_{av} - Average penetration depth

P_j - Degree of pozzolanic activity

P_{max} - Maximum pit penetration depth

R - Universal gas constant (8.313 Nm/Kmol)

$R_{1,2,3}$ - Regression coefficients based on the binder type and exposure

R_{ohm} - Concrete resistance

R_p - Polarisation resistance

R_{thix} - Flocculation rate

S - Sorptivity

S_{Cl} - Chloride ingress width

T - Absolute temperature

ToW - Time of wetness

t - Time

t_c - Curing time

t_e - Effective exposure time

t_i - Time to corrosion initiation

t_r - Reference time

t_{rf} - Re-flocculation time

V - Permeability cell volume

V_{dif} - Voltage difference

$\bar{v}$ - Average fluid velocity

ΔW_c - Weight loss owing to corrosion

W_m - Metals' molecular weight (55.845 g/mol for iron)

WSI_{28} - 28-day WSI

x - Distance

Z - Metals' valency (+2 for iron)

z - Slope of linear regression line

$\frac{dC}{dx}$ - Concentration gradient

$\emptyset_{bar}$ - Bar diameter

$\emptyset_{CE}$ - Diameter of the counter electrode

$\emptyset_{o}$ - Original reinforcement diameter

$\emptyset_{t}$ - Residual reinforcement diameter at a specific time

$\tau_{D,i}$ - Dynamic shear yield stress

$\tau_{S,i}$ - Initial static yield shear stress

α_{b} - Amorphous content

α_{pit} - Pitting factor

α_{RH} - RH curing parameter

ϑ_{k} - Permeability calibration factor

ϑ_{σ} - Conductivity calibration factor

γ - Aging factor

φ - Constant based on binder type

β - RH coefficient

ρ_{e} - Concrete resistivity

ρ_{s} - Density of the salt solution (1.19×10^{-3} g/mm^3)

ρ_w	-	Density of water (10^{-3} g/mm^3)
ω	-	Oxygen molecular mass (0.032 kg/mol)
σ	-	Sample's chloride conductivity
σ_{cal}	-	Calibrated conductivity
σ_c	-	Compressive strength
σ_f	-	Flexural strength
Δ	-	Slope
$[i]$	-	Molar concentrations of the compound
$[j]$	-	Molar concentrations of the admixture

1 Introduction

Chapter 1 outlines the background of the study and the need to investigate the durability performances of 3D concrete printed structures in aggressive environments. Objectives are set out for the durability investigation, and the limitations of the tests conducted in the study are also discussed.

1.1 Background

Alexander and Beushausen (2019) define the durability of a reinforced concrete structure as 'The ability of a structure or component to withstand the design environment over the design life, without undue loss of serviceability or need for major repair.'. The corrosion of the steel reinforcement is one of the deterioration mechanisms that reduces structural service life.

The reinforcement in concrete structures is protected against corrosion by the concrete cover and the protective passive layer that form owing to the alkaline nature of the concrete. Reinforced concrete structures in marine and urban environments are susceptible to chloride- and carbonation-induced corrosion. In marine environments, concrete structures are exposed to chlorides, which penetrate the concrete cover, lower the concrete's pH by forming hydrogen chloride (HCl), and destroy the protective passive layer. A similar mechanism occurs in urban environments with high levels of carbon dioxide (CO_2). The CO_2 penetrates the concrete cover, reduces the hydroxide ion concentration, lowers the pH and destroys the protective passive layer. Once the passive layer is destroyed, the reinforcement is susceptible to corrosion if there is sufficient oxygen and moisture (Richardson, 2002; Beushausen, Otieno & Alexander, 2021).

Traditionally, concrete structures are constructed by casting concrete formwork and involve a lot of manual labour. Converting to automated construction will reduce or eliminate the amount of formwork used in a construction project and can be beneficial to the construction industry. Since the early 2000s, automation has increased in almost all the manufacturing sectors to reduce costs and increase production. This is not true for the construction industry (Khoshnevis, 2004). Only recently has automation been intensely studied and implemented in the construction industry, specifically referring to additive manufacturing (AM) (Paul, van Zijl & Gibson, 2018). The most widely applied AM technique in the construction industry is three-dimensional concrete printing (3DCP), which is rapidly increasing in popularity worldwide in

the construction industry. Companies are implementing 3DCP methods to print large concrete structures such as bridges and houses. Recently, ETH Zurich and Zaha Hadid Architects completed the 3D printing of a concrete footbridge in Venice, Italy (Parks, 2021). Mense-Korte ingenieure+architekten completed the first 3D printed house in Germany (ALLPLAN, 2020). These 3DCP structures will be exposed to the same marine and urban environments as conventional cast structures and should be able to withstand chloride exposure and have a sufficient service life.

Much research has been conducted over the years regarding concrete carbonation and chloride-induced corrosion of cracked and uncracked beams and structures (Papadakis & Vayenas, 1989; Salvoldi, Beushausen & Alexander, 2015; Carević & Ignjatović, 2019; Scott & Alexander, 2007; Otieno, Beushausen & Alexander, 2016; Bezuidenhout & van Zijl, 2019). The 3DCP construction field is fairly new and research results on water and chloride ingress into 3DCP are limited to the pioneering works by Van Der Putten, Azima, van der Heede, Snoeck, Carminati et al. (2020) and Van Der Putten, De Volder, Van den Heerde, De Schutter and Van Tittelboom (2020) respectively. As far as the author could determine, no research results on carbonation and chloride-induced corrosion of reinforcing steel in 3DCP are yet available in literature. Thus, a gap is identified in knowledge of carbonation and chloride ingress and associated corrosion processes in 3DCP. In particular, few to no literature is available on the role of the interfaces between layers in 3DCP as potential pathways for ingress of deleterious substances. As known regions of mechanical weakness (e.g. Kruger and van Zijl, 2021) and higher porosity (Kruger, du Plessis & van Zijl 2021), investigation of carbon and chloride ingress through these interfaces are required.

1.2 Aim and objectives

The aim of this study is to characterise the durability performance, with regard to concrete carbonation and chloride-induced corrosion, of the 3DCP concrete mix design used at Stellenbosch University. It is known that concrete material composition has significant influence on its durability. Varying for instance water to cement ratio, or binder composition in 3D printable concrete mixes is possible to an extent but requires careful mix development for appropriate 3D printability and mechanical properties in the hardened state. In this thesis, the choice is made to use a single mix design known to be printable, and study the influence of pass time, which is a print parameter known to significantly influence interfacial strength (Moelich, Kruger Combrinck, 2021b). The 3DCP durability performance characterisation is

crucial to quantify and predict the service life of 3DCP structures. The interfaces in the layered structure of 3DCP are identified as regions of potential faster ingress of deleterious matter, leading to the deterioration processes of chloride- and carbonation-induced corrosion of embedded steel. Interfacial characteristics, such as adhesive bond, are known to depend on the time between depositing successive layers, expressed as the printer nozzle pass time (Kruger & van Zijl, 2021). Hence, this thesis postulates a relationship between pass time and durability performance.

A test methodology was designed and executed to achieve the following objectives:

(i) To investigate the effect of the interlayer region (IR) of 3DCP samples (with pass times from 0 to 30 min) on the mechanical performance, specifically the flexural strength, compared to conventional cast concrete consisting of the same concrete mix design.

(ii) To do performance-based durability testing, Durability Index (DI) testing, to characterise the concrete's durability class, investigate the effect of the IRs of 3DCP samples on oxygen permeability, water sorptivity, and chloride conductivity, and to compare them to reference cast concrete. Performance-based durability testing and design refers to the use of knowledge of material composition and deterioration processes to design for a particular durability performance whereas prescriptive durability design refers to, for instance a prescribed cover depth, that ignores the fact that the same cover depth can lead to significantly different durability performance depending on the cover density as influenced by for instance the binder composition.

(iii) To explore the influence of the IRs of 3DCP samples on the concrete carbonation resistance (under accelerated conditions) compared to conventional cast concrete.

(iv) To investigate the chloride-induced corrosion performance of 3DCP samples compared to conventional cast concrete. The performance indicators under consideration are chloride penetration depth, time to corrosion initiation, corrosion rates during the corrosion propagation phase and electrochemical damage quantification (mass loss and pitting depth).

(v) To process and analyse the obtained DI and accelerated carbonation depth results to predict the carbonation depth progression for structures under natural conditions.

(vi) To process and analyse the obtained DI and chloride-induced corrosion results to predict the chloride profiles at any given time and the time to corrosion initiation for various cover depths.

1.3 Limitations

Deterioration processes of chloride-induced corrosion and concrete carbonation of reinforced concrete evolve over a number of years in corrosive and urban environments. Despite accelerated processes of higher chloride and CO_2 concentrations and drying–wetting chloride exposure cycles in experimental programmes, an MEng trajectory does not allow sufficient time to develop significant deterioration. Nevertheless, deterioration trends were observed and reported.

2 Literature review

2.1 Introduction

Chapter 2 presents the literature applicable to the corrosion of steel and carbonation of concrete in marine and urban environments. Chapter 2.2 discusses the durability of steel reinforcement in concrete, which focuses on the transport mechanisms in concrete, stages of corrosion, corrosion mechanisms, corrosion types, and monitoring of corrosion. Chapters 2.3 and 2.4 elaborate on the spectrum of chloride-induced corrosion and concrete carbonation, respectively. Each chapter describes the ingress process and factors that affect each deterioration mechanism. Models for the prediction of time for chloride- and carbonation-induced corrosion to initiate are also outlined in Chapter 2.3 and 2.4, respectively. Chapter 2.5 covers the topic of 3DCP, their inherent nature of lack of fusion, and the durability performance of 3DCP samples.

2.2 Durability of reinforced concrete structures

2.2.1 Concrete transport mechanisms

The durability and service life of concrete structures are directly related to the permeability and penetrability of the concrete. Permeability refers to the ingress pathways of a material. Permeability is influenced by pore size, pore distribution, pore interconnectivity, the degree of cement hydration, curing procedures, and environmental conditions (Beushausen et al., 2021). Penetrability describes the ease with which contaminates, ranging from ions to gasses and fluids, move through a material. Therefore, concrete with high permeability is highly penetrable and will influence a structure's durability negatively. The three main transport mechanisms of contaminates in penetrable concrete are permeation, absorption, and diffusion (Richardson, 2002; Beushausen et al., 2021)

2.2.1.1 Permeation

Permeation describes the fluid flow through the saturated pore structure of the same fluid, of the material under an externally applied pressure. Permeation depends on the interconnectivity of the pore structure. The velocity of the fluid under pressure is modelled according to D'Arcy's Law and is shown in Equation 2-1 (Beushausen et al., 2021; Otieno, Alexander & Beushausen, 2010a).

$$\bar{v} = -\left(\frac{k}{n}\right).\left(\frac{dh}{dx}\right) \quad 2\text{-}1$$

where

$\bar{v}$ - Average fluid velocity

k - Permeability coefficient

n - Porosity of material

h - Hydraulic head

x - Distance

2.2.1.2 Capillary absorption

Capillary absorption is the migration of a liquid into unsaturated or partially saturated pores of a material under capillary pressures. As absorption takes place, the fluid's wetting front moves through the concrete's pores and the front's depth increases with time. The front's movement is defined as sorptivity and is a material characteristic. Capillary absorption only plays a significant role at and near the surface of the concrete. Therefore, proper curing of the concrete is essential to enhance the pore structure and decrease the absorption ability of the concrete (Beushausen et al., 2021; Otieno et al., 2010a). Absorption is one of the main mechanisms responsible for the development of high chloride concentration near the concrete surface (Richardson, 2002).

2.2.1.3 Diffusion

Diffusion refers to the movement of ions, gasses or fluids from an area of high concentration to an area of low concentration, i.e. under a concentration gradient, to establish equilibrium. Gaseous and ionic diffusion takes place in unsaturated and partially saturated to saturated pore conditions, respectively. Gaseous diffusion only requires a deviation in concentration to occur and is modelled according to Fick's first law of diffusion (Equation 2-2). Fick's first law of diffusion (steady state of diffusion) is applicable for the diffusion of gasses such as oxygen (O_2) and CO_2 into a uniformly permeable material (Richardson, 2002; Beushausen et al., 2021; Otieno et al., 2010a).

$$J = -D\frac{dC}{dx} \qquad 2\text{-}2$$

where

J - Mass transport rate

D - Diffusion coefficient

$\frac{dC}{dx}$ - Concentration gradient

C - Concentration of deleterious solvent in aqueous solution in a fluid

Ionic diffusion requires a concentration gradient and a transportation medium. The free moisture in the concrete pores acts as a transport medium for the diffusion of chloride and sulphate ions. Ionic diffusion is modelled according to Fick's second law of diffusion (non-steady state of diffusion) (Equation 2-3) (Beushausen et al., 2021; Otieno et al., 2010a).

$$\frac{dC}{dt} = D\frac{d^2C}{dx^2} \qquad 2\text{-}3$$

2.2.2 Corrosion damage model

Beushausen et al. (2021) defines the durability of a concrete structure as the ability of the structure to withstand environmental deterioration and loss of serviceability over the specified life expectancy of the structure. The corrosion of reinforcement is the biggest threat to the durability of reinforced concrete (RC) structures. Tuutti (1982) proposed the first service life model developed for the corrosion deterioration of RC structures. The model is divided into two periods, namely the initiation and the propagation period. However, the three-stage corrosion damage model developed by Heckroodt (2002) interprets the severity of active corrosion, better. The model is illustrated in Figure 2-1 and consists of an initiation, a propagation, and an acceleration period.

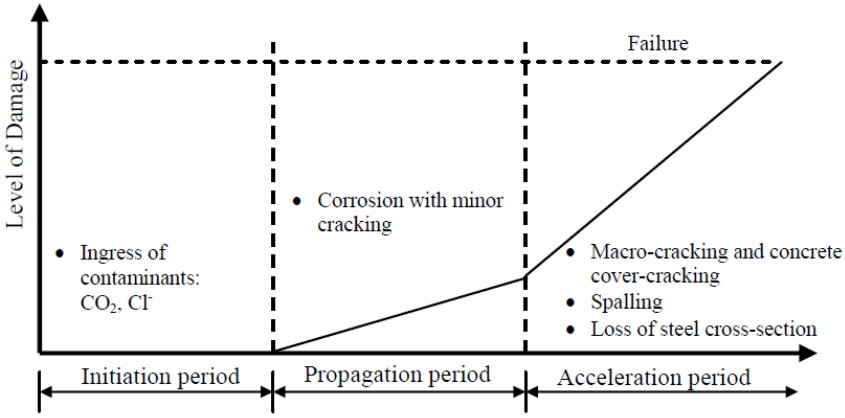

Figure 2-1: Three-stage corrosion damage model (Heckroodt, 2002)

During the initiation period, the naturally occurring passive ferric oxide layer protects the reinforcement from corrosion. No active corrosion takes place and any deterioration that occurs is regarded as insignificant. Contaminates such as chlorides and CO_2 penetrate the permeable concrete cover to reach the reinforcement. The duration of the initiation period is dependent on the cover quality and degree of contaminant exposure. The penetration of these contaminates is usually a lengthy process, especially for dense impermeable concrete. When the threshold criteria of the contaminates are met at the reinforcement depth, the passive ferric oxide layer protecting the reinforcement from corrosion is destroyed and active corrosion commences. This marks the start of the propagation period when active corrosion occurs. The increasing active corrosion causes the formation of micro-cracks at the concrete surface owing to pressure build-up in the matrix by the low-density corrosion product. The presence of surface cracks reduces the effective cover depth and eases the contaminant ingress. The acceleration period commences when the micro-cracks transform into macro-cracks resulting in the direct exposure of the reinforcement to H_2O and O_2. The corrosion accelerates and the structure suffers loss of reinforcement cross-section, and loss of interfacial bond strength between the reinforcement concrete and spalling of the cover. The degradation increases until the structure reaches the ultimate level of damage and fails owing to structural incapacity (Mackechnie & Alexander, 2001; Heckroodt, 2002; Alexander & Beushausen, 2019).

2.2.3 Electrochemical process of steel corrosion

The corrosion of reinforcement is electrochemical in nature and classifies as a redox reaction, which involves the transfer of electrons between species. The occurrence of steel corrosion is

due to the instability of metals. These metals will inevitably revert to their stable forms of oxides, carbonates, and sulphides (Mackechnie & Alexander, 2001; Heckroodt, 2002).

Once the depassivation of steel is complete, corrosion relies on the presence of four elements. These elements are an anode, a cathode, an electrolyte, and a metallic path. The anode is the region where corrosion takes place. The iron at the anode undergoes oxidation and dissolves into the pore solution in the form of iron ions (Fe^{2+}) and electrons. These electrons flow towards the cathodic region via a metallic path, which connects the anode and the cathode. The reinforcement in RC structures acts as the metallic path to support electron flow. A reduction reaction takes place at the cathode that allows for the utilisation of the released electrons. The reduction reaction between H_2O, O_2 and released electrons forms OH^-. No active corrosion takes place at the cathode. Equations 2-4 and 2-5 show the oxidation and reduction reaction at the anodic and catholic regions, respectively. The equations are also visually represented in Figure 2-2. The electrolyte facilitates the flow of OH^- from the cathode to the anode to complete the current of the electrochemical cell. The alkaline pore solution of the concrete acts as the electrolyte in RC (Mackechnie & Alexander, 2001; Richardson, 2002; Otieno et al., 2010a).

$$Fe \rightarrow Fe^{2+} + 2e^- \qquad 2\text{-}4$$

$$H_2O + 0.5O_2 + 2e^- \rightarrow 2OH^- \qquad 2\text{-}5$$

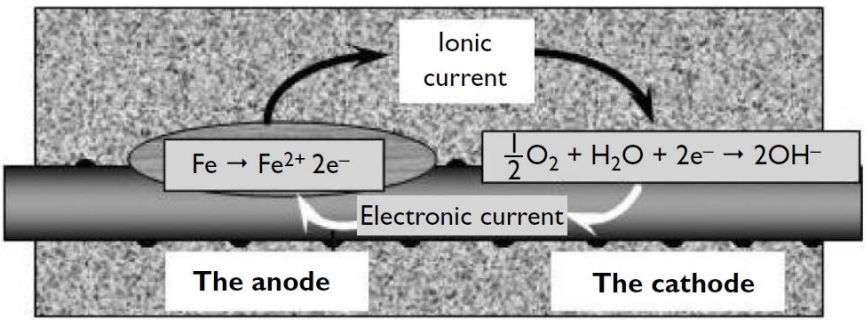

Figure 2-2: Electrochemical process of steel corrosion (Broomfield, 2006)

The initial reaction is between Fe^{2+} and H^-. These two ions combine to form ferrous hydroxide, as shown in Equation 2-6. The secondary reactions involve further oxidation to

produce rust-related compounds. Some of these secondary corrosion products are shown in Equations 2-7 and 2-8, which yield the formation of ferric hydroxide and hydrated ferric oxide, respectively (Mackechnie & Alexander, 2001; Broomfield, 2006).

$$Fe^{2+} + 2(OH)^{-} \rightarrow Fe(OH)_2 \quad 2\text{-}6$$

$$4Fe(OH)_2 + O_2 + 2H_2O \rightarrow 4Fe(OH)_3 \quad 2\text{-}7$$

$$2Fe(OH)_3 \rightarrow Fe_2O_3H_2O + 2H_2O \quad 2\text{-}8$$

2.2.4 Steel depassivation

Reinforcement is prone to corrode in an environment where sufficient O_2 and moisture is present; for instance, if reinforcement lies around on a construction site. However, in RC structures, the reinforcement is embedded in the concrete. The embedded nature provides two corrosion protection mechanisms. The first mechanism is the concrete cover. Highly impermeable cover and sufficient cover depth will decrease the ingress rate of contaminates, O_2 and water. The second mechanism is the formation of a passive ferric oxide film around the reinforcement owing to the high alkalinity of concrete (pH>12.5). The alkalinity is ascribed to presence of hydroxyl ions (OH^-) that are released when calcium hydroxide ($Ca(OH)_2$) that is produced during cement hydration, dissolves in the pore solution. The passive film is between 1 mm and 10 mm thick and restrains cation and anion movement to suppress corrosion. The depassivation of the reinforcement occurs when the threshold criteria of the chlorides and CO_2 at the depth of reinforcement are met occur (Mackechnie & Alexander, 2001; Heckroodt, 2002; Richardson, 2002). Chapters 2.3.2 and 2.4 elaborate on chloride induced corrosion initiation and concrete carbonation. It is important to note that the governing factor of corrosion is not depassivation of the reinforcement. The passive layer can be non-existent but if there is no O_2 and H_2O available, corrosion will not occur (Mackechnie & Alexander, 2001; Heckroodt, 2002; Richardson, 2002).

2.2.5 Factors that influence active corrosion

After depassivation, environmental factors such as O_2 and relative humidity (RH) are crucial to ensure that active corrosion takes place. As can be seen from the reaction in Equation 2-7, the presence of O_2 and H_2O is needed for the corrosion reaction. The diffusion rate of O_2 is higher in permeable and unsaturated concrete, but when the RH is very low the concrete pores

are empty and, as a result, the concrete pores cannot function as a medium for an electrolyte to complete the electrochemical circuit. On the other hand, when the RH is very high, the pores are saturated and block O_2 diffusion. Generally, optimal active corrosion takes place between 80% and 95% relative humidity. The increase in temperature also aids corrosion (Richardson, 2002).

2.2.6 The effect of corrosion in reinforced concrete structures

Corrosion not only reduces the reinforcement cross-section and structural capacity but also degrades the concrete (Beushausen et al., 2021). The corrosion products have lower densities and occupy larger volumes compared to Fe. The increasing volume causes internal tensile pressure to build up at the anode region. Figure 2-3 illustrates that the volume of corrosion products is up to seven times that of Fe. Concrete is known for having a limited tensile capacity, and volume expansion results in cracks and spalling (Liu, 1996; Richardson, 2002).

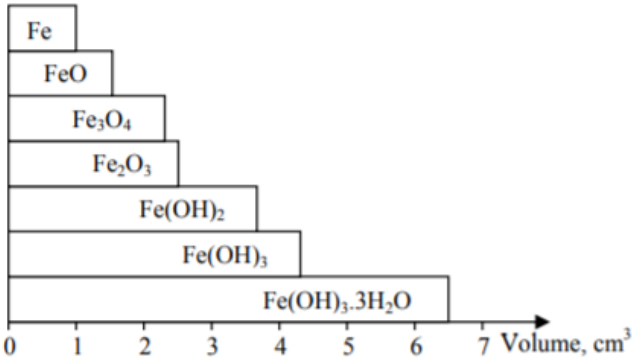

Figure 2-3: Histogram of the volume of iron corrosion products relative to the volume of iron (Liu, 1996)

2.2.7 Types of corrosion

Steel corrosion is either a localised attack, which is referred to as pitting corrosion, or is uniform along the reinforcement surface, which is referred to as uniform corrosion. Figure 2-4 illustrates the difference between uniform and pitting corrosion. In the case of carbonation-induced corrosion, corrosion is generally uniform across the cross-section of the reinforcement, whereas pitting corrosion is associated with chloride-induced corrosion (Andrade & Alonso, 1996, 2001; Richardson, 2002).

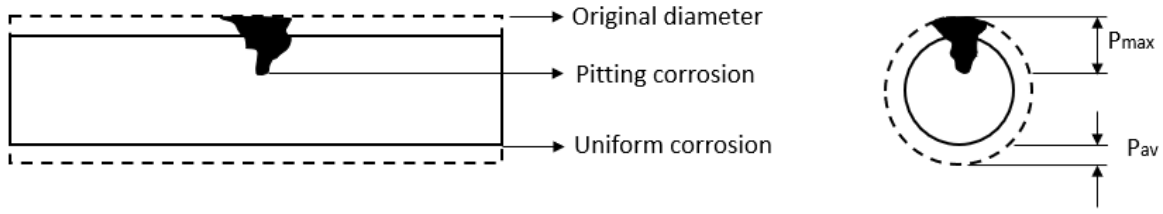

Figure 2-4: Visual representation of uniform and pitting corrosion, reproduced from Andrade and Alonso (1996),

Pitting corrosion results in a larger reduction in residual reinforcement area compared to uniform corrosion (Figure 2-5). The pitting effect is accounted for by the incorporation of a pitting factor (α_{pit}), which describes the relationship between maximum pit penetration depth of localised corrosion and the average penetration depth of general corrosion. Equations 2-9 and 2-10 incorporate the α_{pit} (Andrade & Alonso, 1996, 2001; Richardson, 2002).

where

$$\emptyset_t = \emptyset_o - \alpha_{pit}.x \qquad 2\text{-}9$$

$$\alpha_{pit} = \frac{P_{max}}{P_{av}} \qquad 2\text{-}10$$

$\emptyset_t$ - Residual reinforcement diameter at a specific time

$\emptyset_o$ - Original reinforcement diameter

P_{max} - Maximum pit penetration depth

P_{av} - Average penetration depth

(a) (b)

Figure 2-5: Comparison of the reduction in residual reinforcement area of uniform (a) and pitting (b) corrosion, reproduced from Andrade and Alonso (2001)

For carbonation-induced corrosion, α_{pit} is considered to be 1 owing to its dominantly uniform nature, but various pitting factors owing to chloride attacks have been reported by researchers. Tuutti (1982) reports an α_{pit} range of 4 to 10. González, Andrade, Alonso and Feliu (1995) investigated local chloride attack on uncracked concrete beams. The results show that an α_{pit} range from 4 to 8 is applicable for natural corrosion testing, whereas results for accelerated corrosion testing through applied currents ranged from 5 to 13. Andrade and Martínez (2005) found that α_{pit} of 10 is suitable for uncracked concrete beams containing chlorides. Bezuidenhout and van Zijl (2019) report that an α_{pit} of 4 for 0.4 mm widely cracked concrete beams shows sensible agreement for the gravimetric mass loss compared to the calculated electrochemical mass loss. However, 3 of their 54 bars tested showed high levels of pitting corrosion, which corresponded to an α_{pit} of 10. Andrade and Alonso (1996) recommend a conservative α_{pit} of 10 when pitting corrosion occurs.

2.2.8 Type of corrosion mechanisms

In RC structures, macro and/or microcell corrosion can occur. Microcell corrosion occurs when the anodic and cathodic reactions take place adjacent to each other. Macrocell corrosion occurs when the anodic and cathodic reactions take place on separate regions. For a single bar, the reactions take place on the same bar with a large cathode region and small anode region. In the case where steel bars are connected, the anodic reaction will take place on the actively corroding steel bar and the cathodic reaction will take place on another steel bar, which is in a passive state. Macrocell corrosion results in a high cathode to anode size ratio, which leads to greater corrosion rates (Richardson, 2002; Zhou, Genturck, Willam & Attar, 2014).

The corrosion mechanisms for carbonation and chloride-induced corrosion are illustrated in Figure 2-6. In the case of carbonation-induced corrosion, the corrosion is uniform and microcell corrosion occurs. For chloride-induced corrosion, the pitting corrosion occurs dominantly. When the O_2 required for the cathodic reaction is supplied through the crack or at the pit formation, microcell corrosion occurs, but when the O_2 supplied is through the uncracked regions at the passive steel, macrocell corrosion occurs (Andrade & Alonso, 1996; Otieno et al., 2010a).

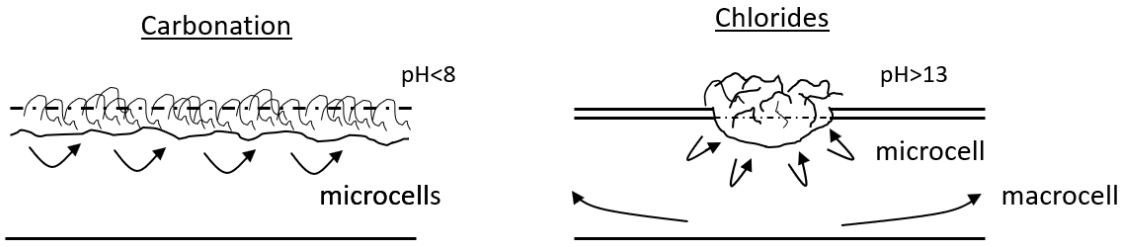

(a) (b)

Figure 2-6: Corrosion mechanisms for carbonation- (a) and chloride-induced (b) corrosion, reproduced from Andrade and Alonso (1996)

2.2.9 Steel cross-sectional area loss estimation based on the corrosion rate

Andrade and Alonso (1996) define the corrosion rate (i_{corr}) as the total amount of corrosion products produced per unit surface area for a specific time period. The gravimetric mass loss can be determined from the weight difference of the reinforcement before and after exposure to the corrosion environment but involves the destruction of the concrete. Currently, non-destructive electrochemical techniques are available to monitor the corrosion rate. Faraday's law can be used to convert the electrochemical parameters to steel mass loss. Faraday's law is presented as Equation 2-11.

$$\frac{It}{F} = \frac{\Delta W_c}{W_m/Z} \qquad 2\text{-}11$$

where

I - Electrical current

t - Time

F - Faraday's constant (96 500 Coulombs)

ΔW_c - Weight loss owing to corrosion

W_m - Metals' molecular weight (55.845 g/mol for iron)

Z - Metals' valency (+2 for iron)

The electrical current in Equation 2-11 is referred to as the corrosion intensity (I_{corr}), which is an instant value that represents the corrosion intensity at the specific time of measurement. I_{corr} is typically expressed in μA/cm^2 and assumes a uniform corrosion attack. In the case of pitting corrosion, I_{corr} can be underestimated. By continuously monitoring I_{corr} over time, i_{corr} can be determined by integrating the I_{corr}-time curve. The weight loss calculated using the electrochemical parameters should show a good correlation with the gravimetric mass loss (Andrade & Alonso, 2001; Bezuidenhout & van Zijl, 2019).

2.2.10 Monitoring the corrosion activity

The corrosion activity can be tracked with various techniques. The three main methods used to monitor the corrosion activity are concrete resistivity (ρ_e), half-cell potential (HCP)/corrosion potential (E_{corr}), and corrosion rate (Broomfield, 2006).

The concrete resistivity reflects the concrete resistance to electrical current and is dependent on the moisture content of the concrete pores. Poor quality concrete combined with a high saturation level has a low resistivity, whereas high quality concrete that is dry has a high resistivity (Mackechnie & Alexander, 2001). The concrete resistivity is typically measured with a 4-point Werner Probe (isdcorr, 2015). Alternatively, the concrete resistivity can be determined using a single electrode but must be interpreted in combination with the linear polarisation measurements using Equation 2-12 (Newman, 1966).The resistivity can give an indication of possible corrosion activity, but only if the steel is already de-passivated (Broomfield, 2006). Andrade and Alonso (1996) propose a relationship between the corrosion risk and resistivity. The relationship is listed in Table 2-1. Alonso, Andrade and González (1988) and Otieno (2008) report good relationships between the corrosion rate and corrosion resistivity.

where

$$\rho_e = 2.\emptyset_{CE}.R_{ohm} \qquad 2\text{-}12$$

$\emptyset_{CE}$ - Diameter of the counter electrode

R_{ohm} - Concrete resistance

Table 2-1: Relationship between the concrete resistivity and the corrosion risk (Andrade & Alonso, 2001)

Resistivity (kΩ.cm)	**Risk level**
ρ_e > 100	Negligible corrosion rate
50 ≤ ρ_e ≤ 100	Low corrosion rate
10 ≤ ρ_e ≤ 50	Moderate to high corrosion rate
ρ_e < 10	Resistivity is not the controlling parameter

HCP is the most common electrochemical technique used to monitor the corrosion potential or probability of RC. The methods measure the difference in potentials between the embedded steel and the reference electrode. The reference electrode is in the form of a half-cell, which consists of a metal and a solution, typically copper/copper sulphate ($Cu/CuSO_4$) or silver/silver chloride ($Ag/AgCl$) (Broomfield, 2006). The HCP is affected by temperature, concrete saturation level, concrete resistivity, and degree of carbonation, and only serves as an indication of the corrosion risk. It does not serve as an indication of the corrosion rate or the corrosion reactions (ASTM C876-91, 1999; Andrade & Alonso, 2001; Broomfield, 2006). Table 2-2 shows the E_{corr} and the corresponding corrosion risk based on the type of reference electrode. It is recommended that I_{corr} is measured with the E_{corr} to interpret the potentials obtained properly (Broomfield, 2006).

E_{corr} and ρ_e only give an indication of corrosion risk and the likelihood of corrosion activity, which are qualitative techniques (Andrade & Alonso, 1996). The only electrochemical techniques that can quantify the corrosion activity is the linear polarisation resistance (LPR) technique that measures the polarisation resistance (R_p) (Andrade & Alonso, 2001). The LPR involves the measurement of the shift in potential when a small current of 10 mV to 20 mV is applied to the reinforcement for a short period of time. At small potentials, the current and potential have a linear relationship, and the ratio of the change in potential to the change in current defines R_p (Equation 2-13) (Andrade & Alonso, 1996; Broomfield, 2006).

$$R_p = \frac{\Delta E}{\Delta I} \quad 2\text{-}13$$

where

ΔE - Change in potential

ΔI - Change in current

Table 2-2: Corrosion risk for corrosion potentials of different electrodes (ASTM C876-91, 1999)

Corrosion potential		**Corrosion risk**
$Cu/CuSO_4$ **Electrode (mV)**	$Ag/AgCl$ **Electrode (mV)**	
$E_{corr} \geq$ -200	$E_{corr} \geq$ -106	Low (10% corrosion risk)
-200 $\leq E_{corr} \leq$ -350	-106 $\leq E_{corr} \leq$ -256	Intermediate corrosion risk
$E_{corr} \leq$ -350	$E_{corr} \leq$ -256	High corrosion risk (>90% corrosion risk)
$E_{corr} \leq$ -500	$E_{corr} \leq$ -406	Severe corrosion risk

The corrosion current (Equation 2-14) is calculated by dividing the R_p by Stern's constant (B), depending on the corrosive state of the steel. B is 26 mV for corroding steel and 52 mV for steel in a passive state (Andrade & Alonso, 1996; Broomfield, 2006).

$$I = \frac{B}{R_p} \quad 2\text{-}14$$

Ultimately, the corrosion current is divided by the polarised steel area (Figure 2-7) to determine the corrosion intensity (Equation 2-15 and 2-16) (Andrade & Alonso, 1996; Broomfield, 2006). Typically, the modulated confinement of current technique is used to confine the current to a predetermined steel area using a ring guard (Andrade & Alonso, 2001).

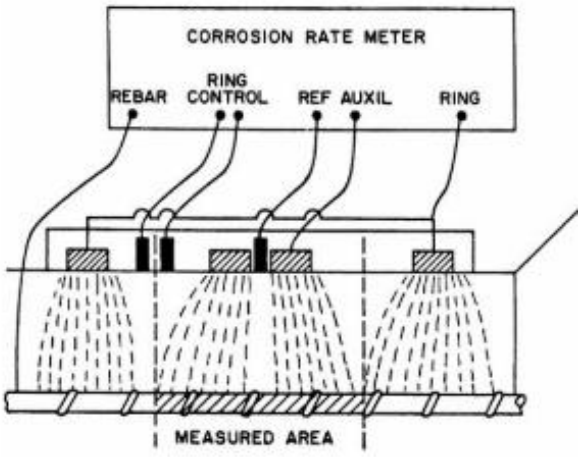

Figure 2-7: Polarised area (measured area) using the modulated confinement of current technique (Andrade & Alonso, 2001)

$$I_{corr} = \frac{I}{A_{pol}} \quad 2\text{-}15$$

$$A_{pol} = \pi \emptyset_{bar} l_{pol} \quad 2\text{-}16$$

where

A_{pol} - Polarised steel surface area

$\emptyset_{bar}$ - Bar diameter

l_{pol} - Polarised length

The embedded steel changes from a passive to a corrosive state when the corrosion intensity surpasses 0.1 µA/cm^2. The corrosion level severity of the corrosion intensity is shown in Table 2-3. Corrosion intensity measurements are influenced significantly by environmental conditions. Measurements taken when the concrete is dry, result in decreased corrosion intensities that are misleading (Andrade & Alonso, 2001).

Table 2-3: Corrosion level severity of corrosion intensity on-site and lab intensity measurements (Andrade & Alonso, 2001)

Corrosion intensity (µA/cm^2)	**Corrosion level**
$I_{corr} < 0.1$	Negliglbe
$0.1 \leq I_{corr} < 0.5$	Low
$0.5 \leq I_{corr} < 1$	Moderate
$I_{corr} \geq 0.1$	High

2.2.11 Performance-based concrete durability testing

Currently, a largely prescriptive specification approach is used to assure that a RC structure meets the durability requirements. These specifications, for different environmental conditions, vary from limiting the binder and cement content, the water to binder (w/b) ratio, concrete compressive strength, cover depth, etc. Significant emphasis is placed on high compressive strength concrete as an implication of high durability, which may be misleading. The mechanical properties, however, give an indication of the bulk concrete and not the concrete cover, which protects the rebar from contaminates (Alexander & Beushausen, 2019).

The University of Cape Town and the University of the Witwatersrand have developed a performance-based approach to determine concrete durability, which focuses on the quality and transport properties of the concrete cover at early ages (28 days). This approach consists of three DI tests, namely O_2 permeability, H_2O sorptivity and chloride conductivity tests. The O_2 operability test measures the permeability of the concretes pore structure and gives an indication of the concrete's permeation characteristics. The H_2O sorptivity test measures the transport of moisture through the pore structure via capillary forces. The chloride conductivity test measures the diffusion of chlorides under a 10 V potential difference, which gives an indication of the concrete resistance to chloride penetration (Alexander, Mackechnie & Ballim, 1999). Research has shown that these tests are sensitive to binder content, curing environment and concrete age (Du Preez & Alexander, 2004; Alexander & Beushausen, 2019). The durability classes for the O_2 permeability index (OPI), water sorptivity index (WSI) and chloride conductivity index (CCI) are presented in Table 2-4. Good correlations have been

established between the 28-day CCI and measured diffusion coefficient after two years of marine exposure as well as the OPI and the concrete carbonation depth. The WSI is yet to be correlated to a deterioration mechanism (Mackechnie, 1995; 2001; Alexander, Mackechnie et al., 1999; Salvoldi et al., 2015).

Table 2-4: DI classification ranges (Alexander, Mackechnie et al., 1999)

Durability class	**OPI (log scale)**	**WSI (mm/√h)**	**CCI (mS/cm)**
Excellent	> 10	<6	<0.75
Good	9.5 – 10	6 – 10	0.75 – 1.50
Poor	9.0 – 9.5	10 – 15	1.50 – 2.50
Very poor	<9.0	>15	>2.50

2.3 Chloride-induced corrosion

2.3.1 Chloride diffusion through concrete

The ingress of chlorides occurs owing to capillary absorption near the concrete surface and diffusion in the bulk concrete. Diffusion is the governing transport mechanism in submerged concrete. Absorption plays a bigger role in the transport of chlorides during the early concrete ages and in concrete that is continuously exposed to wetting and drying cycles (marine splash zone) (Richardson, 2002; Beushausen et al., 2021). The continuous wetting and drying prevent the development of pure diffusion and lead to the development of a convection zone near the surface. The convection zone ends where the concrete's RH reaches 100% and diffusion dominates. Figure 2-8 shows the development of high chloride concentrations near the surface though absorption, forming a convection zone (Δx) (Beushausen et al., 2021).

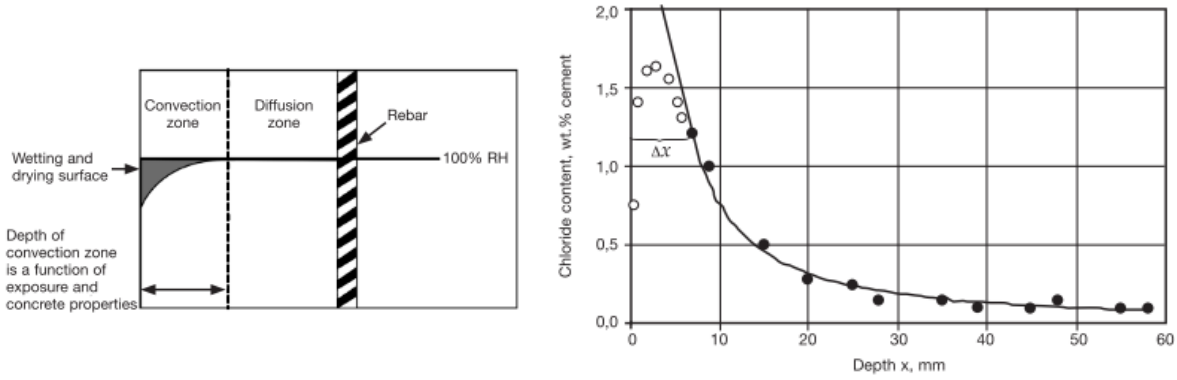

(a) (b)

Figure 2-8: Convection zone (a) and chloride profile (b) of concrete exposed to the marine splash zone (Beushausen et al., 2021)

The diffusion of chlorides through concrete can be modelled based on Fick's second law of diffusion (Equation 2-3 in Chapter 2.2.1.3). Crank proposed an error function solution to Fick's second law (Equation 2-19) with the following boundary conditions (Richardson, 2002; Beushausen et al., 2021):

$$C_{x,t} = 0 \; at \; t = 0 \; and \; 0 < x < \infty \tag{2-17}$$

$$C_{x,t} = C_s at \; x = 0 \; and \; 0 < t < \infty \tag{2-18}$$

where

$C_{x,t}$ - Chloride concentration at a depth x at time t

C_s - Chloride concentration at the surface

$$C_{x,t} = C_s . \left[1 - erf\left(\frac{x}{2\sqrt{D_a . (t)}}\right)\right] \tag{2-19}$$

where

erf - Mathematical error function

D_a - Apparent diffusion coefficient

Aging influences the transport properties of the concrete. The diffusion coefficient is not constant and reduces over time owing to various factors, such as ongoing cement hydration and chloride binding (Beushausen et al., 2021). In general, the time-dependency equation is used to calculate the change in D_a (Equation 2-20) (Nilsson, 2004).

$$D_a = D_{a,r}\left(\frac{t_r}{t}\right)^{\gamma} \quad 2\text{-}20$$

where

$D_{a,r}$ - Apparent diffusion coefficient at a reference time

t_r - Reference time

γ - Aging factor

2.3.2 Chloride-induced corrosion initiation

RC structures in chloride rich environments, such as coastal regions, are highly susceptible to chloride-inducted corrosion. Chlorides penetrate through the concrete cover and/or cracks and locally depassivate the embedded steel (Richardson, 2002). The chlorides do not participate in the corrosion reactions, but only act as a catalyst for the reaction (Broomfield, 2006). The initiation process is shown in Figure 2-9.

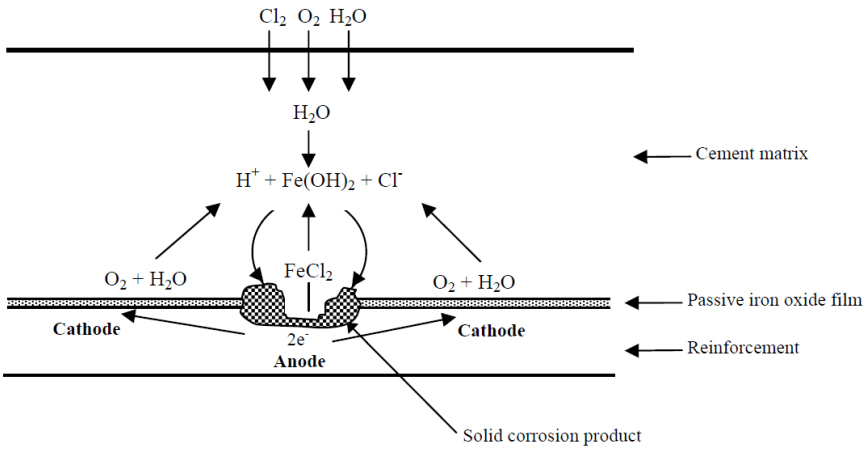

Figure 2-9: Visual representation of chloride induced corrosion (Otieno et al., 2010a)

The chemical reactions of chloride-induced corrosion are shown in Equations 2-21 to 2-24. The first step involves the oxidation of the iron, as shown in Chapter 2.2.3. The chloride ions react with the oxidised ferrous ions (Fe^{2+}) to form chloride and oxychloride compounds, such as $FeCl_2$ (Equation 2-21) and FeOCl, respectively (Richardson, 2002).

$$2Fe^{2+} + 4Cl^- \rightarrow 2FeCl_2 \qquad 2\text{-}21$$

The HCl produced in Equation 2-22, locally destroys the protective passive layer by lowering the pH at the anode and creates an acidic environment at the anodic region (Otieno et al., 2010a). The increase in acidity further promotes the continuous recycling of chloride ions (Equations 2-23 and 2-24), which results in self-propagation of the corrosion process and the oxidation of iron. The acidic environment also prevents the precipitation of the corrosion products ($Fe(0H)_2$), which promotes the migration of $FeCl_2$ and FeOCl (Richardson, 2002). Once the chloride threshold of the concrete at the reinforcement is reached, the passive layer is destroyed, and corrosion commences (Richardson, 2002; Broomfield, 2006). Chapter 2.3.3 elaborates on the chloride threshold and limits.

$$2FeCl_2 + 4H_2O \rightarrow 2Fe(0H)_2 + 4HCl \qquad 2\text{-}22$$

$$2FeCl_2 + 4H_2O \rightarrow 2Fe(0H)_2 + 4H^+ + 4Cl^- \qquad 2\text{-}23$$

$$2FeCl_2 + 2H_2O \rightarrow 2Fe(0H)_2 + 2Cl^- \qquad 2\text{-}24$$

2.3.3 Chloride threshold

The chloride threshold refers to the minimum amount of chlorides required at the steel reinforcement for active corrosion to commence. The chloride threshold is not a fixed value and is dependent on various factors, such as environmental exposure, concrete quality, concrete composition, etc. The threshold level can be expressed by the total/free chloride content by weight of the concrete/binder or by the ratio between the free chloride to hydroxyl ion concentration (Nilsson, Poulsen, Sandberg, Sørensen, & Klinghoffer, 1996).

The chlorides in the concrete are either free or bound (strongly or loosely) (Richardson, 2002). Bound chlorides are chemically bound by the aluminates in the concrete or are physically bound in the pores by absorption. Bound chlorides do not participate in the corrosion reactions, but free chlorides are free to react and therefore pose the highest risk of corrosion (Broomfield, 2006). In practice, the total chloride content is considered to represent the chloride threshold owing to the difficulty of measuring the free chloride content. Various chloride threshold values ranging from 0.03% to 3.08 % have been reported (Table 2-5) but a general conservative threshold of 0.4% by weight of binder has been considered by several researchers (Richardson, 2002; Otieno et al., 2010a). Chloride content by mass of binder of 0.4% –1% and above 1% have a moderate and high probability of corrosion, respectively (Mackechnie & Alexander, 2001).

Table 2-5: Chloride threshold values reported by various researchers

Reference	Binder type	Chloride threshold by mass of binder (%)
Scott (2004)	Various binders	0.08 – 0.53
Trejo & Pillai (2003)	OPC	0.02 – 0.24
Alonso, Castellote & Andrade (2002)	Various binders	0.73
Alonso, Andrade & Castellote (2000)	OPC	1.24 – 3.08
Lambert, Page & Vassie (1991)	OPC, SRPC	1.0 – 3.0

2.3.4 Factors that influence chloride-induced corrosion initiation

Many factors contribute to the duration before chloride-induced corrosion initiates. Factors such as the chloride threshold, chloride binding of the binder type, and cover quality play immense roles. The presence of cracks also contributes to the length of the initiation period (Otieno et al., 2010a).

2.3.4.1 Chloride threshold

As discussed in Chapter 2.3.3, the chloride threshold is affected by various factors. Scott (2004) determines various chloride threshold levers for different binders. The results show that the partial replacement of Ordinary Portland Cement (OPC) with fly ash (FA) and ground granulated blast-furnace slag (GGBS) reduces the chloride threshold. The decreases in chloride threshold for the blended cement may be the result of the slow hydration and pozzolanic reaction, resulting in high permeability during early concrete ages. However, in the long term, the continuous hydration and pozzolanic reactions can result in a denser microstructure that slows down the corrosion activity.

2.3.4.2 Chloride binding of the binder

The chloride binding capacity of the binder promotes the durability of the concrete. First of all, chloride binding decreases the amount of free chloride in the pore solution, thus reducing the chloride ion transport. The reduction in total free chlorides and transportation increases the initiation period and makes the reinforcement less prone to corrosion (Nilsson et al., 1996). Chloride binding studies conducted by Arya, Buenfeld and Newman (1990) show that binders containing 30% FA and 70% GGBS had superior chloride binding abilities compared to OPC. The percentage of bound/total chloride for OPC, FA and GGBS binders were 50%, 57% and 43 % respectively. Glass, Hassanein and Buenfeld (1997) also report the superior chloride binding ability of binders containing GGBS and FA compared to OPC (Figure 2-10).

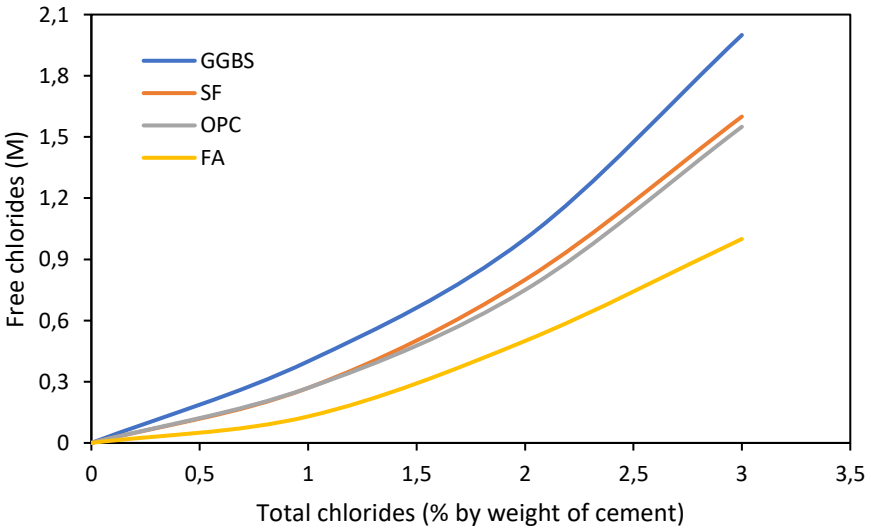

Figure 2-10: Relationship between the free chloride content compared to the total chloride content for various binders, reproduced from Glass et al. (1997)

2.3.4.3 Concrete cover

The concrete cover protects the reinforcement from chloride ingress. Larger concrete cover thickness increases the chloride ingress path, thus increasing the time before corrosion initiation. The quality of the cover also influences the time to corrosion initiation. Factors such as binder type, w/b and curing procedures affect the cover performance characteristics. As mentioned in Chapter 2.2.11, the CCI values give an indication of the cover's resistance to chloride penetration. The partial replacement of OPC with supplementary cementitious materials (SCM) (FA, GGBS and silica fume (SF)), good curing practices (wet curing compared to air curing), and lower w/b ratios all increase the cover quality (reduce CCI values) (Alexander, Streicher & Mackechnie, 1999). Mackechnie and Alexander (1997) investigated the chloride profiles of various binders in marine environments. The results showed that concrete containing 30% FA and 50% GGBS had about half the chloride levels at specific depths compared to the OPC concrete samples. The difference in chloride content became more pronounced as the concrete aged. Van Zijl and Paul (2018) performed accelerated corrosion tests by applying electrical potential to RC specimens. The results indicate that specimens with a larger cover recorded a lower mass loss for accelerated testing under the same applied electrical potential and duration because for the smaller cover depth, corrosion occurred over a longer period of time than in the specimens with larger cover depths, due to earlier corrosion initiation.

2.3.4.4 Presence of cracks

Cracks reduce the effective cover depth, resulting in shorter chloride ingress paths. Paul, Van Zijl, Babafemi and Tan (2016) evaluated the chloride ingress in cracked and uncracked strain-hardening cement-based composites. The results showed that the cracked specimens had larger chloride concentrations at the same depth and exposure duration compared to uncracked specimens. Paul and van Zijl (2016) also investigated the short-term chloride ingress process by applying a silver nitrate ($AgNO_3$) solution to the sawn surface of cracked specimens that were subjected to chloride ponding for seven days. The results showed that the chlorides penetrated to the maximum crack depth within one hour of ponding (average crack widths below 50 μm), followed by horizontal penetration through the concrete matrix. Chloride-induced corrosion studies conducted by Otieno et al. (2010b) showed that the presence of cracks reduced the corrosion initiation time.

Djerbi, Bonnet, Khelidj and Baroghel-Bouny (2008) investigated the chloride diffusion though cracked and uncracked concrete specimens under a steady-state migration test. The ratio between the diffusion coefficients of cracked and uncracked concrete (D/D_0) is shown in Figure 2-11. A moderate increase in diffusion coefficient was observed for cracks widths between 30 μm and 80 μm, where the chlorides diffuse through the uncracked concrete and the crack. A remarkable increase in the D/D_0 ratio was noted for crack widths above 80 μm. As the crack width increased, diffusion through the cracked region (path of least resistance) became more predominant and less chlorides diffused through the uncracked concrete regions (Djerbi et al., 2008; Boshoff, Altmann, Adendorff & Mechtcherine, 2016). In Figure 2-11, w, OC, HPC and HPCSF stands for crack width, ordinary concrete, high performance concrete and high-performance concrete containing silica fume, respectively.

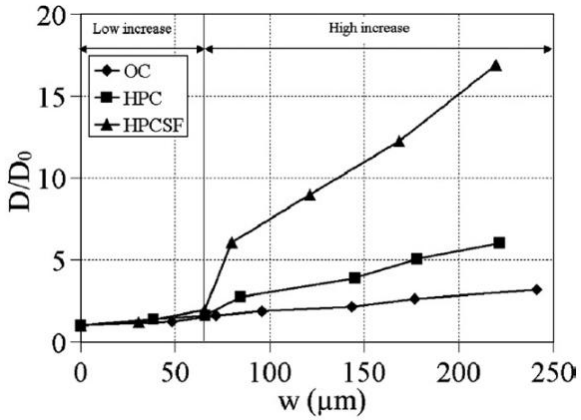

Figure 2-11: D/D0 versus the average crack width for various binders (Djerbi et al., 2008)

2.3.5 Factors that influence chloride-induced corrosion propagation

When the chloride threshold is reached at the reinforcement and O_2, H_2O and Cl^- are available to sustain the cathode and anode reactions, the RC structure enters the corrosion propagation phase (Otieno et al., 2010a). In general, the transition from initiation to propagation occurs when the corrosion rate reaches 0.1 $\mu A/cm^2$ (Andrade & Alonso, 2001). Factors that influence this phase include environmental conditions (chloride exposure, RH, and temperature), cover depth, concrete quality (curing procedures, w/b ratio and binder type), and the presence of cracks (Beushausen et al., 2021; Otieno et al., 2010a). The effect of these factors is assessed based on the corrosion rate, CCI results, and pitting characteristics.

2.3.5.1 Environment conditions

Environmental conditions, such as chloride exposure from seawater, RH, and temperature affect corrosion propagation significantly. Concrete structures in South Africa that experience chloride exposure in coastal marine environments. BS EN 206-1 (2000) have been adapted to suit South African conditions, as shown in Table 2-6 (Beushausen et al., 2021). A RC structure in exposure class XS1 is only exposed to airborne salts, which is not as significant compared to XS2 and XS3. In class XS2, the chloride penetrations are governed by diffusion, but the saturated conditions block O_2 ingress and lead to low corrosion rates. The continuous wetting and drying of the concrete in XS3 accelerate the chloride penetration via capillary absorption near the concrete surface and diffusion beyond the convention zone. During the drying period the dissolved salts can crystallise, cause stress within the concrete matrix, and lead to spalling. The destructive nature of abrasion also reduces the cover quality (Richardson, 2002; Beushausen et al., 2021)

Table 2-6: Adapted BS EN 206-1 (2000) environmental classes for South African costal environment

BS EN 206 Class	**Description**
XS1	Exposed to airborne salt but not in direct contact with water
XS2a*	Permanently submerged
XS2b*	XS2a* + exposed to abrasion
XS3a*	Tidal, splash and spray zone
	Buried elements in desert areas exposed to salt spray
XS3b*	XS3a* + exposed to abrasion

*These subclasses have been added to the BS EN 206-1 (2000) classes for the South African coastal conditions

RH affects the diffusion of O_2 and the ability of the concrete to act as an electrolyte for corrosion activity. In dry conditions, O_2 diffuses relatively easily through concrete, but the concrete cannot function as an electrolyte. In saturated conditions, the O_2 is blocked by

moisture-filled pores (Richardson, 2002). Bentur, Diamond and Berke (1997) found that the O_2 diffusion coefficient reduced with an increase in RH. Chloride-induced corrosion activity increases radically when the RH surpasses 80% and is at an optimum at 90% to 95%. RH levels below 50% cannot support the corrosion activity conditions and reactions (Richardson, 2002).

High temperatures are known to increase the corrosion rate. High temperatures increase the electrode reactions and O_2 solubility, which increase the corrosion rate. This acceleration phenomenon occurs at temperatures up to 40 ºC. For temperatures beyond 40 ºC, an inhibiting effect can occur if the environment is not conductive to corrosion activity. The inhibiting effect is due to the decreased O_2 solubility, which results in a lower corrosion rate (Zivica, 2003; Otieno et al., 2010a).

2.3.5.2 Curing procedures

Good curing procedures prevent moisture evaporation and maintain suitable moisture and temperature conditions to facilitate the cement hydrations and pozzolanic reactions that ensure high cover quality to prevent the ingress of corrosion agents (Beushausen et al., 2021). Du Preez and Alexander (2004) investigated the effect of site curing practices such as curing compounds, hessian cloth, damp sand, and air curing on blended concretes. The CCI values were compared to laboratory wet cured samples. The results showed that wet cured concrete outperformed the site curing procedures at 28 and 120 days of testing. Initial wet curing, especially with regard to low-grade concretes, is important to achieve low CCI values (Alexander, Streicher et al., 1999).

2.3.5.3 Cover depth

In the absence of cracks, the concrete cover depth and penetrability characteristics are the steel's main defence against corrosion initiation and propagation (Otieno et al., 2016; Bezuidenhout & van Zijl, 2019). Greater cover depths increase the travel path for O_2, chloride, and moisture. Restricted and/or limited O_2 and moisture availability during the propagation period at the cathodic region will reduce the corrosion rate (Richardson, 2002; Otieno et al., 2016).

Otieno et al. (2016) reported that for a given binder type and w/b ratio, the average corrosion rate (exposure week 104–120) decreased with an increase in cover depth of 20 mm to 40 mm for uncracked specimens. This trend was observed in the lab and field-tested specimens and is shown in in Figure 2-12. Overall, the blended cements reported the highest reduction in

corrosion rates compared to the OPC. The increase in cover depth also resulted in decrease in corrosion rates for specimens with 0.4 mm and 0.7mm cracks. In Figure 2-12, PC, FA, SL, U, L and F stands for Portland cement, fly ash, slag, uncracked sample, lab sample and field sample, respectively. The 40 and 55 indicates the w/b ratio.

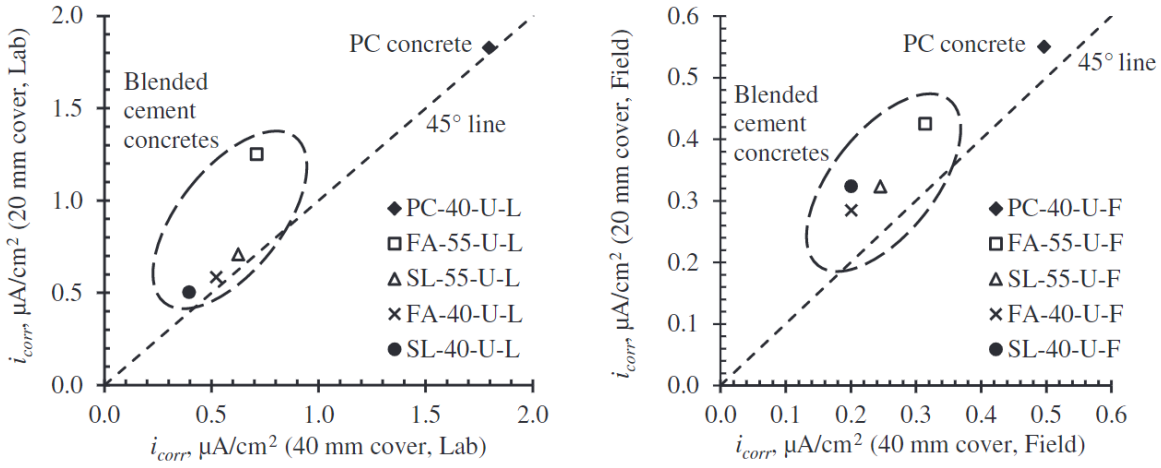

(a) (b)

Figure 2-12: Corrosion rates comparison of uncracked specimens with 20 mm and 40 mm cover depths for lab (a) and field (b) beams (Otieno et al., 2016)

Scott and Alexander (2007) found that for OPC, the corrosion rate decreased with an increase in cover depth from 20 mm to 40 mm. The average corrosion rate for the two crack widths of 0.2 mm and 0.7 mm decreased from 2.94 µA/cm^2 to 1.34 µA/cm^2, which is a 54.4% decrease. The blended cements did not show the same degree of corrosion rate reduction. Blended cement comprising 50% GGBS, 30% FA and 7% SF only resulted in a 2.2%, 33.8% and 10% reduction of corrosion rate, respectively when the cover was increased. The blended cements had sufficiently high resistivity that controlled the corrosion rates. The addition of SCM also decreased the permeability of the concrete, which reduced the O_2 availability at the cathode, thus the increase in cover depth by 20 mm had little to no effect on the corrosion rate.

2.3.5.4 Binder type

The partial replacement of cement with SCM such as SF, slag, and FA improves the porosity and permeability of the concrete matrix, resulting in a denser microstructure. The denser microstructure enhances the concrete's resistance to chloride ingress. SCM such as SF, FA, and slag also has exceptional chloride binding capabilities (Nilsson et al., 1996; Mackechnie,

2001; Beushausen et al., 2021). CCI values decrease by replacing cement with FA, GGBS, and SF and with an increase in concrete grade (Alexander et al.,1999; Mackechnie, 2001).

Otieno et al. (2016) report that the partial replacement of OPC with GGBS and FA increased the concrete quality. For a 0.4 w/b ratio, the 28-day CCI results, OPC, FA and GGBS were 1.24 mS/cm, 0.37 mS/cm and 0.26 mS/cm, respectively. The addition of GGBS and FA also reduced the corrosion rate. Figure 2-12 shows the results for the uncracked field and lab-tested specimens. For the same w/b ratio, the blended cement reduced the corrosion rate between 48% and 78%. The same trend was observed for specimens with incipient. 0.4 mm and 0.7 mm cracks. Scott and Alexander (2007) also report similar reduction in corrosion rates to Otieno et al. (2016) owing to the inclusion of SCM. The experimental work presented by Scott and Alexander (2007) show that the average corrosion rate (crack widths of 0.2 mm and 0.7 mm) for OPC, GGBS, FA, SF were 2.94 μA/cm^2, 0.45 μA/cm^2, 0.68 μA/cm^2 and 0.90 μA/cm^2 respectively. These results are visually represented in Figure 2-13 below. Otieno et al. (2010b) also found that partial replacement of OPC with GGBS resulted in lower corrosion rates

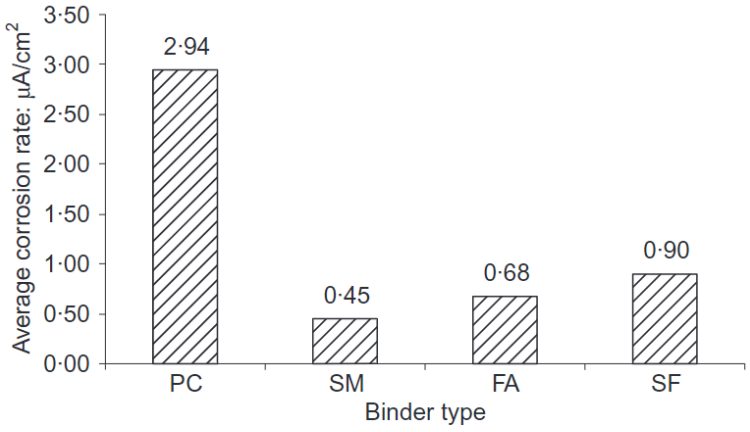

Figure 2-13: Average corrosion rate for specimens with 0.2 mm and 0.7 mm crack widths and 20 mm cover (Scott & Alexander, 2007)

2.3.5.5 Water to binder ratio

The w/b ratio influences concrete strength and cover qualities such as pore structure and permeability. High w/b ratios result in an increase in permeability and lower concrete resistivity. The increase in permeability allows for faster chloride and O_2 ingress that can accelerate the corrosion rate. Low w/b ratios will therefore suppress corrosion propagation (Beushausen et al., 2021; Otieno et al., 2010a).

Otieno et al. (2016) report a decrease in 28-day CCI values and corrosion rates when the w/b decreased from 0.55 to 0.4. CCI values for FA and GGBS reduced with 58.4% and 55.9% respectively. Corrosion rate reductions were as high as 60 % for specimens with a 40 mm cover consisting of FA binder (Figure 2-12). The same trend was observed for specimens with incipient, 0.4 mm and 0.7 mm cracks. Chloride-induced corrosion studies conducted by Mangat, Khatib and Molloy (1994) also report that a reduction in w/b ratio reduced the corrosion rate. Concrete specimens with a 0.45, 0.58 and 0.76 w/b ratio had a corrosion rate of 0.13 94 μA/cm^2, 0.65 94 μA/cm^2 and 2.16 94 μA/cm^2 respectively. Chloride-induced corrosion studies conducted by Otieno et al. (2010b) also report a reduction in corrosion rate with a reduction in w/b ratio.

2.3.5.6 Presence of cracks

The presence of cracks acts as a contaminant ingress pathway, which increases steel corrosion (Beushausen et al., 2021). Crack characteristics, such as crack width and crack spacing are two important factors that influence the corrosion rate.

Larger crack width is known to increase the corrosion rate during corrosion propagation. Scott and Alexander (2007) report that an increase in crack width from 0.2 mm to 0.7 mm resulted in higher corrosion rates. The averaged corrosion rates (exposure week 58–86) for various binders are shown in Figure 2-14. All the corrosion rates increased with an increase in crack width. The largest corrosion rate increase recorded was for a 20 mm cover depth sample consisting of SF, which increased with 67%. Scott and Alexander (2007) state that larger cack widths prevent the autogenous healing of the cracks and facilitate easy chloride transport to the reinforcement, thus leading to a higher corrosion rate. Scott and Alexander (2007) also point out that an increase in crack width increases the exposed steel area, but the exposed area was not explicitly measured in their study. In Figure 2-14, PC, SM, FA and SF stands for Portland cement, slag, fly ash and silica fume, respectively. The 20 and 40 indicated the cover depth and the 0.2 and 0.7 uncracked the crack width. Otieno et al. (2010b) and Otieno et al. (2016) also report an increase in corrosion rate with an increase in crack width. The highest corrosion rate was recorded for specimens with a crack width of 0.7 mm, followed by 0.4 mm, for incipient crack and uncracked specimens.

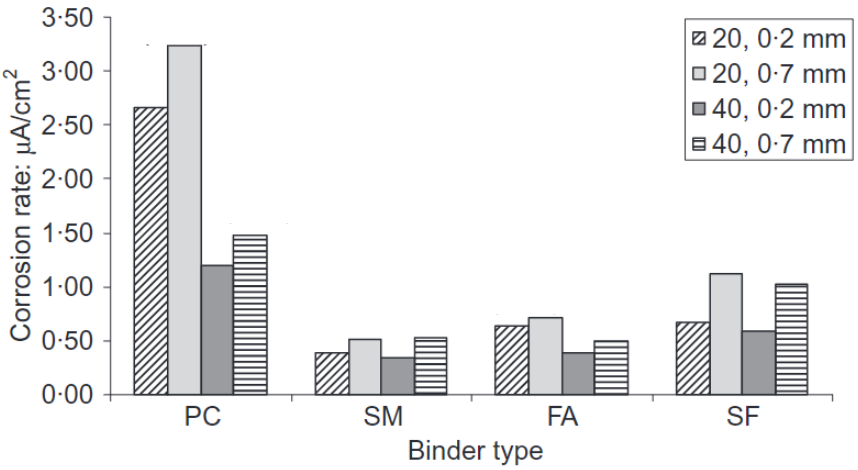

Figure 2-14: Average corrosion rates (week 58–86) for various binders with crack width of 0.2 mm and 0.7 mm (Scott & Alexander, 2007)

Crack spacing has an influence on the corrosion mechanisms during the corrosion propagation phase. Chloride-induced chorion studies by Paul and van Zijl (2017) on reinforced strain-hardening cement-based composites (SHCC) show that the crack spacing had a significant effect on the corrosion damage of the embedded steel. The results show that a decrease in crack spacing (larger number of cracks in a given specimen) resulted in less corrosion damage compared to larger crack spacings. Larger crack spacings increase the cathode to anode ratio, which results in dominant pitting corrosion. The average crack spacing versus the average pitting depth is showed in Figure 2-15. In Figure 2-15, R, FS2, CS2, FS31 stands for reinforced SHCC sample, fine sand with CEM I 41.5 cement, coarse sand with CEM I 41.5 cement and fine sand with CEM I 521.5 cement, respectively. The same trend was observed by Paul and van Zijl (2016), where higher pitting corrosion was observed when the crack spacing increased. Reports from Van Zijl, Bezuidenhout and van Rooyen (2018) also indicate that chloride-induced corrosion is higher for larger crack spacings.

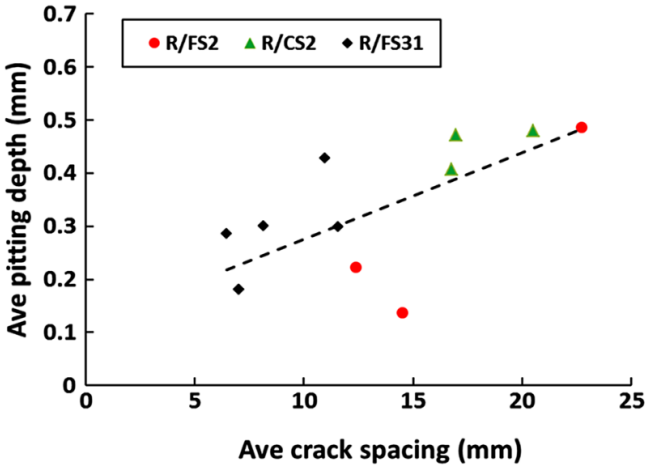

Figure 2-15: The average crack spacing compared to the average pitting depth (Paul & van Zijl, 2017)

Van Zijl and Boshoff (2018) studied the effect of the crack pattern on the corrosion of the steel reinforcement of SHCC. The results show that average and maximum pitting depth increased with an increase in average crack spacing. The authors propose corrosion mechanisms based on the crack spacing width and chloride ingress. The three regions are shown in Figure 2-16. In region one, the crack spacing is smaller than the chloride ingress width (S_{Cl}) that causes the steel depassivation to occur over the total length of the bar. This leads to a uniform corrosion over the bar length with microcell corrosion being the dominant corrosion mechanism taking place. In region three, the crack spacing is larger than the chloride penetrating width. The increases in cathode to anode ratio result in pitting corrosion, with macrocell corrosion being the dominant corrosion mechanism present. Pitting corrosion results in larger corrosion rates. Region two is the transition region between micro- and macrocell corrosion.

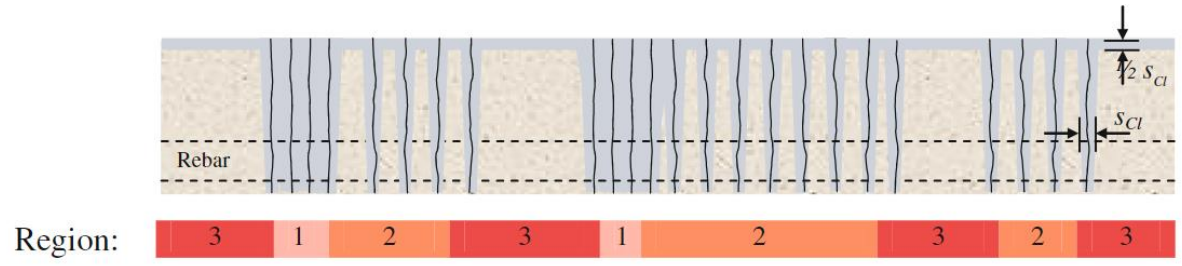

Figure 2-16: Three crack spacing regions based on the chloride ingress profile (Van Zijl & Boshoff, 2018)

2.3.6 South African chloride ingress model

The South African chloride ingress model was developed based on RC structures and marine concrete testing of samples at numerous sites in the Cape Peninsula in the Western Cape of South Africa. Good correlations have been established between the 28-day CCI values and two-year apparent diffusion coefficient (Mackechnie & Alexander, 1999; Mackechnie, 2001).

The chloride ingress is modelled according to Fick's second law of diffusion and incorporates the reduction in diffusion coefficient with time (Equations 2-19 and 2-20). This model uses the 28-day CCI value, binder type, and exposure category as input parameters. The binder considered is limited to OPC and standard conventional SCM replacement types (10% SF, 30% FA, and 50% GGBS) used in South Africa. Exposure conditions considered are extreme, very severe, and severe, which is based on BS 8110-1 (1985) guidelines. Factors such as chloride binding and continuous cementing reactions are considered in this model (Mackechnie, 2001). The input values for Equations 2-19 and 2-20 are established using the input parameters in Table 2-7.

Table 2-7: Applicable input parameters to obtain input values for Equations 2-19 and 2-20

Value	Input parameters considers
C_s	Binder type, exposure condition
$D_{a,r} = D_{a,2\ years}$	28-day CCI value, binder type, exposure condition
t_r	2 years
γ	Binder type

2.4 Concrete carbonation

2.4.1 Carbonation process and overview

Carbonation is the physiochemical reaction between the CO_2 and the unhydrated cement constituents and cement hydration products. Typically, more than 85% of the hardened cement paste mass consists of calcium hydroxide ($Ca(OH)_2$ or CH) and calcium silicate hydrate (CSH). The unhydrated cement constituents such as dicalcium silicate and tricalcium silicate, are also susceptible to carbonation, but only near the concrete surface. Since the unhydrated cement

constitutes only make up less than 15% of the final hardened cement paste mass and have no influence on the bulk cement carbonation, they are neglected. The CO_2 diffuses through the concrete cover and dissolves into the concrete pore solution. The CO_2 reacts with CH and CSH in the concrete pore solution (Bensted, 1983; Papadakis & Vayenas, 1989). Both of these reactions produce calcium carbonate ($CaCO_3$) in the form of calcite, vaterite or aragonite. The presence of moisture in the pores is essential because it acts as a medium for both reactions (Papadakis & Vayenas, 1989; Šavija & Luković, 2016). The two main carbonation reactions between CH and CSH with CO_2 are shown in Equations 2-25 and 2-26 (Šavija & Luković, 2016).

$$Ca(OH)_2 + CO_2 \rightarrow CaCO_3 + H_2O \qquad 2\text{-}25$$

$$(CaO)_x.(SiO_2).(H_2O) \ + x\, CO_2 \rightarrow xCaCO_3 + SiO_2(H_2O)t + (z-t)H_2O \qquad 2\text{-}26$$

As mentioned in Chapter 1.1, the high alkalinity of the concrete forms a passive layer around the reinforcement that protects it against corrosion. The reaction in Equation 2-25 results in a reduction in OH^- which is responsible for the alkaline state of the concrete. This reaction ultimately lowers the pH of the concrete's pore solution to 8.3 and results in the formation of a carbonation front. The carbonation front divides the concrete into a carbonated and uncarbonated region, as shown in Figure 2-17. A phenolphthalein indicator is normally sprayed on the fresh concrete surface to detect the depth of the carbonation front. The indicator will turn purple when the pH of the concrete is higher than 9. Carbonated areas will remain a clear grey colour, whereas the uncarbonated region turns purple. Once the carbonation front reaches the reinforcement, the low pH of the pore solution (pH< 9) destroys the passive layer (Heckroodt, 2002). In the presence of sufficient O_2 and moisture content, steel corrosion occurs (Richardson, 2002) .

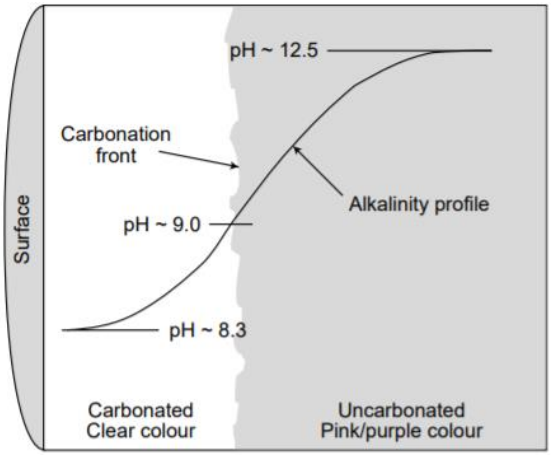

Figure 2-17: Carbonation profile of a partially carbonated core (Heckroodt, 2002)

2.4.2 Microstructural changes owing to carbonation

Concrete carbonation results in microstructural changes to the concrete matrix. Changes in the porosity and permeability occur, as well as carbonation shrinkage.

2.4.2.1 Changes in porosity

The formation of calcium carbonate changes the porosity of the concrete matrix. Binders consisting only of OPC experience a decrease in porosity and permeability when exposed to CO_2. The carbonation of CH results in the net increase of volume (Equation 2-25) owing to the net increase in the volume from the hydration products to calcium carbonate. The increases in volume are dependent on which calcite polymorph is formed (Šavija & Luković, 2016). The increase in volume for calcite, aragonite, and vaterite is 11.2%, 2.9% and 18.7% respectively (Arandigoyen, Bicer-Simsir, Alvarez & Lange, 2006). The low soluble calcium carbonate refines the pore structure by causing pore blocking (Šavija & Luković, 2016). Paul, Panda, Huang, Garg and Peng (2018) studied the permeability and porosity of carbonated OPC. The results show that the carbonation reduced the porosity and permeability. Qin, Gao and Chen (2019) used carbonation as a curing method to densify the concrete matrix. They also reported that the carbonation of OPC reduced the total porosity and pore diameter. In the case of blended cements, the amount of CH is reduced owing to the pozzolanic activity. The reaction between the CSH and CO_2 results in the decalcification of the CSH. Calcium ions are released into the porous media to form a silica gel (Equation 2-26) that has a smaller molar volume than CSH before carbonation commenced (Morandeau, Thiéry & Dangla, 2014). Ngala and Page (1997) report that the partial replacement of OPC with FA and GGBS resulted in a coarser capillary pore structure that contributed to the decalcification of the CSH.

2.4.2.2 Carbonation shrinkage

Carbonation shrinkage may cause cracking that reduces the concrete's ability to combat CO_2 ingress. There are two mechanisms regarding the root of carbonation shrinkage. The first mechanism regards the carbonation of CH. Evaporation of the H_2O (produced during Equation 2-25), that is not trapped within the passivation layer of the calcium carbonate will result in a moisture content gradient and will cause cracking. The second mechanism is based on the decalcification of the CSH. Decalcification causes polymerisation of the silicate chains in CSH, loss in interparticle cohesion of CSH, and structural reorganisation. All of these factors lead to carbonation shrinkage and, if restrained, to cracking (Šavija & Luković, 2016).

2.4.3 Factors that influence concrete carbonation

The rate of concrete carbonation is dependent on various factors. Exposure conditions, such as RH, temperature, and CO_2 play an important role. The partial replacement of OPC with SCM (binder type) and the w/b ratio will also affect the carbonation rate. The presence of cracks will also implicate concrete resistance to carbonation.

2.4.3.1 Relative humidity

The RH controls two mechanisms, i.e. the gaseous diffusion of CO_2 and the carbonation reaction rate. Low RH levels (below 45%) allow for fast CO_2 diffusion but hinder the rate of carbonation owing to the lack of moisture that facilitates the carbonation reactions and the dissolution of CH and CO_2. When RH is elevated (above 75%), moisture partially and fully saturates the pores, that block or reduce the rate of CO_2 ingress. The carbonation rate is at a maximum when the RH is between 50% and 75%, which provides a balanced environment for CO_2 diffusion and the carbonation reactions (Richardson, 2002).

Papadakis and Vayenas (1989) studied the carbonation front on OPC at various levels of RH. The results show that the carbonation front reached a peak between 50% and 65%. An increase in RH resulted in a decrease in the carbonation front (Figure 2-18). Lu, Wang, Li, Hao and Xu (2018) studied the carbonation resistance of various concrete moistures at relative humidities of 50%, 60%, 70%, 80%, and 90%. The results show that the highest carbonation depth for all the concrete mixtures was recorded at 50% RH and deceased with an increase in RH.

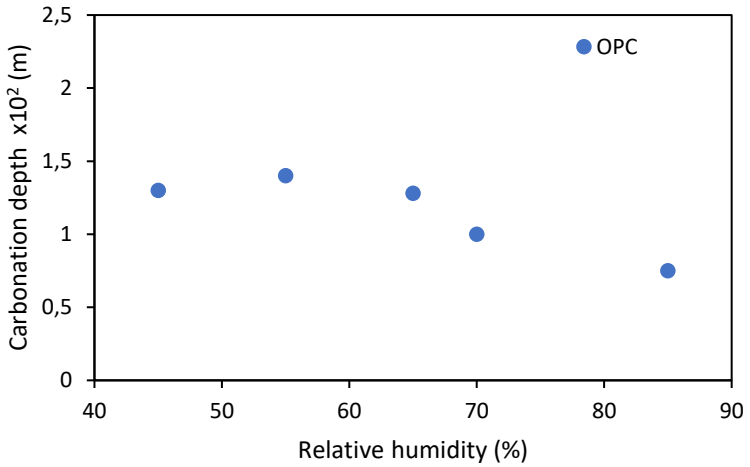

Figure 2-18: Five-day carbonation depth of OPC at 50% CO_2 exposure, reproduced from Papadakis and Vayenas (1989)

2.4.3.2 CO_2 concentration

CO_2 in the natural environment forms the basis of carbonation-induced corrosion. The higher the concentration of CO_2 in the atmosphere, the higher the degree of carbonation will be (Richardson, 2002). The main contributor to the increasing CO_2 concentration in the atmosphere is the increasing fossil fuel energy consumption that releases CO_2 when it is burnt (Cui, Tang, Liu, Dong & Zing, 2015). Ades, Adler, Aldeco, Alejandro, Alfaro et al. (2019) report, in the State of the Climate in 2018, that the global concentration of CO_2 in the atmosphere in 2018 was 407.4 ppm (0.04074 %). Over the past 10 years the increase in CO_2 content is 2.33 ppm per year on average. The concerning concentration increase will make RC more susceptible to carbonation-induced corrosion in the future.

2.4.3.3 Temperature

The increase in temperature results in an increase in carbonation reaction rate (Beushausen et al., 2021). Lu et al. (2018) report that an increase in micro-temperature (6 ℃ to 33 ℃) at a constant micro-humidity of 80%, resulted in an increase in carbonation depth. Lu et al. (2018) explain that higher temperatures promote the gaseous diffusion rate of CO_2 into concrete and increase the carbonation reaction rate. The high temperatures, at the specific relative humidity, decrease the pore saturation, which also increases the CO_2 diffusion rate. Papadakis, Vayenas and Fardis (1991b) recorded a slight increase in carbonation depth when increasing the temperature from 22 ℃ to 42 ℃. The RH was kept constant at 65%. The CO_2 uptake increased by more than 600% when the temperature increased from 20 ℃ to 60 ℃. However, for

temperatures above 60 ℃, the uptake reduced for increasing temperatures. The decrease in concrete carbonation for temperatures above 60 ℃ is attributed to the decrease in solubility of calcium and CO_2 in water.

2.4.3.4 Curing

The quality of the concrete cover, referring to porosity and permeability, is affected significantly by the curing conditions. The curing of concrete in a moist environment provides the necessary moisture for a high degree of cement hydration and pozzolanic activity, which will densify the microstructure. Longer curing durations will also ensure a denser microstructure. The dense microstructure acts as a barrier for CO_2 ingress (Beushausen et al., 2021). Younsi, Turcry, Rozire, Aït-Mokhtar, & Loukili (2011) investigated the degree of carbonation under different curing conditions. The specimens were stripped 24 hours after casting and were either cured in H_2O or in room conditions for the remaining 27 days. Porosity studies done on the specimens showed that the H_2O cured specimens were 10%–20% less porous that the room-cured specimens. A 14-day accelerated carbonation test at 50% CO_2 concentrations was performed on the specimens. The reduction in porosity was reflected in the carbonation resistance of the concrete cover. The H_2O cured specimens outperformed the room-cured specimens. The carbonation depths for H_2O curing was 20%–50% lower compared to room curing, showing that the dense microstructure yielded from proper curing conditions can enhance carbonation resistance.

2.4.3.5 Binder type

SCM such as GGBS, SF, and FA are high silica industrial by-products that are used to replace OPC in concrete mixtures. The SCM silica content reacts with the CH and H_2O to form CSH. The CSH produced from the pozzolanic reaction is similar to the CSH produced during cement hydration reactions (Domone & Illston, 2010). The consumption of CH reduces the alkalinity of the concrete making it more suspectable to carbonation and carbonation-induced corrosion. The reduction of alkalinity is neutralised by the refinement of the pore structure, and permeability decreases as a result of the filler effect produced by pozzolanic reaction. The permeability reduction effect of SCM will improve the concrete's carbonation resistance (Richardson, 2002).

Salvoldi et al. (2015) studied the effect of partial replacement of OPC with GGBS (50%), FA (30%), and SF (10%) on the concrete's permeability and carbonation resistance. The results

showed that the inclusion of SCM improved the pore structure by reducing the permeability. The O_2 permeability coefficients are shown in Figure 2-19a. In this case, the permeability was not the governing factor determining the concrete's resistance to carbonation. The 12-week accelerated carbonation depth (Figure 2-19b) shows that OPC yielded slightly lower carbonation depths compared to SF and outperformed the blended cements containing FA and GGBS. This was because of the amount of carbonatable material each concrete mixture had. The OPC mix did not have any pozzolanic activity that consumes the Portlandite, which results in a larger amount of carbonatable material and reserve alkalinity. Papadakis (2000) found similar results when OPC was replaced with FA and SF. The carbonation depth also increased with an increase of cement replacement. High calcium FA and SF performed the same with the same amount of OPC replacement. Low calcium FA resulted in the highest carbonation depth, for the same amount of cement replacement.

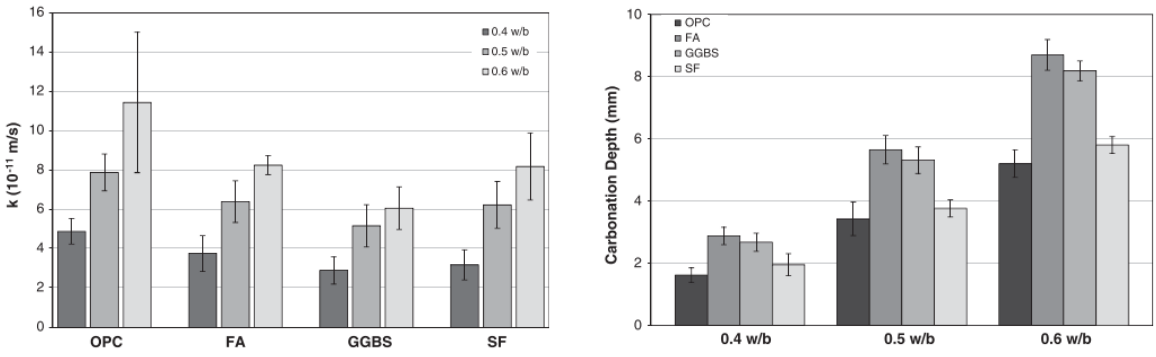

(a) (b)

Figure 2-19: O_2 permeability coefficient (a) and 12-week carbonation depth (b) for various binder and w/b ratios (Salvoldi et al., 2015)

2.4.3.6 Water to binder ratio

It is well known that an increase in the w/b ratio results in an increase in permeability, pore diameter, and porosity, thus leaving it more prone to carbonation (Papadakis et al., 1991c; Beushausen et al., 2021). From Figure 2-19a and 2-18b, the influence of the w/b ratio is pronounced. For a given binder type, an increase in w/b ration resulted in a more permeable concrete matrix that resulted in higher carbonation depths. For all the binder types, the 0.4 w/b ratio outperformed the 0.5 w/b and 06 w/b ratio binders (Salvoldi et al., 2015). Papadakis and Vayenas (1989) also reported that an increase in w/b ratio results in a high carbonation depth.

2.4.3.7 Presence of cracks

The presence of cracks influences the concrete resistance to CO_2 ingress negatively, where the cracks act as an ingress path for the CO_2 (Song, Kwon, Byun & Park, 2006). Carević and Ignjatović (2019) studied the effect of loading cracks on concrete carbonation. Crack widths of 0 mm, 0.05 mm, 0.10 mm, 0.15 mm, 0.2 mm, and 0.3 mm were studied under 28-day accelerated carbonation conditions. The results showed that the cracks behaved as an additional exposed surface and CO_2 ingresses perpendicular to the crack wall. On each side of the crack, about 10 mm, also resulted in higher CO_2 ingress compared to other uncracked regions. The carbonation depth increased with an increase in crack width, and the smallest crack width (0.05 mm) recorded a carbonation depth of more than double that of the uncracked regions. The 28-day carbonation depths are shown in Figure 2-20. In Figure 2-20, $x_{c,Acc}$ and w stands for carbonation depth and crack width, respectively. Al-Ameeri, Rafiq, Tsioulou and Rybdylova (2021) also report an increase in carbonation depth with an increase in crack width.

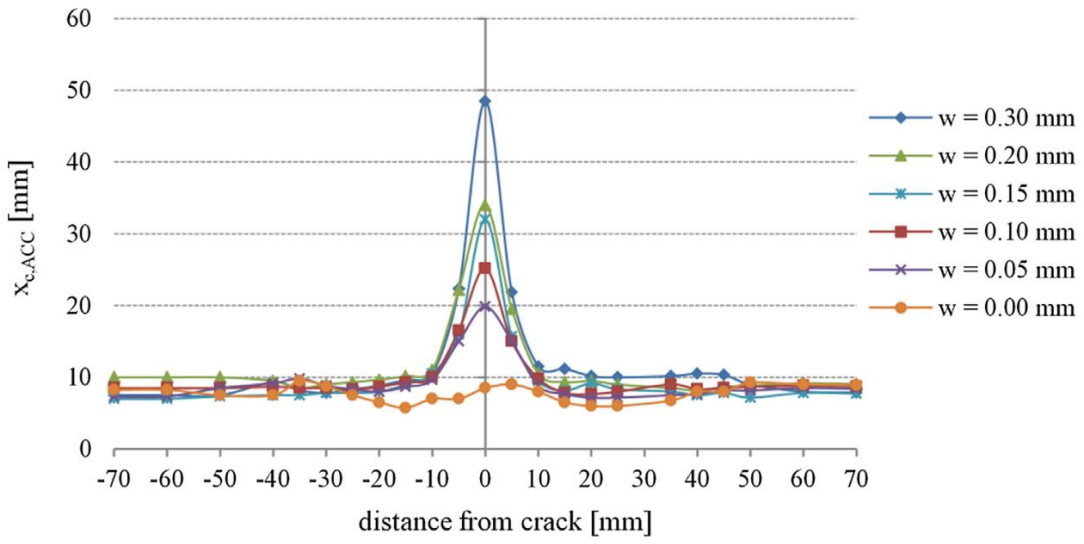

Figure 2-20: 28-day Carbonation depths for various crack widths (Carević & Ignjatović, 2019)

2.4.4 Carbonation depth prediction models

To be able to predict the carbonation depth at a given point in time enables us to estimate the time until the carbonation front reaches the reinforcement. This ability plays an import role in determining the durability of a RC structure. Literature has shown that the carbonation depth is proportional to the square root of time, as shown in Equation 2-27. The carbonation

coefficient is a value that combines the effect of the diffusivity, reserve alkalinity of the concrete, environmental exposure conditions, and CO_2 concentration (Richardson, 2002).

$$x_c = A_{CO2}.\sqrt{t} \qquad 2\text{-}27$$

where

x_c - Carbonation depth

A_{CO2} - Carbonation coefficient

2.4.4.1 The Meyer, Wierig and Husmann (1967) model

Meyer et al. (1967) developed a mathematical model of CO_2 ingress to verify the square root of the relationship between the carbonation depth and time. The theoretical model is based on the constant diffusion of CO_2 into the concrete, according to Fisk's first law of diffusion (Chapter 2.2.1.3) and the chemical reaction between CO_2 and Portlandite/CH. The parameters associated with the Meyer et al. (1967) model is illustrated in Figure 2-21.

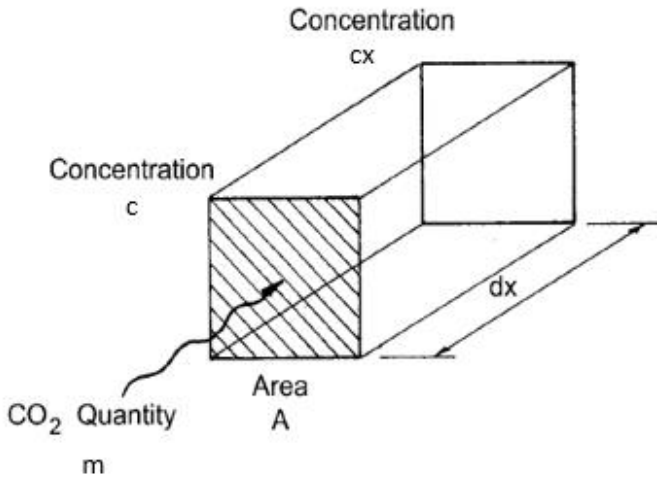

Figure 2-21: Visual representation of the Meyer et al. (1967) model (Richardson, 2002)

where

m - Amount of CO_2 diffusing though the diffusion area

A - Area of CO_2 diffusion

c - CO_2 surface concentration

c_x - CO_2 concentration at distance x

a - Amount of carbonatable material (CH)

The diffusion of CO_2 into concrete is modelled according to Fick's first law and is shown in Equation 2-2. The model assumes that the carbonation front can only increase if all the CH at depth x is consumed by the CO_2. The chemical reaction between CH and CO_2 is based on Equation 2-25 and is expressed in Equation 2-28. The carbonation depth equation can be determined by assuming that CO_2 concentration at depth x is equal to zero, substituting Equation 2-28 into Equation 2-29 and integrating with respect to time and depth. The final solution is shown in Equation 2-30.

$$dm = -D.A.\frac{c - c_x}{x}.dt \quad \text{2-28}$$

$$dm = \text{a.A.dx} \quad \text{2-29}$$

$$x_c = \sqrt{\frac{2.D.c.t}{a}} \quad \text{2-30}$$

This model forms the basis for most of the carbonation depth models that have been developed. Researchers have adjusted the model by incorporating the influence of wetting periods, RH, loading, temperature, etc.

2.4.4.2 South African carbonation model

The South African carbonation prediction model was adapted from Equation 2-27. The model considers the 28-day OPI value, binder type, and environmental conditions (RH) as input parameters. In Equation 2-31, the carbonation coefficient is related to the OPI and environmental conditions. The power 'φ' is determined by the binder type. This model is limited to OPC and conventional SCM replacement types and levels (10% SF, 30% FA, and 50% GGBS/GGCS) used in South Africa. It is also only applicable to dry inland, coastal, and partly wet environments that correspond to 60%, 80%, and 90% RH respectively (Alexander, Mackechnie et al., 1999).

where

$$x_c = A_{SA,DI}.t^{\varphi} \quad 2\text{-}31$$

$A_{SA,DI}$ - Carbonation coefficient based on 28-day OPI and exposure environment

φ - Constant based on binder type

2.4.4.3 The Salvoldi et al. (2015) model

Salvoldi et al. (2015) expanded on Meyer et al. (1967) and the South African model. This model expanded on the South African model by incorporating various other influential conditions, such as time of wetting, CO_2 concentration, RH, and the chemical composition of the binder under consideration. The chemical composition incorporates the degree of hydration, pozzolanic activity as well the amount of carbonatable martial (CH in this case). The broader range of input parameters makes this model more applicable to different binder combinations. The Salvoldi et al. (2015) model equation is shown in Equation 2-32.

$$x_c = \sqrt{\frac{2.D_{dry}.\beta.c.t_e}{a}} \quad 2\text{-}32$$

where

D_{dry} - Effective dry CO_2 diffusion coefficient

β - RH coefficient

t_e - Effective exposure time

2.4.4.4 Otieno, Ikotun and Ballim (2020) model

Otieno et al. (2020) proposed an empirical model for natural carbonation. The model was developed by exposing concrete cubes to natural carbonation conditions. The samples were exposed to typical urban inland environments such as indoor, outdoor sheltered, and outdoor unsheltered. OPC formed the basis of the binder and was partially replaced with FA (30%), GGBS (50%), SF (10%), and GGBS/SF (30% and 10%). Various w/b ratios were also

investigated. The 28-day WSI and OPI results were used to characterise the concrete quality. The model showed a perfect coefficient of determination (R^2) between the predicted carbonation depth and actual carbonation depths for all the binder types and exposure conditions (R^2 of 1). The binder chemistry is not directly incorporated into the model but is indirectly incorporated through the regression and constant. The carbonation model is expressed in Equations 2-33 and 2-34.

$$x_c = A_{28}.\sqrt{t} \qquad 2\text{-}33$$

$$A_{28} = R_1.(OPI_{28}) + R_2.(WSI_{28}) + R_3 \qquad 2\text{-}34$$

where

A_{28} - Carbonation coefficient based on the 28-day DI results

OPI_{28} - 28-day OPI

WSI_{28} - 28-day WSI

$R_{1,2\ and\ 3}$ - Regression coefficients based on the binder type and exposure

2.5 Three-dimensional concrete printing

The traditional method of concrete construction involves the installation of temporary structures (formwork), which act as a mould for the construction of structural concrete elements. The concrete is poured into the formwork and compacted to remove all the entrapped air to ensure a high density. Formwork plays an essential role in the current construction process but makes a large contribution towards total construction cost and time. It is estimated that formwork labour and material contribute 34% and 20% of the total concrete construction cost respectfully. It also accounts for 50% to 75% of the construction time (Chua & Leong, 2014; Paul, van Zijl et al., 2018). Converting from formwork-based construction to automated construction, especially referring to AM, will result in time- and cost savings and will utilise materials more efficiently (Paul, van Zijl et al., 2018).

The most widely applied AM technique in the construction industry is 3DCP, which is an extrusion-based technique that constructs concrete elements by printing consecutive concrete layers, pumped through a nozzle, upon each other (Le, Austin, Lim, Buswell, Gibb et al., 2012). 3DCP mix designs differ from a conventional concrete mix design and should have good pumpability, extrudability, buildability, and open time (Le et al., 2012; Paul, van Zijl et al., 2018).

2.5.1 Thixotropic behaviour of 3D concrete printing mix designs

The thixotropic behaviour of the 3DCP mix design is needed to ensure good pumpability, extrudability, and buildability. Thixotropic materials have a high static viscosity and have two behaviour phases. When the static material experiences shear stress, the intermolecular forces of the material deconstruct, become less viscous and turn into flowable material. This phase is known as the break-down phase and the static yield shear stress needs to be exerted on the material to ensure flowability. After flowability is reached, only the dynamic yield shear stress is needed to ensure that the material remains in a flowable state (Figure 2-22). The flowable state allows the material to be pumped and extruded efficiently and without clogging (Björn, Segura de la Monja, Karlsson, Ejlertsson & Bo, 2012; Kruger, van den Heever, Cho, Zeranka & van Zijl, 2019; Kruger, Zeranka & van Zijl, 2019). The rebuilding phase starts after the pumping and extruding of the material. After extrusion, the material experiences zero pumping agitation shear stress and is at rest. This results in an increase in intermolecular forces and the recovery of the material's viscosity. The increase in viscosity enhances the buildability of the material and reduces the deformation of the layers under self-weight (Kruger, van den Heever et al., 2019; Kruger, Zeranka et al., 2019).

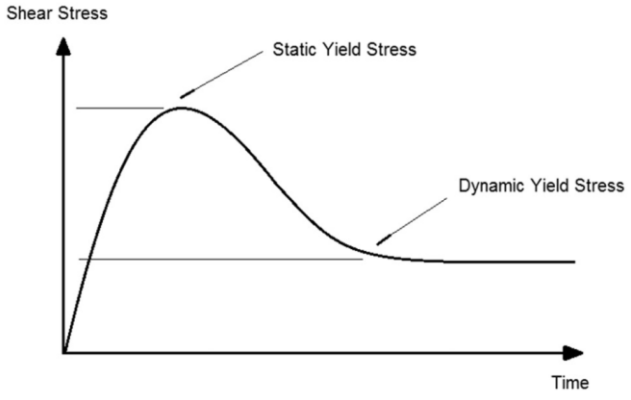

Figure 2-22: Thixotropic material shear stress growth versus time behaviour (Kruger, Zeranka et al., 2019)

2.5.2 Incorporation of reinforcement in 3D concrete printing

Concrete has high compressive strength and relatively low tensile capacity. The ratio of concrete tensile to compressive strength is about 1:10. Therefore, reinforcement is added to concrete structures to account for the lack of tensile capacity (Domone & Illston, 2010). One of the challenges in 3DCP is the incorporation of reinforcement in printed elements to account for the lack of tensile strength, to counteract shrinkage, and to provide ductility (Stefanoni, Angst & Elsener, 2019). Reinforcement in 3DCP can either be preinstalled, installed during printing, or post-installed.

2.5.2.1 Pre-installed reinforcement

Pre-installed reinforcement can be incorporated by enveloping concrete around pre-installed vertical and horizontal reinforcement using a forked nozzle. This method uses two nozzles that deposit vibrated conventional concrete on each side of the vertical reinforcement (Scott, 2016; Sanjayan, Nazari & Nematollahi, 2019). A similar enveloping technique is also used by Marchment and Sanjayan (2020a). The Mesh Mould method is an approach that combines the concepts of formwork and reinforcement. A robot is programmed to produce the complex, free-form reinforced mesh by bending, cutting, and welding the steel together. The mesh is subsequently filled with concrete and the surface of the element is finished off with a cover layer (Hack, Wangler, Mata-Falcón, Dörfler, Kumar et al.,2017).

2.5.2.2 In-process reinforcement

The in-process technique involves incorporation of horizontal and/ or vertical reinforcement during the printing procedure. Andrey Rudenko from Total Kustom incorporates horizontal reinforcement by placing the steel bars manually between the printed layers during the printing procedure (Print 3D, 2014). This process is illustrated in Figure 2-23a. The Eindhoven University of Technology uses a hybrid down/back-flow nozzle with a metal cable that feeds into it. The nozzle extrudes a metal cable and concrete layer simultaneously, as shown in Figure 2-23b. The hybrid nozzle also improves the inter-layer bond strength between subsequent layers and ensures that the metal cable is placed in the centre of the extruded layer (Bos, Ahmed, Jutinov & Salet, 2017). Bester, van den Heever, Kruger, Cho & van Zijl (2020) and Kruger, Cicione, Bester, van den Heever, Cho et al. (2020) installed vertical reinforcement by manually placing steel fibres in the printed layers during printing. The steel fibres are placed orthogonal to the extrusion direction and connect the subsequent layers. This technique was

implemented to improve the ductile behaviour of printed elements, and of printed elements exposed to fire (Figure 2-23c).

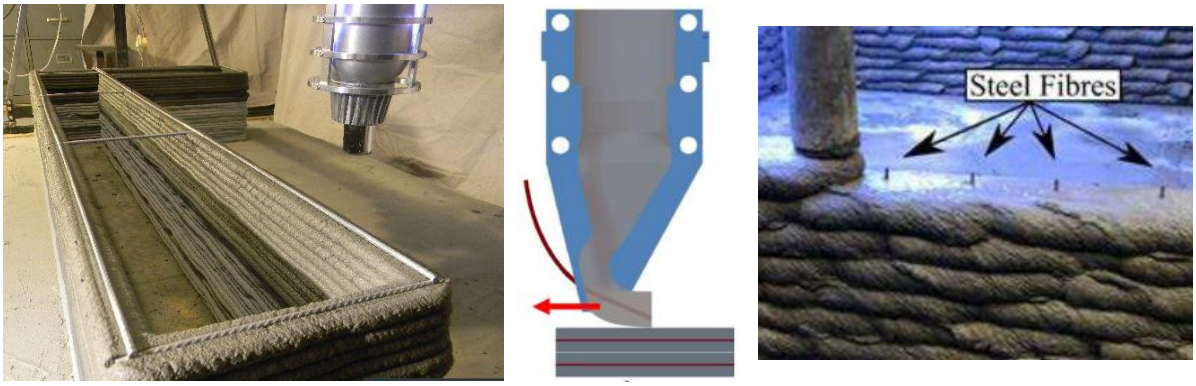

(a) (b) (c)

Figure 2-23: In-process incorporation of horizontal (a and b) (Print 3D, 2014; Salet, Ahmed, Bos & Laagland, 2018) and vertical (c) reinforcement (Kruger et al., 2020)

2.5.2.3 Post-installed reinforcement

The most used technique to incorporate vertical and horizontal reinforcement simultaneously is the '3D-printed integrated formwork' technique. WinSun and Apiscor are 3D printing construction companies that use this technique. The outer shell of the element is 3D printed, and after printing is completed, the reinforcement is manually placed inside the printed element. The printed element acts as permanent formwork. The element is filled with conventional concrete and vibrated to compact the concrete. The integrated formwork approach is the most effective way to date to incorporate vertical reinforcement (Sevenson, 2015; Nerella, Ogura & Mechtcherine, 2018). Marchment and Sanjayan (2020b) use the bar penetration technique to incorporate reinforcement. After printing is completed, the reinforcement is pushed into the printed layers so that the reinforcement aligns perpendicular to the printed layers. The reinforcement bars are guided by a metal jig to ensure that the bar follows a straight line.

2.5.3 Lack of fusion in 3D concrete printing

One of the main disadvantages associated with 3DCP elements is the weak interlayer bond strength between subsequent printed layers that creates a heterogeneous structure. Several studies have found that the lack of fusion between printed layers resulted in a decrease in mechanical, durability, and thermo-mechanical performance (Kruger & van Zijl, 2021). These reductions are mainly caused by the formation of cold joints at the IR owing to the principle of

layer extrusion-based 3DCP (Roussel & Cussigh, 2008; Nerella et al., 2017; 2019). These cold joints are similar to those found in conventional cast concrete were fresh concrete is placed on older concrete that has already passed the initial setting time, thus limiting the intermixing of the two layers (Kruger & van Zijl, 2021).

2.5.3.1 Mechanisms that result in lack of fusion at the interlayer region

A comprehensive review on the lack of fusion presence in 3DCP by Kruger and van Zijl (2021) investigated several research publications regarding the mechanical performance and microstructure of 3DCP elements. The review reported four mechanisms responsible for lack of fusion, namely surface moisture, air entrapment, thixotropic behaviour, and surface roughness. The mechanisms reported are mostly based on the reduction in mechanical performance with the aid of microstructural characteristics. Even though the mechanical performance is not a precise measurement of the concrete's potential durability performance, it does give a clear indication that the lack of fusion at the IR can result in durability issues. In Chapters 2.5.3.1.1 to 2.5.3.1.4 more focus is placed on the IR porosity and permeability as a result of the lack of fusion mechanisms.

2.5.3.1.1 Surface moisture

Various researchers have attributed the lack of fusion and reduction in mechanical strength of 3DCP samples to the reduction in surface moisture through evaporation. The mechanism of surface moisture evaporation is illustrated in Figure 2-24 below. After the first layer is printed, H_2O evaporates from the surface of the printed layer leaving a more dry, rigid, and porous surface for the second layer to be printed on. As a result, the layer also has limited layer-intermixing capabilities (Nerella et al., 2019; Kruger & van Zijl, 2021). After the second layer is printed, H_2O migrates from the second to the first layer through capillary absorption and causes air to be forced out of the first layer into the IR, where it is trapped. This is known as the moisture transfer/exchange phenomenon that causes an increase in porosity and permeability at the IR (Van der Putten, Deprez, Cnudde, De Schutter & Van Tittelboom, 2019; Kruger & van Zijl, 2021). H_2O migration results in an increase in unhydrated cement particles at the IR. The H_2O shortage influences the degree of hydration of the second layer negatively, resulting in a weak chemical bond at the IR (Luković & Ye, 2016; Kruger & van Zijl, 2021). Factors such as low RH, high temperatures, high wind speeds, and long pass time contribute to a high degree of moisture evaporation that will result in lack of fusion at the IR (Beushausen et al., 2021). The pass time refers to the duration between the printing of consecutive layers

(Van Der Putten, De Schutter & Van Tittelboom, 2019). The absence of formwork also amplifies evaporation of the printed layers that can result in plastic shrinkage and micro-cracks (Van Der Putten, Deprez et al., 2019; Van Der Putten, Azima et al., 2020).

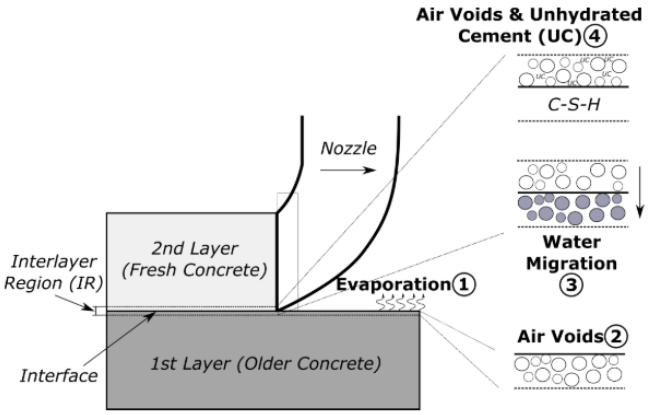

Figure 2-24: Illustration of surface moisture reduction owing to evaporation (Kruger & van Zijl, 2021)

Kruger et al. (2021) investigated the porosity and permeability of extrusion-based 3DCP. X-ray micro-computed tomography (μCT) tests were performed on printed samples with pass times varied from 0 min to 60 min in increments of 15 min. These samples were printed in environmental conditions of 16ºC and 40% RH, which resulted in the evaporation mass loss of the specimens to be at 0.04 +-m0.02 kg/m^2/h. The μCT scans in Figure 2-25 show that for a 0 min pass time the IR is not visible owing to minimal surface moisture evaporation. As the pass time increases, resulting in surface moisture evaporation, the IR region becomes more visible and prominent (Figure 2-25). For the 15 min and 30 min pass time, the IR consists mainly of smaller voids and has the same pore size and shape of the printed layer, whereas for longer pass times (45 min and 60min), the pores at the IR are more interconnected and elongated resulting in larger voids.

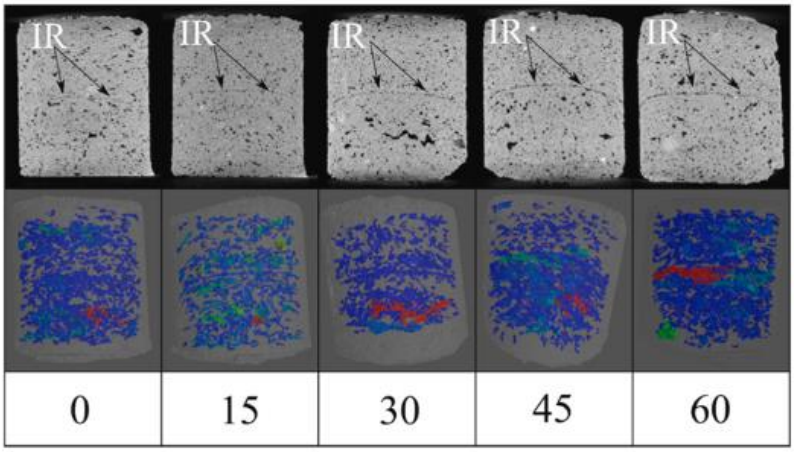

Figure 2-25: μCT-scan images and 3D porosity rendered from 3DCP samples for 0 min, 15 min, 30 min, 45 min, and 60 min pass time (Kruger et al., 2021)

Van Der Putten, Deprez et al. (2019) investigated the influence of the pass time (0 min, 10 min, 30 min, and 60 min) on the microstructural characteristics of the printed specimens by conducting scanning electron microscope (SEM) tests, mercury intrusion porosimetry (MIP) tests, and μCT scans tests on the printed specimen. The SEM analysis revealed that the experiments with a pass time larger than 0 min had a larger amount of unhydrated cement particles in the top layer compared to the bottom. This is as a result of the moisture transfer from the top to bottom layer, reducing the available H_2O for cement hydration in the top layer. MIP results, comparing the top layer, showed that introducing a pass time resulted in an increase in pore size compared to the 0 min pass time samples. The IR between the top and bottom layer also showed an increase in porosity and pore size for samples with an induced pass time compared to the 0 min pass time samples. The μCT-scan images for the 0 min (Figure 2-26a) and 10 min pass time (Figure 2-26b) in Figure 2-26 below show the voids between 0.1 and 0.45 flatness, where 0 is flat and 1 is round. The results show that the voids at the IR are flatter, more elongated and interconnected compared to the bulk layer, which increases the IR's permeability. This occurrence is pronounced in the 10 min pass time owing to the high level of evaporation and moisture transfer.

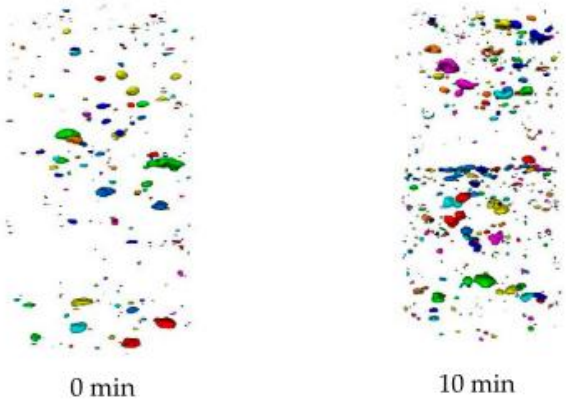

(a) (b)

Figure 2-26: μCT-scan images for the 0 (a) and 10 (b) min pass time (Van Der Putten, Deprez et al., 2019)

Keita, Bessaies-Bey, Zuo, Belin and Roussel (2019) studied the effect of wind exposure on the IR at various pass times ranging from 10 min to 24h. The specimens are placed in a wind tunnel where they are exposed to a 3.8 $x10^{-3}$ m/s wind and a dew point that correspond to a RH below 1%. For the concrete mixture with a ratio of 0.35, the moisture loss tests showed an increase in H_2O loss with an increase in pass time. Increasing the wind exposure pass time from 120 min to 24 h more than doubled the H_2O loss of the first layer and resulted in an increased porous IR from 100 μm to 500 μm. These observations were made from SEM images shown in Keita et al. (2019), who found that specimens (0.2 ratio) that had a pass time of 10 min, were sealed with plastic film and did not experience wind exposure; hence, they did not show a porous zone. All three SEM images are shown in Figure 2-27 below. Thus, the authors emphasise the importance of having a favourable printing environment to ensure a proper bond between successive layers. A study conducted by Wolfs, Bos and Salet (2019) investigated the effect of surface dehydration on covered and uncovered specimens when a 4 h pass time is introduced. Plastic sheets are used to cover the specimen during the pass time to prevent evaporation. Microscopic images of the cracked IR surface revealed that, as a result, by not covering the specimen, the surface moisture evaporated leaving behind a smoother IR with an increasing void content compared to the covered specimen. Keita et al. (2019) also observed an increase amount of layered dehydration for uncovered specimens compared to covered specimens, which resulted in a reduction of interlayer bond strength.

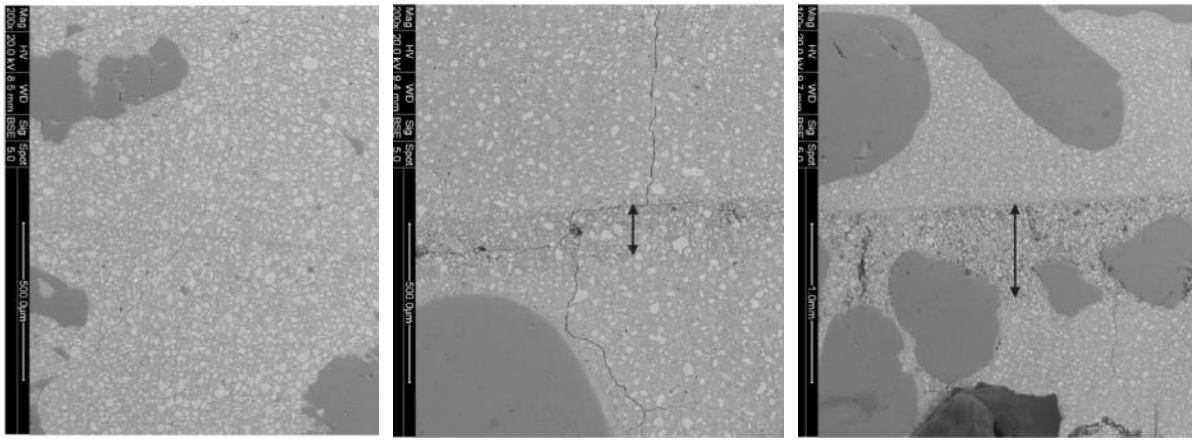

(a) (b) (c)

Figure 2-27: SEM images of the IR for specimens with a 0.2 ratio and 10 min pass time (a), 0.35 ratio 120 min pass time (b) and 0.35 ratio 24h pass time (c) (Keita et al., 2019)

Moelich, Kruger and Combrinck (2021a) investigated the effect of restrained early age shrinkage in the interlayer bond strength and durability of 3D printed concrete. The samples were printed in an environment that maintained a constant temperature of 22.5 ± 0.5℃ and a RH of 60 ± 3%. These conditions resulted in a water evaporation rate of 0.02 kg/m^2/h and represent 'lab' printing conditions. A fan, producing a 6.3 ± 0.3 m/s airflow, was used to simulate 'on-site' printing conditions. The airflow resulted in a water evaporation rate of 0.36 kg/m^2/h and the samples were introduced to these conditions for three hours after printing was completed. The increase in water evaporation increased lack of fusion and resulted in an increase in permeability. The implementation of restraint also resulted in an increase in permeability.

A study that contradicts the previous studies, is that conducted by Sanjayan, Nematollahi, Xia & Marchment (2018), where the surface moisture after 0 min, 10 min, 20 min and 30 min was investigated. The results show that, with an increase in pass time from 0 min to 20 min, the layer experienced surface moisture evaporation and a decrease in interlayer bond strength. But for a 30 min pass time the surface moisture increased, and interlayer bond strength increased, compared to the results obtained at 20 min. The authors contribute the increase in moisture to concrete bleeding, which provided a better bond between consecutive layers.

2.5.3.1.2 Air entrapment

Air entrapment at the IR increases the lack of fusion between printed layers (Kruger & van Zijl, 2021). Nerella et al. (2019) explain that air entrapment occurs when a fresh layer is printed onto an uneven surface, resulting in wide layer separation that cannot be bridged by the cement hydration products during self-healing. The occurrence of air enclosure is very pronounced in the study conducted by Nerella et al. (2019). SEM images show that the entrapped air results in long-layer separation and elliptical cavities at the IR, as shown in Figure 2-28. Nerella et al. (2017; 2019) state that the degree of air entrapment is dependent on various factors, such as the rheological properties of the concrete, printing speed, nozzle standoff distance, shape of the printed layer, etc. Panda, Noor Mohammed, Paul, Bagath Singh, Tan et al. (2019) show that by reducing the printing distance, overlay compaction can be achieved during the printing process to reduce IR porosity. At a nozzle standoff distance of 20 mm, the control mix has very distinct macro pores at the IR. By decreasing the nozzle standoff distance to 15 mm, layer adhesion is promoted that results in macro pore reduction. Le et al. (2012) investigated the void structure of high-performance printing concrete. The results showed that the void content reduced from 4.8% to 1% by improving the printing procedure and the concrete's rheological characteristics. The mould-casted specimens had void content of 4% and had larger void sizes compared to the printed samples.

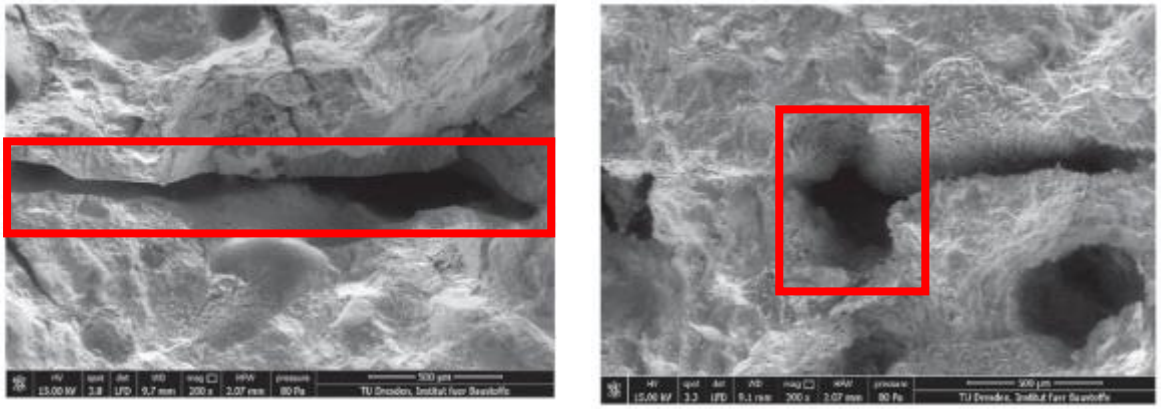

(a) (b)

Figure 2-28: SEM images showing long layer separation (a) and elliptical cavities (b) as a result of air enclosure (Nerella et al., 2019)

2.5.3.1.3 Thixotropy

The bi-linear thixotropy model, developed by Kruger, Zeranka et al. (2019), shown in Figure 2-29, illustrates static yield stress evolution in the rebuilding phase, i.e. when the concrete is extruded. The rebuilding phase has two thixotropic mechanisms, namely re-flocculation and structuration. During re-flocculation, a physical bond forms between subsequent layers, whereas during structuration it is a chemical bond. Flocculation starts after the concrete is extruded, and at the time of extrusion the material has an initial dynamic shear yield stress ($\tau_{D,i}$). The shear stress increases at a constant flocculation rate (R_{thix}) until the initial static yield shear stress ($\tau_{S,i}$) is reached and the particles are in equilibrium. After $\tau_{S,i}$ is reached, structuration commences, and the shear yield stress increases at a constant structuration rate (A_{thix}). During structuration, a chemical bond forms between subsequent layers via early hydration products (Kruger, van den Heever et al., 2019; Kruger, Zeranka et al., 2019; Kruger & van Zijl, 2021). Kruger and van Zijl (2021) suggest that in order to gain a high degree of layer fusion and reduce IR porosity, the pass time must be kept shorter than the re-flocculation time (Figure 2-29). This will ensure minimal moisture evaporation, which is the medium in which re-flocculation occurs. A higher degree of re-flocculation enhances the physical bond between the layers, resulting in more contact points for structuration to occur.

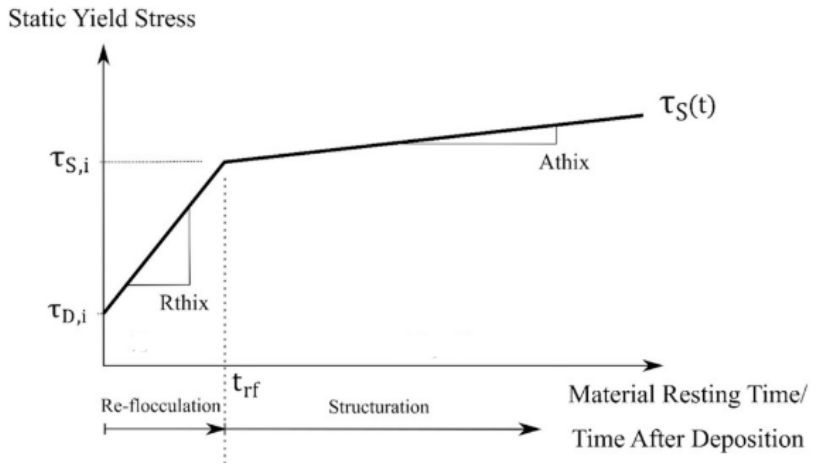

Figure 2-29: Thixotropic material static yield shear stress versus time of the rebuilding phase (Kruger, Zeranka et al., 2019)

2.5.3.1.4 Surface roughness

For conventional concrete structures the concrete surface is prepared by increasing the surface roughness to enhance concrete-to-concrete bonding. Common techniques include scabbling and sand blasting or, if the concrete is still in its fresh state, vibration is used to enhance fresh-

on-fresh concrete bonding (Beushausen et al., 2021; Nerella et al., 2019). These techniques are not applicable to 3DCP, and external vibration can cause the plastic collapse of the element.

Van Der Putten, Deprez et al. (2019) investigated the surface roughness effect caused by various printing speeds (17 mm/s and 30 mm/s). A high-precision laser beam was used to test the surface roughness in the printing direction. The results showed that by decreasing the printing speed from 30 mm/s to 17 mm/s, the surface roughness increases, promoting layer interlocking, which was verified by mechanical testing. ImageJ analysis of the first 2 mm of the printed layer showed a difference in the cumulative sand volume content below the top surface of the layer. The cumulative sand volume 1 mm beneath the surface was 6.74% more for the slower printing speed, resulting in a rougher surface. At the second mm, the sand volume for the lower and higher printing speed increased by 24% and 76% respectively. Van Der Putten, Deprez et al. (2019) contribute the difference in surface roughness and sand particle distribution to the formation of a lubrication layer, where the inner bulk layer contains larger particles than near the outer surface.

The lubrication layer occurs at the contact surface between the bulk concrete and pipe wall owing to pressurised bleeding (Sanjayan et al., 2018). By pumping concrete under pressure, the concrete develops a hydraulic pressure gradient that results in particle migration. This flow-induced particle migration leads to the formation of the lubrication layer, as illustrated in Figure 2-30 (Secrieru, Cotardo, Mechtcherine, Lohaus, Schröfl et al., 2018). During the pumping procedure, the shear rate is the highest at the pipe wall and decreases to almost zero at the centre of the bulk cement. The shear difference results in sand particles separating from the H_2O and migrating towards the centre of the bulk cement, leaving a cement-rich paste at the interface. Larger particles migrate faster than smaller particles, thus resulting in larger particles at the centre and smaller particles at the pipe wall (Choi, Roussel, Kim & Kim, 2013; Secrieru, Khodor, Schröfl & Mechtcherine, 2018). The thickness is dependent on the concrete composition, pressure, and pipe shape and can vary from less than 1mm to 9 mm (Secrieru, Khodor et al., 2018).

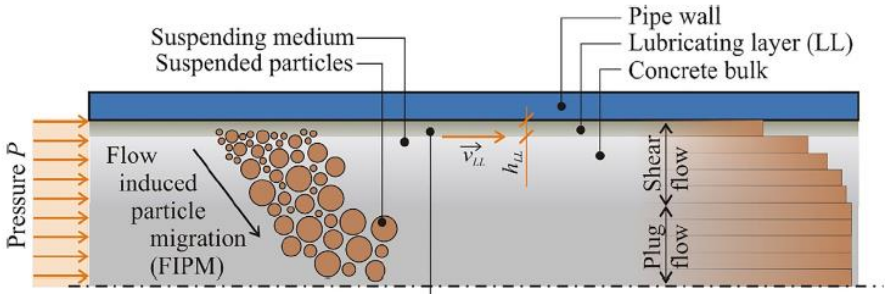

Figure 2-30: Illustration of flow-induced particle migration and lubrication layer of concrete in the pumping system (Secrieru, Khodor et al., 2018)

Kruger and van Zijl (2021) point out that the lubrication layer holds both advantages and disadvantages. On the upside, the lubrication layer will enhance the surface moisture and provides the perfect condition for re-flocculation to occur, increasing layer fusion. On the downside, the presence of free H_2O at the surface increases the ratio, reduces interlayer bond strength, and increases the porosity of the IRs when the concrete hardens.

2.5.4 Methods of improving the lack of fusion

As presented in Chapter 2.5.3, the lack of fusion in 3D printed elements are prominent and reduce mechanical performance. It has been reported that the interlayer bond can be improved by applying additive mortars between printed layers and by utilizing topological interlocking for longer interface pathways and mechanical interlocking (Kruger & van Zijl, 2021). Additive mortars containing a combination of OPC, Calcium Sulfoaluminate cement and cellulose fibres have shown to improve the interlayer bond strength (Ma, Salman, Wang & Wang, 2020). Wang, Tian, Ma and Zhang (2020) reported that an additive mortar containing high belite Calcium Sulfoaluminate mortars containing either epoxy resin or chloroprene latex-based polymers also increased the interlayer bond strength. Zareiyan and Khoshnevis (2017) reported that topological interlocking improved the mechanical strength (splitting strength) of the printed samples."

2.5.5 3D concrete printing durability

3DCP structures will be exposed to the same environments as conventional cast concrete structures. The exposure to marine environments with high chloride concentration and urban environments with high CO_2 concentration will cause deterioration of the structure. Excessive chloride and CO_2 exposure lead to reinforcement corrosion that reduces the lifespan of the

structure (Beushausen et al., 2021; Domone & Illston, 2010). The lack of fusion between subsequent layers is evident in the studies presented in Chapter 2.5.3. Voids at the interlayer are more elliptical and interconnected, compared to the random void distribution in the layer itself (Kruger & van Zijl, 2021; Kruger et al., 2021). It is believed that the combination of high porosity, permeability and cold joints at the layer interfaces will act as highways for chloride and CO_2 ingress, thus reducing the service life of the 3DCP structure dramatically (Stefanoni et al., 2019).

2.5.5.1 Ingress theory of chlorides in 3D concrete printing elements

Mohan, Rahul, De Schutter and Van Tittelboom, (2021) developed a possible chloride transport theory for 3DCP structures that is based on the permeability and porosity of the IR and capillary H_2O ingress studies (Nerella et al., 2019; Schröfl, Nerella & Mechtcherine, 2019; Van Der Putten, De Schutter et al., 2019; Van Der Putten, Azima et al., 2020). The 3-stage transport model is shown in Figure 2-31 below. Stage one is where the printed element is exposed to the chloride solution. Stage two involves the absorption of the chloride solution near the surface of the element by capillary forces as well as the layer surfaces at each IR. The absorption is indicated as green arrows in Figure 2-31b. Following the absorption, the chloride ions will enter the bulk of each layer via diffusion. The red arrows indicate diffusion (Figure 2-31c). Mohan et al. (2021) pointed out two things that will lead to an increase in deterioration of 3DCP element compared to conventionally cast concrete. First, the exposure surface of 3DCP elements is much higher compared to that of cast concrete. 3DCP elements experience exposure at the top, bottom and side of each layer compared to cast concrete, which only experiences side exposure. Second, the cyclic wetting and drying cycle will increase deterioration of 3DCP elements. During wet cycles, the chloride solution will be absorbed by the capillary forces in the IRs and will saturate the pores. The saturated pores will enhance the diffusion of chloride ions through the bulk layer. During the dry cycles, the moisture will be evaporated, resulting in a high chloride concentration at the IR and an increase in O_2 availability to aid corrosion. The formation of micro-cracks might also occur when capillary stresses develop owing to evaporation of pore moisture.

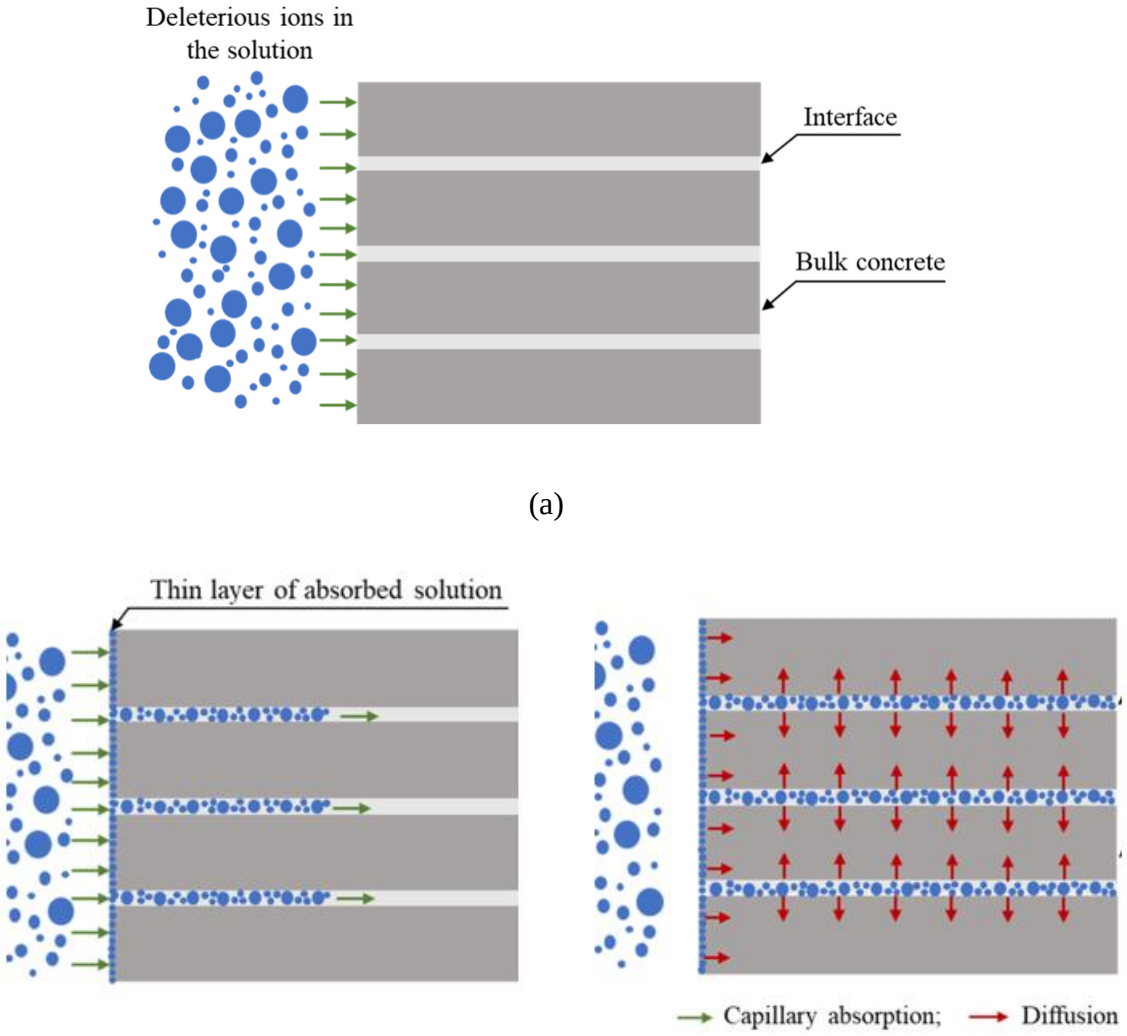

Figure 2-31: The hypothesised 3-stage chloride transport model developed by Mohan et al. (2021)

2.5.5.2 Ingress of contaminates

Since 3DCP is a new concept, not much research has been conducted regarding the ingress of contaminates and concrete transport properties, nor has there been any research done on the corrosion of steel in 3DCP.

2.5.5.2.1 Chloride ingress

Bran Anleu (2018) investigated the chloride ingress through cold joints in 3DCP. The 3DCP specimens were exposed to chloride via capillary rise and were analysed. Chloride ingress was monitored and visualised through μ-X-ray fluorescence (XRF) mapping after 24 hours of

exposure. Pass times of 2 min, 13 min and 1440 min were considered in this study. The results clearly show that an increase in pass time results in an increase in layer personality which results in faster ingress through the IR (Figure 2-32). The yellow colour in Figure 2-32 is an indication of the presence of chlorides. From Figure 2-32, the 2 min chloride ingress front is uniform though the IR and bulk layer. For the 13 min pass time the ingress though the IR is much more visible, and for the 1440 min pass time the ingress is the most pronounced. The ingress though the IR compared to the bulk layer for the 2 min, 13 min and 1440 min pass time were 35%, 63%, and 92% more, respectively. Bran Anleu (2018) attributed the occurrence to the increase in porosity and operability associated with longer pass times.

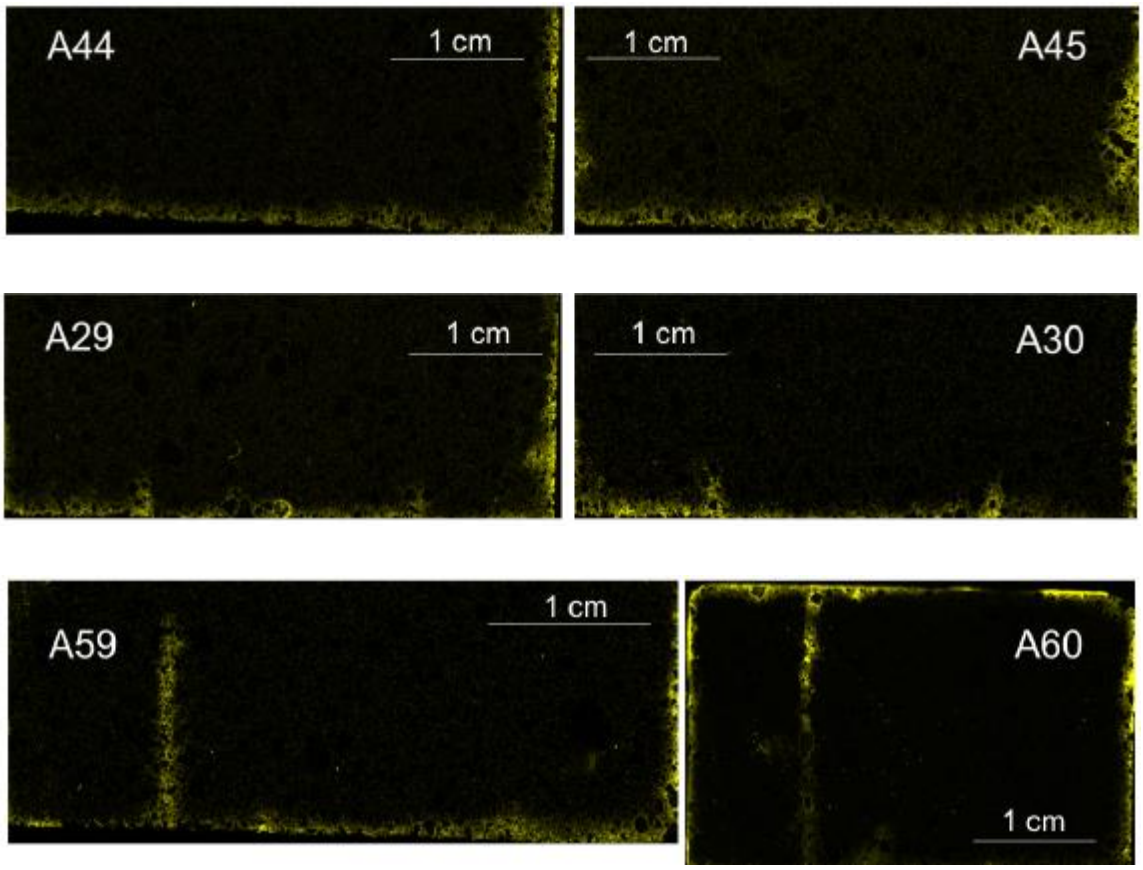

Figure 2-32: μ-XRF mapping images of the chloride ingress at a 2 min (A44 & A45), 13 min (A29 & A30), and 1440 min pass time (A59 & A60) (Bran Anleu, 2018)

Van Der Putten, De Volder et al. (2020) investigated the chloride ingress on 3DCP samples at various pass times (0 min, 10 min and 60 min) and compared it to cast samples. The samples were cured at 20 ± 3ºC and 60% RH for 28 days and were tested according to the NT Build 443 (1995). ImageJ analysis on the chloride ingress penetration (as a percentage of the width of the specimen) across the height of the sample at various times is shown in Figure 2-33 below.

In Figure 2-33, REF, T and W stands for reference cast sample pass time and ingress duration in weeks, respectively. The results show that the cast specimens performed better than the printed specimens owing to the porosity induced by the printing nature of 3DCP. For the homogenous cast sample, ingress front is uniform and increases slowly with time. For the 0 min pass time, the ingress front is more pronounced owing to the increase in porosity at the IR. The authors still considered the ingress front as uniform. It is evident from Figure 2-33 (c) and (d) that an increase in pass time resulted in a more penetrable specimen, which decreased the specimen's resistance to chloride penetration. The authors contributed the increase in chloride penetration to the effect of the environment on the freshly printed layer, which led to an increase in micro cracks and pores at the IR.

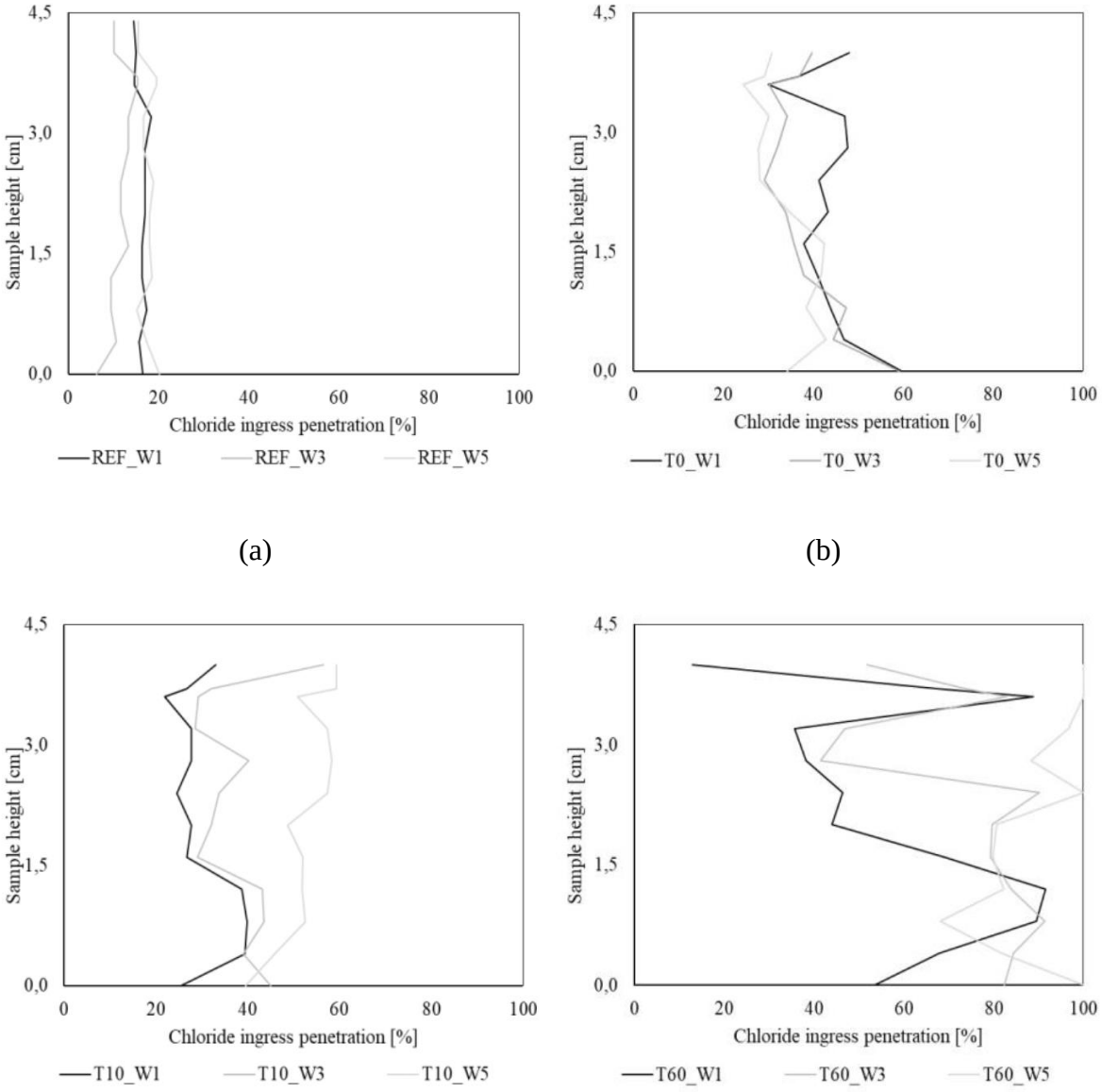

Figure 2-33: Chloride ingress penetration across the height of the specimen at various times for the (a) cast, (b) 0 min, (c) 10 min and 60 min pass time (Van Der Putten, De Volder et al., 2020)

2.5.5.2.2 H_2O ingress

H_2O transports through concrete via absorption, as mentioned in Chapter 2.2.1.2 (Richardson, 2002). Several researchers have used neuron radiography to vassalize and quantify the absorption of moisture for 3DCP specimens. Bran Anleu (2018) investigated the effect that the curing regime and pass time had on the moisture ingress of the 3DCP samples. Bran Anleu

(2018) used neuron imaging to track the moisture ingress in the 3DCP samples and pass times of 2 min and 1440 min were considered. The results showed that for the wet cured samples, the pass time had no effect on the moisture ingress and a uniform moisture front was present across the bulk layer and IRs (Figure 2-34). For the dry cured samples, the pass time had an immense effect on the moisture profile. The moisture front for the 2 min pass time and the bulk layer were identical, but a sharp increase of moisture content was observed at the 1440 min pass time IR owing to the high porosity at the IR (Figure 2-34).

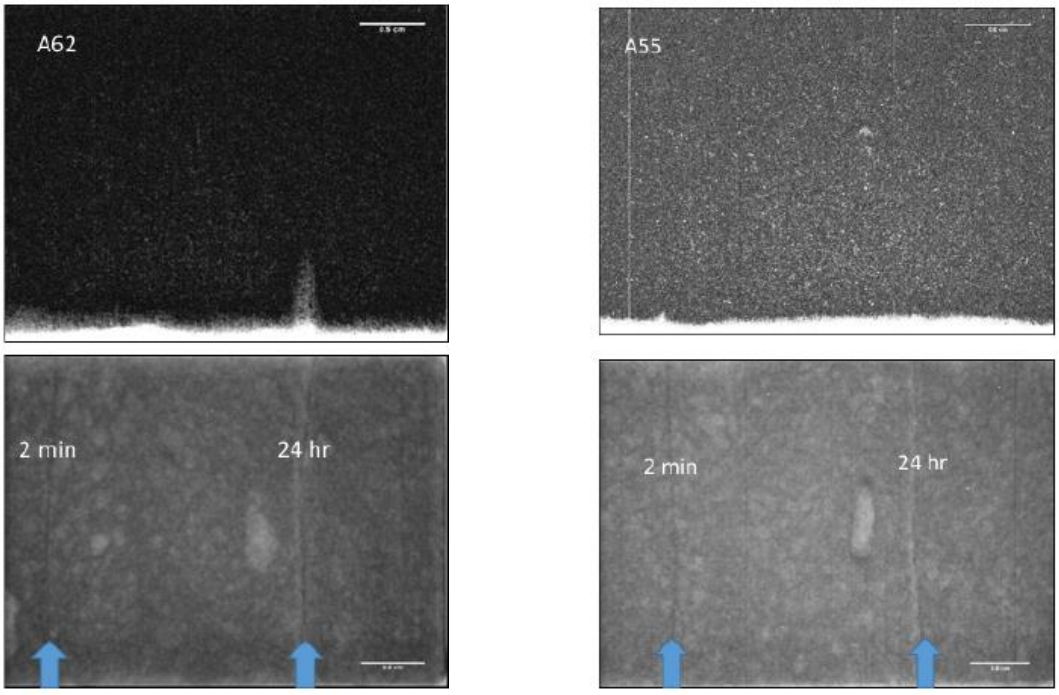

(a) (b)

Figure 2-34: Neuron images of the moisture profile of the dry (a) and wet (b) cured samples at a 2 min and 24 h pass time (Bran Anleu, 2018)

Van Der Putten, Azima et al. (2020) also investigated the ingress of H_2O via the IRs of printed specimens. Two- and four-layer printed specimens were considered, and the pass time was kept constant at 15 s. The specimens undergo capillary suction tests from the front (bulk layers and IRs) of the specimen for 360min. Neutron radiographs were taken after 15 min, 30 min, 60 min, 120 min, and 360 min of H_2O exposure. For both layer combinations, of which the results are shown in Figure 2-35, the results show the uniform H_2O intake throughout the specimen, and no H_2O uptake peak was observed at the interlayer. Van Der Putten, Azima et al., 2020 contributed the uniform H_2O uptake to the short pass time, which results in a more homogenous

material where the void amount, size, and distribution of the bulk layer are the same as at the IRs. Schröfl et al. (2019) also investigated the capillary H_2O intake of two concrete mix designs through the IRs at various pass times (2 min and 24 h). The binder content of Mixture G consisted of PC, and the binder content of Mixture A consisted of PC, SF, and FA. After 26 h of capillary suction testing, neuron radiography was used to visualise and quantify the capillary H_2O intake. For Mixture A, the results showed no H_2O increase at the 2 min and 13 min pass time IRs or the bulk layer. But an increase in pass time to 24 h, resulted in a visible H_2O increase at the IR. Schröfl et al. (2019) contributed the intake owing to the cold joint and shrinkage cracks that formed because of the long pass time. For Mixture G, the results showed that, for a pass time of 13 min or longer, the layer adhesion was dramatically less active, which resulted in a high H_2O intake at the IRs.

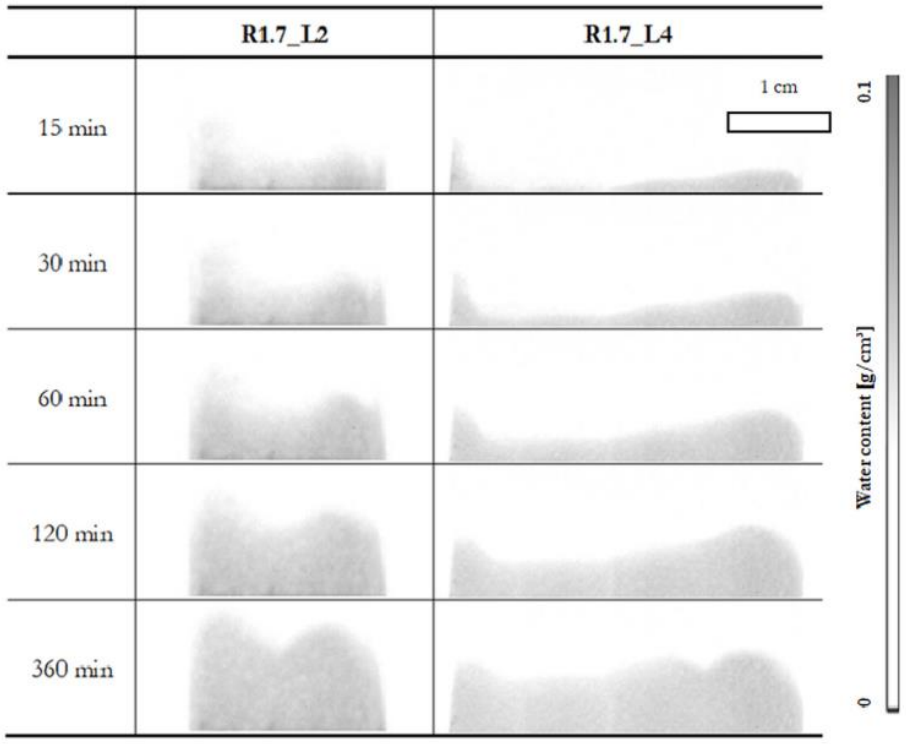

Figure 2-35: Neutron radiograph images of two (left) and four (right) layered printed specimens after various H_2O exposure times (Van Der Putten, Azima et al., 2020)

2.5.5.3 Reinforcement corrosion theories

Kruger and van Zijl (2021) proposed two corrosion theories for reinforcement, which are parallel and perpendicular to the interlayers. Parallel reinforcement is susceptible to general corrosion, which will largely be affected by carbonation-induced corrosion. As mentioned in Chapter 2.2.6, the corrosion products cause internal pressures, thus leading to layer

delamination (Richardson, 2002; Kruger & van Zijl, 2021). Perpendicular reinforcement is more susceptible to pitting corrosion at each IR, which will largely be influenced by chloride-induced corrosion. Kruger and van Zijl (2021) hypothesise that smaller layer heights will result in lower pitting corrosion. The theory is based on the results found by van Zijl et al. (2018), mentioned in Chapter 2.3.4.4, which showed that the rebar pitting corrosion is greater for larger crack spacing compared to smaller crack spacing, thus proposing that the high porous IRs will function as micro cracks in the 3DCP element.

2.5.5.4 Durability index performance of 3D concrete printing elements

Moelich et al. (2021a) quantify the durability performance of the 3DCP mix design used at Stellenbosch University by conducting OPI and CCI tests. The samples were printed and cured in a climate-controlled room with a temperature of 22.5 ± 0.5 ºC and 60 ± 3% RH. Lightly vibrated mould-casted samples of the same concrete were also tested for comparison purposes. The OPI results showed that the printed samples had a higher permeability, resulting in an OPI of 10.58 compared to the mould-casted samples that yielded an OPI of 10.6. In the CCI tests, the printed samples also yielded a higher porosity than the mould-casted samples. The CCI of the printed samples were 0.4 mS/cm compared to the 0.32 mS/cm of the mould-casted samples. Although the printed samples were outperformed by the mould-casted samples, the results are still excellent based on the durability classifications. The OPI of 10.58 and CCI of 0.4 fall within the excellent durability classification class (Alexander, Mackechnie et al., 1999). It is important to note that the tests were performed on 21-day old concrete and not at 28 days, as by Alexander, Streicher et al. (1999). Only one side of the printed disk specimen was saw cut. This can result in unrealistic ‘good’ results owing to pore blocking that may occur at the uncut face.

2.6 Literature summary

This chapter provided a summary of the literature presented and the relance to 3DCP. Chapter 2.2 describes the durability of steel reinforcement in concrete and the applicable transport mechanisms. It elaborates on the electrochemical process of steel corrosion, steel depassivation, and the corrosion types and mechanisms. The corrosion rate was defined and the different corrosion monitoring methods and their accuracy in predicting corrosion potential, risk, and rate were discussed. Performance-based durability testing was also outlined in this chapter.

The two durability performances discussed in the literature review are chloride-induced corrosion and concrete carbonation. Chloride-induced corrosion and concrete carbonation were covered in Chapters 2.3 and 2.4 respectively. Each chapter discussed the transport mechanism of the contaminant under consideration. Factors influencing chloride-induced corrosion and concrete carbonation, such as environmental exposure, concrete composition, cover quality, curing methods, and the presence of cracks were outlined, and ingress models based on performance-based durability testing were presented.

Chapter 2.5 presented the principle of 3DCP and the thixotropic behaviour of concrete. Different methods of incorporation steel reinforcement such as pre-installed, in-process, and post-installed reinforcement were outlined. The lack of fusion present in 3DCP samples play an important role in the mechanical performance. The lack of fusion is contributed to 4 mechanisms: surface moisture, air entrapment, thixotropy, and surface roughness. Each mechanism was discussed and the influence on the porosity and permeability at the IRs were presented. The limited literature regarding the durability performance of 3DCP sample was also discussed.

The presence of cracks in reinforced concrete members drastically reduces the service life of concrete structures. The cracks function as ingress pathways for corrosion contaminants, allowing the chloride threshold to be reached quicker; thus, shortening the time to corrosion initiation. Cracks reduce the carbonation resistance of concrete. As in the case for concrete exposed to a chloride environment, the cracks also function as ingress pathways for CO_2 and result in greater carbonation depths. Very limited research results are available regarding the transport mechanisms and durability of 3DCP samples in chloride and CO_2 environments to quantify their durability performance. Literature does show an increase in porosity and permeability at the IRs that results in a decrease in mechanical performance and allows for faster chloride ion transport compared to cast samples. Thus, it is hypothesised, that the IRs of 3DCP samples will function as cracks owing to lack of fusion and will ultimately reduce the service life of the concrete structure.

3 Experimental framework

3.1 Introduction

This chapter describes the research methodology followed to achieve the achieve the aim and objectives set out. The 3DPC mix design and 3D concrete printing procedure are described. The sample sizes, amounts, preparations, curing practices and procedure for each test performed are outlined. The measurement techniques used to monitor the corrosion are also descried.

3.2 Research methodology

This research focused on the durability performance of 3DPC and conventionally cast concrete of the same concrete mix design. The effect of the pass time (0, 10, 20 and 30 min) was also considered as an experimental variable and is investigated. The pass time induces a weak interlayer region, as discussed in Chapter 2.5.3, and each printed sample contains one interlayer region, at the centre, that has an induced pass time. This interlayer region is referred to as the critical layer and the incorporation process is further addressed in Chapter 3.5.4.

The aim and objectives set out in Chapter 1.2 were achieved by conducting durability and mechanical strength testing. The durability performance was tested and characterised by performing durability index, accelerated concrete carbonation and chloride-induced corrosion testing. The durability index testing characterises the concrete transport properties and consist of oxygen permeability, water sorptivity and chloride conductivity testing. The accelerated concrete carbonation testing was carried out in a controlled environment at elevated CO_2 levels to quantify the concrete ability to resist the penetration of CO_2. Chloride-induced corrosion testing consisted of cyclic wetting-and-drying of a saline solution (NaCl solution) to simulate a corrosive coastal environment during which the corrosion rate was monitored to determine the time to corrosion initiation and degree of corrosion during the propagation phase. The chloride penetration depth is also investigated to further characterize each variable resistance to chloride ingress. In addition to the durability performance testing conducted, mechanical testing (4-point bending) was done to investigate the interlayer bond strength and lack of fusion between the subsequent printed layers.

The durability index results in conjunction with the accelerated concrete carbonation and chloride-induced corrosion testing was applied to service life predictions models to quantify the long-term durability effects the interlayer region and critical layer regions might have compared to cast concrete.

3.3 Experimental variables and testing outlined

A summary of the experimental variables considered in this study is given in Figure 3-1. For the cast samples, different compaction methods were considered. For the printed samples various pass times (0 min, 10 min, 20 min, and 30 min) were investigated.

The method of compaction is not a primary focus of the study presented even though two methods of compaction are outlined as experimental variables in Figure 3-1. During the sample preparation and testing of cast samples subjected to vibration table compaction, it was noted that the cast samples had many voids present due to insufficient vibration. The vibration table was not an effective way of ensuring a dense concrete matrix. The printed layers have a dense matrix and the same degree of compaction for the cast samples was desired. Thus, it was proposed to use the poker vibrator for compaction and some tests were reproduced. Table 3-1 contains a summary of the tests performed on the specific experimental variables.

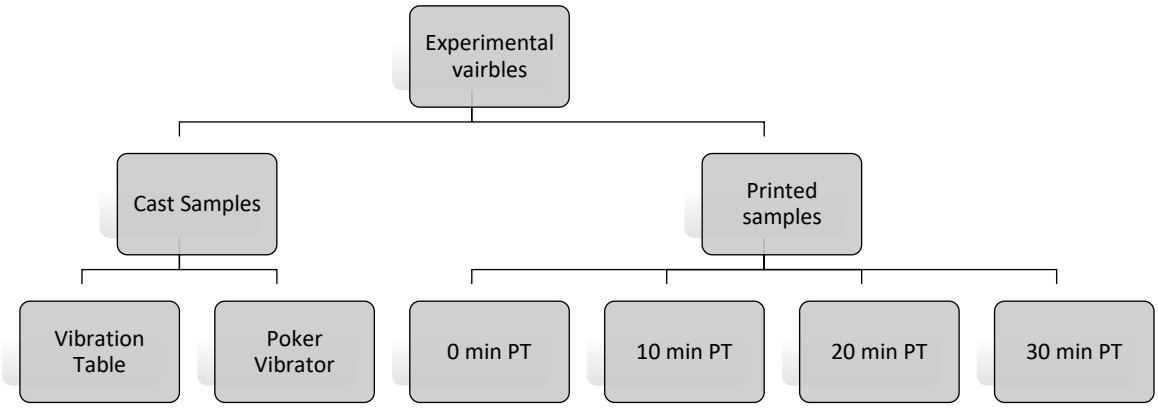

Figure 3-1: Summary of experimental variables under consideration

Table 3-1: Experimental variable testing

Test	Cast samples	Printed samples	
	Vibration Table	Poker vibrator	All pass times
Flexural strength		X	X
Durability index	X	X	X
Accelerated concrete carbonation	X		X
Chloride-induced corrosion	X		X

3.4 3D concrete printing mix design

The concrete mix design used in this study was proposed by Malan (2020), and is listed in Table 3-2. The standard fibre 3DCP mix design used at Stellenbosch University was used as the baseline and incorporated results from Munemo (2020) showing that increasing the super plasticizer (SP) content increases the interlayer bond strength (direct tensile strength). Malan (2020) proposes a more economical mix design, based on the findings of Munemo (2020), by decreasing the water content by 20 ℓ (litres) and increasing the SP content from 0.6% to 1%. The mix design has a slump cone flow (mini-slump) of 150 mm and the rheological parameters of the 3DCP mix design used in this study is listed in Table 3-4 (Christen, Cho, van Zijl & de Villiers, 2021). The chemical composition of the cement, FA and SF are outlined in Appendix B. Figure 3-2 shows the grading curve of the fine Malmebsury sand and Table 3-3 contains the properties of the fibres used.

Table 3-2: 3DPC mix design

Material	**Product**	**kg/m^3**	**Additional comments**
Cement	PPC CEM II/A-L 52.5N	521.4	
FA	Durapozz	161.2	Class F
SF	FerroAtlantica Micro-SF	81.1	
Water	Municipal tap water	235	0.45 w/c and 0.31 w/b
Sand	Malmesbury fine sand	1229	Fineness modules of 1.094
SP	Chryso Priema 310	7.637	1% by mass of binder Modified polycarboxylate polymer-based SP
Viscosity modifying agent (VMA)	Chryso Quad 20	2.291	0.3% by mass of binder
Fibre	SAPY Corehfil 6 mm polypropylene	9	1% by total volume

Table 3-3: SAPY Corehfil polypropylene fibre properties

Description	**Value**
Youngs Modulus	3 GPa
Yield stress	300 MPa
Diameter	30 µm
Length	6 mm

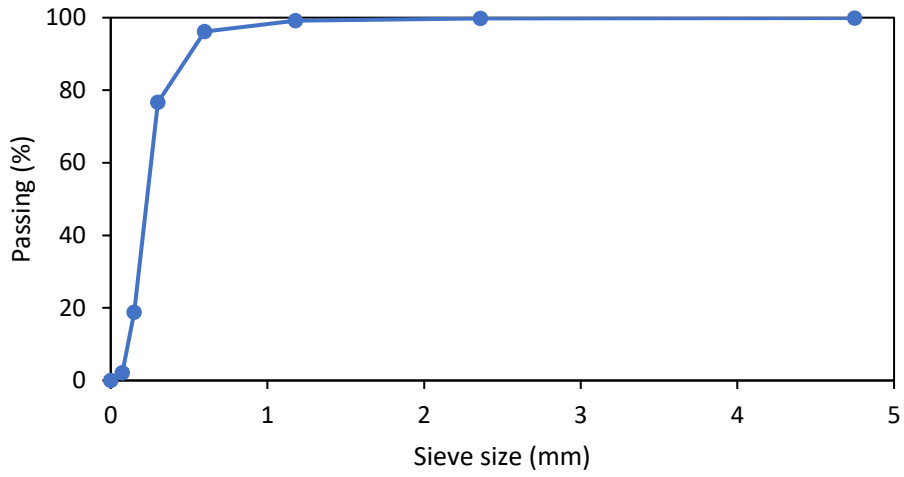

Figure 3-2: Malmesbury fine sand grading curve

Table 3-4: 3DCP Rheological parameters (Christen et al., 2021)

$\tau_{S,i}$	$\tau_{D,i}$	R_{thix}	A_{thix}	t_{rf}
1223.8 Pa	334.7 Pa	1.7187 Pa/s	0.3115 Pa/s	410.8 s

3.5 3D concrete printing procedures

3.5.1 Concrete mixing and printing procedure

The printing procedure was divided into four steps: mixing, transportation, priming, and printing. The mixing of the concrete was performed in a 50 ℓ concrete mixer. Similar 40 ℓ concrete mixes were prepared for each print. First, the dry materials were added in the following order: sand, cement, FA, and SF. Each dry material is sieved with a 2.36 mm sieve to break down any clumps. Munemo (2020) reports that sieving increases the interlayer bond strength. The dry materials are mixed for five minutes until all the materials are evenly distributed. The VMA and SP were added to the water. The water acts as transportation agent and ensures good distribution. The water was slowly added over a duration of 2 minutes and allowed to mix through for another 3 minutes. Finally, the fibres were added in small portions to ensure that they do not clump together. The fibres were added over a duration of 3 minutes and allowed to mix for another 2 minutes.

As the concrete reached the desired consistency, the concrete was transferred from the mixer to the climate control room (CCR) and transferred to the pump. The printing is performed in

the CCR that maintains a constant temperature and RH of 22 ± 3ºC and 65 ± 5% respectively. The pump was connected to the printing pipe that was fastened to the 3DCP. The printing pipe was rinsed with water to form a lubrication layer. The pipe was primed by pumping the concrete through the pipe into a bucket until a continuous layer with no tears could be extruded. This means that all the air was removed, and the pipe is filled with concrete. After the priming procedure, printing commenced. During the priming and printing procedure, a poker vibrator was used to reagitate the concrete.

The 3DCP was performed using an industrial-grade gantry printer. The printer has a build volume of 1 m^3, operates in three degrees of freedom (X, Y and Z-direction), and is fitted with a 25 mm diameter circular nozzle. The wooden printing platform is covered with plastic sheeting to prevent any moisture absorption by the wood. The printing setup is shown in Figure 3-3.

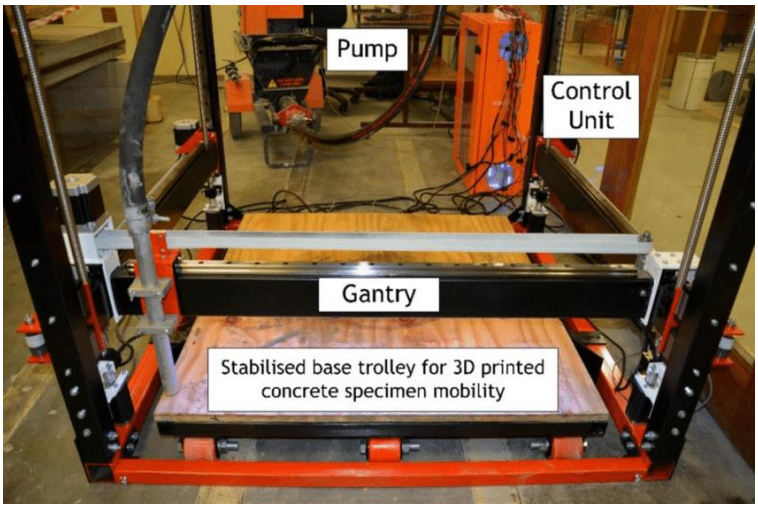

Figure 3-3: 3D concrete printer setup (Cho, Kruger, Zeranka & van Zijl. 2019)

3.5.2 Printing parameters

All the samples were printed at a constant printing speed of 60 mm/s and had a layer height of 10 mm. The selected printing speed and layer height are typical in regular 3D concrete printing with the selected concrete mix and are fixed in order to isolate pass time as test variable in this research programme. The layer width for all the tests was roughly 30 mm, except for the DI testing specimens, which had a layer width of 40 mm. Other printing parameters such as print path, number of layers, and the position of the critical layer were unique for each print and are summarised in Table 3-5. The print path for all the tests were kept equal to or less than 3600

mm. This corresponds to a maximum duration of 1 min between the printing of subsequent layers to minimise surface moisture evaporation and allows for re-flocculation to occur.

Table 3-5: Printing parameters of various 3DPC tests

Test	Print path (mm)	Total Layers	Critical Layer Position
Flexural strength	1500	16	8-9
DI	3600	10	5-6
Accelerated concrete carbonation	2760	10	5-6
Chloride-induced corrosion	3600	25	12-13

3.5.3 Printing of 3D concrete printing samples

For all prints performed in this research, 40 ℓ mixes were prepared in a 50 ℓ laboratory pan mixer, to remove mix volume as an influencing parameter. In the cases where the printed sample had a small volume, more than one sample was printed from the same concrete mix. Table 3-6 provides a summary of the experimental variables that were printed from each concrete mix.

Table 3-6: Experimental variables printed from each concrete mix

Test	Concrete mix	Experimental Variable
Flexural strength	1	0 and 30 min pass time
	2	10 and 20 min pass time
DI	1 to 4	0 to 30 min pass time
Accelerated concrete carbonation	1	0 min pass time
	2	20 min pass time
	3	10 and 30 min pass time
Chloride-induced corrosion	1 to 4	0 to 30 min pass time

3.5.4 Incorporation of the pass time and critical layer

The incorporation of the critical layer was performed by printing 50% of the sample, whereafter a pass time was introduced to induce a weak IR. During the duration of the pass time, concrete was continuously vibrated and pumped through the nozzle into a bucket. Once the bucket was full, the concrete was poured back into the mixer and recycled. This process continued until the pass time duration passed. After the specified pass time duration was complete, the top 50% of the sample was printed. Figure 3-4 shows a fully printed section and a partially printed section behind it. While the critical layer was induced during the duration of the pass time, the concrete was pumped through the nozzle and collected in a bucket at the back.

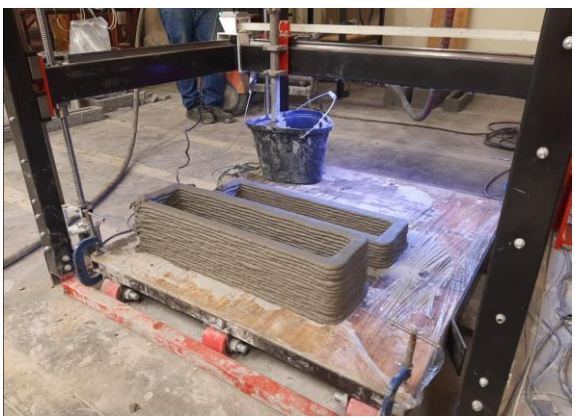

Figure 3-4: Procedure to incorporate the critical layer with various pass times

3.6 Sample sizes and amounts

The samples sizes varied for each test. All the printed samples were extracted from a larger printed specimen, either while the concrete was still in its fresh state, or with a diamond blade cutter when hardened. The cast specimens were either cast in the correct sample size or cut into the correct size. Table 3-7 contains a summary of the final sample sizes and amounts that were used to perform the various tests. Chapters 3.9 to 3.13 will elaborate on how the samples were prepared for each test.

Table 3-7: Summary of sample sizes and amounts for various tests

Test	**Cast**		**3DCP**	
	Size (mm)	**Amount**	**Size (mm)**	**Amount/ pass time**
Compressive strength	100 x 100 x 100	5/compaction method	-	-
Flexural strength	40 x 40 x 160	10	30 x 40 x 160	10
DI	70 mm diameter 30 mm width	12/compaction method	70 mm diameter 30 mm width	12
Accelerated concrete carbonation	100 x 100 x 100	4/print batch	90 x 100 x 100	4
Chloride-induced corrosion	150 x 150 x 250	3	180 x 150 x 250	3

3.7 Curing

The curing procedure for all the printed and cast samples was the same. The 3DCP samples were printed in the CCR. One day after printing, the sample was removed from the printing bed and stored in the CCR. The cast samples were transported to the CCR after compaction. The samples were removed from the moulds the next day and stored in the CCR. All the

samples were air cured in the CCR for 28 days. Any sample curing or conditioning beyond the 28 days CCR curing will be outlined in each testing section. Any additional curing is unique for each test.

3.8 Slump cone flow test

The slump cone flow test was performed to ensure that the 3DPC mix design had good printability. The slump cone flow test apparatus used in this test was in accordance with the ASTM C230/C230M (2014). The test apparatus, shown in Figure 3-5. Cho, Kruger, Bester, van den Heever, van Rooyen and van Zijl (2020) proposed an ideal range of mini-slump (150 mm–165 mm) values suitable for concrete printing. The tests were performed according to the Cho et al. (2020) procedure in order to use the ideal range. The slump cone flow test was performed directly after the concrete mix was prepared. The brass mould was filled halfway and tamped 15 times with the steel ramping rod. The mould was then filled to the top and tamped 15 times. Any additional concrete was scraped off the top. The mould was lifted upwards without causing any disturbance to the concrete sample. The concrete was agitated by turning the handle, which results in a 12.7 mm drop of the table surface. The handle was turned 15 times at a constant rate of 1 turn per second. After the 15th drop, the diameter of the concrete was measured in four directions and the average was used as the mini-slump value.

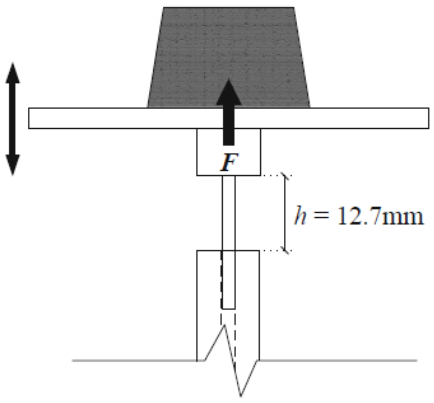

Figure 3-5: Schematisation of the slump cone flow test setup (Cho et al., 2020)

3.9 Compressive strength test

3.9.1 Sample preparation and curing

Compressive strength test was performed on 100 mm cubes that were compacted using the vibrating table and poker vibrator. For the vibrating table samples, waterproofed wooden 100 mm cube moulds were used to prepare the cube samples (Figure 3-6). The poker vibrator samples were prepared by casting a 100 x 100 x 600 mm beam in waterproofed wooden moulds and a diamond blade cutter was used to cut out cubes. A larger mould was required for poker vibrated samples, because the printable concrete could not be effectively compacted by poker vibration in the smaller cube moulds. The mould and extracted beam for the poker vibrator are shown Figure 3-7.

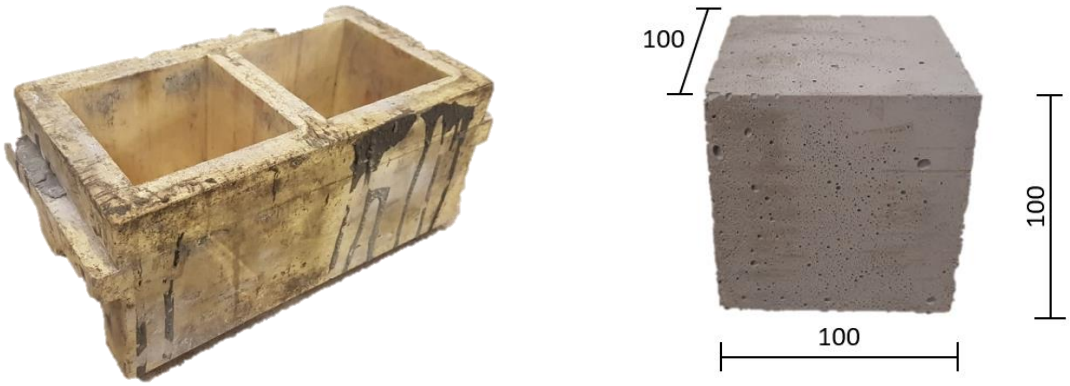

(a) (b)

Figure 3-6: Mould used (a) and sample produced (b) using vibrating table compaction

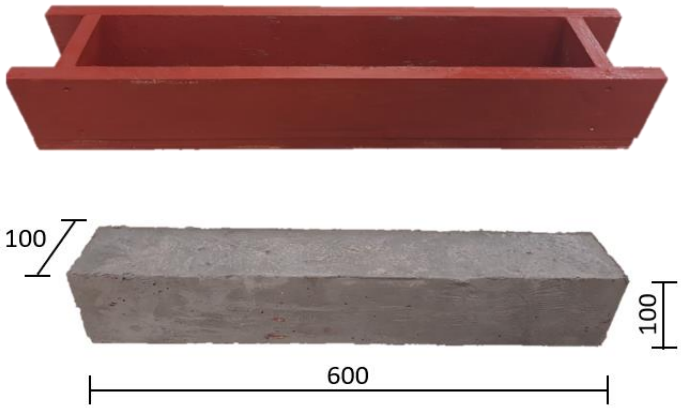

Figure 3-7: Moulds used (top) and sample produced (bottom) using the poker vibrator for compaction

3.9.2 Compressive strength test procedure

The compressive strength tests were performed on the 28-day old concrete. The 100 mm cubes were crushed using the Contest materials testing machine (MTM) and the tests were performed according to SANS 5863 (2006). All of the samples were crushed perpendicular to the casting dictation at a rate of 0.3 MPa/s $\pm$ 0.1 MPa/s. The test setup is shown in Figure 3-8. The compressive strength was calculated using Equation 3-1 (SANS 5863, 2006).

Figure 3-8: The Contest MTM compression test setup

$$\sigma_c = \frac{F_{load}}{A} \qquad 3\text{-}1$$

where

σ_c - Compressive strength

F_{load} - Failure load

3.10 Flexural strength test

3.10.1 Sample preparation and curing

Flexural strength testing was performed to measure the interlayer bond strength of the 3DCP samples as well as the influence of the pass time. Mould casted samples were also produced for comparison. The 3DCP flexural strength samples were produced from a hollow rectangular beam, as shown in Figure 3-9a. After curing, smaller flexural samples were cut from the large, printed beam (Figure 3-9b) using a diamond blade cutter. The red line shows the position of

the critical layer. The steel moulds used to produce flexural strength cast samples are shown in Figure 3-10. After the second print was completed, the excess concrete was pumped through the nozzle into the steel moulds and further compacted using the vibrating table.

(a) (b)

Figure 3-9: Flexural strength printed beam (a) and saw-cut 3DPC sample (b) showing the critical layer as a red line

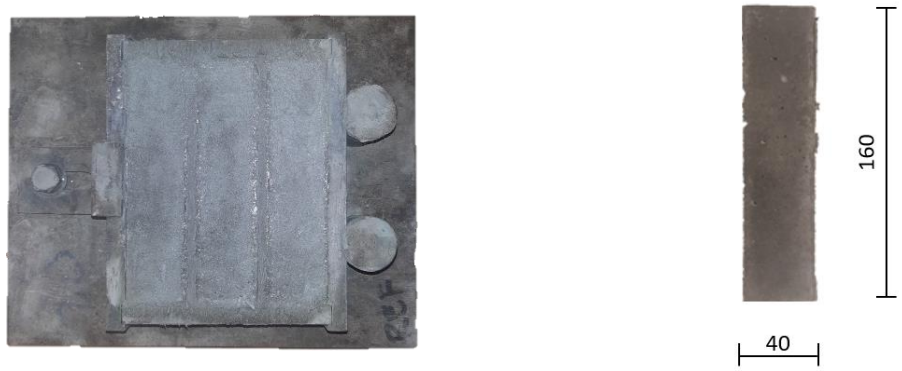

(a) (b)

Figure 3-10: Flexural strength steel mould (a) and sample extracted (b)

3.10.2 4-Point bending test

The flexural strength of the various samples was determined by using 4-point bending. The Zwick 250 was used to perform the 4-point bending test and the samples were tested after 28 days of curing. Displacement of the MTM platen, controlled at a rate of 0.25 mm/s, was used

to perform the test. The loading action was applied perpendicular to the cast direction for the cast samples, as specified BS EN 196-1 (2005). The loading action was applied parallel to the interlayer regions for the printed samples, so simulate the worst-case scenario as reported by Kruger and van Zijl (2021). The test setup is shown in Figure 3-11, and the flexural strength was calculated using Equation 3-2 (SANS 5864, 2006).

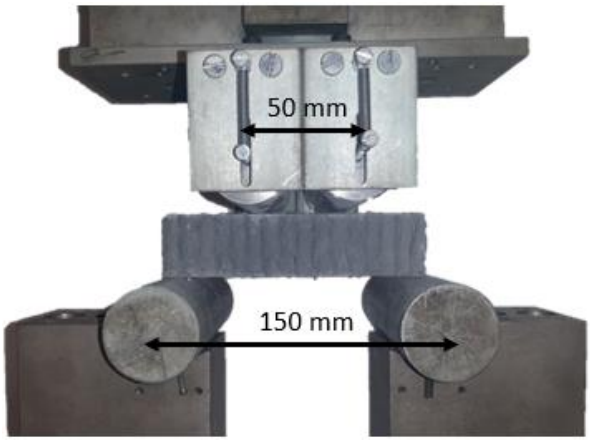

Figure 3-11: 4-Point bending test setup

$$\sigma_f = \frac{F_{load} L}{bd^2} \qquad 3\text{-}2$$

where

σ_f - Flexural strength

L - Span length

b - Sample width

d - Sample thickness

3.11 Durability index testing

DI testing comprises three individual tests (OPI, WSI, and CCI test) that were used to characterise the concrete durability performance. The WSI and CCI tests were performed in the University of Cape Town (UCT) concrete lab. The OPI test was performed in the CCR at Stellenbosch University.

3.11.1 Sample preparation and curing

The cast DI samples were prepared with two methods of compaction. The 100 mm wooden cube moulds were used to cast cubes and were compacted using the vibration table (Figure 3-6). Two large beams were cast and compacted, using the poker vibrator (Figure 3-7). The printed DI samples were produced from a large print sample. After curing, a water core drill was used to core out 70 ± 2 mm disks from the printed and cast samples. The disks were cored perpendicular to the casting and printing direction. Figure 3-12 shows the coring position for all the cast and printed samples. The printed samples were cored between layers 2 and 8, so that the critical layer is at the centre of the sample. The red line indicates the critical layer.

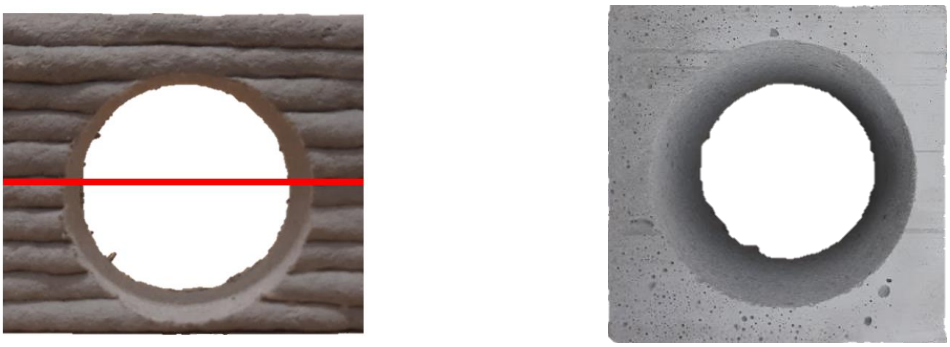

(a) (b)

Figure 3-12: Core position for the 3DPC (a) and cast (b) samples

A diamond blade cutter was used to remove the outer 5 mm and inner 20 mm of the cast samples. The outer 5 mm of both sides of the printed disks were removed. As previously mentioned in Chapter 3.5.2, the printed DI beam had a layer width of 40 mm. The increase in layer width was needed so that the disk would still be within the width limits (30 ± 2 mm) after the outer 5 mm were removed from both sides. After coring and cutting, both the printed and cast samples yielded a disk with a 30 ± 2 mm width and 70 ± 2 mm diameter. A total of 20 ± 3 disks were cored and cut per experimental variable. During the cutting procedure to remove the outer 5 mm of the cored disks, some edge chipping did occur, resulting in some of the samples being discarded. The best 12 disks were selected for testing. These disks were not damaged. The selected disks were marked on the inner face, and oven dried at a constant temperature of 50 °C. After seven days of oven drying, the samples were removed from the oven and put in a sealed desiccator for 2 to 4 hours to cool down. After cooling down, the samples were removed from the desiccator and the diameter and thickness of the samples were recorded at 4 points using a vernier calliper (0.01 mm resolution). The tests started within 30

min after being removed from the desiccator. Some deviation occurred during the testing process of the CCI and WSI samples. Chapter 3.11.2 elaborates on the deviation. Figure 3-13 shows the cast and printed samples before cutting. The red lines indicate the cutting positions.

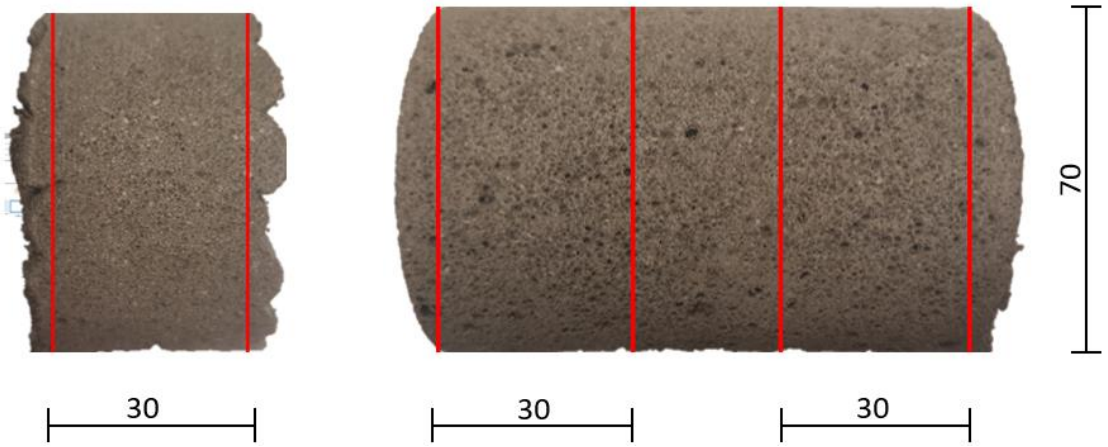

(a) (b)

Figure 3-13: Side view of the 3DPC (a) and cast (b) cores

3.11.2 Durability index testing procedures

The OPI, WSI, and CCI testing was performed according to the Durability Index Testing Procedure Manual (University of Cape Town & University of Witwatersrand, 2017). The WSI and CCI testing at UCT was hindered at the start of the testing. Owing to unforeseen circumstances, UCT had to close their lab for two days because of a COVID-19 related problem. This resulted in a deviation from the prescribed testing procedures. The manual specifies that the samples should be placed in a desiccator for 2 to 4 hours once they are removed from the oven. Testing should commence within 30 min after samples are removed from the desiccator. It also states that the samples should soak in the calcium hydroxide solution ($Ca(OH)_2$) and sodium chloride (NaCl) solution for 18 ± 1 hours after the vacuum is released. All the samples were placed in a sealed desiccator after seven days of oven drying to maintain the moisture content of the sample. The desiccator was stored in the CCR and the samples were removed at the time of testing. All the deviations in the testing procedure are listed in Table 3-8. The OPI testing conducted at Stellenbosch University was performed without any deviations. Four samples were tested per index per experimental variable.

Table 3-8: Deviation in WSI and CCI testing

Variable	**Total time spent in the:**		
	Desiccator	**NaCl solution**	**$Ca(OH)_2$ solution**
Cast vibrating table	2 days	-	-
Cast poker vibrator	3 days	-	-
0 min pass time	3 hours	3 days	3 days
10 min pass time	2 days	-	-
20 min pass time	1 days	-	-
30 min pass time	3 hours	-	-

3.11.2.1 OPI

The OPI test was conducted in the CCR using a permeability cell, comprisable silicone collar, rigid sleeve, solid ring, and cover plate. The sample was placed in the collar with the exterior face at the bottom and then placed inside the rigid sleave. This assembly was then placed on top of the permeability cell. The solid ring was placed on top of the collar, followed by the cover plate, and tightened using the screw at the top of the cell. Following the setup, the permeability cells were purged to remove any foreign gasses in the cell. The setup was also checked for leaks. The cell was filled with oxygen and the inlet valve was closed when a pressure of 100 ± 5 kPa was recorded. Data loggers were used to log the change in pressure over time and the test was terminated when the pressure dropped below to 50 ± 2.5 kPa or after 6 hours ± 15 min. The test setup is shown in Figure 3-14. The OPI and permeability were calculated using Equations 3-3 and 3-4 respectively. The OPI was taken as the average of the individual OPIs of the tested samples.

$$\text{OPI} = -log_{10}(k) \qquad 3\text{-}3$$

$$\text{k} = \frac{\omega.V.g.d.z}{R.A.T} \qquad 3\text{-}4$$

where

ω - Oxygen molecular mass (0.032 kg/mol)

V - Permeability cell volume

g - Gravitational acceleration (9.81 m/s^2)

z - Slope of linear regression line

R - Universal gas constant (8.313 Nm/Kmol)

T - Absolute temperature

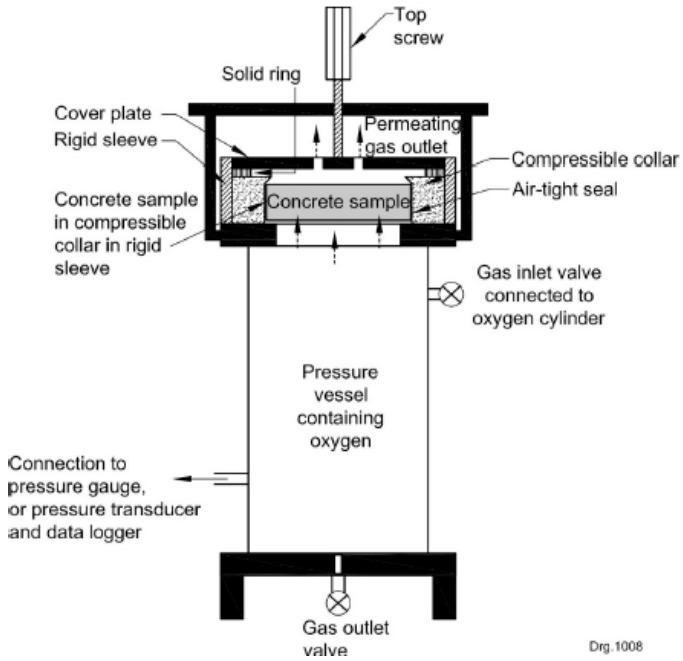

Figure 3-14: OPI test setup (University of Cape Town & University of Witwatersrand, 2017)

3.11.2.2 WSI

The WSI test was conducted using 10 layers of paper towels in a plastic tray. The tray was filled with a Ca $(OH)_2$ solution (5 g of Ca $(OH)_2$ per 1 ℓ of water) until the towels were covered with the solution (maximum of 2 mm) and all the air bubbles under the towels were removed. The curved edges of the exterior face were sealed using packaging tape. The mass of the sample together with the tape was recorded before testing (M_{s0}). The exterior face was placed on the towels and the mass of the sample was recorded at 3, 5, 7, 9, 12, 16, 20 and 25 minutes. The mass was recorded to the nearest 0.01 g within 10 s of removal and the timer was not stopped

during the measurement procedure. The sorptivity setup is shown in Figure 3-15. After testing, the samples were placed in a tank under a vacuum pressure of -80 to -75 kPa for 3 hours ± 15 min. After the duration, the tank was filled with the Ca $(OH)_2$ solution and kept under a vacuum pressure of -80 to -75 kPa for 1 hours ± 15 min. The samples were covered with 40 mm of the solution. Once the time had passed, the vacuum was released, and the samples were allowed to soak in the solution for 18 ± 1 hours. The vacuum saturated mass (M_{sv}) was recorded to the nearest 0.01 g after soaking. The sorptivity (S) and porosity (n) was calculated using Equations 3-5 and 3-6 respectively. The S and n were taken as the average of the individual tested samples results.

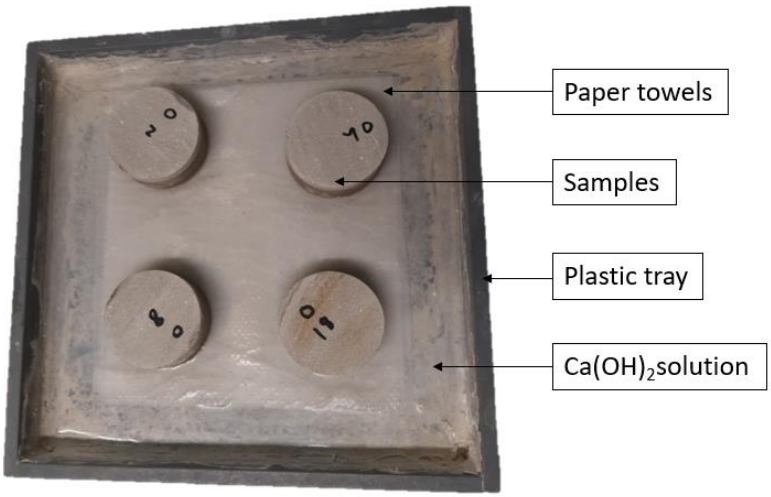

Figure 3-15: Sorptivity test setup

$$S = \frac{F_{slope}.d}{M_{sv} - M_{s0}} \quad 3\text{-}5$$

where

F_{slope} - Slope of best fit

$$n = \frac{M_{sv} - M_{s0}}{A.d.\rho_w} \times 100 \quad 3\text{-}6$$

where

ρ_w - Density of water (10^{-3} g/mm^3)

3.11.2.3 CCI

To start the CCI test, the dry mass of the samples (M_d) were measured to the nearest 0.01 g. After measuring, the samples were placed in a tank under a vacuum pressure of -80 to -75 kPa for 3 hours ± 15 min. After the duration, the tank was filled with a 5 mole NaCl solution and kept under a vacuum pressure of -80 to -75 kPa for 1 hours ± 15 min. The samples were covered with 40 mm of the solution. Once the time had passed, the vacuum was released, and the samples were allowed to soak in the solution for 18 ± 1 hours. The vacuum-saturated mass (M_s) was recorded to the nearest 0.01 g after soaking. Once the masses were measured, the samples were placed in the conduction cell. The anode and cathode chambers were filled with the salt solution and the test rig was assembled. An ammeter and voltmeter were connected to the rig and about 10 V was applied by the DC power supply. The current- and volt reading were recorded simultaneously. The CCI test setup is shown in Figure 3-16. The chloride conductivity (σ) and n were calculated using Equations 3-7 and 3-8 respectively. The σ and n are taken as the average of the individual tested samples results.

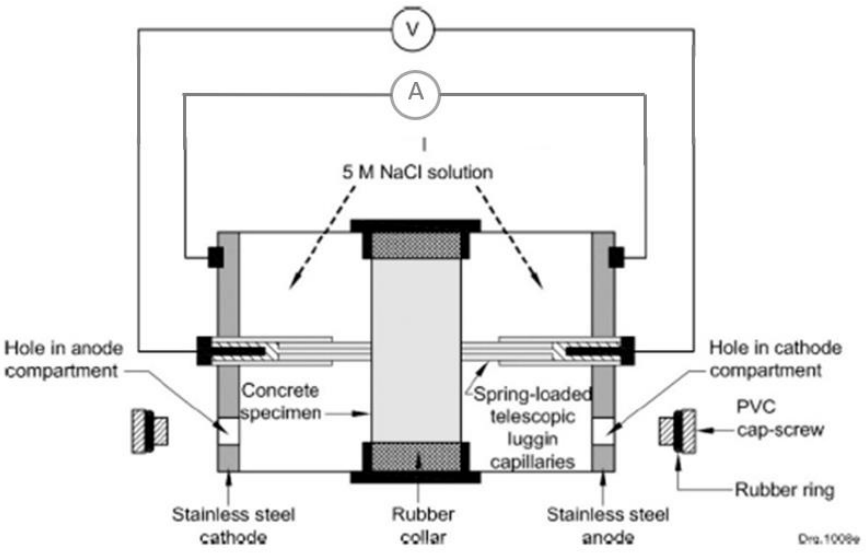

Figure 3-16: CCI test setup (University of Cape Town & University of Witwatersrand, 2017)

$$\sigma = \frac{i.d}{V_{dif}.A} \qquad 3\text{-}7$$

where

i - Electric current

d - Sample thickness

V_{dif} - Voltage difference

$$n = \frac{M_s - M_d}{A.d.\rho_s} \times 100 \quad (3\text{-}8)$$

where

ρ_s - Density of the salt solution (1.19 x 10^{-3} g/mm^3)

3.12 Accelerated concrete carbonation testing

Accelerated concrete carbonation testing was performed on 3DPC and cast cubes from each printing batch. The accelerated carbonation test was performed over a 12-week period and the carbonation depths were inspected after 3, 6, 9 and 12 weeks of CO_2 exposure.

3.12.1 Sample preparation and curing

One large beam was printed for each pass time. From each beam, printed cubes were cut out 40 min after the final layer was extruded. The cubes were cut using a metal sheet that was covered with demoulding fluid to assist with the cutting procedure. From each of these mixtures, concrete cubes were cast as a reference. The cube moulds were lightly smeared with demoulding fluid. These moulds were filled with concrete and compacted using a vibrating table. The weight of the printed and cast samples was monitored weekly to track the drying front progress, i.e. internal moisture content, during the curing procedure. The average weight loss after four weeks was 0.0339% and 0.0296% per week for the cast and printed samples respectively.

After four weeks of curing, the samples were painted with Sikadur 32N epoxy on four of the six sides to allow for one-dimensional carbonation ingress. For the cast samples, carbonation was allowed perpendicular to the casting direction and for the printed samples, the undulating horizontal layers were left unpainted for carbonation exposure (Figure 3-17). Once the paint had dried, the samples were moved to the carbonation chamber. The samples were conditioned in the chamber climate for 14 days before the accelerated carbonation testing began.

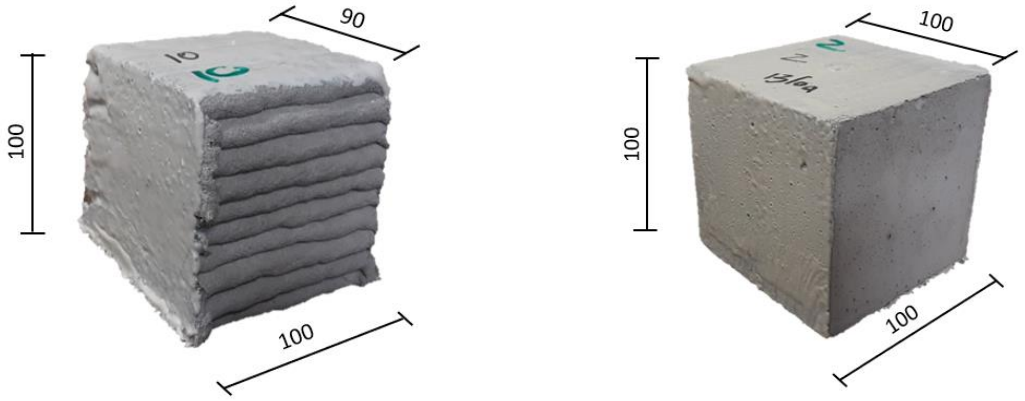

(a) (b)

Figure 3-17: Epoxy-coated accelerated concrete carbonation 3DPC (a) and cast (b) sample

3.12.2 Carbonation chamber

A schematic layout of the carbonation chamber used in this study is shown in Figure 3-18. The carbonation system comprises four units: a CO_2 gas cylinder, a drum with saturated salts, the carbonation chamber, and a CO_2 sensor. The cylinder was filled with CO_2 gas, which was used to increase the CO_2 concentration in the chamber. The CO_2 passes through the drum into the chamber. The drum contained an ammonium nitrate (NH_4NO_3) saturated solution. The salts were used to maintain a RH of 65±5 %. The chamber was fitted with various shelves to store the concrete samples and had an outlet valve to prevent any pressure build-up (Mubatapasango, 2017). The CO_2 concentration was monitored using a Vernier CO_2 gas sensor, which is capable of measuring CO_2 concentration of up to 10 000 ppm (Vernier, 2021). The levels were checked daily, and CO_2 was adjusted accordingly. The carbonation setup is in the CCR.

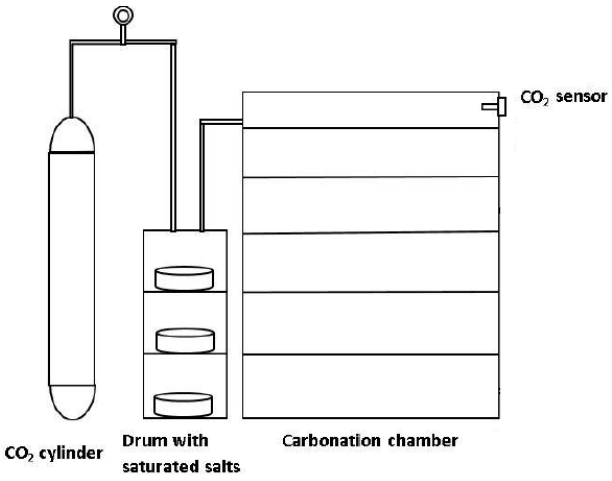

Figure 3-18: Carbonation chamber setup (Mubatapasango, 2017)

3.12.3 Accelerated concrete carbonation test

The accelerated concrete carbonation test started after the concrete samples were conditioned in the chamber for two weeks. The testing conditions were according to the fib Model Code for Service Life Design. The code specifies a 20 ± 2 °C, 65% RH ± 5% and CO_2 concentration of 2 ± 0.1% (Fédération internationale du béton, 2010). The saturated salts in the drum were responsible for maintaining the desired RH and the CCR was responsible for maintaining the temperature. The CO_2 concentration was maintained by manually checking the CO_2 levels with the Vernier CO_2 gas sensor. The checks were performed daily. Generally, the CO_2 concentration was increased to 2.5% each day and when the levels were checked the next day, the CO_2 concentration would be at 1.5%. Thus, an average concentration of 2% was maintained.

The test was performed over a 12-week period, with carbonation depth inspections at 3, 6, 9 and 12 weeks. At each inspection date cube per pass time and cast batch were used to check the carbonation depth. The concrete samples were removed from the chamber and saw-cut in half with a diamond cutter. A wind pressure hose was used to remove any excess dust from the freshly cut surface and then sprayed with a phenolphthalein solution. The solution, consisting of 1 g of phenolphthalein dissolved in 70 ml of ethanol and 30 ml of de-ionised water, as specified in BS 1881-210 (2013). Once the surface was dried, the carbonation depth was measured with a vernier calliper (0.01 mm resolution). The portion of the concrete with a pH > 9.0 would result in the solution turning pink. The part of the concrete that is carbonated will remain clear (refer to Figure 2-17 in Chapter 2.4.1) (Heckroodt, 2002). Six measurements were taken along the exposed side of the cast sample. The average of the six measurements were

taken to be the carbonation depth. For the printed samples, measurement was taken from the IR between layer 1 and 2 to the IR between later 9 and 10. Measurements were taken at the IR and at the centre of each layer. The carbonation depth at the critical layer was taken on both sides of the samples. The average was taken as the carbonation depth at the critical layer. The measurement positions for the cast and printed samples are shown in Figure 3-19. The black arrows indicate the position of the measurements, and the black line represents the critical layer.

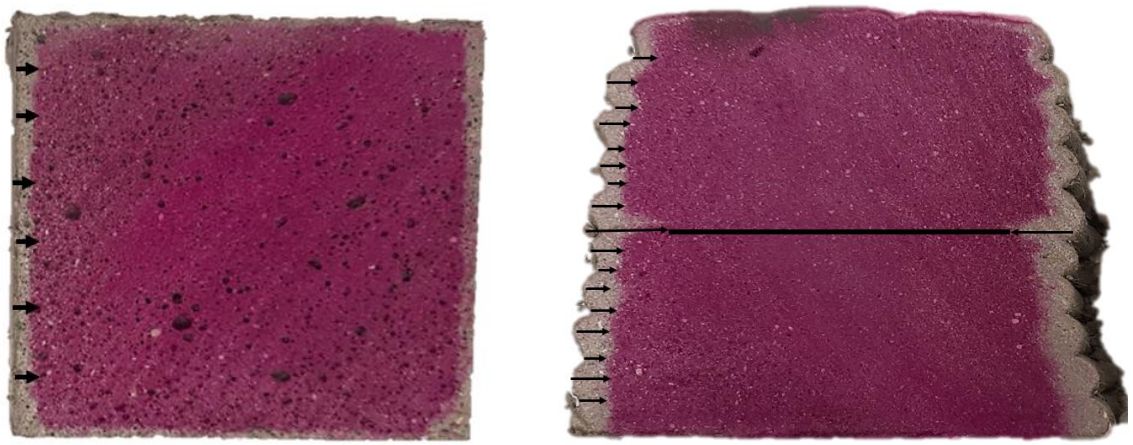

(a) (b)

Figure 3-19: Carbonation depth measurement positions for the cast (a) and printed (b) samples

3.13 Chloride-induced corrosion testing

The chloride-induced corrosion testing was performed on 3DPC and cast beams. All these beams had a 20 mm cover and were reinforced with one R8 steel bar. An 18-week cyclic wetting and drying procedure with a saline aqueous solution was used to simulate a coastal environment to induced corrosion. Testing started 35 days after casting and printing.

3.13.1 Sample preparation and curing

The cast samples were prepared using steel moulds. Each steel mould was used to prepare two concrete beams. Figure 3-20a shows the setup of the steel moulds. The concrete was vibrated with a poker to remove all the entrapped air. The reinforcement was kept in place with wooden frames and allowed for a cover of 23 mm. After 28 days of curing, the excess 3 mm was grinded down with MATEST C299 grinding machine to ensure a smooth surface for corrosion measurement. The reinforcement was placed at the top of the beam mould to ensure that the

concrete near the reinforcement was as densely compacted as possible. The reinforcement was also placed at the top to ensure that the face (i.e. cover face) that will be exposed to the NaCl solution will experience the same evaporation conditions during the first 24h, because the printed beams does not have any formwork preventing evaporation at the cover. Figure 3-20b shows the top view of the cast beam.

One large beam was printed for each pass time. From this beam, three smaller beams were produced. The three beams were pre-cut out of the large beam 40 minutes after the final layer was printed. This was done by cutting along a wooden frame using a metal sheet. The metal sheet was covered in demoulding fluid to assist with the cutting procedure by reducing the friction between the sheet and the concrete. The cutting procedure is shown in Figure 3-21a. After cutting was complete, the reinforcement was inserted into the concrete so that the reinforcement would align perpendicular to the printed layers (Figure 3-21b). Chapter 3.13.2 elaborates on the preparation and insertion procedure of the reinforcement. Each beam was separated into three individual beams 24h after printing.

(a) (b)

Figure 3-20: Steel mould and setup (a) for producing cast beams (b)

The uneven exposed surface is due to the inherent nature of 3DCP using a circular nozzle. This results in a variation in cover depth and increases the difficulty of corrosion rate measurement. The uneven surface makes it difficult for the sensors of the measurement equipment to make a good connection. Thus, a diamond cutter was used to cut off the excess concrete to ensure a uniform concrete cover and smooth surface for corrosion rate measurement. The beams were cut to a uniform cover of 20 mm after 28 days of curing using a diamond blade cutter. The uncut and cut surfaces of the 3DPC beams are shown in Figure 3-22.

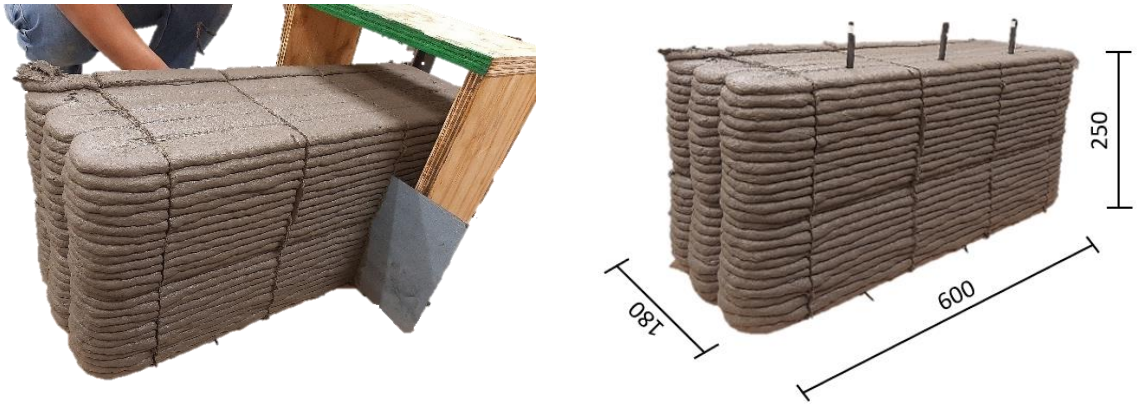

(a) (b)

Figure 3-21: Beam cutting procedure (a) and reinforcement insertion (b)

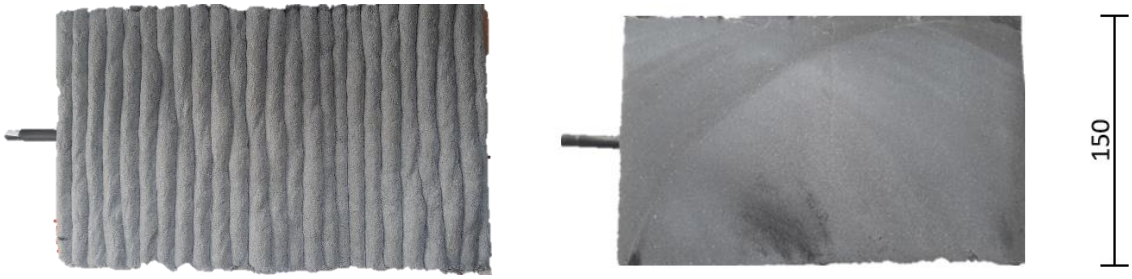

(a) (b)

Figure 3-22: 3DPC beams before (a) and after (b) cutting with the diamond cutter

3.13.2 Incorporation of reinforcement

In this study, R8 reinforcement bars were used. All the bars were cleaned with acetone to remove any dirt and rust from the bars. For the cast samples, the reinforcement was incorporated, as explained in Chapter 3.13.1. The bar penetration technique used by Marchment and Sanjayan (2020b) was implemented to incorporate reinforcement in the 3DPC sample to ensure 3 beams with the same critical layer characteristics could be produced from one printed sample. The end of the bar was sharpened to ease the insertion (Figure 3-23a). R-bars were used instead of Y-bars to avoid any air entrapment or voids formulation between the ribbed bar and the concrete during the insertion procedure. After cutting was completed, the reinforcement was pushed into the printed layers so that the reinforcement aligned perpendicular to the printed layers. A wooden jig was used to guide the path of the bars during insertion (Figure 3-23b). The location of the bar is shown in Figure 3-23c. For the longest pass

time (30 min), the reinforcement was inserted 95 min after the first layer was printed, which is much lower than the concrete's initial setting time of 210 min as reported by Moelich, Kurger and Combrinck (2020).

(a) (b) (c)

Figure 3-23: Sharpened reinforced tip (a), insertion procedure (b) and position (c)

3.13.3 Saline ponding layout and cycle

The clean cut and grinded surface of each beam was used as the exposure face. A Perspex basin was made to fit onto the exposed concrete surface. The four Perspex parts were glued together to form a rectangular basin (160 x 150 mm). The pond was fitted onto each beam and properly sealed with a neutral silicone to prevent any leakages. For the 3DPC beams, the pond was placed so that the critical layer was at the centre of the pond, and for the cast beams the pond was placed where the least surface voids occurred. Figure 3-24a shows the plan view of the 3DPC beam with the fitted saline basin. The red line in the middle of the basin indicates the critical layer. For the cast beams, the pond was placed at the surface where no surface voids occurred. After placing and sealing the pond, a leakage test was performed. In some cases, leakages occurred at the critical layer on the side of the beams. These leaks on the side and any additional leaks on the outside of the pond were sealed with Sikadur 32N epoxy. Figure 3-24b shows the side view of the 3DPC beam painted with epoxy to seal leakages.

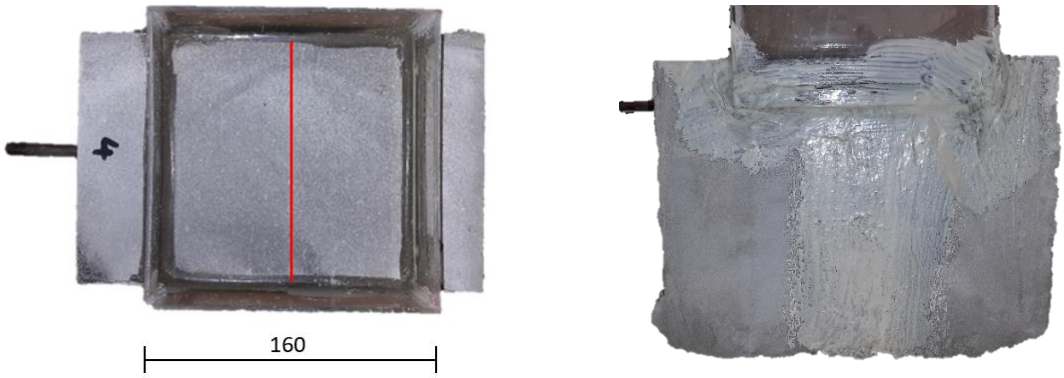

(a) (b)

Figure 3-24: Plan (a) and side (b) view of the 3DPC beam with the saline basin

The approach followed by Bezuidenhout and van Zijl (2019) to simulate chloride-induced corrosion was implemented in this study. The saline solution was made by dissolving sodium chloride (NaCl) in municipal tap water. Bezuidenhout and van Zijl (2019) recommended a 5% NaCl solution to simulate an extreme chloride environment (XS3a), which is 2 % more than the NaCl content of the Cape Town sea water, as reported by Otieno (2014). The NaCl used had a purity of 99.9 %. The concrete was exposed to a 14-day cyclic wetting and drying period. The basins were filled to a height of 10 mm with the saline solution. After three days of wetting, the basins were drained using a sponge to remove the solution and experienced 11 days of air drying in the climate-controlled room. The cyclic wetting and drying started 35 days after printing and casting.

3.14 Corrosion monitoring

3.14.1 Corrosion measurement equipment

Corrosion monitoring was done using the GECOR 10 instrument. The GECOR 10 is a potentiostat-galvanostat system that uses the galvanostatic pulse technique (a type of LPR technique) to measure the corrosion (isdcorr, 2015). The galvanostatic pulse technique involves monitoring the change in potential while a fixed current is applied (Broomfield, 2006). The GECOR 10 Sensor A was used to measure the corrosion rate. Sensor A (Figure 3-25) consists of a $CuSO_4$ reference electrode, counter electrode, two $CuSO_4$ auxiliary refence electrodes and a guard ring. The use of the two auxiliary reference electrodes and a ring guard allows for the implementation of the advanced modulated confinement of technique (AMCT). The two

auxiliary reference electrodes control the applied currents through the ring guard and counter electrode. This dynamic balancing of currents confines the signal to a known area of steel that is being polarised (Figure 2-7). The AMCT is a technique that can measure the true R_p and guarantee the correct corrosion rate measurement. Sensor A also measured the E_{corr} and R_{ohm} (isdcorr, 2015).

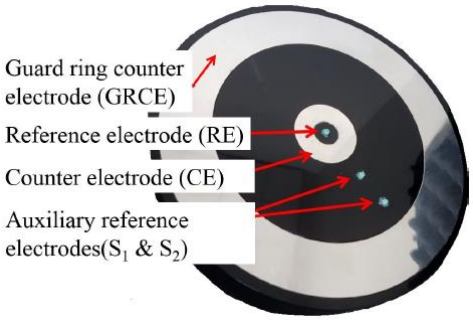

Figure 3-25: GECOR 10 Sensor A (Bezuidenhout, 2017)

3.14.2 Corrosion measurement schedule and procedure

The corrosion readings were taken using the GECOR 10 Sensor A. The diameter of the reinforcement was used as an input parameter (8 mm). The concrete surface was lightly brushed with the saline solution and a thin saline-saturated sponge was placed on the surface. Sensor A was placed on the sponge to establish good contact between the electrodes and the concrete. It also served as a conductive for the applied galvanic pulse. Once good contact was established, the corrosion rate reading was taken over a 45-second duration, as recommend by isdcorr (2015). One reading per beam was taken per wet and dry measurement. The corrosion measurement setup is shown in Figure 3-26a. The same corrosion measurement schedule used by Bezuidenhout (2017) was implemented in this study. These measurements comprise a wet and a dry meaurment, as shown in the corroson measurement schedule in Figure 3-26b. The wet measurement was performed one day after the saline basin was drained and the dry measurement was taken seven days later.

(a)

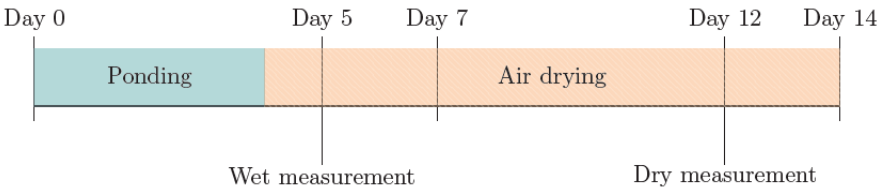

(b)

Figure 3-26: Corrosion measurement setup (a) and schedule (b) (Bezuidenhout, 2017)

3.15 Chloride penetration testing

After the completion of the chloride-induced corrosion testing (9th ponding cycle), the chloride penetration was investigated for each beam. The chloride penetration was tracked by cutting the beams in half. A wind pressure hose was used to remove any excess dust from the freshly cut surface and a $AgNO_3$ solution was sprayed onto the surface. The solution contained 0.1 moles of $AgNO_3$ per 1 ℓ of deionised water, as specified by NT Build 443 (1995). The Ag ions react with the free chlorides resulting in a precipitation of a white/grey precipitation of silver chloride. The region that has a dark colour is free from chlorides. The precipitation only occurs when chloride concentration is about 0.07 mol/dm^3 or 2.48 g/dm^3. There might be chlorides present in the dark area but not enough to react with the Ag ions (Otsuki, Nagataki & Nakashita, 1993; Van Der Putten, De Volder et al., 2020). The distinction between grey and dark is shown in Figure 3-27. The chloride ingress depths were measured using a vernier calliper (0.01 mm resolution) and the black arrows in Figure 3-27 indicate the measurement positions.

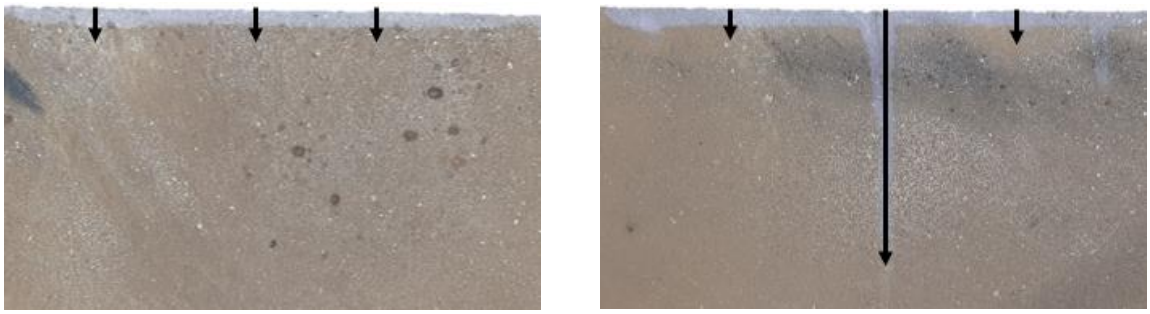

(a) (b)

Figure 3-27: Chloride penetration depth measurement positions for the cast (a) and 3DCP (b) samples

3.16 Corrosion inspection

After the chloride penetration testing was completed, the steel rods were removed from the beams to investigate the corrosion. A chipper was used to extract the steel rods and a hard plastic brush was used to remove any excess concrete on the steel surface. The corrosion location was established, and the length of the anodic region was measured using a vernier calliper.

4 Results and discussion

4.1 Introduction

This chapter presents the results obtained in conjunction with an analysis and discussion of the tests outlined in Chapter 3. The results are discussed in the following order: mechanical strength characterisation, DI performance, accelerated concrete carbonation, and chloride-induced corrosion. The notation used in this study to identify each sample is listed in Table 4-1.

Table 4-1: Experimental variable notation

Notation		
# - & - @	#	Sample type: 3D (3DCP sample), C (Cast sample)
	&	3DPC pass time: 0, 10, 20, 30 (For 0-, 10-, 20-, and 30-min pass time) Cast compaction method: V (Vibrating table), P (Poker vibrator)
	@	Sample number: 1 to 3 (Sample 1 to 3), AVG (Average)

4.2 Mechanical strength results

The mechanical strength results are divided into compressive strength and flexural strength results, discussed in Chapters 4.2.1 and 4.2.2 respectively.

4.2.1 Compressive strength

The compressive strength of the cast samples compacted with the vibration table and poker vibrator are listed in Table 4-2. The CV in Table 4-2 stands for coefficient of variance. The C-V samples yield a 40.44 MPa compressive strength, whereas the C-P samples yield a 63.18 MPa. The C-P samples yield a larger compressive strength owing to the increases in compaction provided by the poker vibrator, which removes more voids and results in a denser matrix.

Table 4-2: Compressive strength results

Experimental variable	σ_c (MPa) (%CV)
C-V	40.44 (6.27)
C-P	63.18 (3.24)

4.2.2 Flexural strength

As mentioned in Chapter 2.5.3.1, mechanical performance is not a precise measurement of the potential durability performance of the concrete, yet it does give a clear indication that the lack of fusion at the IR can result in durability issues. The average flexural strength results listed in Table 4-3 will only serve as an indication of the lack of fusion present at the IRs.

Table 4-3: Flexural strength results

Experimental variable	σ_c (MPa) (%CV)	Failure location
C-P	7.34 (10.79)	Sample centre
3D-0	4.31 (9.67)	Various IRs between layers 5-11
3D-10	2.59 (15.33)	Critical layer
3D-20	2.32 (14.61)	Critical layer
3D-30	2.20 (16.62)	Critical layer

The results from Table 4-3 indicate the following:

(i) The 3D-0 samples yield a flexural strength of 4.31 MPa, which is higher than the results obtained by Moelich et al. (2021a). The flexural strength of the 3DCP samples reduces with an increase in pass time. The 3D-10, 3D-20, and 3D-30 yield flexural strengths of 2.59 MPa, 2.32 MPa, and 2.20 MPa respectively. The decrease in flexural strength with an increase in pass time is attributed to surface moisture evaporation and thixotropy (as discussed in Chapters 2.5.3.1.1 and 2.5.3.1.3). A longer pass time results in a higher degree of surface moisture evaporation, leaving behind a dryer and more rigid layer

with limited intermixing capabilities for the next layer to be printed on. The thixotropic behaviour of the 3DCP mix design also plays a role in the lack of fusion at the critical layer. All the pass times considered in this study are longer than the t_{rf}, which hinders the formation of a physical bond at the IRs of the critical layer. Ongoing structuration also results in a more rigid surface for subsequent layer to be printed on, which increases the lack of fusion at the critical layer. The decrease in flexural strength with an increase in pass time was also presented by Kruger & van Zijl (2021).

(ii) All the 3DCP samples, except for 2 of the 3D-0 samples, fail at the IRs. This is attributed to the lack of fusion present between printed layers (as mentioned in Chapter 2.5.3). The interconnected pores present at the IRs reduce the layer fusion, which increases the failure probability at the IRs. All the 3DCP samples involving a pass time fail at the critical layer, which is attributed to the lack of fusion induced by the pass time.

(iii) The C-P samples yield a flexural strength of 7.34 MPa, which is similar to the results obtained by Moelich et al. (2021a). The C-P samples outperform the 3DCP samples, irrespective of the pass time. This is attributed to the lack of fusion present at the IRs of the 3DCP samples, which does not occur in the homogonous C-P samples.

4.3 Durability index results

The DI results are divided into visual observations and the DI results. As mentioned in Chapter 3.5.2, the DI samples were printed using a layer width of 40 mm compared to the 30 mm used in the other prints. Therefore, in order to incorporate a larger layer width at the same printing speed, a higher extrusion rate in needed. This would increase the compaction of subsequently printed layers, resulting in a higher degree of layer fusion.

4.3.1 Visual observations

Before each DI started, the samples were inspected and information was recorded, from a macro perspective, regarding the visual surface porosity, visible critical layer and sample damage. The porosity on the cut surface for typical C-V, C-P, and 3D-0 samples are shown in Figure 4-1. Figure 4-2 shows a side view of the DI samples. The position of the black arrow indicates the position of the critical layer.

(a) (b) (c)

Figure 4-1: Visible surface porosity for C-V (a), C-P (b), and 3D (c) samples

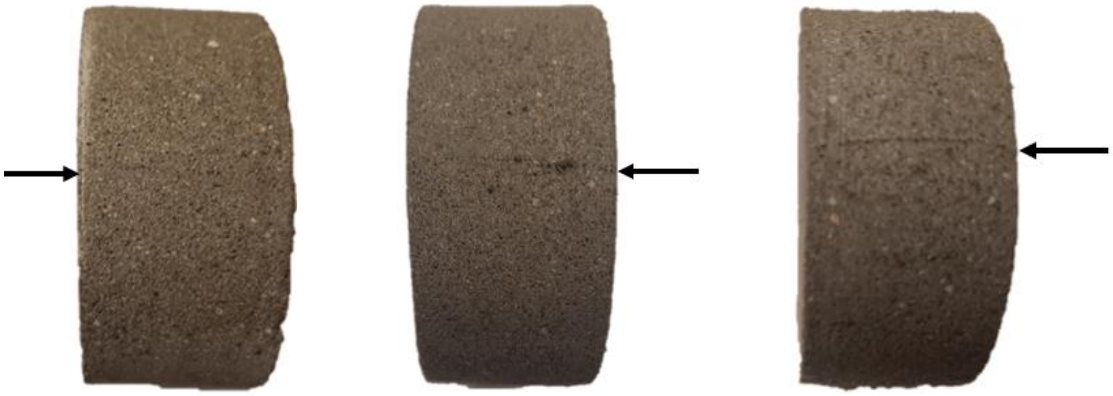

(a) (b) (c)

Figure 4-2: Visible critical layer for 3D-10 (a), 3D-20 (b), and 3D-30(c) samples

From Figure 4-1 and Figure 4-2, the following trends are observed:

(i) Small, randomly distributed voids are visible on the surface of the C-V samples (Figure 4-1a). These voids are not observed in the C-P and 3D-0 samples (Figure 4-1b and Figure 4-1c). This is due to the addition of the poker vibrator, allowing for a higher degree of compaction. The concrete pumping during the printing procedure also increases the compaction.

(ii) No visible IRs are detected in the uniform 3D-0 samples; however, the critical layer became more visible with an increase in pass time. The 3D-10 sample (Figure 4-2a) has a slightly visible critical layer, followed by a more visible critical layer for the 3D-20 sample (Figure 4-2b). The 3D-30 samples (Figure 4-2c) have the most distinctive

critical layer that spanned the width of the sample. The critical layer visibility increases with an increase in pass time owing to the moisture evaporation and thixotropy.

4.3.2 Oxygen permeability index results

The OPI test was conducted at the concrete age of 28 days at Stellenbosch University. The OPI and k results are listed in Table 4-4, and Figure 4-3 shows a visual representation of the results obtained. The error bars in Figure 4-3 indicate ± one standard deviation.

Table 4-4: OPI and k test results

OPI result	**Experimental Variable**					
	C-P	**C-V**	**3D-0**	**3D-10**	**3D-20**	**3D-30**
OPI (log scale) (%CV)	11.09 (0.57)	10.43 (1.38)	10.23 (0.27)	10.10 (0.36)	9.99 (0.20)	9.97 (0.57)
k (x10^{-11} m/s) (%CV)	0.827 (15.22)	3.912 (33.01)	5.894 (6.38)	8.002 (8.35)	10.195 (4.50)	10.825 (13.31)

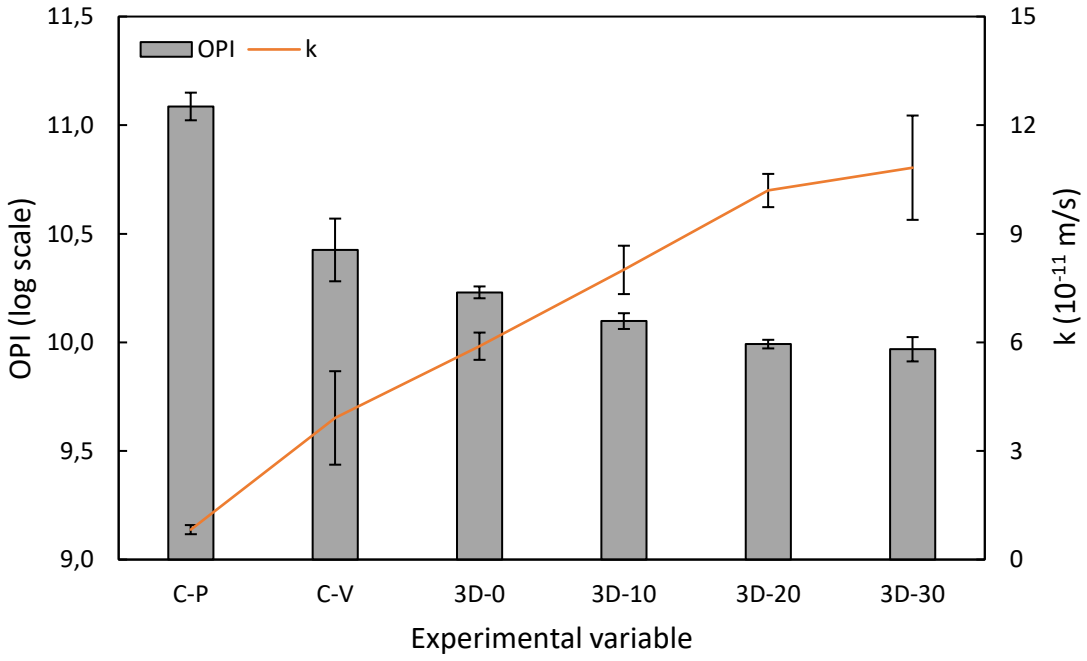

Figure 4-3: Visual representation of the OPI test results

The findings from Table 4-4 and Figure 4-3 indicate that:

(i) For the cast samples, the C-P samples are the least permeable and recorded the highest OPI of 11.09. The C-V area more permeable, which resulted in a lower OPI of 10.43. This was due to the lower degree of compaction achieved by the vibrating table compared to the poker vibrator, resulting in a more permeable matrix.

(ii) For the 3DCP samples, the 3D-0 samples are the least permeable and achieved an OPI of 10.23, followed by the 3D-10, 3D-20, and 3D-30, which recorded an OPI of 10.10, 9.99, and 9.97 respectively. The OPI for the 3D-0 samples are similar to the results reported by Moelich et al. (2021a). The 3DCP samples increase in permeability with an increase in pass time, which is as a result of the lack of fusion at the critical layer induced by the pass time.

(iii) Both the C-V and C-P outperform all the 3D-samples. The interconnected voids at the IRs of the 3DCP result in a more permeable structure, compared to randomly dispersed voids of cast samples Moelich et al. (2021a) also reported that cast samples yielded higher OPI results compared to the printed samples.

(iv) The C-P, C-V, 3D-0, and 3D-10 all fall within the excellent durability class while the 3D-20 and 3D-30 fall within the good durability class (refer to Table 2-4). The OPI results for all the printed samples are in range or higher than conventional cast concrete samples produced by Salvoldi et al. (2015) and Otieno et al. (2020). Salvoldi et al. (2015) and Otieno et al. (2020) performed OPI tests on concrete mixtures consisting of OPC, PC/FA, OPC/SF and OPC/GGBS. Thus, the 3DCP samples are competitive when compared to conventional cast concrete.

4.3.3 Water sorptivity index results

The WSI test was conducted at the concrete age of 28 days at UCT. The S and n results are listed in Table 4-5, and Figure 4-4 shows a visual representation of the results obtained. The error bars in Figure 4-4 indicate $\pm$ one standard deviation.

Table 4-5: S and n test results

WSI result	**Experimental Variable**					
	C-P	**C-V**	**3D-0**	**3D-10**	**3D-20**	**3D-30**
S (mm/√h) (%CV)	4.09 (1.37)	4.31 (1.38)	4.82 (4.48)	5.42 (1.89)	5.49 (11.09)	4.83 (2.78)
n (%) (%CV)	9.23 (1.69)	16.39 (1.38)	18.16 (2.38)	18.48 (1.20)	18.50 (3.03)	19.71 (1.58)

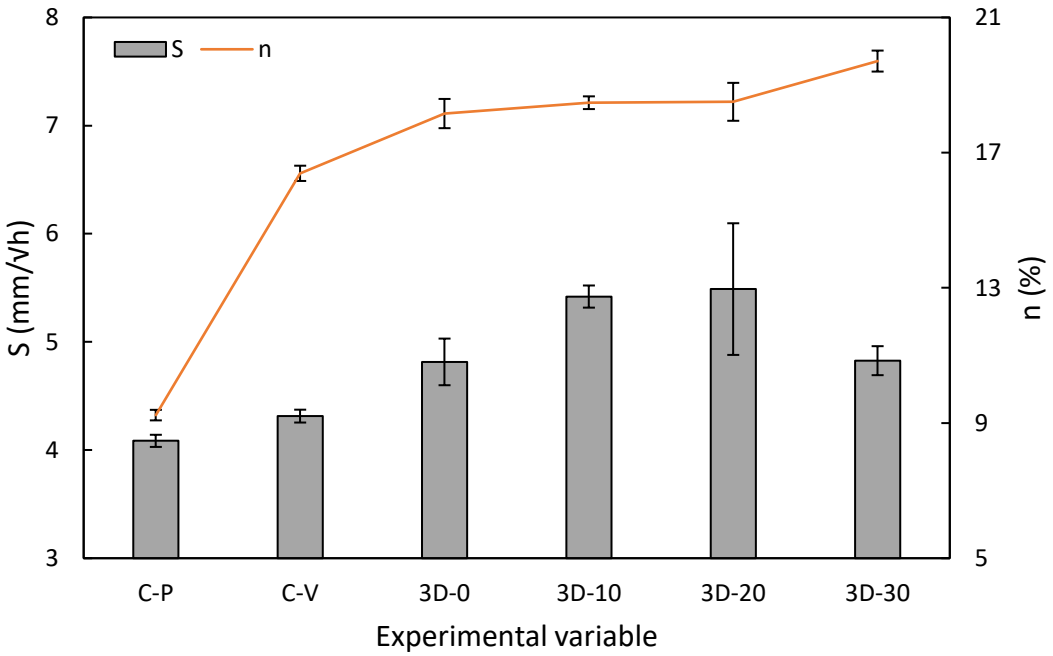

Figure 4-4: Visual representation of the WSI test results

From Table 4-5 and Figure 4-4, the following trends are observed:

(i) For the cast samples, the C-P samples have the lowest porosity and sorptivity rate of 9.23% and 4.09 mm/√h. The C-V are more porous (16.39%) and record a larger sorptivity of 4.31 mm/√h. The difference in porosity and sorptivity is attributed to the method of compaction. The use of the poker vibrator allowed for the formation of a denser matrix.

(ii) For the 3DCP samples, the 3D-0 samples have the lowest porosity, and the porosity increased with an increase in pass time. This could be attributed to the increased porosity at the critical layer that was observed in Figure 4-2.

(iii) The S results for the 3D-0, 3D-10, and 3D-20 increase with an increase in pass time. 3D-10 and 3D-20 record similar results. The 3D-30 did not follow this trend and yielded an S of 4.83 mm/√h, which is similar to 3D-0 of 4.82 mm/√h.

(iv) As mentioned in Chapter 3.11.2, the 3D-0 sample stayed in the solution for three days instead of 18 h, owing to unforeseen circumstances. This leads to an additional absorption of the solution. A higher M_{sv} results in a decrease in S and an increase in n (Equations 3-5 and 3-6).

(v) Overall, the cast samples outperform the 3DCP samples. The cast samples record lower S and n values compared to the 3DCP samples.

(vi) All the experimental variables have S values lower than 6 mm/√h, which classifies all the samples in the excellent durability class (refer to Table 2-4). The S results obtained for all the printed samples are lower than the results produced by Otieno et al. (2020) for conventional cast concrete. Otieno et al. (2020) reported S results of 9 mm/√h and higher. Thus, the 3DCP samples outperform Otieno et al. (2020) conventional cast concrete and are more durable from a sorptivity point of view.

4.3.4 Chloride conductivity index results

The CCI test was conducted at 28 days at UCT. The σ and n results are listed in Table 4-6 and Figure 4-5. The error bars in Figure 4-5 indicate ± one standard deviation.

Table 4-6: σ and n test results

CCI result	**Experimental Variable**					
	C-P	**C-V**	**3D-0**	**3D-10**	**3D-20**	**3D-30**
σ (mS/cm) (%CV)	0.46 (14.61)	0.82 (10.63)	1.08 (12.48)	1.78 (6.49)	1.90 (7.38)	2.05 (13.23)
n (%) (%CV)	3.32 (4.66)	6.15 (4.27)	7.88 (3.41)	7.48 (9.33)	7.58 (3.46)	7.53 (3.02)

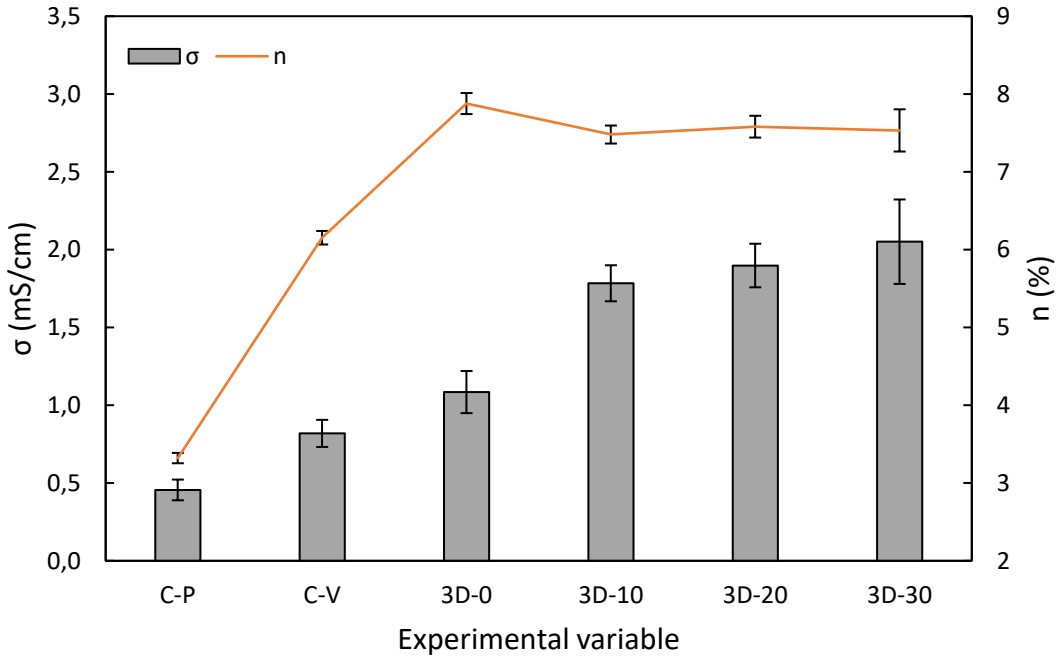

Figure 4-5: Visual representation of the CCI test results

The results from Table 4-6 and Figure 4-5 indicate that:

(i) For the cast samples, the denser matrix C-P yield the lowest σ of 0.48 mS/cm compared to the 0.84 mS/cm of the C-V samples. C-P also yield a lower porosity owing to the denser matrix.

(ii) For the 3DCP samples, there is a clear increase in σ with an increase in pass time. The 3D-0, 3D-10, 3D-20, and 3D-30 samples yield σ values of 1.08 mS/cm, 1.78 mS/cm,

1.90 mS/cm, and 2.05 mS/cm respectively. The increase in pass time reduces the layer fusion at the critical layer allowing for a larger current to pass through the sample.

(iii) For the 3DCP samples, no trend in n is observed. All the n values were within 7.53% and 7.88% with the 3D-0 sample yielding the largest n.

(iv) As mentioned in Chapter 3.11.2, the 3D-0 sample stayed in the NaCl solution for three days instead of 18 h, owing to unforeseen circumstances. The variation led to an additional absorption of the solution. A higher M_s can result in increase in n (Equation 3-8). The additional soaking time will also result in additional chloride binding that will yield lower σ values.

(v) Overall, the cast samples outperform the 3DCP samples, yielding lower σ and n values. The lack of fusion present at the IRs of the 3DCP samples act as a pathway for the applied voltage, thus resulting in higher chloride conductivity. Moelich et al. (2021a) also reported that cast samples yielded lower σ results compared to the printed samples.

(vi) The C-P falls within the excellent durability class. The C-V and 3D-0 fall within the good durability class while the 3D-10, 3D-20, and 3D-30 fall within the poor durability class (refer to Table 2-4). Otieno et al. (2016) reported σ of 1.24 mS/cm for conventional concrete mixtures consisting of OPC and σ between 0.26 and 0.89 mS/cm for blended cement mixtures. The printed samples, especially the ones with induced pass times, are outperformed by conventional cast concrete samples produced by Otieno et al. (2016) and thus have a lower resistance to chloride penetration.

4.4 Accelerated concrete carbonation results

The accelerated concrete carbonation results are divided into visual observations taken after the accelerated concrete carbonation test, the carbonation depth measurements over the 12-week periods, and a discussion of the influence of the IRs and critical layer of the 3DCP samples.

4.4.1 Visual observations

The freshly cut surface was sprayed with a phenolphthalein indicator that turns purple in the areas which are not carbonated. Figure 4-6 and Figure 4-7 show the 12-week carbonation cast and 3DCP samples after the indicator was applied. Chapters 4.4.2 and 4.4.3 elaborate on the

progression of the carbonation front and the influence of the IRs and critical layer present in the 3DCP samples.

(a) (b) (c)

Figure 4-6: 12-week carbonation front for C-V-1 (a), C-V-2 (b), and C-V-3 (c)

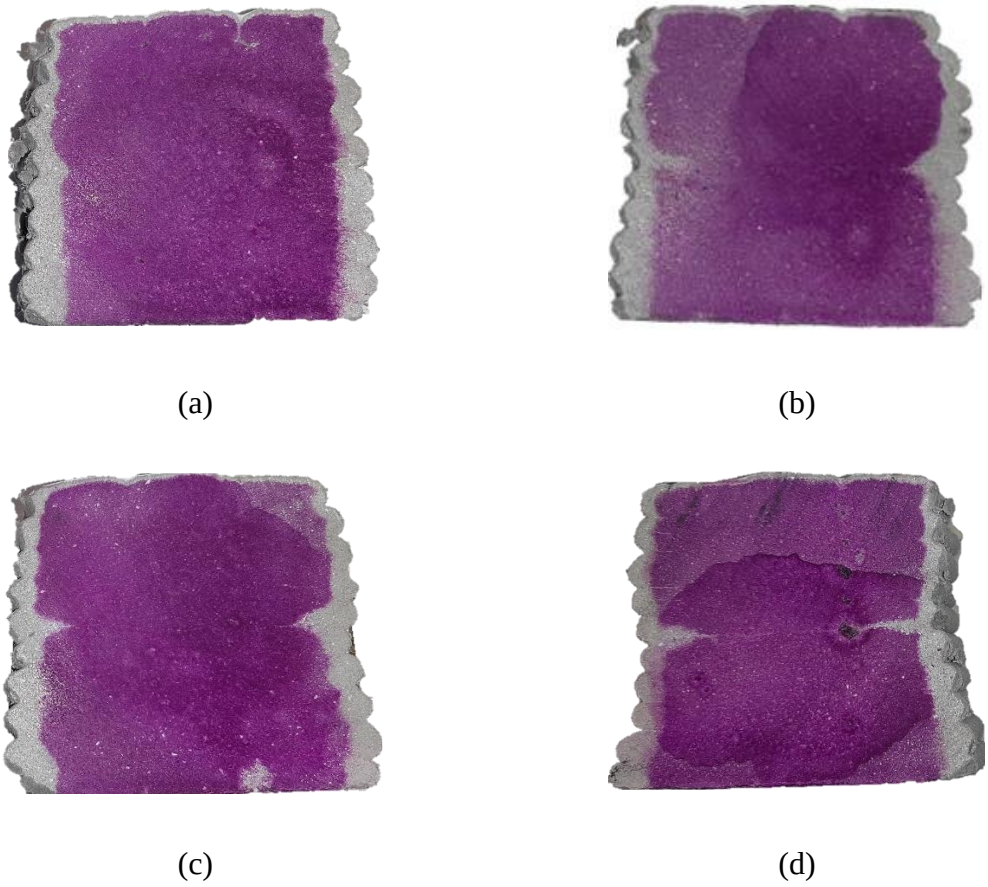

(a) (b)

(c) (d)

Figure 4-7: 12-week carbonation front for 3D-0 (a), 3D-10 (b), 3D-20 (c), and 3D-30 (d)

From Figure 4-6 and Figure 4-7, the following trends are observed:

(i) The carbonation front of the C-V samples is unform across the section.

(ii) The carbonation front for all of the 3DCP samples appears larger through the layer itself than the IRs. Chapter 4.4.2 elaborates on the carbonation depth in the layer compared to the IRs.

(iii) There is a clear increase in the carbonation depth at the critical layer where the pass time is larger than 0 min. This is attributed to the lack of fusion induced by the pass time. Chapter 4.4.3 elaborates on the effect of the critical layer.

(iv) For the 3D-10 and 3D-20 samples, the carbonation depth of the top later (relative to the critical layer region) is larger than for the bottom layer. This is attributed to the moisture change phenomena discussed in Chapter 2.5.3.1.1, that result in a more porous top layer. The more porous top layer allows for faster CO_2 ingress compared to the denser bottom layer. This trend is less prominent in the 3D-30 sample, where CO_2 ingress governed through the highly permeable critical layer.

4.4.2 Carbonation front profiles

The carbonation depth was measured at 3, 6, 9, and 12 weeks. Figure 4-8 to Figure 4-12 show the progression of the carbonation depth for the 3DCP and cast samples over the 12-week period. The average carbonation front of the three cast samples was used to represent the carbonation front of a cast sample.

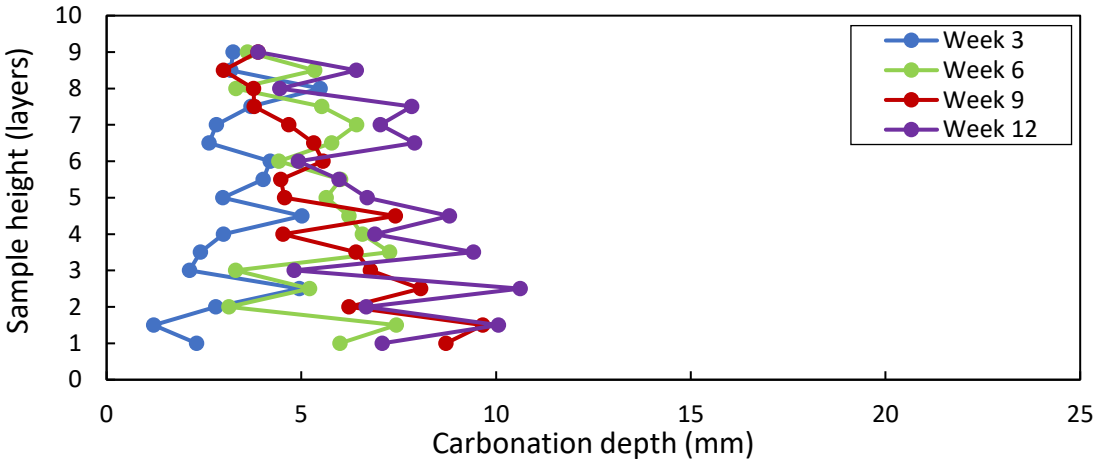

Figure 4-8: 3D-0 12-week carbonation front progress

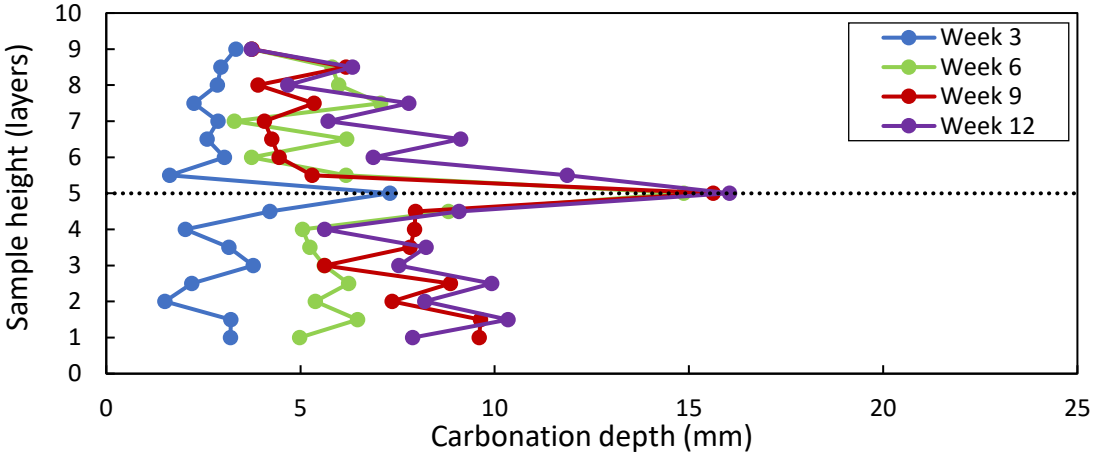

Figure 4-9: 3D-10 12-week carbonation front progress

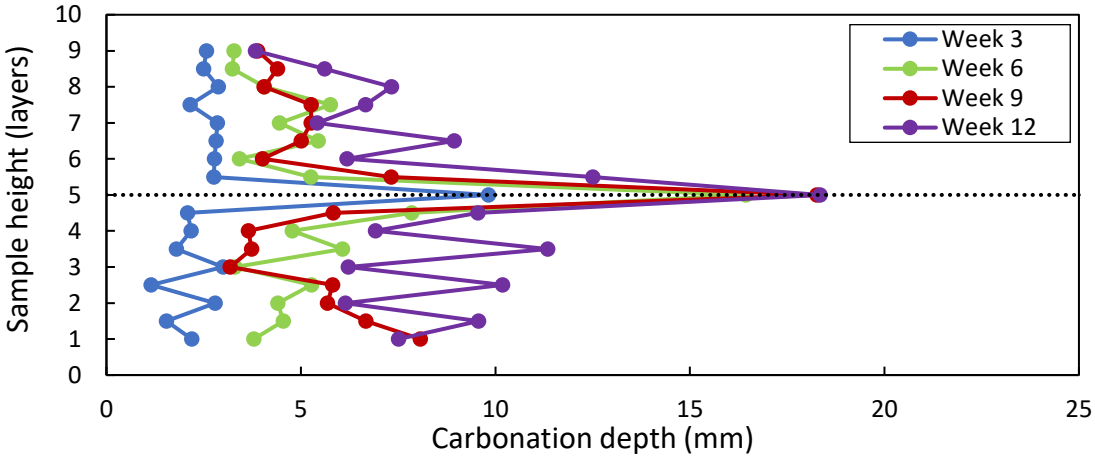

Figure 4-10: 3D-20 12-week carbonation front progress

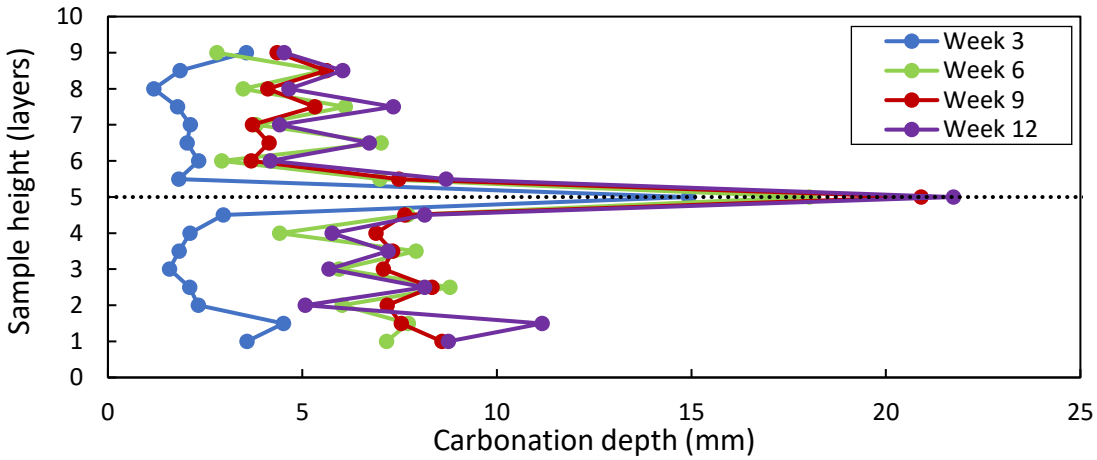

Figure 4-11: 3D-30 12-week carbonation front progress

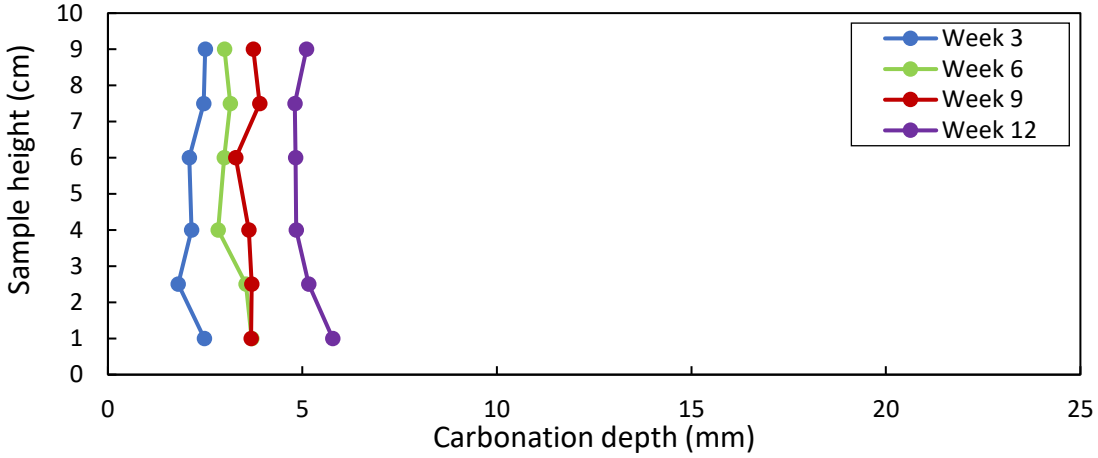

Figure 4-12: C-V 12-week carbonation front progress

The findings from Figure 4-8 to Figure 4-12 reveal the following:

(i) The carbonation front increases with an increase in exposure time. For the 3DCP samples, the carbonation front progressed quickly in the first six weeks, whereafter the rate of progression started to decrease for the final six weeks. The C-V-AVG samples show a gradual progression of the carbonation front over the 12-week period.

(ii) The C-V-AVG samples yield a uniform carbonation front. This is not the case for the 3DCP samples. For all of the 3DCP samples, the average carbonation depth at the IRs, excluding the critical layer, are smaller than in the layer itself. This is due to the increase in exposed surface at the layer edge. The curved edge of the layer has a larger exposed surface area compared to a flat layer edge with the same layer height (Figure 4-13). If the edge is completely circular, the curved area per unit length will be 57% greater than the flat edge, which will result in an increase in concrete carbonation based off first principles (refer to Chapter 2.4.4.1). The increase in exposed surface area overpowers the effect of the IRs, but not at the critical layer.

(iii) The influence of the pass time on the layer fusion at the critical layer is prominent. The 3D-10, 3D-20, and 3D-30 samples show a sharp increase in the carbonation depth at the critical layer in comparison to the rest of the sample. Chapter 4.4.3 elaborates on the effect of the critical layer.

(iv) Overall, at each inspection time, the C-V-AVG samples outperform all the 3DCP samples, irrespective of the pass time.

(a) (b)

Figure 4-13: Exposed surface area of 3DCP layer with a curved (a) and flat (b) edge

4.4.3 Critical layer carbonation depth

The carbonation depth at the critical layer is of importance in order to quantify the lack of fusion induced by the pass time. Figure 4-14 shows the increased carbonation depth at the critical layer over the 12-week exposure period. The average carbonation depth of the IRs for the 3D-0 and the average carbonation depth for the C-V-AVG were used in Figure 4-14. The formula of carbonation trend line in Figure 4-14 is expressed in terms of Equation 2-27, where the gradient corresponds to the A_{CO2}.

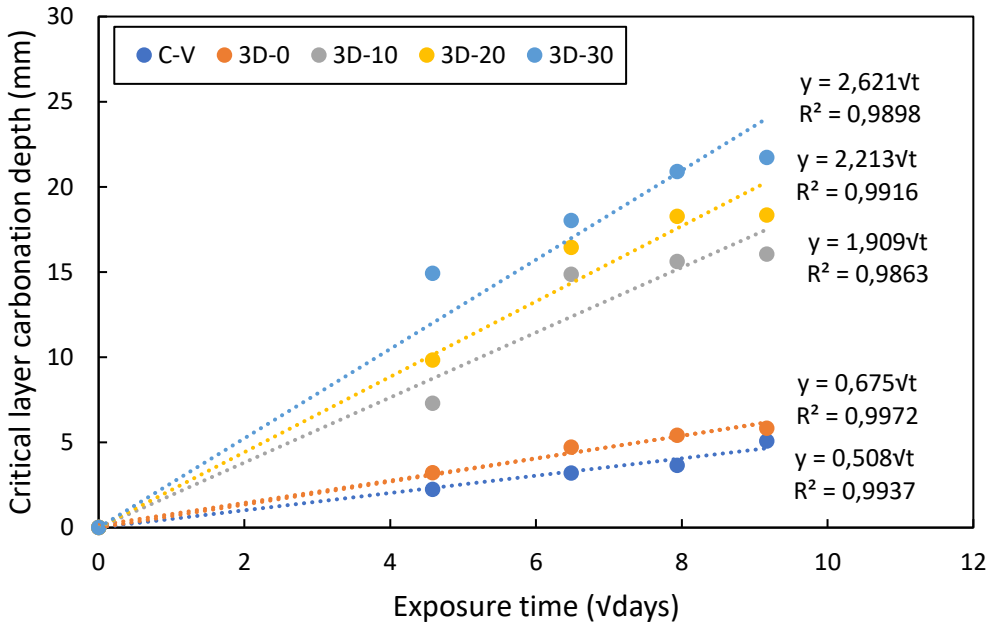

Figure 4-14: Critical layer carbonation depth versus the exposure time

The results from Figure 4-14 indicate that:

(i) As can be seen from the R^2, the carbonation depths for each experimental variable at the various exposure times show a high positive correlation. All the R^2 values are above 0.98. A higher carbonation depth corresponds to a greater A_{CO2}.

(ii) The C-V-AVG samples record smaller carbonation depths compared to the 3D-0 samples. This is contributed to the pore interconnectivity (lack of fusion) at the IR, acting as ingress pathways. This occurrence is similar to cracked concrete (Chapter 2.4.3.7), where the carbonation depth at the cracks is greater compared to the uncracked matrix.

(iii) The inclusion of a pass time decreases the concrete carbonation resistance. The carbonation depth increases with an increase in pass time. Higher pass times increase the lack of fusion (permeability) at the critical layer, which result in a higher carbonation depth. This occurrence is similar to cracked concrete (Chapter 2.4.3.7), where the carbonation depth increased with an increase in crack width. The highest carbonation depth increase between experimental variables is recorded between the 3D-0 and 3D-10 samples. The 12-week depth increase from 5.83 mm to 16.05 mm when a 10-min pass time is introduced as a result of moisture evaporation and thixotropy. The 12-week carbonation depth for the 3D-20 and 3D-30 is 18.35 mm and 21.74 mm, respectively.

(iv) Overall, the C-V-AVG samples outperform the 3DCP samples and yield a 12-week carbonation depth of 5.09 mm.

4.4.4 Correlation between the *k* and A_{CO2}

The correlation between the 28-day OPI (and *k*) and the carbonation depth is well known and forms the basis of the prediction models implemented in South Africa (refer to Chapters 2.4.4.2 to 2.4.4.4). Figure 4-15 shows the correlation between the A_{CO2} and the *k*.

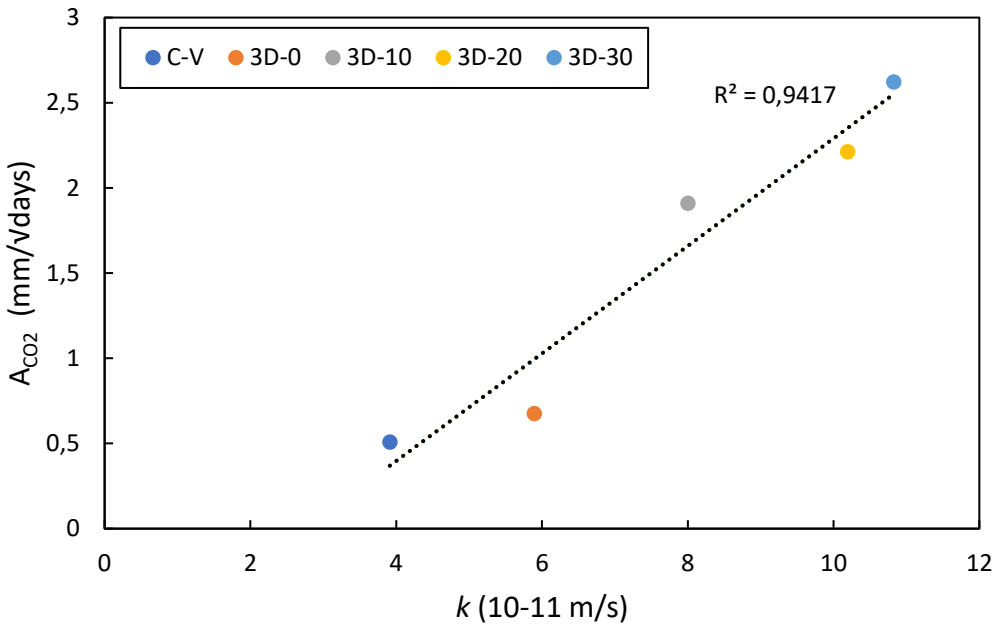

Figure 4-15: Correlation between the *k* and A_{CO2}

From Figure 4-14 and Figure 4-15, the following trends are observed:

(i) In all of the cases, an increase in *k* result in a higher A_{CO2}, proving that a more permeable sample will be more prone to carbonation.

(ii) Overall, the samples yield a high positive correlation. The R^2 for all of the experimental variables was 0.9417.

4.5 Chloride-induced corrosion results

The chloride-induced corrosion was performed on 15 printed samples and three cast beams over an 18-week period of continuous wetting and drying cycles. Corrosion measurements were performed using the GECOR 10 equipment (Sensor A). The I_{corr} readings are the main corrosion measurements under consideration in this thesis. The E_{corr} and R_{ohm} readings are additional measurements obtained through the GECOR 10. The reasons for variations in E_{corr} and R_{ohm} results over the exposure period fall beyond the scope of this study, thus the results will only be reported and not discussed. After the exposure period, the exposed surfaces were inspected, the chloride penetration depth was measured, and the steel bars were removed to investigate corrosion.

4.5.1 Chloride penetration results

4.5.1.1 Visual observations

Figure 4-16 shows the exposed ponding face and the chloride penetration profile for the beams, which best presented three beams from each experimental variable. The black dotted line indicates the top of the steel rods.

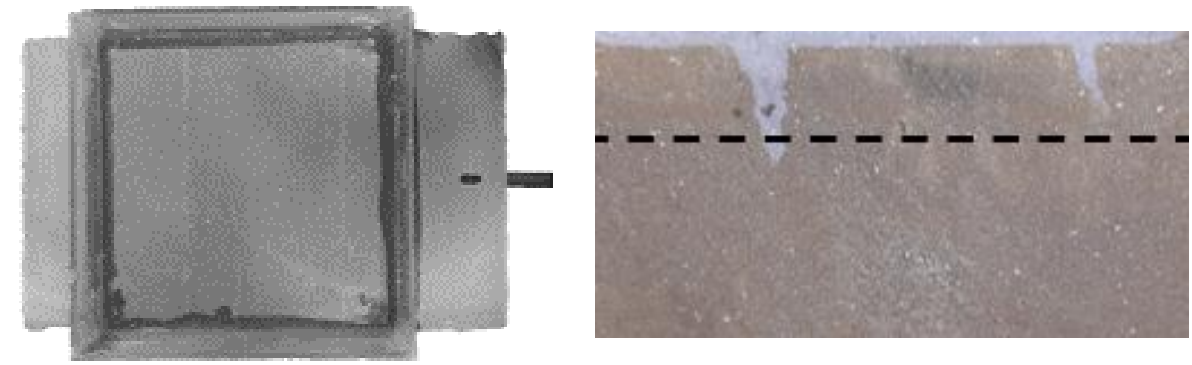

(a)

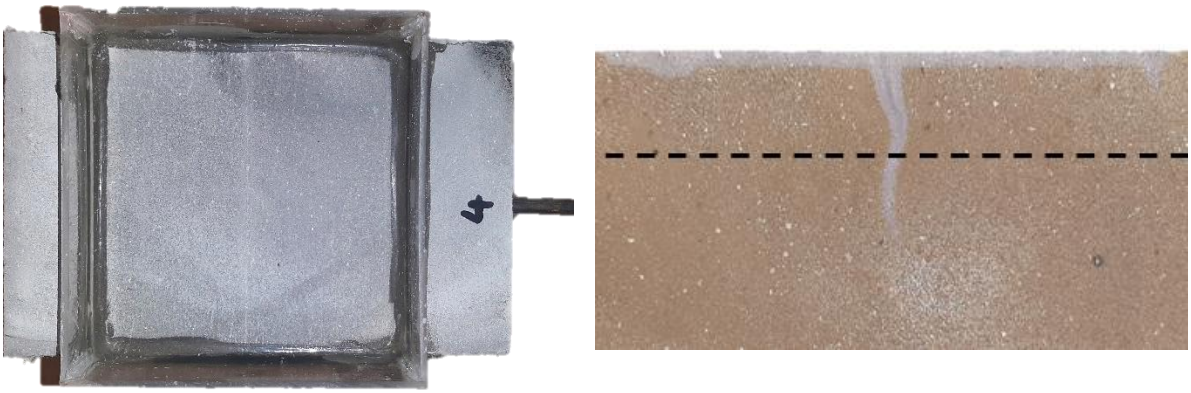

(b)

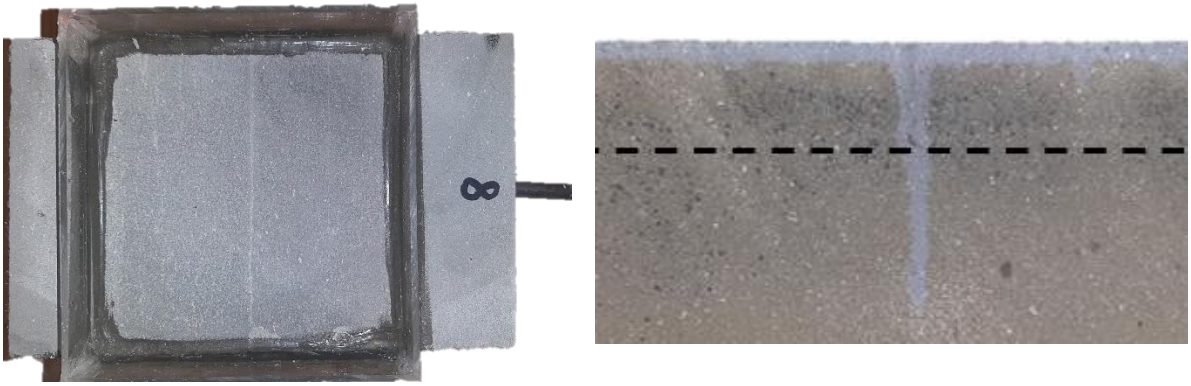

(c)

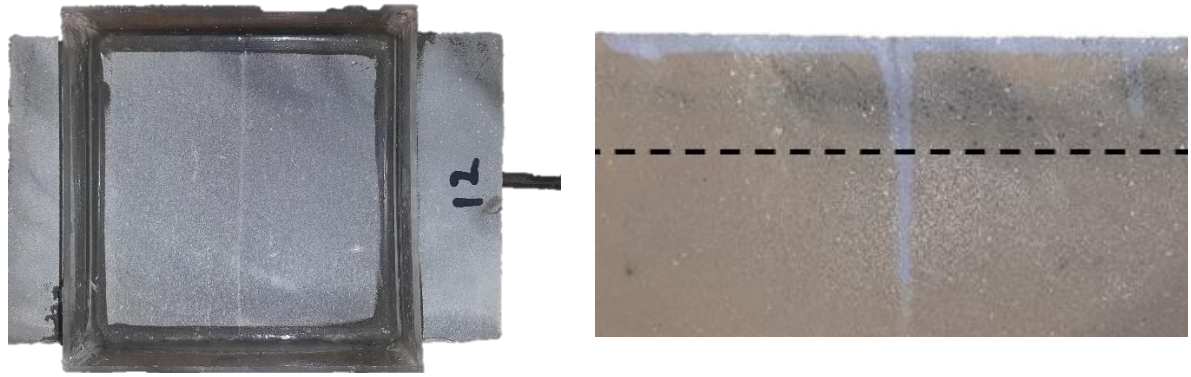

(d)

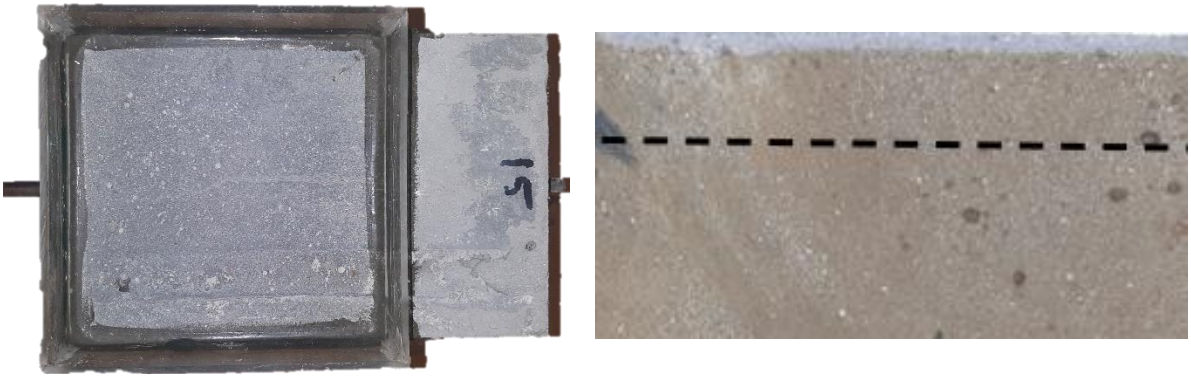

(e)

Figure 4-16: Exposed ponding face (left) and chloride ingress profile (right) for the 3D-0-1 (a), 3D-10-1 (b), 3D-20-2 (c), 3D-30-3 (d), and C-V-3 (e) beams

From Figure 4-16, the following trends are observed:

(i) The 3D-0 beams show two weak IRs (between layers 8 and 9, and between layers 17 and 18) on the ponding face. A sharp increase in chloride penetration is observed at these two locations. This is attributed to layer tearing, which can occur during the printing process. The chloride penetration to the locations of good printing quality shows a uniform chloride ingress. Layer tearing also occur at the IRs between layers 17 and 18 for both the 3D-20 and 3D-30 beams, which result in a sharp increase in chloride penetration depth.

(ii) The effect of the pass time is clearly visible on the exposed ponding surface and on the chloride penetration depths at the critical layer. The critical layer is visible at the centre of the pond for all the 3D-10, 3D-20, and 3D-30 beams. The chloride penetration depth

at the critical layer is also much deeper compared to the uniform penetration in the rest of the beam. This occurrence is due to the lack of fusion induced by the pass time.

(iii) The chloride penetration at the critical layer and torn layers function as cracks (discussed in Chapter 2.3.4.4), where the chloride penetrates through the cracks first, followed by a horizontal penetration through the concrete matrix at the cracked region.

(iv) The 3DCP beams have crack spacings that are larger than the chloride penetrating width, which corresponds to Region 3 in Figure 2-16. Chapter 4.5.5 will elaborate on the corrosion type and mechanism.

(v) The cast samples yield uniform chloride ingress profiles. An important observation regarding the concrete matrix of the cast beam is observed upon inspection of the chloride penetration. The matrix at the bottom of the beams was more compacted than the top part of the beam. The steel rods were located at the top part of the beam where more voids were located, yielding a matrix similar to that of the C-V samples. Thus, although the poker vibrator was used as a compaction method for the beams, the beams are referred to as C-V samples, based on the matrix at the steel location.

(vi) Upon inspection, the chlorides reached the level of the steel rods for all of the 3DCP beams, whereas the chloride penetration for the C-V beams did not reach the reinforcement depth.

4.5.1.2 Chloride penetration depths

The chloride penetration depths are shown in Figure 4-17. It is important to note that the critical layer for the 3D-0 beams corresponds to the penetration depth at the IR between layers 8 and 9. The unform penetration refers to the average penetration depth on both sides of the crack. The error bars in Figure 4-17 indicate $\pm$ one standard deviation.

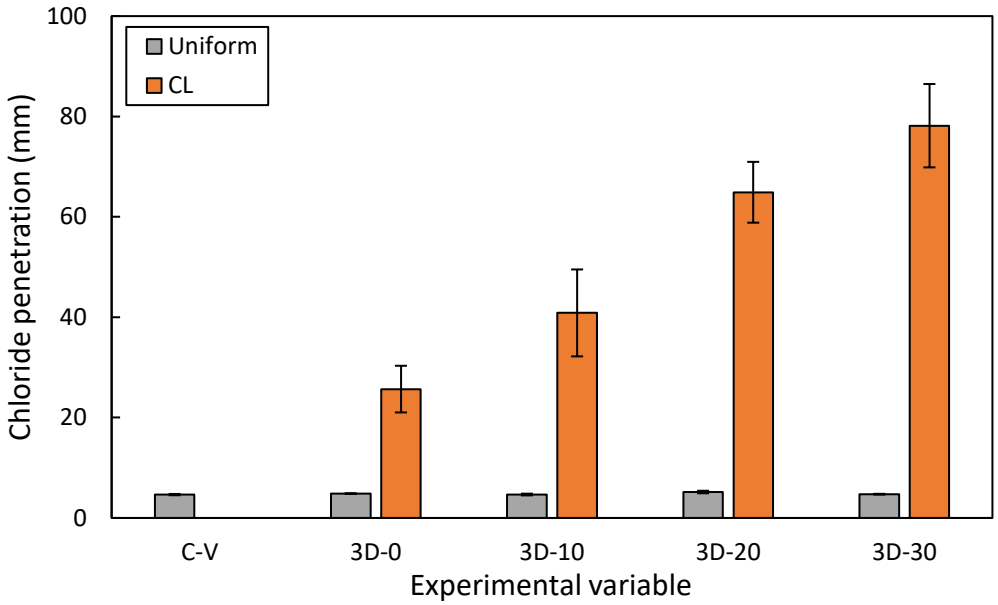

Figure 4-17: Chloride-induced corrosion beam chloride penetration depths

The findings from Figure 4-17 indicate that:

(i) The penetration depth at the critical layer is larger compared to the unform ingress at the rest of the beam. This penetration depth also increases with an increase in pass time caused by the lack of fusion induced by the pass time. Similar trends were reported in Chapter 2.5.5.2.1, where an increase in pass time resulted in deeper chloride penetration. The average penetration depth at the critical layer is 25.67 mm, 40.86 mm, 65.90 mm, and 78.16 mm for the 3D-0, 3D-10, 3D-20, and 3D-30 beams, respectively.

(ii) The uniform penetration through the C-P beam is 4.65 mm compared to the 3DCP beams, which are between 4.67 mm and 5.17 mm on average.

4.5.2 R_{ohm} results

A constant relationship exists between the R_{ohm} and ρ_e, as discussed in Chapter 2.2.10. Generally, the GECOR 10 Sensor B is used to calculate the ρ_e obtained from R_{ohm} reading. Sensor B does not implement the AMCT, and no literature was available to support the use of Equation 2-12 when obtaining R_{ohm} using Sensor A. Owing to the uncertainty of the effect of the guard rings applied current on the R_{ohm} calculation, the equation was not used. Although the R_{ohm} was not used to calculate the ρ_e, it still serves as an indication of the resistance of the concrete cover against the flow of ions. These results should be interpreted with the I_{corr} to establish the corrosion rate risk. The R_{ohm} time-development graphs for each experimental

variable are shown in Figure 4-18 to Figure 4-23. It is important to note that, owing to malfunction of the GECOR 10, the readings of the 3DCP beams during weeks 1 to 4 could not be taken. The values used in the graphs for weeks 1 to 4 were interpolated linearly using the R_{ohm} values before the test started (week 0) and in week 5. The fluctuation of the R_{ohm} results falls beyond the scope of this study and will only be used to justify fluctuations in the I_{corr} results, and to establish a relationship between the R_{ohm} and I_{corr} results.

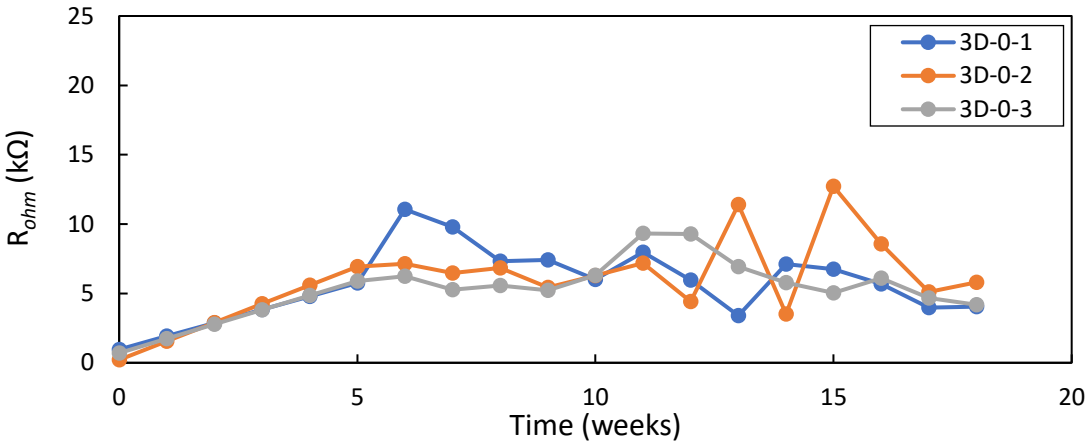

Figure 4-18: 3D-0 R_{ohm} time-development graph

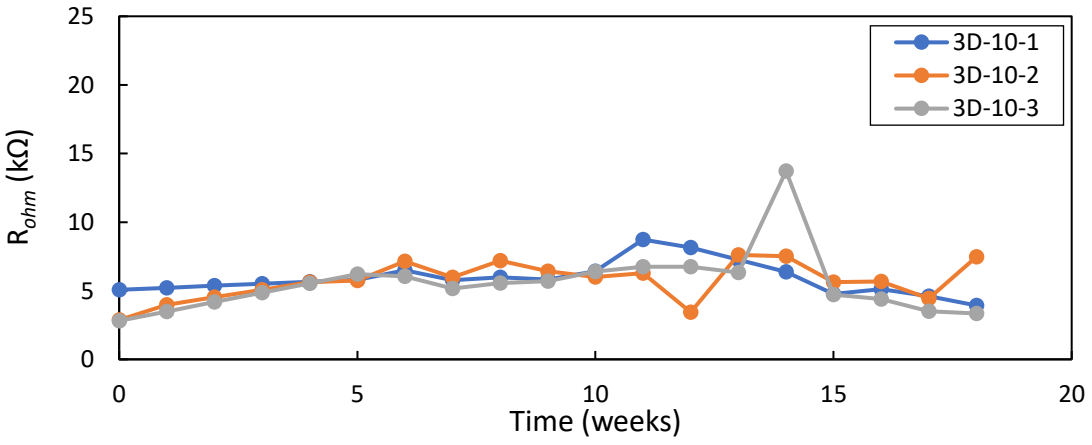

Figure 4-19: 3D-10 R_{ohm} time-development graph

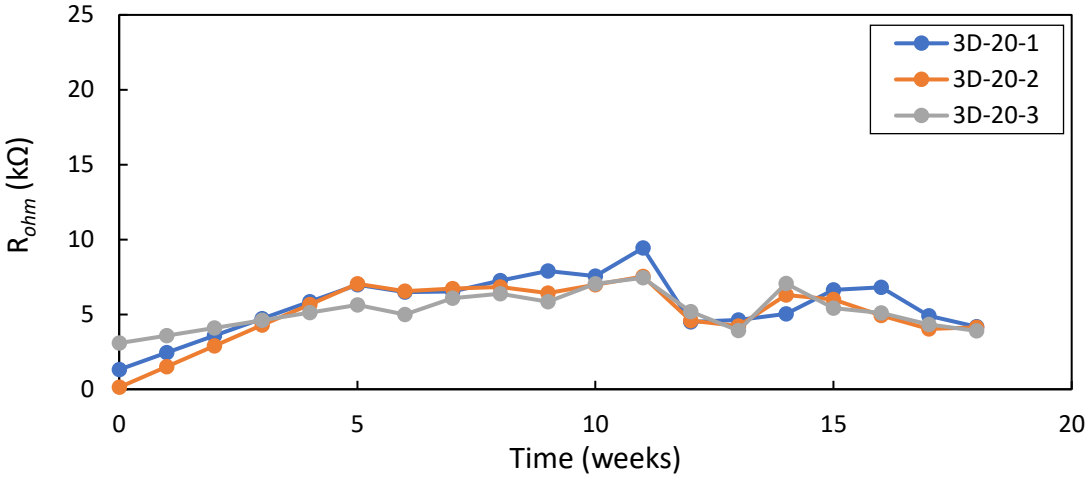

Figure 4-20: 3D-20 R_{ohm} time-development graph

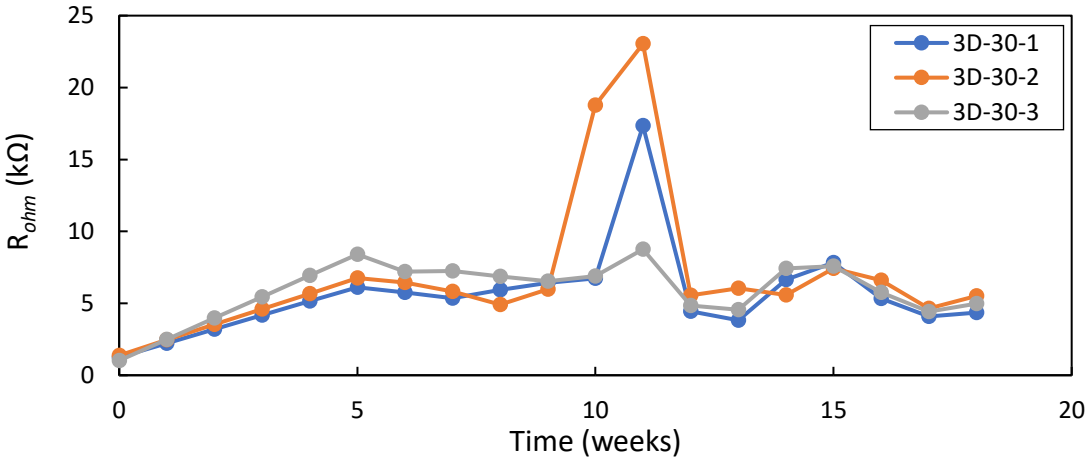

Figure 4-21: 3D-30 R_{ohm} time-development graph

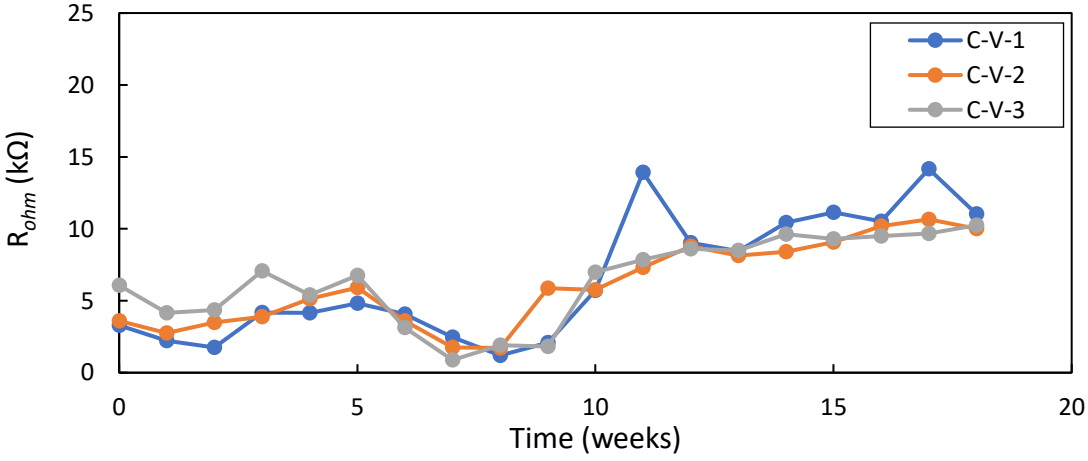

Figure 4-22: C-V R_{ohm} time-development graph

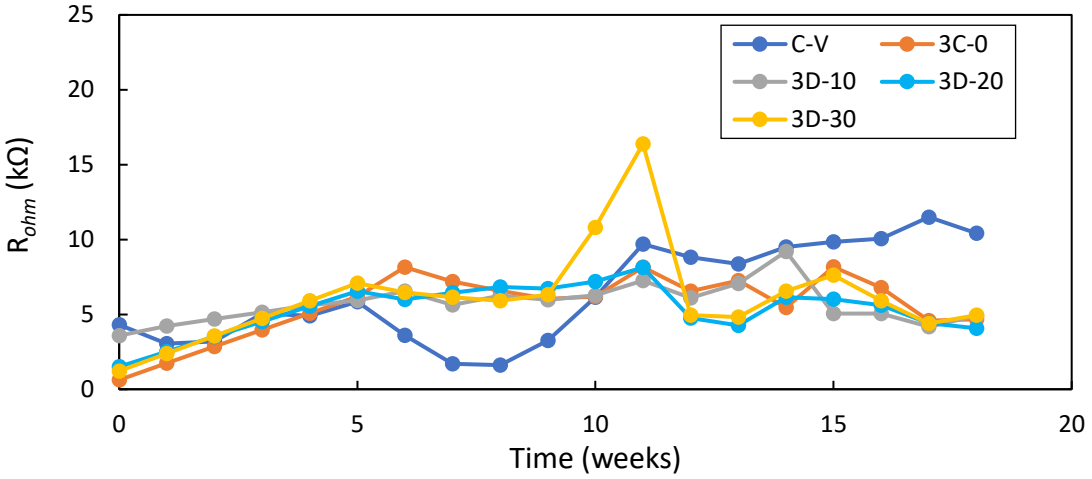

Figure 4-23: Average R_{ohm} time-development graph for all the experimental variables

4.5.3 E_{corr} results

The E_{corr} time-development graphs for each experimental variable are shown in Figure 4-24 to Figure 4-29. The GECOR 10 Sensor A is equipped with a $Cu/SuSo_4$ reference electrode. The three black dotted lines in each graph represent the intervals listed in Table 2-2. The E_{corr} results only give an indication of the corrosion risk but do not quantify the corrosion activity.

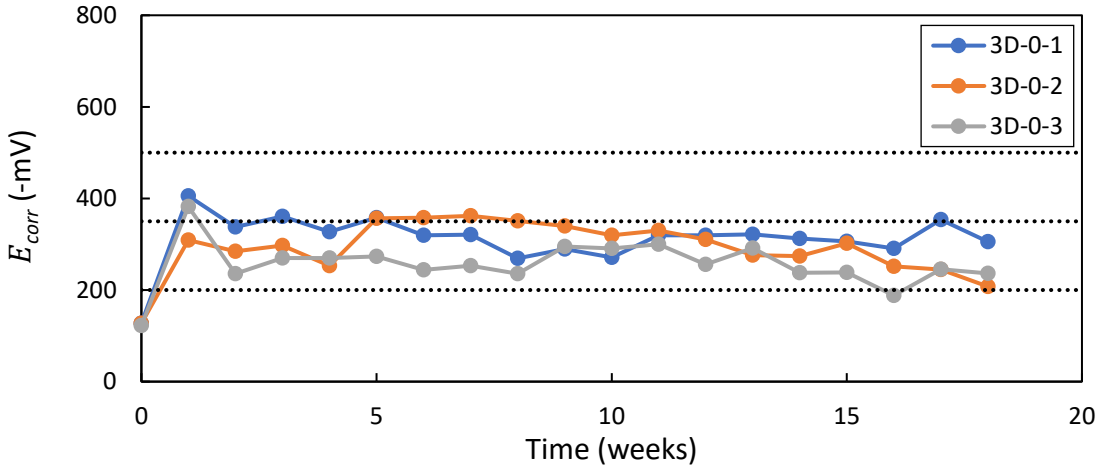

Figure 4-24: 3D-0 E_{corr} time-development graph

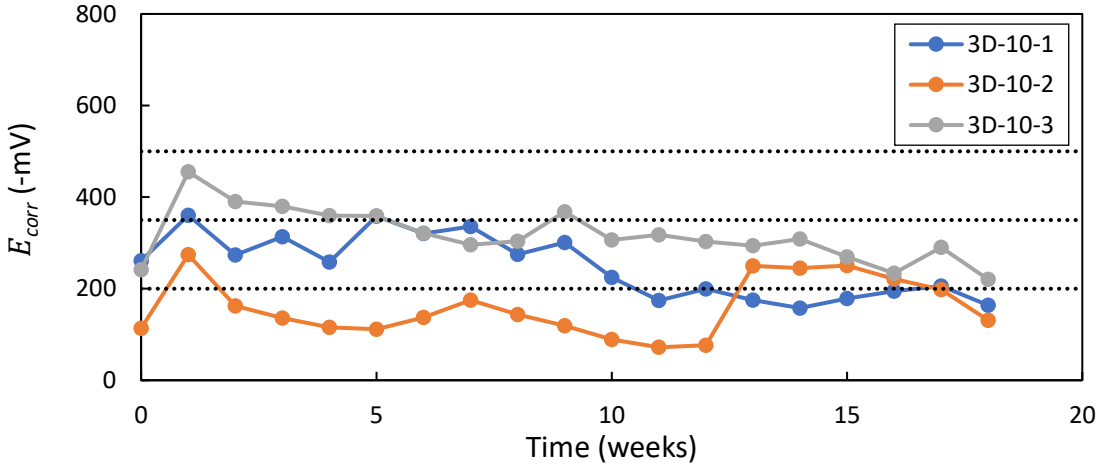

Figure 4-25: 3D-10 E_{corr} time-development graph

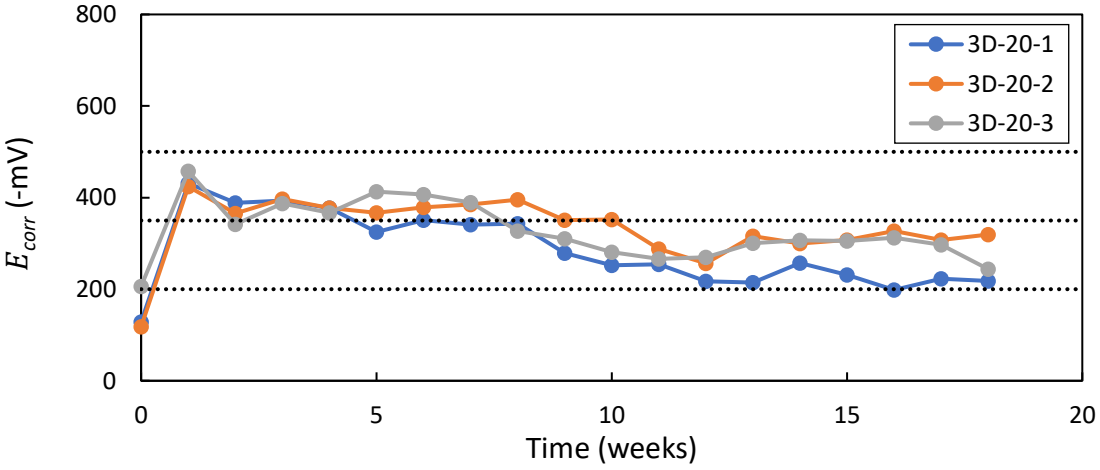

Figure 4-26: 3D-20 E_{corr} time-development graph

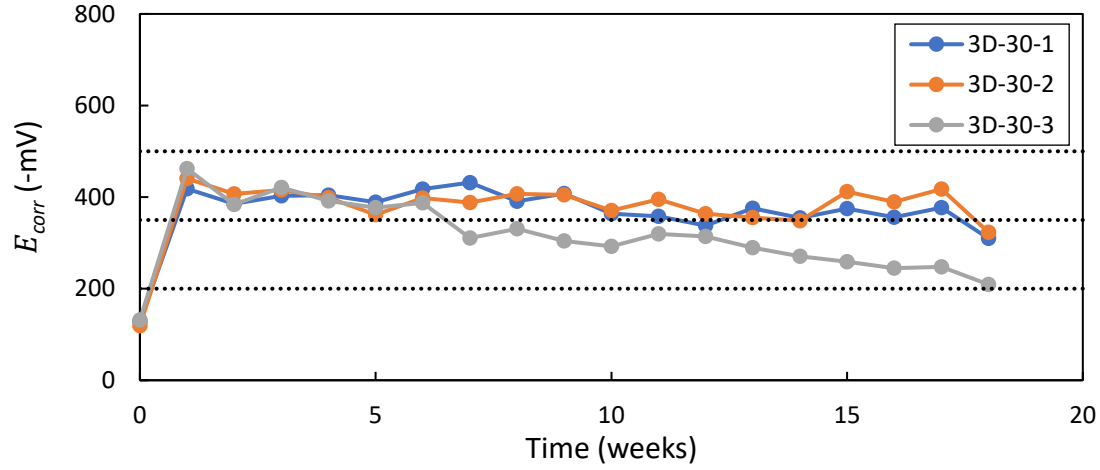

Figure 4-27: 3D-30 E_{corr} time-development graph

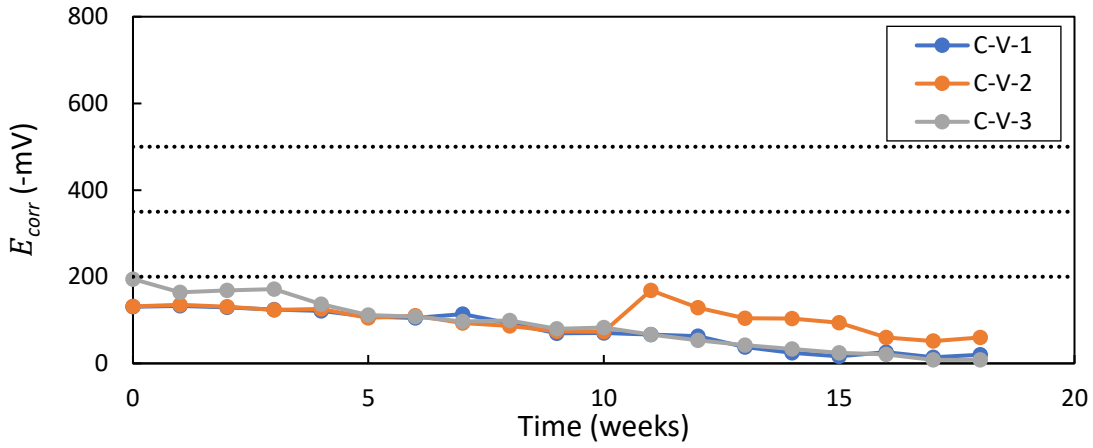

Figure 4-28: C-P E_{corr} time-development graph

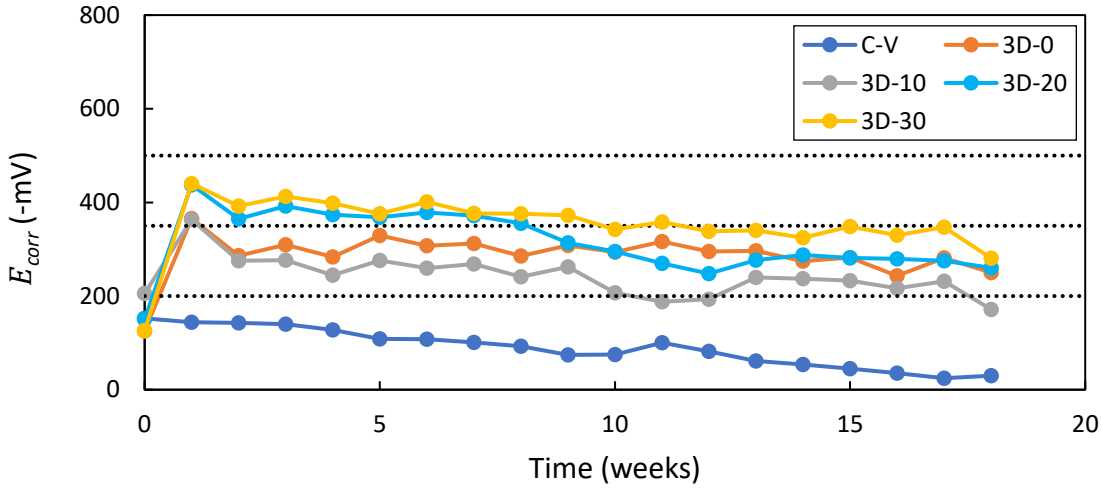

Figure 4-29: Average E_{corr} time-development graph for all of the experimental variables

The results from Figure 4-24 to Figure 4-29 indicate that:

(i) All of the 3DCP beams show a sharp decrease in potential after the first week of ponding. This is contributed to the inclusion of chloride ions. As described in Chapter 2.3.2 (Equation 2-22), the inclusion of chloride ions results in the formation of HCl which reduces the pH and destroys the protective passive layer, which results in a decrease in the potential. During early ages the passive layer is not completely formed, which means the inclusion of chloride ions at an early age will result in a sharp decrease as the passive layer is destroyed. The C-P sample did not follow this trend.

(ii) The 3D-0 samples yield potentials between -200 and -350 mV, showing an intermediate risk of corrosion.

(iii) Most of the potentials recorded for the 3D-10-3 and 3D-10-2 samples are between -200 and -350 mV, showing an intermediate risk of corrosion. The 3D-10-1 beam yield potentials higher than -200 mV and shows a sharp decrease to below -200 mV at 13 weeks.

(iv) The 3D-20 and 3D-30 show the highest corrosion risk. The 3D-20 beams record potential below -350 mV for the first eight weeks, whereafter the potentials increase after nine weeks. The potentials are lower than -350 mV for the remaining exposure duration (intermediate risk). The 3D-30-1 and 3D-30-2 yield potentials lower than -350 mV for the entire exposure duration, showing a high risk of corrosion. The 3D-30-3 has a potential lower than -350 mV from the first six weeks whereafter a potential increase occurs for the remaining duration.

(v) The C-P samples yield potentials higher than -200 mV for the entire 18-week period, which is related to a low risk of corrosion (less than 10 %).

(vi) On average, the 3D-0 and 3D-10 beams show an intermediate risk of corrosion. The 3D-20 and 3D-30 beams show an intermediate- to high corrosion risk. All of the 3DCP samples yield higher corrosion risks compared to the C-P beams, which yield a low corrosion risk.

4.5.4 I_{corr} results

The I_{corr} results are presented individually, followed by a comparison between average I_{corr} values of all the experimental variable to investigate the effect of the lack of fusion present in 3DCP samples. The relationship between the R_{ohm} and I_{corr}, as well as the E_{corr} and I_{corr} are presented. As previously mentioned, owing to malfunction of the GECOR 10, the readings of the 3DCP beams during weeks 1 to 4 could not be taken. The values used in the graphs for weeks 1 to 4 were linearly interpolated using the I_{corr} values before the test started (week 0) and in week 5.

4.5.4.1 General overview

The I_{corr} time-development graphs for each experimental variable are shown in Figure 4-30 to Figure 4-34. The black dotted line corresponds to the transition from passive to active corrosion, as listed in Table 2-3.

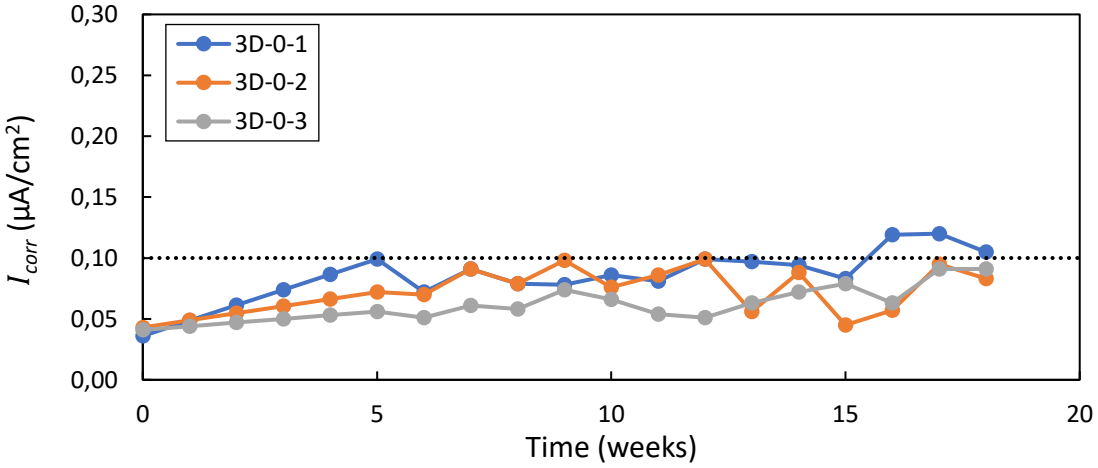

Figure 4-30: 3D-0 I_{corr} time-development graph

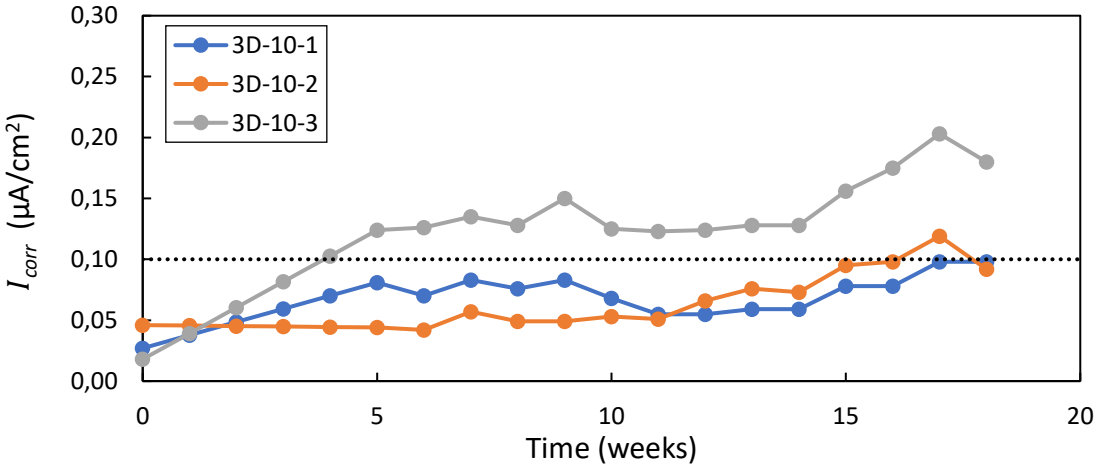

Figure 4-31: 3D-10 I_{corr} time-development graph

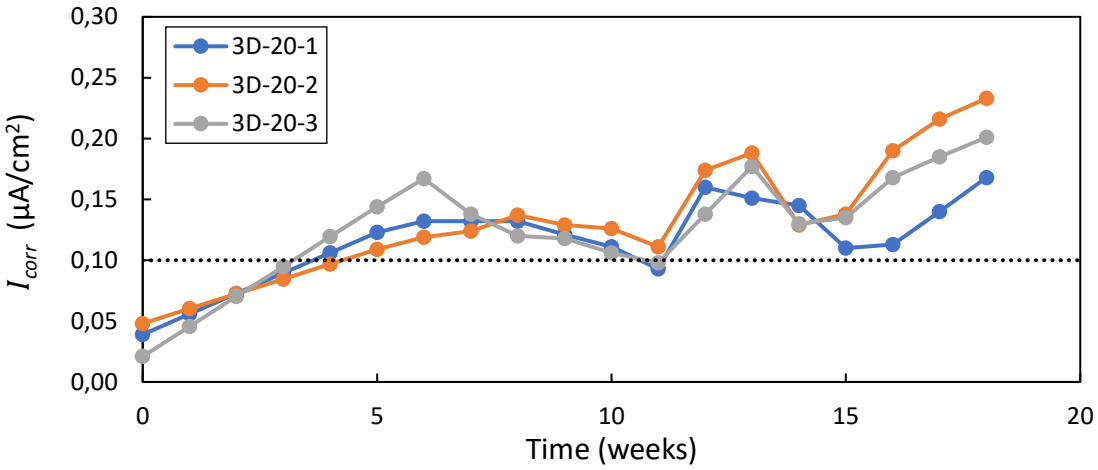

Figure 4-32: 3D-20 I_{corr} time-development graph

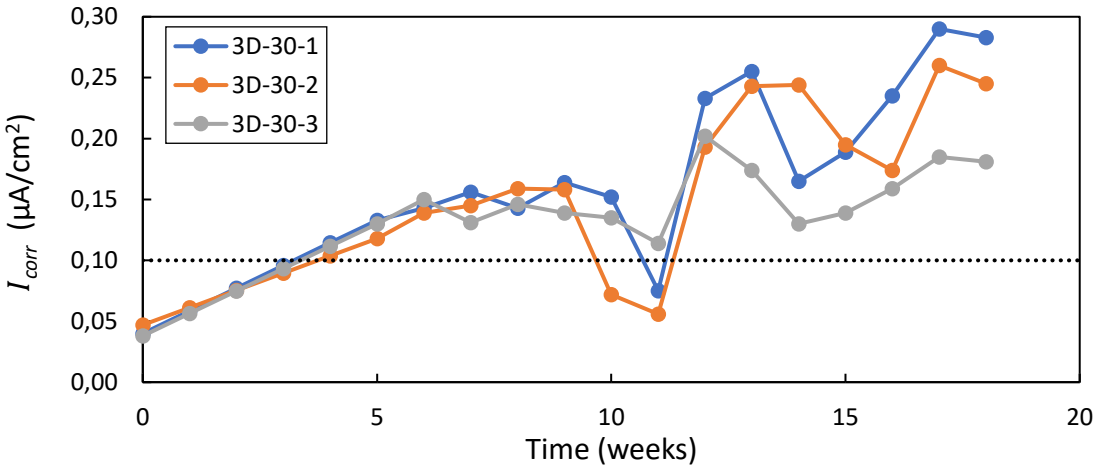

Figure 4-33: 3D-30 I_{corr} time-development graph

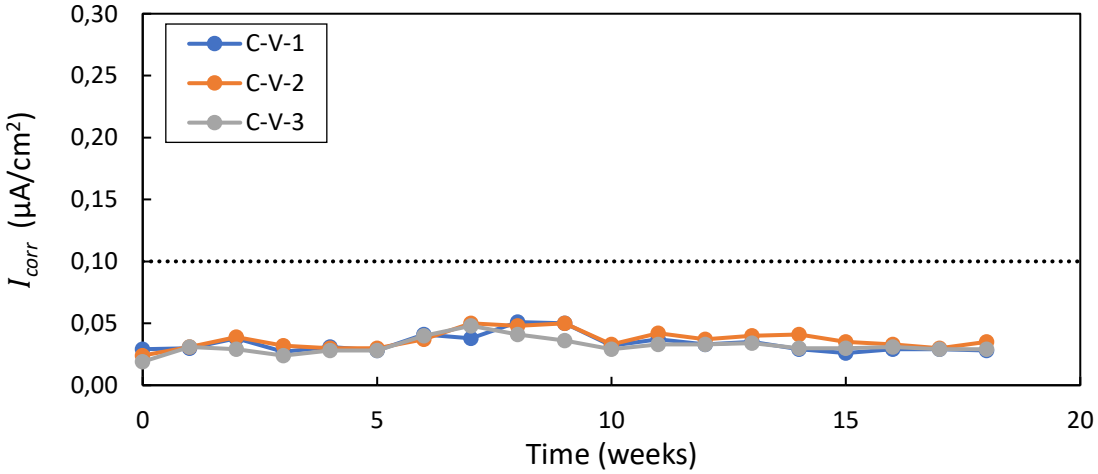

Figure 4-34: C-P I_{corr} time-development graph

From Figure 4-30 to Figure 4-34, the following trends are observed:

(i) The 3D-0 samples are all in a passive state during the experimental period. Only the 3D-0-1 beam transitioned to an active corrosion state after 16 weeks.

(ii) The 3D-10 beams yield a high variability in I_{corr}. Beam 3D-10 reaches corrosion initiation after five weeks and continues being in an active state for the remaining exposure period. A sharp increase in I_{corr} occur at 14 weeks, which corresponds well with a decrease in R_{ohm} (Figure 4-19). Beam 3D-10-2 reaches corrosion initiation after 17 weeks, and beam 3D-10-3 remains in a passive state.

(iii) The 3D-20 and 3D-30 beams record similar trends. All of the beams reach corrosion initiation after five weeks. All of the beams stay in an active state of corrosion for most of the exposure period. Initiation could have occurred earlier than five weeks, but this could not be established owing to malfunctioning of the GECOR 10. Beams 3D-20-1, 3D-20-3, and 3D-30-1 are in a passive state at 11 weeks. The 3D-30-2 beam records a I_{corr} below 0.100 μA/cm^2 during weeks 10 and 11. After the decrease, the I_{corr} increase above 0.100 μA/cm^2 and stays in an active state for the remaining period. All of the beams experience a decrease in I_{corr} around 10 and 14 weeks. This is attributed to the increases in R_{ohm}. The two occurrences of decreases followed by an increase in I_{corr} correspond well with increases and decrease in R_{ohm} (Figure 4-20 and Figure 4-21) respectively.

(iv) All of the C-V beams are in a passive state for the entire exposure period. All of the beams yield I_{corr} below 0.050 μA/cm^2 for the entire period. The C-V beams reach a maximum I_{corr} at weeks 8 and 9, followed by a gradual decrease in I_{corr} for the remaining exposure duration. The decrease in I_{corr} corresponds well with an increase in R_{ohm} (Figure 4-22).

4.5.4.2 Durability influence of lack of fusion

The durability performance with respect to chloride-induced corrosion is shown in Figure 4-35 where the average I_{corr} from the three beams per experimental variable are plotted against the exposure time.

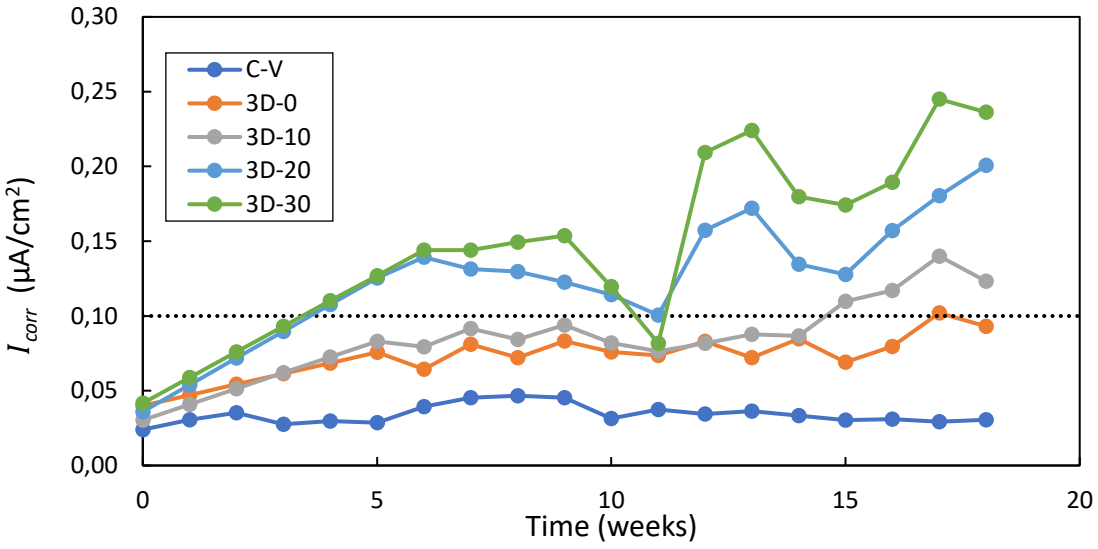

Figure 4-35: Average I_{corr} time-development graph for all the experimental variables

The results from Figure 4-35 reveal that:

(i) The time to corrosion initiation is affected by the pass time; the higher the pass time, the faster initiation is reached owing to the lack of fusion induced by the pass time. Both the 3D-20 and 3D-30 samples reach initiation after five weeks. Initiation could have been earlier than five weeks, but this could not be established owing to malfunctioning of the GECOR 10. The 3D-10 and 3D-0 beams reach initiation at 15 and 17 weeks, respectively. The C-V samples are still in a passive state of corrosion. The chloride penetration results discussed in Chapter 4.5.1 show that larger pass times result in deeper chloride penetration at the critical layer for the pass time beams and at the torn layers for the 3D-0 beams. These weak IRs cause the chlorides to reach the depth of the steel rods faster, reaching the chloride threshold quicker, breaking down the passive protective layer and decreasing the time to corrosion initiation. The C-V beams have randomly distributed voids compared to the interconnected pores of the 3DCP beams. They are also less permeable and have lower porosity compared to the 3DCP samples, which slows down chloride penetration and increases the time to corrosion initiation (refer to the DI results in Chapter 4.3). The chloride penetration results in Chapter 4.5.1 also show that the chlorides are yet to reach the steel rods, thus explaining why the beams are still in a passive state of corrosion.

(ii) There is a good correlation between the time to corrosion initiation and the σ results previously discussed in Chapter 4.3.4. It was to be expected that the samples with higher σ values would reach corrosion initiation faster.

(iii) The increase in pass time result in higher I_{corr}, which is attributed to the increase of lack of fusion at the critical layer induced by the pass time. The 3D-30 beam yields the highest I_{corr} and the C-V beams the lowest. As discussed in Chapter 2.3.5.6,larger crack widths result in higher corrosion rates. Based on the results from Figure 4-35, it is clear the torn layer of the 3D-0 beams and the critical layer of the other 3DCP beams function as cracks, where more permeable critical layer regions result in higher I_{corr}.

(iv) The C-P beams are still in a passive state after the exposure duration and outperformed all of the 3DCP samples. It is known from the literature presented in Chapter 2.3.5.6, that uncracked beams have a higher resistance to chloride-induced corrosion compared to cracked beams (3DCP beams function as cracked beams).

4.5.4.3 Relationship between R_{ohm} and I_{corr}

Alonso et al. (1988) report a good relationship between the R_{ohm} and I_{corr} readings when the rebar is depassivated. In a logarithmic diagram of R_{ohm} plotted against I_{corr}, it is possible to fit a straight line (power trend line), as shown in Equation 4-1. The log of the trendline yields a linear equation (Equation 4-2). Figure 4-36 to Figure 4-41 show the relationship between the R_{ohm} and I_{corr} for all of the chloride-induced corrosion beams. The trendline equations in the figures are according to the format used in Equation 4-1.

$$I_{corr} = I_{corr,0}.R_{ohm}{}^{\Delta} \qquad 4\text{-}1$$

$$log(I_{corr}) = log\left(I_{corr,0}\right) + \Delta.log(R_{ohm}) \qquad 4\text{-}2$$

where:

Δ - Slope

$I_{corr,0}$ - Intercepted value of the linear line at the I_{corr} axis

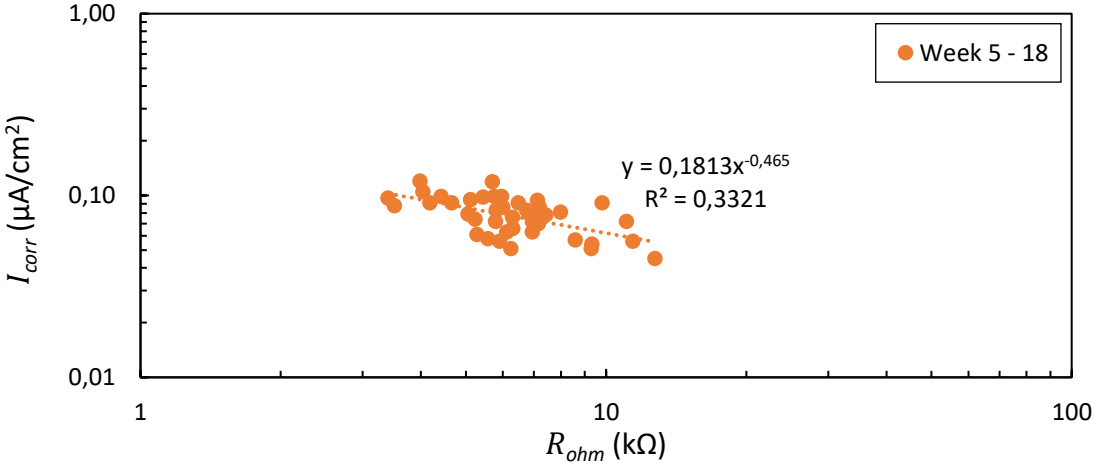

Figure 4-36: 3D-0 relationship between R_{ohm} and I_{corr}

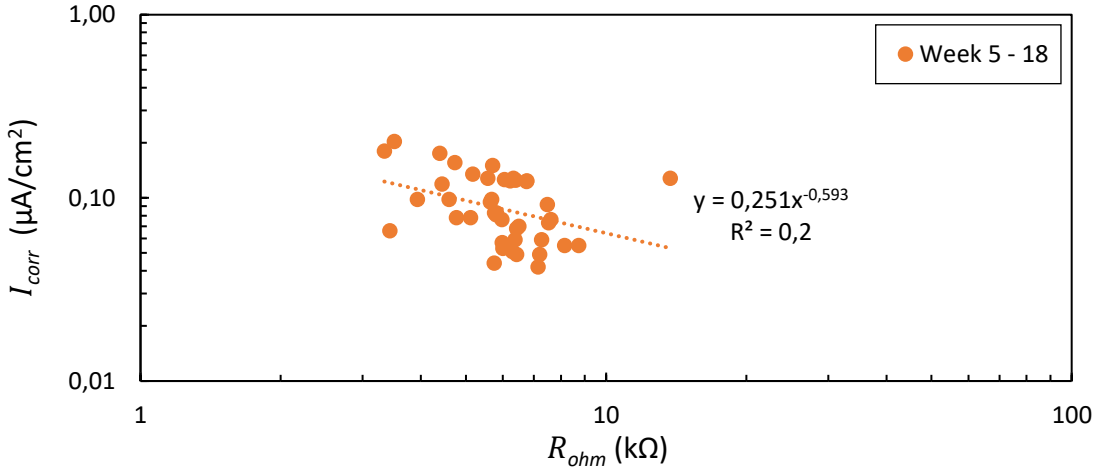

Figure 4-37: 3D-10 relationship between R_{ohm} and I_{corr}

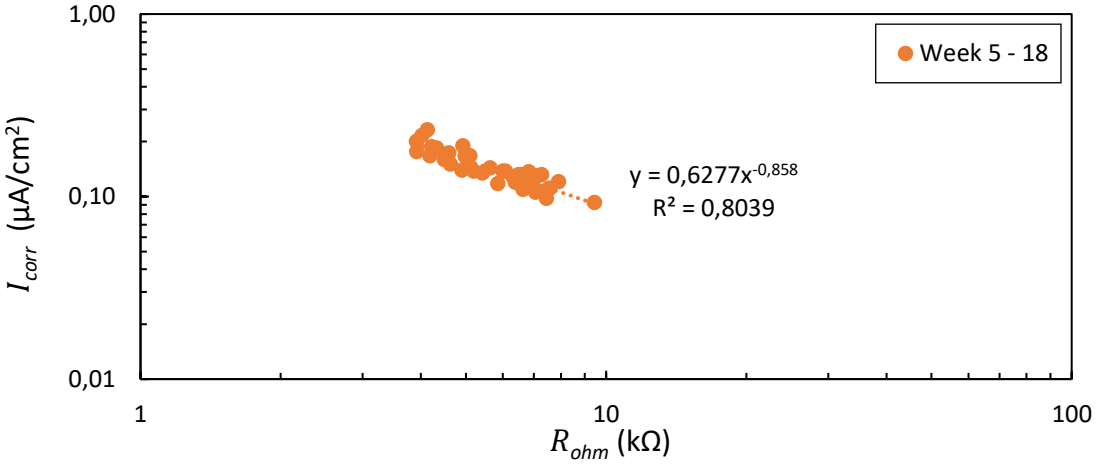

Figure 4-38: 3D-20 relationship between R_{ohm} and I_{corr}

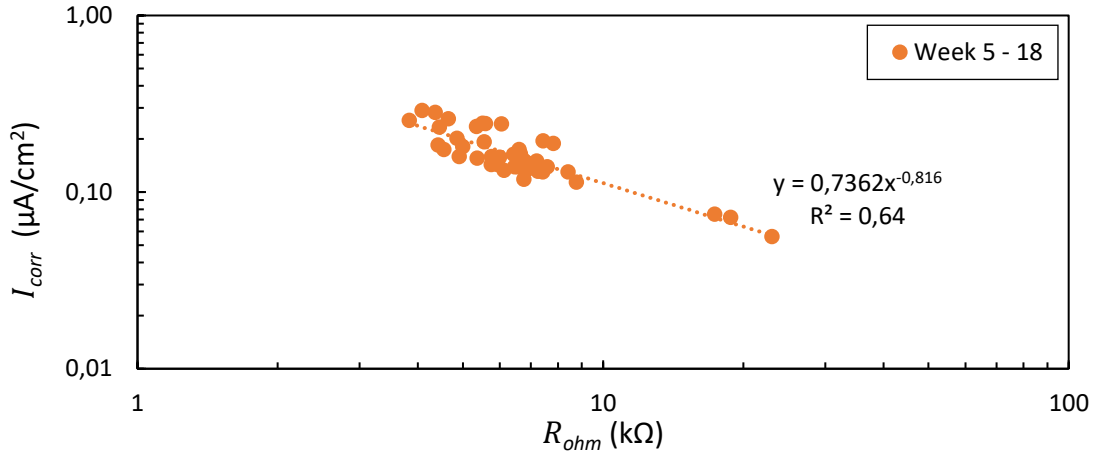

Figure 4-39: 3D-30 relationship between R_{ohm} and I_{corr}

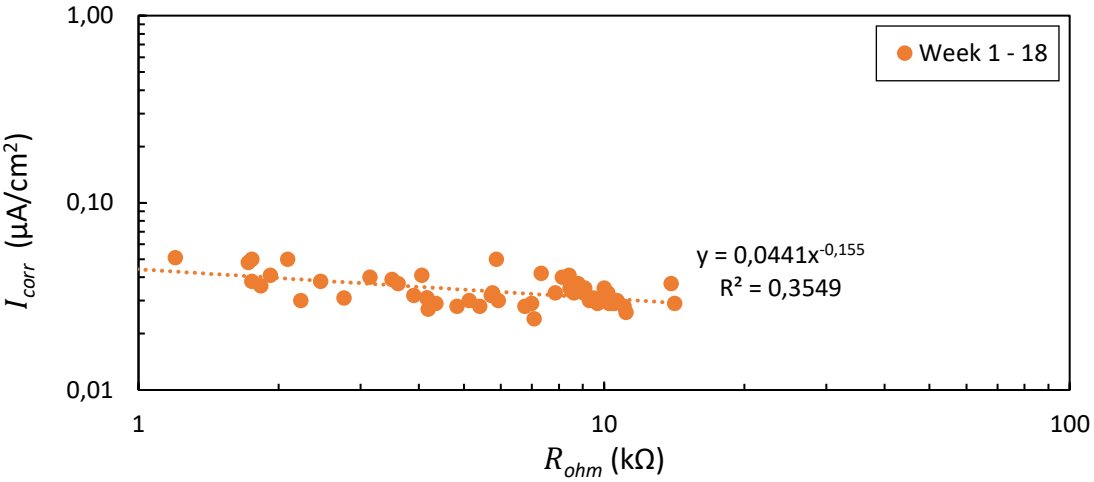

Figure 4-40: C-V relationship between R_{ohm} and I_{corr}

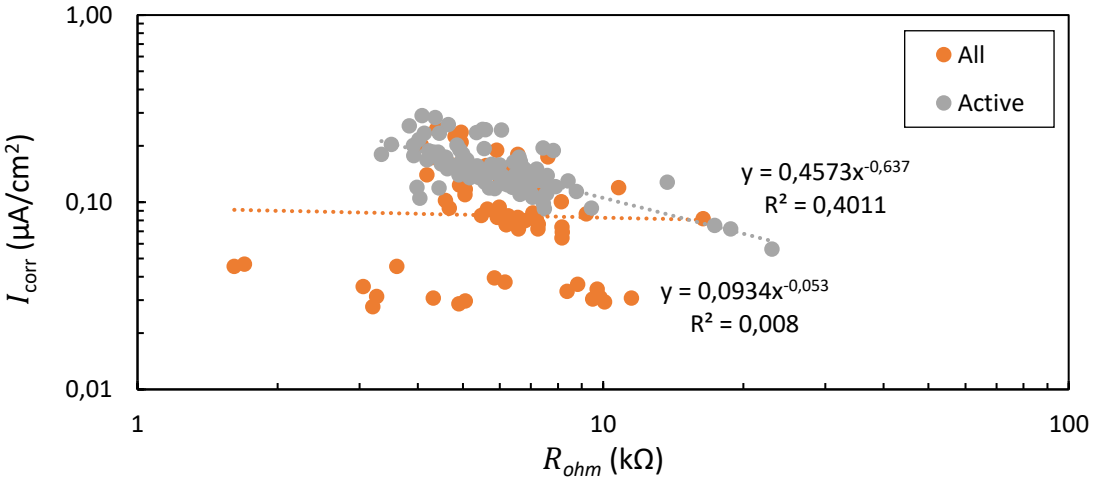

Figure 4-41: Experimental variables relationship between R_{ohm} and I_{corr}

From Figure 4-36 to Figure 4-41, the following trends are observed:

(i) As indicated by the R^2 values, all the beams showed a positive correlation between the R_{ohm} and I_{corr} results, i.e. the smaller R_{ohm} values correspond to higher I_{corr} values. The 3D-10 beams yield a low positive correlation, whereas the 3D-0 and C-V beams yield a moderate positive correlation. These corelations can be misleading when using R_{ohm} to serve as an indication of the corrosion risk and possible I_{corr} value since most of the readings correspond to a passive state of corrosion for the entire exposure period (considered weeks in this chapter). As discussed in Chapter 2.2.10, the ρ_e and R_{ohm} can give an indication of possible corrosion activity, but only if the steel is already depassivated. The 3D-20 and 3D-30 beams yield a high positive correlation. The higher correlation for 3D-20 and 3D-30 beams were expended since all the beams were in an active corrosion state for the entire exposure period.

(ii) Overall, when considering all readings obtained from all the experimental variables (Figure 4-41), no correlation was established between the R_{ohm} and I_{corr} owing to a large number of passive corrosion readings. However, when only depassivated beams that are in an active state of corrosion are considered, a moderate positive correlation is established. Thus, a decrease in R_{ohm} correlated to a greater I_{corr} for depassivated reinforced beams.

4.5.4.4 Relationship between E_{corr} and I_{corr}

As discussed in Chapter 2.2.10, the E_{corr} results only give an indication of the corrosion risk but do not quantify the corrosion activity. The E_{corr} results should be interpreted in conjunction with the corresponding I_{corr} results to predict the corrosion risks accurately. Figure 4-42 to Figure 4-47 show the exponential relationship between the E_{corr} and I_{corr} for all of the chloride beams.

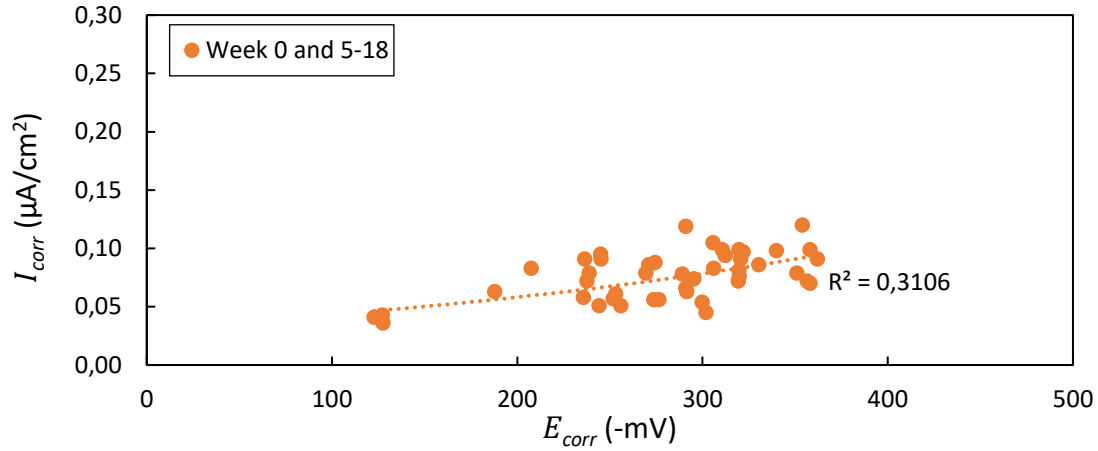

Figure 4-42: 3D-0 relationship between E_{corr} and I_{corr}

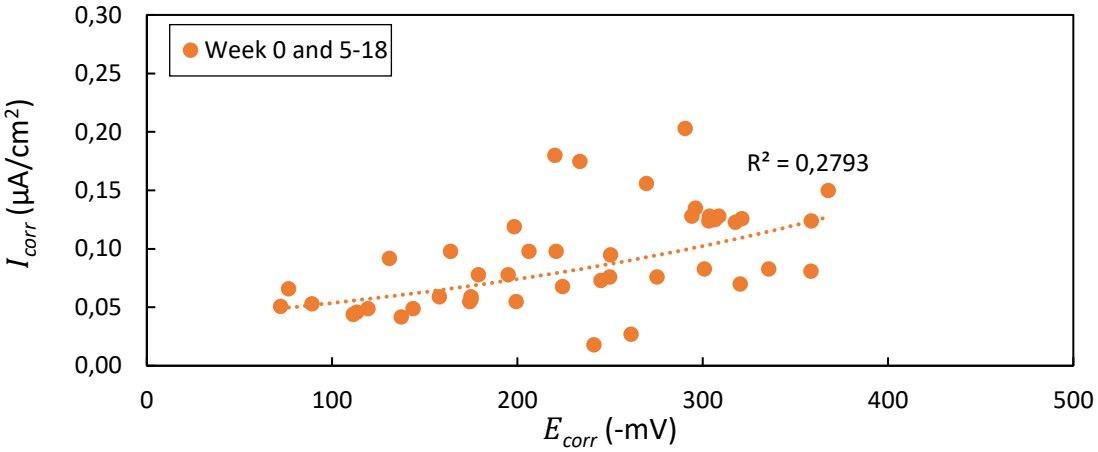

Figure 4-43: 3D-10 relationship between E_{corr} and I_{corr}

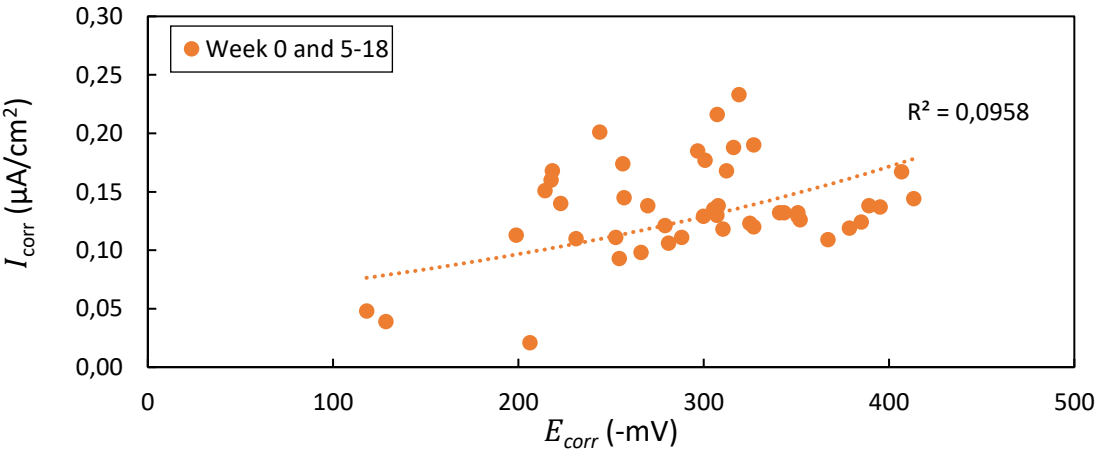

Figure 4-44: 3D-20 relationship between E_{corr} and I_{corr}

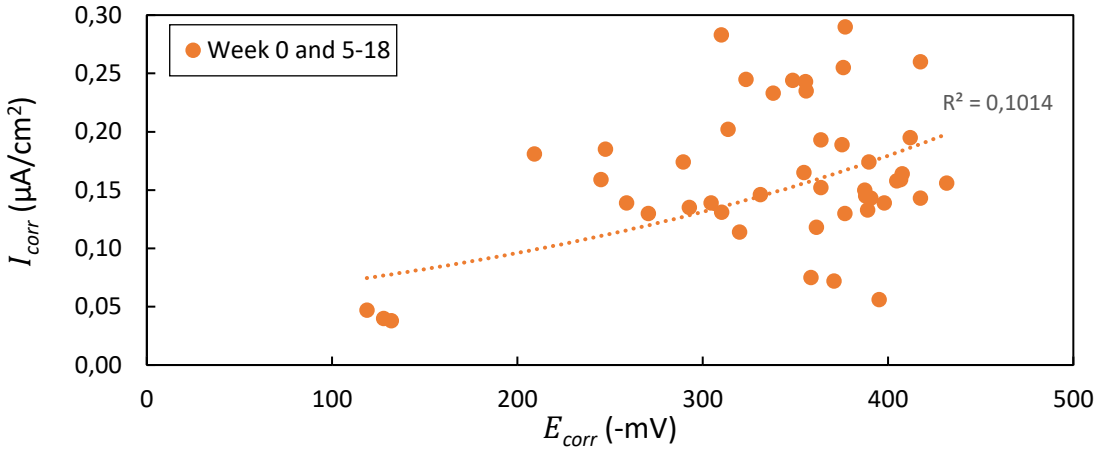

Figure 4-45: 3D-30 relationship between E_{corr} and I_{corr}

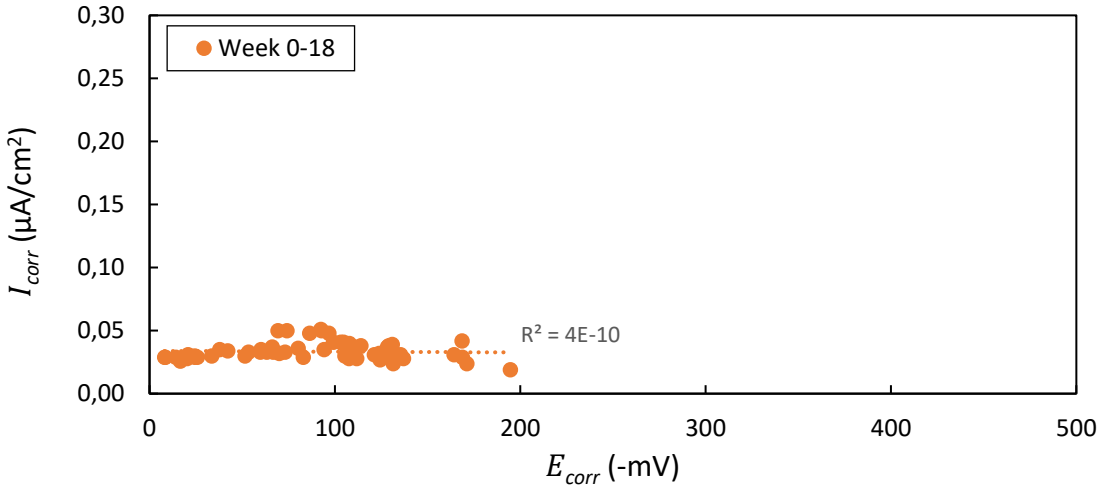

Figure 4-46: C-P relationship between E_{corr} and I_{corr}

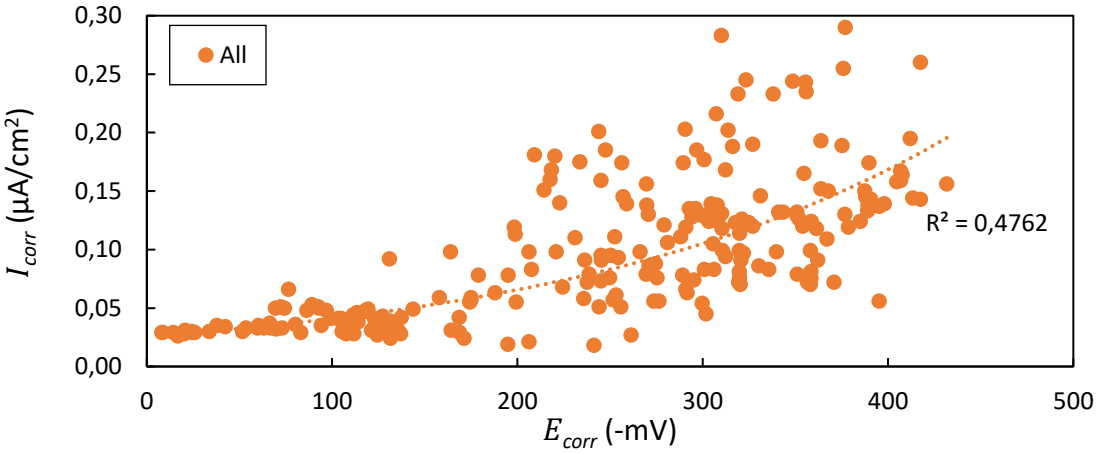

Figure 4-47: Experimental variables relationship between E_{corr} and I_{corr}

The findings from Figure 4-42 to Figure 4-47 reveal that:

(i) As indicated by the R^2 values, all of the 3DCP beams show a positive correlation between the E_{corr} and I_{corr} results, i.e. a more negative E_{corr} corresponded to a higher I_{corr}. The 3D-0 and 3D-10 beams yield a moderate positive correlation, whereas the 3D-20 and 3D-30 beams yield a low positive correlation.

(ii) The C-V beams show a negligible correlation between the E_{corr} and I_{corr} results. This is to be expected as the E_{corr} decreased during the exposure time and the I_{corr} mostly stayed constant.

(iii) Overall, when considering all readings obtained from all of the experimental variables (Figure 4-47), moderate positive correlation is obtained. The results show that a decrease in E_{corr} correlated to a greater I_{corr}. Bezuidenhout and van Zijl (2019) also reported that a decrease in E_{corr} correlated to a greater I_{corr}.

4.5.5 Electrochemical mass loss and pitting corrosion

After completion of the chloride-induced corrosion testing, the steel rods were removed from the beams for corrosion inspection. Upon inspection, corrosion is detected on the embedded bars, but the extent of corrosion appears limited, and less than that visible at the exposed ends. It is believed that gravimetric mass loss determination would be skewed by the corrosion damage outside of the region of interest. Thus, only electrochemical mass loss and pit depths were considered.

4.5.5.1 Pitt formation

Upon inspection, the C-V steel rods did not show signs of corrosion. This is to be expected since the beams were in a passive state of corrosion for the entire exposure period. All of the 3DCP beams experienced localised attack (pitting corrosion). Pit formation is visible for all of the 3DCP beams and are shown in Figure 4-48. The locations of all the pits corresponded to the position of the critical layer for beams with induced pass times and at the torn layer for the 3DCP beams (Figure 4-16). In conjunction with the chloride profiles, the 3DCP beams correspond to Region 3 in Figure 2-16. A high cathode to anode size ratio results in pitting corrosion, with macrocell corrosion being the dominant corrosion mechanism present. The beams that record higher I_{corr} values corresponded to larger and more prominent pit formation.

The 3D-0, 3D-10, 3D-20, and 3D-30 beams record average anodic lengths of 8.77 mm, 10.80 mm, 14.74 mm, and 22.37 mm, respectively.

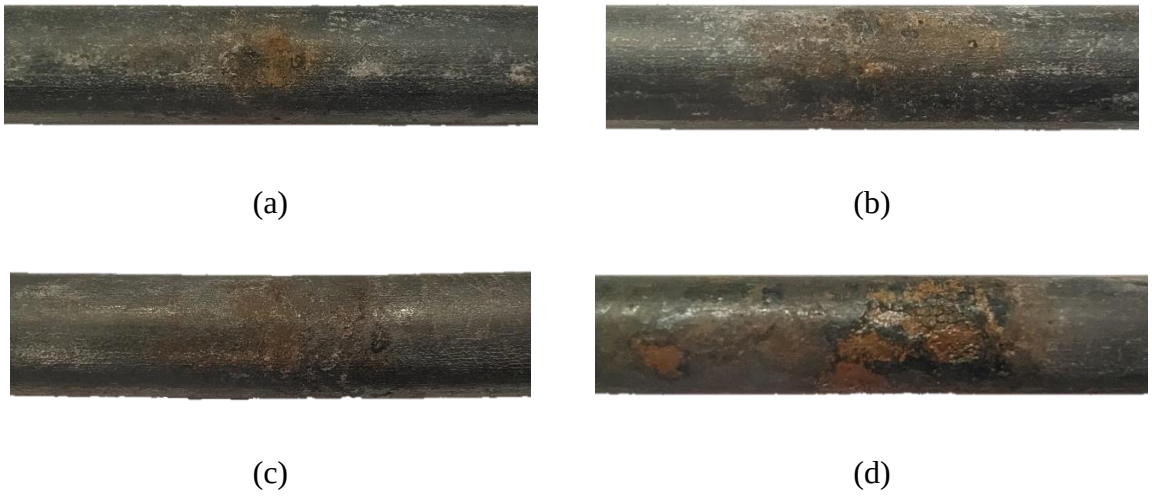

(a) (b)

(c) (d)

Figure 4-48: Pit formation at the critical layer for the 3D-0-2 (a), 3D-10-3 (b), 3D-20-1 (c), and 3D-30-2 (d) samples

4.5.5.2 Electrochemical calculations

The electrochemical calculations are performed using Faraday's Law (Equation 2-11). Faraday's Law only accounts for uniform corrosion and should be adjusted to account for pitting corrosion (Figure 4-48). Equation 4-3 shows the incorporation of the pitting factor in Faraday's Law. The I in Equation 4-3 is calculated by integrating the I_{corr} -time curve (Figure 4-35) and a pitting factor of 4 is used, based on the research conducted by Bezuidenhout and van Zijl (2019). Figure 4-49 and Figure 4-50 show the electrochemical calculated pit depths and cumulative electrochemical mass for each experimental variable.

$$\Delta W_c = \frac{I \alpha_{pit} t W_m}{FZ} \qquad 4\text{-}3$$

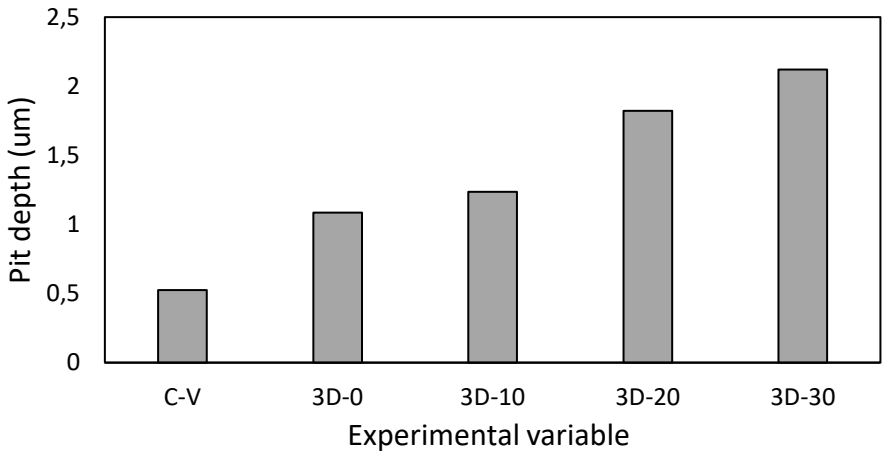

Figure 4-49: Electrochemical calculated pit depths

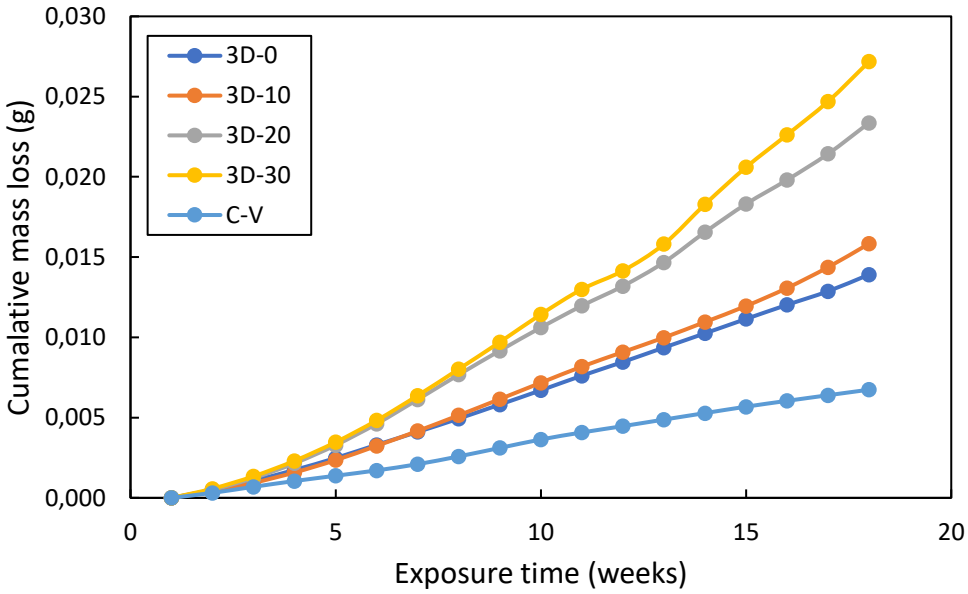

Figure 4-50: Electrochemical mass loss

From Figure 4-49 and Figure 4-50, the following trends were observed:

(i) The 3DCP samples yield higher pitting depths and cumulative mass losses compared to the C-V beams, which is contributed to the higher I_{corr}.

(ii) The lack of fusion induced by the pass time and layer tearing results in larger pitting depths and cumulative mass losses. The pit depths and cumulative mass loss increases with an increase in pass time.

5 Service life predictions

5.1 Introduction

Chapter 5 presents the adaption of the carbonation depth and chloride ingress models. Both models are adapted to incorporate the effect of the IR induced by the inherent nature of 3DCP samples and the critical layer induced by the pass time incorporation. A calibration factor is proposed for the DI results of 3DCP samples with induced pass times. This is done in order to calculate the DI value at the critical layer from the DI results of the samples, in order to predict carbonation depth and chloride ingress at the critical layer.

It is acknowledged that there are significant differences between traditional concrete and 3D printable concrete, and their influence on carbonation and chloride ingress remain to be carefully investigated. Firstly, the interfacial transition zones between paste and aggregate that are influential in ingress processes in concrete differ in printable concrete from those in traditional concrete. Printable concrete contains significantly lower aggregate content and smaller aggregate particle sizes of maximally 4.8 mm, than traditional concrete with typical coarse aggregate particle size range of 6 to 19 mm. Secondly, microstructural differences are caused in concrete by 3D printing, by altered void dispersion, interconnectivity and shape (Kruger et al. 2021). Hence, the service life estimations presented in Chapter 5 are indicative and remain to be confirmed by careful and systematic characterisation studies of ingress in 3D printed concrete materials.

5.2 Adapted carbonation depth prediction model

The Salvoldi et al. (2015) model is outlined in Chapter 5.2.1 The model is applicable to cast samples and is adapted in Chapter 5.2.2 to predict the carbonation depth of 3DCP samples. Chapter 5.3.3 proposes an adapted carbonation model to incorporate the effect of the 3DCP sample microstructure. Using the adapted approach, Chapter 5.2.4 outlies the progression of the carbonation depth over a 100-year period for a concrete structure consisting of all the experimental variables.

5.2.1 Salvoldi et al. (2015) layout

The Salvoldi et al. (2015) model consists of the calculation of various factors and variables regarding the concrete composition, curing and exposure environment to predict the

carbonation depth. Chapters 5.2.1.1 to 5.2.1.4 outline the calculation of these factors and variables.

5.2.1.1 RH factor

The model takes the effect of the RH during CO_2 exposure into account. Salvoldi et al. (2015) propose a relative RH factor (β), which combines the modification factors obtained by Papadakis et al. (1991a) and Wierig (1984). The expression for β is shown in Equation 5-1.

$$\beta = 23.32\left(1 - \frac{RH}{100}\right)^2\left(\frac{RH}{100}\right)^{2.6} \quad 5\text{-}1$$

5.2.1.2 Time of exposure (t_e)

The t_e is calculated using Equation 5-2. The time of wetness (ToW) is equal to the number of days in the year that recorded rainfall equal to or higher than 2.5 mm (Fédération internationale du béton, 2006; Salvoldi, Beushausen & Alexander, 2011)

$$t_e = t\left(1 - \frac{ToW}{365}\right) \quad 5\text{-}2$$

5.2.1.3 Carbonatable material

Salvoldi et al. (2015) propose the calculation of the amount of carbonatable material (a is equal to CH) based on the mass balance equations developed by Papadakis et al. (1991c). Equation 5-3 shows the mass balance equation and incorporates the addition of SCM (Salvoldi et al., 2015).

$$[CH] = 1.5[C_3S]F_{C_3S} + 0.5[C_2S]F_{C_2S} - 4[C_4AF]F_{C_4AF} - [C_3A]F_{C_3A} + \left[\widehat{CS}H_2\right] + [C]P_C - 1.5[S]P_S - 4[A]P_A \quad 5\text{-}3$$

where:

$[i]$ - Molar concentrations of the compound

$[j]$ - Molar concentrations of the admixture

F_i - Degree of hydration

P_j - Degree of pozzolanic activity

The degree of hydration and pozzolanic activity is calculated using the method developed by Bahador and Cahyadi (2009). Equation 5-4, developed by Papadakis et al. (1991a), and improved by Sabet and Jong (2006), is used to determine the OPC degree of hydration. The degree of pozzolanic activity can be calculated using Equation 5-5 and incorporates the activity of the admixtures (Salvoldi et al., 2015).

$$F_i = \alpha_{RH}\left(1 - \left(1 - K_{H,i}e^{\frac{E_a}{R}\left(\frac{1}{293}-\frac{1}{T}\right)}t_c(1-n_i)\right)^{\frac{1}{1-n_i}}\right) \quad 5\text{-}4$$

$$P_j = \alpha_b.\alpha_{RH}\left(1 - \left(1 - K_{H,j}e^{\frac{E_a}{R}\left(\frac{1}{293}-\frac{1}{T}\right)}t_c(1-n_j)\right)^{\frac{1}{1-n_j}}\right) \quad 5\text{-}5$$

where:

α_{RH} - RH curing parameter calculated using Equation 5-6 (Parrott, 1988)

$K_{H,i\ \&\ j}$ - Coefficients listed in Table 5-1 and Table 5-2

$n_{i\ \&j}$ - Coefficients listed in Table 5-1 and Table 5-2

t_c - Curing time

E_a - Activation energy (38.2 kJ/mol)

α_b - Amorphous content calculated using Equation 5-7

$$\alpha_{RH} = \left(\frac{RH - 0.55}{0.45}\right)^4 \ for\ RH > 0.55 \quad 5\text{-}6$$

$$\alpha_{RH} = 0\ for\ RH \leq 0.55$$

$$\alpha_b = (1 - christaline\ phase\ content) \quad 5\text{-}7$$

Table 5-1: Degree of hydration coefficients (Papadakis et al., 1991a)

Compound	C_3S	C_2S	C_4AF	C_3A
n_i	2.65	3.10	3.81	2.41
$K_{H,i}$ (day^{-1})	1.17	0.16	1.00	2.46

Table 5-2: Degree of pozzolanic activity (Bahador & Cahyadi, 2009)

Mineral admixture	**SF**	**Low calcium FA**
n_j	2.9	6
$K_{H,j}$ (day^{-1})	$\frac{1}{\sqrt{250d_n}}$	$\frac{1}{\sqrt{100d_n}}$

*d_n is particle diameter

5.2.1.4 Effective dry diffusion coefficient

Salvoldi et al. (2015) established a relationship between the k and the D_{dry}. The D_{dry} considers the diffusion of CO_2 through the microstructure of the sample without the influence of the RH. The D_{dry} of each experimental variable was calculated by substituting the calculated factors and carbonation depth after 12 weeks of carbonation into Equation 2-32. The k was plotted against the D_{dry} and the trendline obtained is shown in Equation 5-8. The trendline yielded a R^2 of 0.94 with the experimental data.

$$D_{dry} = \left(1.412\left(\frac{k}{10^{-11}}\right)^{2.217}\right)\cdot 10^{-11} \qquad 5\text{-}8$$

5.2.2 Model adaption

Figure 5-1 shows the relationship between the k and D_{dry}. The measured D_{dry} was calculated using the same principle as Salvoldi et al. (2015), as discussed in Chapter 5.2.1.4. The chemical composition of the binders and other constants applicable to Equations 5-1 to 5-8 can be found in Appendix B. The D_{dry} is also calculated using Equation 5-8 for comparison.

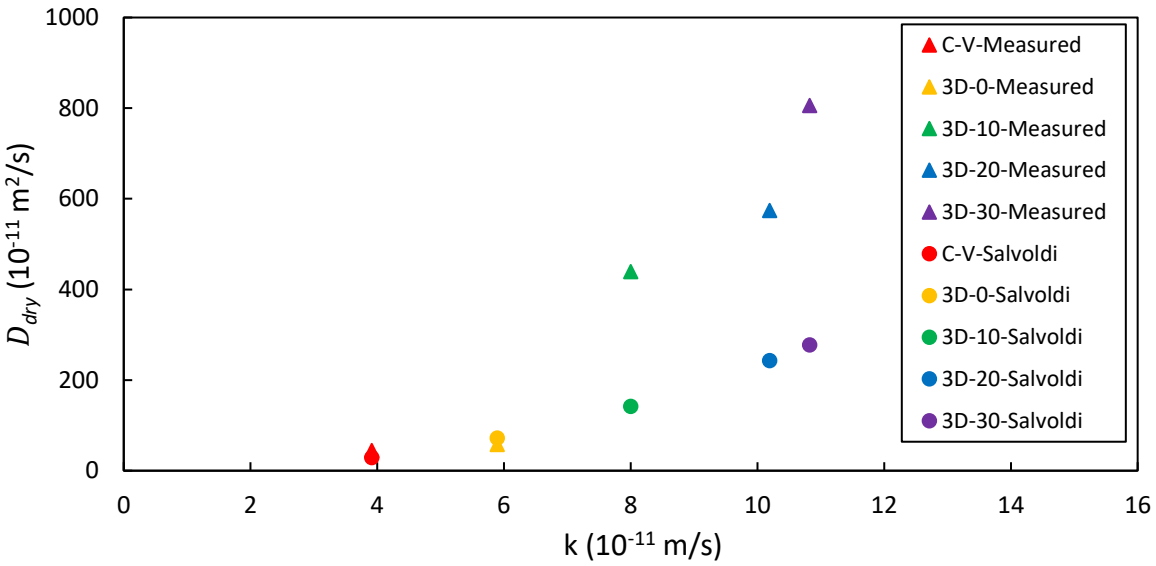

Figure 5-1: Relationship between k and D_{dry}

From Figure 5-1, the following trends are observed:

(i) Equation 5-8 fairly accurately predicts the D_{dry} of C-V and 3D-0 samples. This is to be expected since the model is formulated on the results obtained using cast samples where the D_{dry} is constant over the entire area. The C-V samples yielded a uniform carbonation front. A uniform carbonation front was not observed in the 3D-0 samples owing to the curved edges of the 3DCP samples. Based on the carbonation depth at the 3D-0 samples IRs and the carbonation depth of the C-V samples, a uniform carbonation front with a slight increase in carbonation depth at the IRs is to be expected if the sides were to be flat.

(ii) Equation 5-8 underestimates the D_{dry} of the 3D-10, 3D-20, and 3D-30 samples. Equation 5-8 was derived from uncracked cast samples, which yield a constant D_{dry}. When calculating the k using Equation 3-4, it is assumed that the k is constant over the entire area. Based on the results obtained in Chapter 4.4, it was clear that the samples with induced pass times functioned as cracked samples. The k and, in effect, the D_{dry} is constant at the positions next to the critical layer and is much higher at the critical layer itself. Thus, when calculating the k for the 3DCP samples with pass times, the effective area contributing to the pressure drop is overestimated (when only considering the characteristics of the critical layer), which leads to lower k values. The value

obtained using Equation 3-4, is an average k of the entire specimen, which will be less permeable than the critical layer itself. This concept is shown in Figure 5-2.

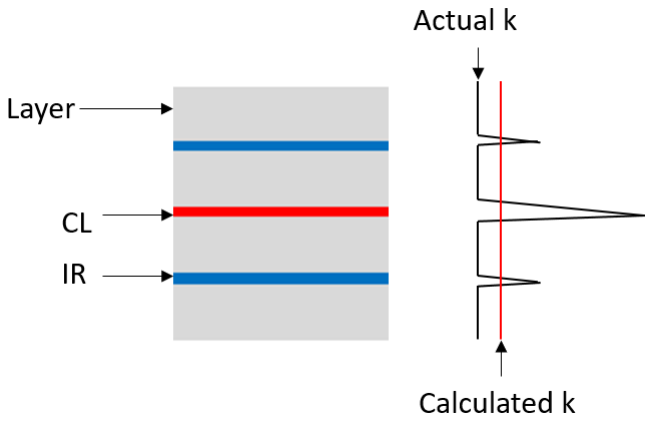

Figure 5-2: Actual and calculated k of 3DCP samples

Using Equation 5-8, the actual k at the critical layer for the pass time induced 3DCP samples can be calculated from the measured D_{dry}. The original k and calibrated k (k_{cal}) values are listed in Table 5-3. Table 5-3 also contains the calibrated OPI values and corresponding durability class (refer to Table 2-4 for the durability ranges). A k calibration factor (ϑ_k) is proposed to calibrate (i.e. increase) the k obtained with Equation 3-4 for the pass time induced 3DCP samples to represent the k of the critical layer. The calibration equation shown in Equation 5-9 and Table 5-4 contains ϑ_k for all of the experimental variables. The ϑ_k for the C-P, C-V, and 3D-0 samples are equal to 1 since the CO_2 diffusion is uniform across the entire area of the sample.

$$k_{cal} = \vartheta_k k \qquad 5\text{-}9$$

Table 5-3: Actual and calibrated k

Variable	k (10^{-11} m/s)	k_{cal} (10^{-11} m/s)	OPI_{cal}	OPI_{cal} Durability class
3D-10	8.002	13.317	9.88	Good
3D-20	10.195	15.027	9.82	Good
3D-30	10.825	17.511	9.76	Good

Table 5-4: ϑ_k for all the experimental variables

Experimental variable						
C-P	**C-V**	**3D-0**	**3D-10**	**3D-20**	**3D-30**	**3D- pass time -AVG**
1	1	1	1.6642	1.4740	1.6176	1.5853

5.2.3 Proposed model

The Salvoldi et al. (2015) model can be adapted to suit 3DCP samples. Based on the results discussed in Chapter 5.2.2, by applying ϑ_k and substituting the k with k_{cal} in Equation 5-8, the carbonation depth at any time t can be calculated using Equation 2-32. The ϑ_k factor approach is only applicable to samples with 1 critical layer. The ϑ_k factor of 1.5853 can be used for any pass time between 10 min and 30 min. Figure 5-3 shows the actual compared to the predicted carbonation depths using the adapted model. A ϑ_k of 1.5853 is used for the samples with a pass time ≥ 10 min. A good correlation between the actual and predicted values is established using the ϑ_k factor.

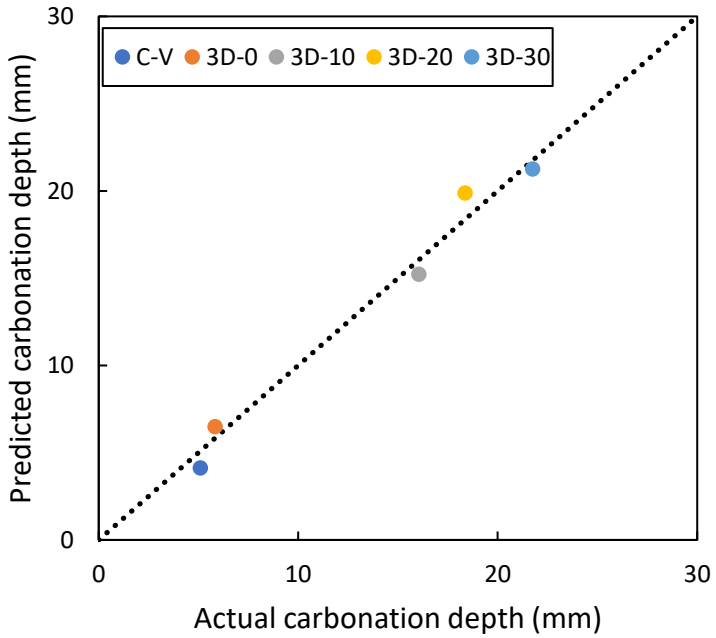

Figure 5-3: The 12-week actual versus predicted carbonation depths

5.2.4 Natural carbonation depth predictions

The Salvoldi et al. (2015) model, implementing the ϑ_k factors, can be used to predict the carbonation depth under natural conditions. A hypothetical structure in Stellenbosch is used as an example and the following assumptions are made:

(i) The structure cast/printed in January. It is air cured for 28 days at 21.4 ℃ at a 60% RH (Climate Data, 2020)**.**

(ii) The structure is exposed to a constant 0.04% CO_2 environment at a 68.67% RH and experiences 65 days of wetting per year (Climate Data, 2020).

(iii) The ϑ_k used are the unique values listed in Table 5-4, not the average ϑ_k.

The 100-year natural carbonation depth progression for the samples tested in this study is shown in Figure 5-4. Figure 5-4 also includes the natural carbonation depth progression of samples produced by Salvoldi et al (2015). These mixtures have w/b ratios and compressive strengths that are similar to the 3DCP mixture used in this study. Table 5-5 contains the characteristics of Salvoldi et al. (2015) mixtures and the amount of carbonatable material (a) was calculated according to Chapter 5.2.1.3. From Figure 5-4 it can be seen that cast structures (C-V and C-P) outperforms the 3DCP structures, even when no pass time is induced. The inclusion of any pass time notably decreases the structure's resistance against carbonation and the time to carbonation-induced corrosion initiation (t_i). The 3D-0 structures outperform Salvoldi et al. (2015) mixtures, which is contributed to the amount of carbonatable material produced during curing. The 3DCP mixture contains a more cement compared to Salvoldi et al. (2015) mixtures and produced 105 mol/m^3 of carbonatable material which increases the structures carbonation resistance.

Table 5-5: Salvoldi et al. (2015) mixtures characteristics

Concrete mix	**w/b ratio**	**σ_c (MPa)**	**k (10^{-11} m/s)**	**a (mol/m^3)**
100% OPC	0.5	50.7	7.9	70
70/30% OPC/FA	0.5	48.8	6.4	48
90/10% PC/SF	0.5	52.7	6.2	62

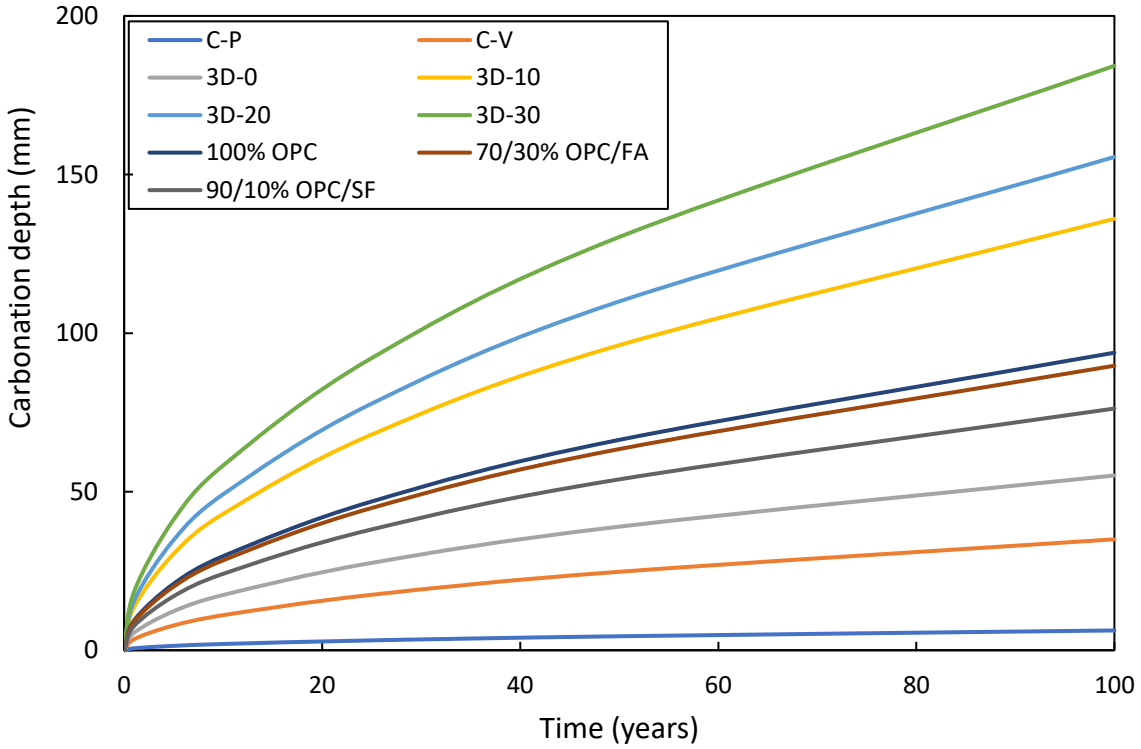

Figure 5-4: Natural carbonation depth progression over 100 years

5.3 Adapted chloride ingress model

The South African chloride ingress model is outlined in Chapter 5.3.1. The model is applicable to cast samples and calibrated in Chapter 5.3.2 to predict t_i of 3DCP samples. Chapter 5.3.3 proposes the calibrated binder type model, which is used to predict t_i for concrete structures consisting of all the experimental variables with different cover depths (Chapter 5.3.4).

5.3.1 South African chloride ingress model layout

The South African chloride ingress model can be used to predict the t_i and the chloride concertation profile. The beams were exposed to cyclic wetting and drying ponding cycles with a 5% NaCl solution, which corresponds to very severe conditions in the marine tidal and splash zones (Mackechnie, 2001). The model is limited to a few binder combinations, as discussed in Chapter 2.3.6. The mix design used in this study is more complex; thus, to implement the model, a few binder composition assumptions will have to be made:

a) Assume the FA as part of the OPC component and use the SF as an addition; thus, the binder will consist of 10.62% SF.

b) Assume the SF as part of the OPC component and use the FA as an addition; thus, the binder will consist of 21.11% FA.

Assumptions (a) and (b) will correspond to the 10% SF and 30% FA binder type chloride models respectively.

The model is implemented using the following steps:

(i) Establish the C_s and γ factors at very server exposure conditions. These values are listed in Table 5-6.

Table 5-6: C_s and γ for various binder types at very severe conditions

Binder	C_s	γ
10% SF	2.5	0.25
30% FA	4.5	0.68

(ii) Calculate the $D_{a,2years}$ based on the binder type and σ. For the 10% SF binders, use Equations 5-10 and 5-11, and for the 30% FA binders use Equation 5-12.

$$D_{a,2years} = 1 \cdot 10^{-9} \cdot 2.718^{4.8\sigma} \quad for \ \sigma < 0.5 \tag{5-10}$$

$$D_{a,2years} = 6 \cdot 10^{-9} \cdot 2.718^{1.6\sigma} \quad for \ \sigma \geq 0.5 \tag{5-11}$$

$$D_{a,2years} = 6.8 \cdot 10^{-9} \cdot 2.718^{0.95\sigma} \tag{5-12}$$

(iii) Calculate the short-term apparent diffusion confident (D_i) using Equation 5-13.

$$D_i = D_{a,2years} \left(\frac{t_{2years}}{t_{1second}}\right)^{\gamma} \tag{5-13}$$

(iv) Calculate the D_a at a given time t using Equation 5-14.

$$D_a = 10^{\log D_i - \gamma \log t} \tag{5-14}$$

(v) Calculate the value of fnc (calculated value) at a depth x (Equation 5-15), and find the solution to the error function (Equations 5-16 and 5-17).

$$fnc = \frac{x}{2\sqrt{D_a.(t)}} \quad 5\text{-}15$$

$$erf(fnc) = 1.44 \cdot (1 - 2.718^{-0.88fnc}) \quad for \ fnc < 1 \quad 5\text{-}16$$

$$erf(fnc) = (1 - 2.718^{-3.1fnc})^{3.75} \quad for \ fnc \geq 1 \quad 5\text{-}17$$

(vi) Insert the value obtained using Equations 5-16 and 5-17 into Cranks' formulation (Equation 5-18) to find the chloride concertation at depth x at time t.

$$C_{x,t} = C_s.[1 - erf(fnc)] \quad 5\text{-}18$$

5.3.2 Model adaption

The model assumes that the chloride threshold is 0.4% (by weight of binder), irrespective of the binder's composition. Table 5-7 contains the chloride content at the cover depth at the t_i calculated with the model. Assumptions must be made for the 3D-20 and 3D-30 beams t_i owing to the malfunction of the GECOR 10. For the 3D-20 beams, it is assumed that t_i occurs at 4 weeks, based on the interpolated I_{corr} results (Figure 4-35). Based on the σ results (Chapter 4.3.4), the 3D-30 samples yielded a larger σ compared to the 3D-20 samples, implying that t_i will occur faster. Thus a t_i of 3 weeks is assumed for the 3D-30 beams. The 3D-0 beams are not considered owing to layer tearing that occurred during the printing procedure, which resulted in a premature t_i. The C-V beams were yet to reach t_i and are therefore also not considered in Table 5-7.

Table 5-7: $C_{20mm,ti}$ for the pass time induced 3DCP beams

Variable	t_i **(weeks)**	**10% SF**	**30% FA**
		C_{20mm,t_i} **(% binder)**	C_{20mm,t_i} **(% binder)**
3D-10	15	0.67	0.97
3D-20	4	0.22	0.63
3D-30	3	0.26	0.71

From Table 5-7 it is clear that by assuming the 30% FA binder type, the model overestimates the chloride content at the reinforcement at t_i. By assuming the 10% FA binder type, the model underestimates the chloride content for the 3D-20 and 3D-30 beams and overestimates the chloride content. This is to be expected since the model is formulated based on the results of cast samples, which have randomly disturbed pores, compared to the interconnected pores of the 3DCP samples at the IRs. The σ for the cast samples is also based on uncracked samples, whereases 3DCP with pass times function as cracked samples (previously discussed in Chapter 4.5.1).

A σ calibration factor (ϑ_σ) is proposed to calibrate the σ obtained from the 3DCP samples to σ for cast samples and is shown in Equation 5-19. The factor is determined by adjusting the σ factor to obtain 0.4 C_{20mm,t_i} for each experimental variable. The ϑ_σ factors are shown in Table 5-8 for the C-P and C-V are equal to 1 because they are cast samples. The 3D-0 factor are also considered to be 1 based on the uniform chloride penetration in the area that has no torn layers (Figure 4-16a), which are similar compared to the C-V beams.

$$\sigma_{cal} = \vartheta_\sigma \sigma \qquad 5\text{-}19$$

where:

σ_{cal} - Calibrated σ value

Table 5-8: ϑ_σ for all the experimental variables according to binder type

Binder	**Experimental variable**					
	C-P	**C-V**	**3D-0**	**3D-10**	**3D-20**	**3D-30**
10% FA	1	1	1	0.8548	1.1269	1.1102
30% FA	1	1	1	0.6551	0.8481	0.8333

By applying ϑ and substituting the σ with σ_{cal} in Equations 5-10 to 5-12, the chloride concentration profile can be obtained. Figure 5-5 and Figure 5-6 shown the chloride concentration profiles for all of the experimental variables after 18 weeks of ponding exposure consisting of a binder containing 10% SF and 30% FA respectively.

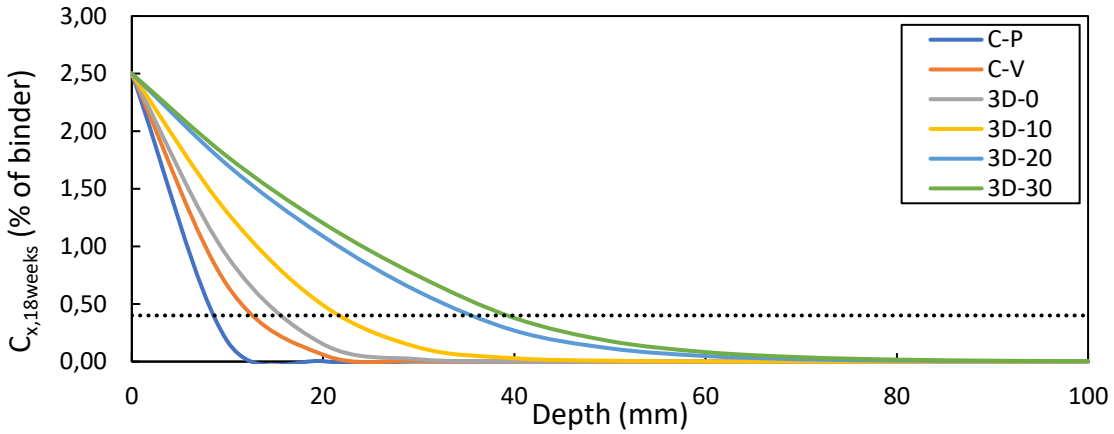

Figure 5-5: Chloride concentration profile for the 10% SF binder type

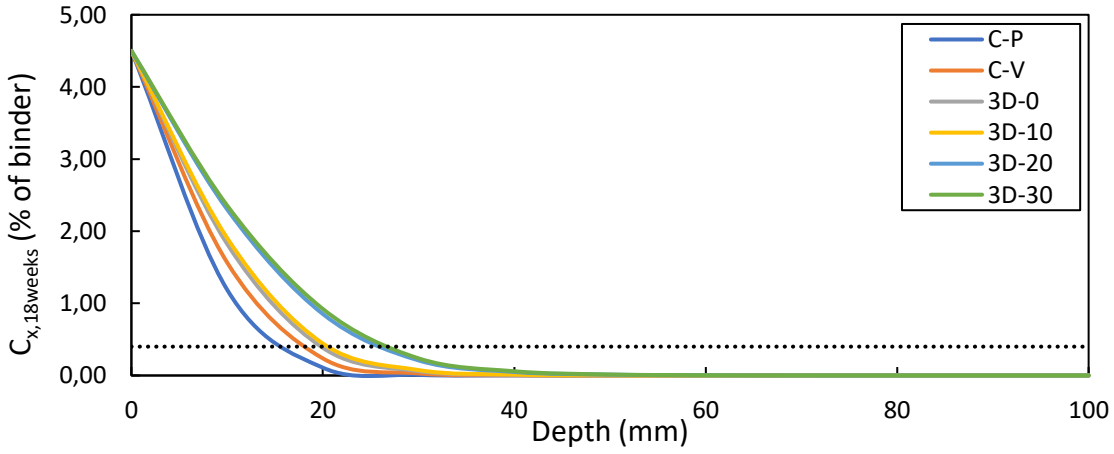

Figure 5-6: Chloride concentration profile for the 30% FA binder type

5.3.3 Proposed binder type model

The proposed binder type mode is based on the chloride concentration at the critical layer penetration depth and the σ calculation. To begin with, based on the chloride penetration results in Chapter 4.5.1, the model should be able to predict the chloride concentration at the average chloride penetration depth. Table 5-9 shows the chloride concentration at the penetration depth after 18 weeks of chloride exposure. The 10% SF binder model predicts a 0.03%, 0.02%, and 0.03% chloride concentration for the 3D-10, 3D-20, and 3D-30 beams at their respective depths. The 30% FA binder model only calculates a 0.1% concentration for the 3D-10 beams and does not predict that there will be any chloride present at the respective depths of the 3D-20, and 3D-30 beams.

In addition, when calculating the σ using Equation 3-7, it is assumed that the σ is constant over the entire area. This is true for a cast sample but not for a 3DCP sample with an induced pass time, where D varies over the area (Chapter 4.5.1). The D is constant at the positions next to the critical layer and is much higher at the critical layer itself. The σ and D are related, thus for 3DCP samples the σ will also vary over the exposed area. When calculating the σ for the 3DCP samples with pass times, using Equation 3-7, the σ is assumed to be constant over the sample, and the effective area contributing to the current flow is overestimated (when only considering the characteristics of the critical layer) and results in an underestimation of the σ at the critical layer itself. The ϑ_σ should be greater than 1 to account for the underestimation of σ. This concept is shown in Figure 5-7. It should be noted that the reason for the ϑ_σ smaller than 1 for the 3D-10 beams could be due to the high degree of variation of the I_{corr} measured over time. Based on the two points mentioned, it is recommended to use the 10% SF binder model.

Table 5-9: $C_{x,18weeks}$ at various depths per 3DCP pass time beams

Binder	$C_{x,18weeks}$ **(% of binder)**		
	3D-10 at 40.86mm	**3D-20 at 64.90 mm**	**3D-30 at 78.16 mm**
10% SF	0.03	0.03	0.02
30% FA	0.01	0.00	0.00

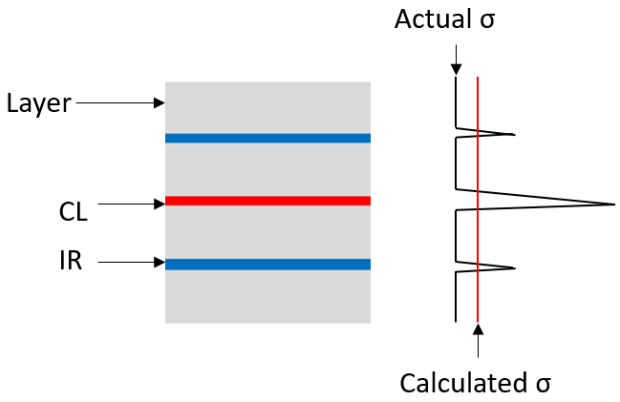

Figure 5-7: Actual and calculated σ of 3DCP samples

5.3.4 Chloride-induced corrosion initiation prediction

Table 5-11 lists the chloride-induced corrosion initiation prediction using the 10% binder prediction model exposed to very severe conditions for the samples tested in this study. Table 5-11 also includes the initiation prediction of concrete samples produced by Otieno et al. (2016). These mixtures have w/b ratios and compressive strengths that are similar to the 3DCP mixture used in this study. Table 5-10 contains Otieno et al. (2016) mixtures characteristics. It can be seen that cast samples (C-V and C-P) outperform the 3DCP structures, even when no pass time is induced. The inclusion of any pass time notably decreases the structure's service life. The printed samples (any pass time) underperform when compared to typical cast concrete compositions from Otieno et al. (2016), which is due to the low σ_c values and dense concrete matrixes with randomly distributed voids from Otieno et al. (2016). The chloride binding capacity of the mixtures containing FA and GGBS also increases the time to corrosion initiation.

Table 5-10: Otieno et al. (2016) mixtures characteristics

Concrete mix	**w/b ratio**	**σ_c (MPa)**	**28-day σ (mS/cm)**
100% OPC	0.4	58.2	1.24
70/30 % OPC/FA	0.4	50.7	0.37
50/50 % PC/GGBS	0.4	48.1	0.59

Table 5-11: Chloride-induced corrosion t_i (years) predictions

Variable	**Cover (mm)**			
	20	**50**	**80**	**100**
C-P	4.25	48.96	171.46	310.89
C-V	1.29	14.83	51.93	94.16
3D-0	0.74	8.52	29.82	54.07
3D-10	0.29	3.32	11.63	21.09
3D-20	0.08	0.89	3.10	5.63
3D-30	0.06	0.66	2.32	4.21
100% OPC	2	26.5	100	186
70/30% OPC/FA	3	>500	>500	>500
50/50% PC/GGBS	7.2	>500	>500	>500

6 Conclusions, recommendations, and future work

6.1 Conclusions

In this study, the durability performance of three-dimensional concrete printing (3DCP) and cast concrete was investigated. The effect of the 3DCP interlayer regions and critical layer was quantified. The investigation was motivated by the need to understand the durability performance of 3DCP structures in marine and urban environments since there is limited research covering this topic. The conclusion is divided into compressive strength, flexural strength, durability index (DI), accelerated concrete carbonation, chloride-induced corrosion and prediction models after which a general conclusion is made regarding the durability performance.

6.1.1 Compressive strength

Compressive strength tests were performed on 28-day old cubes. The following conclusion is drawn:

- Poker vibrated cast sample yielded higher concrete compressive strengths compared to the vibration table samples, which was attribute to the higher degree of compaction and denser matrix achieved with the poker.

6.1.2 Flexural strength

Flexural strength tests were performed using 4-point bending to establish the interlayer bond strength. The following conclusions are drawn:

- Cast samples yield higher flexural strength compared to 3DCP samples, which is attributed to the interconnected pores at the IRs and critical layer of the 3DCP samples.
- An increase in pass time results in a decrease in flexural strength owing to the lack of fusion induced by the pass time at the critical layer.
- Failure for the 3DCP samples occurs at the IRs for samples printed with no pass time. The pass time induced samples fail at the critical layer.

6.1.3 Durability index

The DI results consisted of the oxygen permeability index (OPI), water sorptivity index (WSI) and chloride conductivity index (CCI) tests. The following conclusions are drawn:

- OPI results: Cast samples yield lower permeability (*k*) and higher OPI values compared to 3DCP samples, which is attributed to the interconnected pores at the IRs and critical layer of the 3DCP samples. An increase in pass time also results in an increase in *k* and decreases in OPI, owing to the lack of fusion induced by the pass time at the critical layer.

- WSI results: Cast samples yield lower porosity (*n*) and sorptivity (S) values compared to 3DCP samples. An increase in pass time results in an increase in *n* and S, owing to the lack of fusion induced by the pass time at the critical layer. The 3D-30 were the only samples that did not follow the trend and yielded a S value lower than the 3D-10 samples.

- CCI results: Cast samples yield lower *n* and conductivity (σ) values compared to 3DCP samples. The interconnected pores at the IRs and critical layer of the 3DCP samples that increase the *n* and allow for a larger current to pass through the sample, yielding a larger σ. An increase in pass time resulted in an increase in σ, owing to the lack of fusion induced by the pass time at the critical layer. No trend was noticed regarding the *n* between the 3DCP samples.

6.1.4 Accelerated concrete carbonation

The accelerated concrete carbonation tests were conducted over a 12-week period. The following conclusions are drawn:

- Cast samples yield lower carbonation depths compared to 3DCP samples, which is attributed to interconnected pores at the IRs and critical layer of the 3DCP samples that reduce the carbonation resistance.

- The carbonation depth increases with an increase in pass time, owing to the lack of fusion induced by the pass time at the critical layer. The critical layer function as a crack (ingress pathway) with the carbon dioxide (CO_2) penetrating through the critical layer first, followed by the penetration upwards and downwards through the matrix.

- The penetration depth is larger through the layer above the critical layer compared to the layer below for samples with induced pass times. It is concluded that the moisture transfer from the latter above the critical layer to below the critical layer results in a more porous top layer, which is more prone for increased CO_2 diffusion rate.

- The increase in surface area of the 3DCP circular layer edges results in higher carbonation depths at the layer compared to the depth at the IRs itself.

6.1.5 Chloride-induced corrosion

Chloride-induced corrosion testing was performed over an 18-week cyclic wetting and drying period and the corrosion progression was monitored weekly. The following conclusions are drawn:

- The cast beams yielded a uniform chloride penetration profile. The 3DCP samples showed a sharp increase in chlorides penetration at the critical layer and location where layer tearing occurred.

- The torn layers and critical layer induced by the pass times function as cracks where penetration first occurs through the critical layer followed by horizontal penetration through the concrete matrix. The torn layers and critical layer function as ingress pathways for corrosion containments.

- Cast samples yielded lower chloride penetration depths, corrosion intensity (I_{corr}) readings, electrochemical mass loss and pitting depths than the 3DCP samples, which is attributed to interconnected pores at the IR's and critical layer of the 3DCP samples.

- The chloride penetration depth at the critical layer, time to corrosion initiation and I_{corr} readings, electrochemical mass loss and pitting depths increased with an increase in pass time owing to the lack of fusion induced by the pass time at the critical layer.

- Pitting corrosion and macro-cell corrosion are the corrosion type and mechanism taking place in the 3DCP beams. A pit formation was noted at the torn layer and critical layer location for the 3DCP beams.

- A moderate positive correlation was recorded between the corrosion potential (E_{corr}) and I_{corr} results. The relationship between the actively corroding concrete resistance

(R_{ohm}) and I_{corr} results showed moderate positive correlation; thus, showing that lower E_{corr} and R_{ohm} reading indicated a high I_{corr} potential and risk respectively.

6.1.6 Prediction models

The Salvoldi et al. (2015) carbonation model and the South African chloride ingress model were adapted to predict the carbonation depth and chloride profiles of the 3DCP samples since both models are formulated on cast samples. Both models required the inclusion of the calibration factors for the pass time induced 3DCP samples to calculate accurately the true k and σ of the critical layer itself since the k and σ calculated are an average across the entire sample.

The incorporation of a calibration factor in both models allows for future predictions of the chloride profiles, time to chloride-induced corrosion initiation, and the progression of the carbonation depth over time. When assessing the durability performance with both of the models, the cast samples yield longer corrosion initiation times (for the same cover depth) and lower carbonation depths compared to the 3DCP samples. The carbonation depth and time to corrosion initiation increases and decreases respectively with an increase in pass time. The printed samples outperformed typical conventional cast concrete mixtures in carbonation resistance, owing to the amount of carbonatable material produced curing. The printed samples underperformed with regards to chloride penetration (time to chloride-induced corrosion initiation) to typical conventional cast concrete mixtures, owing to high chloride conductivity of the printed samples.

6.1.7 General conclusion

It was concluded from the results of flexural strength, DI, accelerated concrete carbonation, and chloride-induced corrosion testing that 3DCP samples show a decrease in durability performance compared to cast samples. This is exacerbated by an increase in pass time, i.e. the time between the extrusion of a layer and that of the next, overlaying layer in the 3D concrete printing process, which is known to lead to a reduced interfacial bond between these layers. The Salvoldi et al. (2015) carbonation model and the South African chloride ingress model were adapted to predict the carbonation depth and chlorides profiles.

6.2 Recommendations

As presented, the lack of fusion present in the printed samples, especially the samples with induced pass time, has a great effect on the interlayer bond strength and durability properties. It is recommended that the lack of fusion should be addressed by applying additive mortars between printed layers or by utilizing topological interlocking, especially when large pass time are introduced. It should be noted that these methods, that were presented in Chapter 2.5.4, were only showed to improve the fusion from a mechanical strength point of view and that no durability testing was performed, thus the improvement of the durability properties of interlayer regions is unknown. Durability testing with these methods should be repeated to quantify the durability improvement.

6.3 Future work

The following recommendations with regards to future studies and research topics are made:

- Interlayer bond improvement studies with regards to mechanical and durability performance by utilizing different additive mortars and topological interlocking techniques.
- Systematically characterise ingress into 3D printable concrete, due to the different microstructure caused by printing, and the lower and smaller size aggregate and associated interfacial transition zones.
- Investigate the role of material mix parameters such as water to cement ratio, binder composition and aggregate size and content on durability of 3DCP.
- Extend duration of corrosion testing to more significant levels of steel reinforcement mass loss, to confirm the short-term trends found here also on longer term.
- Conduct corrosion testing on reinforced beams that are reinforced parallel to the interlayer regions.
- Quantity the effect of the extra exposure surface, i.e. curved sides, on the concrete carbonation depth compared to a flat exposure face of the same printed sample.

- Investigate the effect of the pass time on other mechanical strength testing such as direct tensile, compression, and shear strength testing.

7 References

Ades, M., Adler, R., Aldeco, L.S., Alejandra, G., Alfaro, E.J., Aliaga-Nestares, V., Allan, R.P., Allan, R., Alves, L.M., Amador, J.A. & Andersen, J.K., 2019. State of the climate in 2018. *Bulletin of the American Meteorological Society*, 100(9):SI–S305. DOI: 10.1175/2019BAMSStateoftheClimate.1.

Al-Ameeri, A.S., Rafiq, M.I., Tsioulou, O. & Rybdylova, O. 2021. Impact of climate change on the carbonation in concrete due to carbon dioxide ingress: Experimental investigation and modelling. *Journal of Building Engineering*. 44(December 2020):102594. DOI: 10.1016/j.jobe.2021.102594.

Alexander, M. & Beushausen, H. 2019. Durability, service life prediction, and modelling for reinforced concrete structures – review and critique. *Cement and Concrete Research*. 122(February):17–29. DOI: 10.1016/j.cemconres.2019.04.018.

Alexander, M.G., Mackechnie, J.R. & Ballim, Y. 1999. *Guide to the use of durability indexes for achieving durability in concrete structures - Research Monograph 2*. Cape Town: University of Cape Town, Department of Civil Engineering.

Alexander, M.G., Streicher, P.E. & Mackechnie, J.R. 1999. *Rapid chloride conductivity testing of concrete - Research Monograph 3*. Cape Town: University of Cape Town, Department of Civil Engineering.

ALLPLAN. 2020. *First 3d-Printed House in Germany Realized with Support from ALLPLAN*. Available: https://www.allplan.com/press-reports/press-report/first-3d-printed-house-in-germany-realized-with-support-from-allplan/ [2021, September 28].

Alonso, C., Andrade, C. & González, J.A. 1988. Relation between resistivity and corrosion rate of reinforcements in carbonated mortar made with several cement types. *Cement and Concrete Research*. 18(5):687–698. DOI: 10.1016/0008-8846(88)90091-9.

Alonso, C., Andrade, C., Castellote, M. & Castro, P. 2000. Chloride threshold values to depassivate reinforcing bars embedded in a standardized OPC mortar. *Cement and Concrete Research*. 30(7):1047–1055. DOI: 10.1016/S0008-8846(00)00265-9.

Alonso, C., Castellote, M. & Andrade, C. 2002. Chloride threshold dependence of pitting potential of reinforcements. *Electrochimica Acta*. 47(21):3469–3481.

Andrade, C. & Alonso, C. 1996. Corrosion rate monitoring in the laboratory and on-site. *Construction and Building Materials*. 10(5):315–328.

Andrade, C. & Alonso, C. 2001. On-site measurements of corrosion rate of reinforcements. *Construction and Building Materials*. 15(2–3):141–145. DOI: 10.1016/S0950-0618(00)00063-5.

Andrade, C. & Martínez, I. 2005. Calibration by gravimetric losses of electrochemical corrosion rate measurement using modulated confinement of the current. *Materials and Structures*. 38(283):833–841. DOI: 10.1617/14297.

Arandigoyen, M., Bicer-Simsir, B., Alvarez, J.I. & Lange, D.A. 2006. Variation of microstructure with carbonation in lime and blended pastes. *Applied Surface Science*. 252(20):7562–7571. DOI: 10.1016/j.apsusc.2005.09.007.

Arya, C., Buenfeld, N.R. & Newman, J.B. 1990. Factors influencing chloride-binding in concrete. *Cement and Concrete Research*. 20(2):291–300. DOI: 10.1016/0008-8846(90)90083-A.

ASTM C876-91. 1999. *Standard test method for half-cell potentials of uncoated reinforcing steel in concrete*. 03(Reapproved):1–6.

ASTM C230/C230M. 2014. *Standard specification for flow table for use in tests of hydraulic cement*.

Bahador, S.D. & Cahyadi, J.H. 2009. Modelling of carbonation of PC and blended cement concrete. *IES Journal Part A: Civil and Structural Engineering*. 2(1):59–67. DOI: 10.1080/19373260802518091.

Bensted, J. 1983. Hydration of Portland cement. In *Advances in Cement Technology*. S.N. Ghosh, Ed. New York: Pergamon Press. 307–347.

Bentur, A., Diamond, S. & Berke, N. 1997. *Steel corrosion in concrete, Fundamentals and Civil Engineering Practice*. London: E & FN Spon.

Bester, F., van den Heever, M., Kruger, J., Cho, S. & van Zijl, G. 2020. Steel fibre links in 3D printed concrete. *Second RILEM International Conference on Concrete and Digital Fabrication - Digital Concrete 2020*. 2:1–9.

Beushausen, H., Otieno, M. & Alexander, M. 2021. Durability of concrete in M. Alexander (Ed). *Fulton's concrete technology*. 10th ed. Midrand, South Africa: Cement & Concrete SA. 391-468.

Bezuidenhout, S.R. 2017. Corrosion propagation in cracked reinforced concrete structures. (Masters dissertation) Stellenbosch University.

Bezuidenhout, S.R. & van Zijl, G.P.A.G. 2019. Corrosion propagation in cracked reinforced concrete, toward determining residual service life. *Structural Concrete*. 20(6):2183–2193. DOI: 10.1002/suco.201800275.

Björn, A., Segura de la Monja, P., Karlsson, A., Ejlertsson, J. & Bo, H. 2012. Rheological Characterization. *Biogas*. (March). DOI: 10.5772/32596.

Bos, F.P., Ahmed, Z.Y., Jutinov, E.R. & Salet, T.A.M. 2017. Experimental exploration of metal cable as reinforcement in 3D printed concrete. *Materials*. 10(11). DOI: 10.3390/ma10111314.

Boshoff, W.P., Altmann, F., Adendorff, C.J. & Mechtcherine, V. 2016. A new approach for modelling the ingress of deleterious materials in cracked strain hardening cement-based composites. *Materials and Structures/Materiaux et Constructions*. 49(6):2285–2295. DOI: 10.1617/s11527-015-0649-8.

Bran-Anleu, P.C. 2018. Quantitative micro XRF mapping of chlorides: Possibilities, limitations, and applications, from cement to digital concrete. ETH Zurich.

Broomfield, J.P. 2006. *Corrosion of Steel in Concrete: Understanding, investigation and repair*. 2nd Ed. ed. Taylor & Francis.

BS 8110-1. 1985. *Structural use of concrete: Code of practice for design and construction*: BS 8110, Part 1. British Standards Institution.

BS 1881-210. 2013. *BSI Standards Publication Testing hardened concrete Part 210: Determination of the potential carbonation resistance of method*. BSI Standards Limited.

BS EN 196-1. 2005. *Methods of Testing Cement. Part 1, Determination of Strength. British Standard Institution*. London, UK.

BS EN 206-1. 2000. *Concrete. Specification, performance, production and conformity*. London.

Carević, V. & Ignjatović, I. 2019. Influence of loading cracks on the carbonation resistance of RC elements. *Construction and Building Materials*. 227. DOI: 10.1016/j.conbuildmat.2019.07.309.

Cho, S., Kruger, J., Zeranka, S. & van Zijl, G. 2019. 3D Printable concrete technology and mechanics. *Concrete Beton*. (158):11–18.

Cho, S., Kruger, J., Bester, F., van den Heever, M., van Rooyen, A. & van Zijl, G. 2020. A compendious Rheo-mechanical test for printability assessment of 3D printable concrete. In *Second RILEM International Conference on Concrete and Digital Fabrication*. 196–205.

Choi, M., Roussel, N., Kim, Y. & Kim, J. 2013. Lubrication layer properties during concrete pumping. *Cement and Concrete Research*. 45(1):69–78. DOI: 10.1016/j.cemconres.2012.11.001.

Christen, H., Cho, S., van Zijl, G.P. & de Villiers, W. 2021. Phase change material infused recycled brick aggregate in 4D printed concrete. Submitted for *Journal of Building Engineering*.

Chua, C.K. & Leong, K.F. 2014. *3D Printing and additive manufacturing: Principles and applications*. 4th ed. Singapore: World Scientific.

Climate Data. 2020. *Climate Data - Stellenbosch*. Available: https://en.climate-data.org/africa/south-africa/western-cape/stellenbosch-6770/#climate-table [2021, September 27].

Cui, H., Tang, W., Liu, W., Dong, Z. & Xing, F. 2015. Experimental study on effects of CO2 concentrations on concrete carbonation and diffusion mechanisms. *Construction and Building Materials*. 93:522–527. DOI: 10.1016/j.conbuildmat.2015.06.007.

Djerbi, A., Bonnet, S., Khelidj, A. & Baroghel-Bouny, V. 2008. Influence of traversing crack on chloride diffusion into concrete. *Cement and Concrete Research*. 38(6):877–883. DOI: 10.1016/j.cemconres.2007.10.007.

Domone, P. & Illston, J. (Eds) 2010. *Construction materials: Their nature and behavior*. 4th ed. New York: Spon Press.

Du Preez, A.A. & Alexander, M.G. 2004. A site study of durability indexes for concrete in marine conditions. Materials and Structures. 37(267),146–154. DOI: 10.1617/13998.

Fédération internationale du béton. 2006. *fib Bulletin 34 - Model code for service life design*. Lausanne: International Federation for Structural Concrete.

Fédération internationale du béton. 2010. *fib Model code for concrete structures 2010*. Beverley, P. (Ed.) Berlin: Wilhelm Ernst & Sohn.

Glass, G.K., Hassanein, N.M. & Buenfeld, N.R. 1997. Neural network modelling of chloride binding. *Magazine of Concrete Research*. 49:323–335.

González, J.A., Andrade, C., Alonso, C. & Feliu, S. 1995. Comparison of rates of general corrosion and maximum pitting penetration on concrete embedded steel reinforcement. *Cement and Concrete Research*. 25(2):257–264. DOI: 10.1016/0008-8846(95)00006-2.

Hack, N., Wangler, T., Mata-Falcón, J., Dörfler, K., Kumar, N., Walzer, A.N., Graser, K., Reiter, L., Richner, H., Buchli, J. & Kaufmann, W., 2017, March. Mesh mould: An onsite, robotically fabricated, functional formwork. In *Second Concrete Innovation Conference* (2nd CIC) (Vol. 19,1–10).

Heckroodt, R.O. 2002. *Guide to the deterioration and failure of building materials*. Cape Town: Thomas Telford Publishing. DOI: 10.1680/gttdafofbm.31722.

isdcorr. 2015. *GECOR 10 Operator's Manual*.

Keita, E., Bessaies-Bey, H., Zuo, W., Belin, P. & Roussel, N. 2019. Weak bond strength between successive layers in extrusion-based additive manufacturing: measurement and physical origin. *Cement and Concrete Research*. 123(November 2018):105787. DOI: 10.1016/j.cemconres.2019.105787.

Khoshnevis, B. 2004. Automated construction by contour crafting–Related robotics and information technologies. *Automation in Construction*. 13(1):5–19. DOI: 10.1016/j.autcon.2003.08.012.

Kruger, J. & van Zijl, G. 2021. A compendious review on lack-of-fusion in digital concrete fabrication. *Additive Manufacturing*, 37.

Kruger, J., Cicione, A., Bester, F., van den Heever, M., Cho, S., Walls, R. & van Zijl, G. 2020. Facilitating ductile failure of 3D printed concrete elements in fire. *2nd RILEM International Conference on Concrete and Digital Fabrication.* 2:1–10.

Kruger, J., Zeranka, S. & van Zijl, G. 2019. 3D concrete printing: A lower bound analytical model for buildability performance quantification. *Automation in Construction*. 106(February):102904. DOI: 10.1016/j.autcon.2019.102904.

Kruger, J., du Plessis, A. & van Zijl, G. 2021. An investigation into the porosity of extrusion-based 3D printed concrete. *Additive Manufacturing*. 37(November 2020):101740. DOI: 10.1016/j.addma.2020.101740.

Kruger, P.J., van den Heever, M., Cho, S., Zeranka, S. & van Zijl, G. 2019. High-performance 3D printable concrete enhanced with nanomaterials. *Proceedings of the International Conference on Sustainable Materials, Systems and Structures: New Generation of Construction Materials*. (October):533–540.

Lambert, P., Page, G.L. & Vassie, P.R. 1991. Investigations of reinforcement corrosion, Electrochemical monitoring of steel in chloride-contaminated concrete. *Materials and Structures*. 24:351–358.

Le, T.T., Austin, S.A., Lim, S., Buswell, R.A., Gibb, A.G.F. & Thorpe, T. 2012. Mix design and fresh properties for high-performance printing concrete. *Materials and Structures/Materiaux et Constructions*. 45(8):1221–1232. DOI: 10.1617/s11527-012-9828-z.

Liu, Y. 1996. Modelling the time-to-corrosion cracking of the cover concrete in chloride contaminated reinforced concrete structures. (Doctoral dissertation) Virginia Polytechnic Institute and State University.

Lu, C. F, Wang, W., Li, Q. T, Hao, M. & Xu, Y. 2018. Effects of micro-environmental climate on the carbonation depth and the pH value in fly ash concrete. *Journal of Cleaner Production*. 181:309–317. DOI: 10.1016/j.jclepro.2018.01.155.

Lukovic, M. & Ye, G. 2016. Effect of moisture exchange on interface formation in the repair system studied by X-ray absorption. *Materials*. 9(2):1–17. DOI: 10.3390/ma9010002.

Ma, G., Salman, N. M., Wang, L., & Wang, F. 2020. A novel additive mortar leveraging internal curing for enhancing interlayer bonding of cementitious composite for 3D printing. *Construction and Building Materials*, *244*. DOI: 10.1016/j.conbuildmat.2020.118305

Mackechnie, J.R. 1995. Predictions of reinforced concrete durability in the marine environment. (Doctoral dissertation) University of Cape Town, South Africa. (May):140.

Mackechnie, J.R. 2001. *Predictions of reinforced concrete durability in the marine environment.* Research Monograph 1. V. 1. Cape Town: University of Cape Town, Department of Civil Engineering.

Mackechnie, J.R. & Alexander, M.G. 1997. Exposure of concrete in different marine environments. *American Society of Civil Engineers*. 9(1):41–44.

Mackechnie, J.R. & Alexander, M.G. 1999. Predictions of long-term chloride ingress from marine exposure trials. In *International Conference on Ion and Mass Transport in Cement-Based Materials* (pp. 281–291).

Mackechnie, J.R. & Alexander, M.G. 2001. Repair principles for corrosion-damaged reinforced concrete structures. *Research Monograph 5*. Cape Town: University of Cape Town, Department of Civil Engineering.

Malan, J.D. 2020. Design of a new 3DPC mix design with adjusted water and superplasticizer amounts.

Mangat, P.S., Khatib, J.M. & Molloy, B.T. 1994. Microstructure, chloride diffusion and reinforcement corrosion in blended cement paste and concrete. *Cement and Concrete Composites*. 16(2):73–81. DOI: 10.1016/0958-9465(94)90002-7.

Marchment, T. & Sanjayan, J. 2020a. Mesh reinforcing method for 3D concrete printing. *Automation in Construction*. 109(October 2019):102992. DOI: 10.1016/j.autcon.2019.102992.

Marchment, T. & Sanjayan, J. 2020b. Bond properties of reinforcing bar penetrations in 3D concrete printing. *Automation in Construction*. 120(September):103394. DOI: 10.1016/j.autcon.2020.103394.

Meyer, A., Wierig, H.J. & Husmann, K. 1967. Karbonatisierung von schwerbeton (Carbonation of reinforced concrete). *Deutscher Ausschuss fur Stahlbeton*. 182,1–33.

Moelich, G. M., Kruger, J., & Combrinck, R. 2020. Plastic shrinkage cracking in 3D printed concrete. *Composites Part B: Engineering*, *200*(July), 108313. DOI: 10.1016/j.compositesb.2020.108313

Moelich, G.M., Kruger, P.J. & Combrinck, R. 2021a. The effect of restrained early age shrinkage on the interlayer bond and durability of 3D printed concrete. *Journal of Building Engineering*. 43(May):102857. DOI: 10.1016/j.jobe.2021.102857.

Moelich, G.M., Kruger, J. & Combrinck, R. 2021b. Modelling the interlayer bond strength of 3D printed concrete with surface moisture. *Cement and Concrete Research*, 150,106559. 150(September):106559. DOI: 10.1016/j.cemconres.2021.106559.

Mohan, M.K., Rahul, A. V., De Schutter, G. & Van Tittelboom, K. 2021. Extrusion-based concrete 3D printing from a material perspective: A state-of-the-art review. *Cement and Concrete Composites*. 115(June 2020),103855. DOI: 10.1016/j.cemconcomp.2020.103855.

Morandeau, A., Thiéry, M. & Dangla, P. 2014. Investigation of the carbonation mechanism of CH and C-S-H in terms of kinetics, microstructure changes and moisture properties. *Cement and Concrete Research*. 56:153–170. DOI: 10.1016/j.cemconres.2013.11.015.

Mubatapasango, M. 2017. Carbonation induced corrosion in integral and non-integral surface treated lightweight foam concrete. (Masters dissertation) Stellenbosch University.

Munemo, R.E. 2020. Thixotropic characteristics for robust interlayers in 3D printable concrete. Stellenbosch University.

Nerella, V.N., Hempel, S. & Mechtcherine, V. 2017. Micro-and macroscopic investigations on the interface between layers of 3D-printed cementitious elements. In *Proceedings of the ICACMS 2017 International conference on Advances in construction materials and systems*. (9):3–8.

Nerella, V.N., Ogura, H. & Mechtcherine, V. 2018. Incorporating reinforcement into digital concrete construction. *Annual IASS Symposia: Creativity in structural design*. (July).

Nerella, V.N., Hempel, S. & Mechtcherine, V. 2019. Effects of layer-interface properties on mechanical performance of concrete elements produced by extrusion-based 3D-printing. *Construction and Building Materials*. 205,586–601. DOI: 10.1016/j.conbuildmat.2019.01.235.

Newman, J. 1966. Resistance for flow of current to a disk. *Journal of The Electrochemical Society*, 107,501–502.

Ngala, V.T. & Page, C.L. 1997. Effects of carbonation on pore structure and diffusional properties of hydrated cement pastes. *Cement and Concrete Research*. 27(7),5–24.

Nilsson, L. 2004. Concepts in chloride ingress modelling. In *Third International RILEM Workshop on Testing and Modelling Chloride Ingress into Concrete* (pp. 29–48). RILEM Publications SARL. DOI: 10.1617/2912143578.003.

Nilsson, L.-O., Poulsen, E., Sandberg, P., Sørensen, H.E. & Klinghoffer, O. 1996. *HETEK*, Chloride penetration into concrete, state-of-the-art: transport processes, corrosion initiation, test methods and prediction models. Report No. ed. Road Directorate. DOI: 10.13140/RG.2.1.2771.7526.

NT Build 443. 1995. *Concrete, hardened: Accelerated chloride penetration*. Finland.

Otieno, M. 2008. Corrosion propagation in cracked and uncracked concrete. University of Cape Town.

Otieno, M. B. 2014. The development of empirical chloride-induced corrosion rate prediction models for cracked and uncracked steel reinforced concrete structures in the marine tidal zone. PhD thesis. University of Cape Town.

Otieno, M., Alexander, M. & Beushausen, H. 2010a. Transport mechanisms in concrete. Corrosion of steel in concrete (initiation, propagation & factors affecting). Assessment of corrosion. Cape Town.

Otieno, M.B., Alexander, M.G. & Beushausen, H.D. 2010b. Corrosion in cracked and uncracked concrete - influence of crack width, concrete quality and crack reopening. *Magazine of Concrete Research*, 62(6),393–404. DOI: 10.1680/macr.2010.62.6.393.

Otieno, M., Beushausen, H. & Alexander, M. 2016. Chloride-induced corrosion of steel in cracked concrete - Part I: Experimental studies under accelerated and natural marine environments. *Cement and Concrete Research*. 79, 373–385. DOI: 10.1016/j.cemconres.2015.08.009.

Otieno, M., Ikotun, J. & Ballim, Y. 2020. Experimental investigations on the effect of concrete quality, exposure conditions and duration of initial moist curing on carbonation rate in concretes exposed to urban, inland environment. *Construction and Building Materials*, 246,118443. DOI: 10.1016/j.conbuildmat.2020.118443.

Otsuki, N., Nagataki, S. & Nakashita, K. 1993. Evaluation of the AgNO3 solution spray method for measurement of chloride penetration into hardened cementitious matrix materials. *Construction and Building Materials*, 7(4),195–201.

Panda, B., Noor Mohamed, N.A.., Paul, S.C., Bagath Singh, G.V. P., Tan, M.J. & Šavija, B. 2019. The effect of material fresh properties and process parameters on buildability and interlayer adhesion of 3D printed concrete. *Materials*. 12(13). DOI: 10.3390/ma12132149.

Papadakis, V.G. 1999a. Experimental investigation and theoretical modelling of silica fume activity in concrete. *Cement and Concrete Research*. 29(1),79–86. DOI: 10.1016/S0008-8846(98)00171-9.

Papadakis, V.G. 1999b. Effect of fly ash on Portland cement systems: Part I. Low-calcium fly ash. *Cement and Concrete Research*. 29(11),1727–1736. DOI: 10.1016/S0008-8846(99)00153-2.

Papadakis, V.G. 2000. Effect of supplementary cementing materials on concrete resistance against carbonation and chloride ingress. *Cement and Concrete Research*. 30(2),291–299. DOI: 10.1016/S0008-8846(99)00249-5.

Papadakis, V.G. & Vayenas, C.G. 1989. A reaction engineering approach to the problem of concrete carbonation. *AIChE Journal*. 35(10),1639–1650.

Papadakis, V.G., Vayenas, C.G. & Fardis, M. 1991a. Physical and chemical characteristics affecting the durability of concrete. *ACI Materials Journal*, 88(2),186–196.

Papadakis, V.G., Vayenas, C.G. & Fardis, M.N. 1991b. Fundamental modeling and experimental investigation of concrete carbonation. *ACI Materials Journal*. 88(4),363–373. DOI: 10.14359/1863.

Papadakis, V.G., Vayenas, C.G. & Fardis, M.N. 1991c. Physical and chemical characteristics affecting the durability of concrete. *ACI Materials Journal*. 88(2),186–196. DOI: 10.14359/1993.

Parks, J. 2021. *Zaha Hadid Architects and ETH Zurich create 3D-printed concrete bridge in Venice*. Available: https://www.dezeen.com/2021/07/28/zaha-hadid-architects-block-research-group-straitus-3d-printed-concrete-bridge/ [2021, September 28].

Parrott, L.J. 1988. Moisture profile in drying concrete. *Advances in Cement Research*. 1(3),164–170.

Paul, S.C. & van Zijl, G.P.A.G. 2016. Chloride-induced corrosion modelling of cracked reinforced SHCC. *Archives of Civil and Mechanical Engineering*. 16(4),734–742. DOI: 10.1016/j.acme.2016.04.016.

Paul, S.C. & van Zijl, G.P. 2017. Corrosion deterioration of steel in cracked SHCC. *International Journal of Concrete Structures and Materials*. 11(3),557–572. DOI: 10.1007/s40069-017-0205-8.

Paul, S.C., van Zijl, G.P., Babafemi, A.J. & Tan, M.J. 2016. Chloride ingress in cracked and uncracked SHCC under cyclic wetting-drying exposure. *Construction and Building Materials*. 114,232–240. DOI: 10.1016/j.conbuildmat.2016.03.206.

Paul, S.C., van Zijl, G. P. & Gibson, I. 2018. A review of 3D concrete printing systems and materials properties: current status and future research prospects. *Rapid Prototyping Journal*. 24(4),784–798. DOI: 10.1108/RPJ-09-2016-0154.

Paul, S.C., Panda, B., Huang, Y., Garg, A. & Peng, X. 2018. An empirical model design for evaluation and estimation of carbonation depth in concrete. *Measurement: Journal of the International Measurement Confederation*. 124(December 2017),205–210. DOI: 10.1016/j.measurement.2018.04.033.

Print 3D. 2014. *Architect plans to 3D print a 2-story home in Minnesota using a homemade cement printer*. Available: https://3dprint.com/2471/3d-printed-home-in-minnesota/ [Accessed: 2020, May 29].

Qin, L., Gao, X. & Chen, T. 2019. Influence of mineral admixtures on carbonation curing of cement paste. *Construction and Building Materials*. 212,653–662. DOI: 10.1016/j.conbuildmat.2019.04.033.

Richardson, M.G. 2002. *Fundamentals of Durable Reinforced Concrete*. A. Bentur & S. Mindess (Eds). London & New York: Spon Press.

Roussel, N. & Cussigh, F. 2008. Distinct-layer casting of SCC: The mechanical consequences of thixotropy. *Cement and Concrete Research*. 38(5),624–632. DOI: 10.1016/j.cemconres.2007.09.023.

Sabet, D.B. & Jong, H.C. 2006. The effect of environment conditions on concrete carbonation (numerical model). In *Proceedings of the 5th international symposium on new technologies for urban safety of mega cities in Asia*. Thailand. pp. 405–414.

Salet, T.A.M., Ahmed, Z.Y., Bos, F.P. & Laagland, H.L.M. 2018. Design of a 3D printed concrete bridge by testing. *Virtual and Physical Prototyping*, 13(3),222–236. DOI: 10.1080/17452759.2018.1476064.

Salvoldi, B., Beushausen, H. & Alexander, M. 2011. Modelling the carbonation of concrete using performance-based tests: proposition of a conceptual framework. Submitted for *ICCC*. Madrid.

Salvoldi, B.G., Beushausen, H. & Alexander, M.G. 2015. Oxygen permeability of concrete and its relation to carbonation. *Construction and Building Materials*, 85,30–37. DOI: 10.1016/j.conbuildmat.2015.02.019.

Sanjayan, J.G., Nazari, A. & Nematollahi, B. 2019. *3D Concrete printing technology*. Hawthorn, Australia: Butterworth-Heinemann.

Sanjayan, J.G., Nematollahi, B., Xia, M. & Marchment, T. 2018. Effect of surface moisture on inter-layer strength of 3D printed concrete. *Construction and Building Materials*, 172,468–475. DOI: 10.1016/j.conbuildmat.2018.03.232.

SANS 5863. 2006. *South African National Standard Concrete tests — Compressive strength of hardened concrete.*

SANS 5864. 2006. *South African National Standard Concrete tests — Flexural strength of hardened concrete*.

Šavija, B. & Luković, M. 2016. Carbonation of cement paste: Understanding, challenges, and opportunities. *Construction and Building Materials*, 117,285–301. DOI: 10.1016/j.conbuildmat.2016.04.138.

Schröfl, C., Nerella, V.N. & Mechtcherine, V. 2019. Capillary water intake by 3D-printed concrete visualised and quantified by neutron radiography. In *RILEM International Conference on Concrete and Digital Fabrication.* 19, 217–224.

Scott, A.N. 2004. The influence of binder type and cracking on reinforcing steel corrosion in concrete. University of Cape Town.

Scott, C. 2016. *Chinese construction company 3D prints an entire two-story house on-site in 45 days*. Available: https://3dprint.com/138664/huashang-tengda-3d-print-house/ [2020, May 29].

Scott, A. & Alexander, M.G. 2007. The influence of binder type, cracking and cover on corrosion rates of steel in chloride-contaminated concrete. *Magazine of Concrete Research*. 59(7),495–505. DOI: 10.1680/macr.2007.59.7.495.

Secrieru, E., Cotardo, D., Mechtcherine, V., Lohaus, L., Schröfl, C. & Begemann, C. 2018. Changes in concrete properties during pumping and formation of lubricating material under pressure. *Cement and Concrete Research*. 108(March),129–139. DOI: 10.1016/j.cemconres.2018.03.018.

Secrieru, E., Khodor, J., Schröfl, C. & Mechtcherine, V. 2018. Formation of lubricating layer and flow type during pumping of cement-based materials. *Construction and Building Materials*. 178,507–517. DOI: 10.1016/j.conbuildmat.2018.05.118.

Sevenson, B. 2015. *Shanghai-based WinSun 3D prints 6-story apartment building and an incredible home*. Available: https://3dprint.com/38144/3d-printed-apartment-building/ [2020, May 29].

Song, H.W., Kwon, S.J., Byun, K.J. & Park, C.K. 2006. Predicting carbonation in early-aged, cracked concrete. *Cement and Concrete Research*. 36(5),979–989. DOI: 10.1016/j.cemconres.2005.12.019.

Stefanoni, M., Angst, U. & Elsener, B. 2019. Corrosion challenges and opportunities in digital fabrication of reinforced concrete. *RILEM Bookseries*. 19,225–233. DOI: 10.1007/978-3-319-99519-9_21.

Trejo, D. & Pillai, R.G. 2003. Accelerated chloride threshold testing: Part I – ATSM A-615 and A-706 reinforcement. *ACI Materials Journal*. 100(6), 519–527.

Tuutti, K. 1982. *Corrosion of steel in concrete*. Stockholm: Swedish Cement and Concrete Research Institute.

University of Cape Town & University of Witwatersrand. 2017. *Durability Index Testing Procedure Manual*.

Van Der Putten, J., Deprez, M., Cnudde, V., De Schutter, G. & Van Tittelboom, K. 2019. Microstructural characterization of 3D printed cementitious materials. *Materials*. 12(18). DOI: 10.3390/ma12182993.

Van Der Putten, J., De Schutter, G. & Van Tittelboom, K. 2019. The effect of print parameters on the (Micro) structure of 3D printed cementitious materials. *RILEM Bookseries*. 19,234–244.

Van Der Putten, J., Azima, M., Van den Heede, P., Van Mullem, T., Snoeck, D., Carminati, C., Hovind, J., Trtik, P., De Schutter, G. & Van Tittelboom, K. 2020. Neutron radiography to study the water ingress via the interlayer of 3D printed cementitious materials for continuous layering. *Construction and Building Materials*. 258,119587. DOI: 10.1016/j.conbuildmat.2020.119587.

Van Der Putten, J., De Volder, M., Van den Heede, P., De Schutter, G. & Van Tittelboom, K. 2020. 3D printing of concrete: The influence on chloride penetration. *RILEM Bookseries*. 28(July),500–507. DOI: 10.1007/978-3-030-49916-7_51.

Van Zijl, G.P.A.G. & Boshoff, W.P. 2018. The effect of crack patterns on the corrosion of steel reinforced SHCC. In *RILEM Bookseries* – Strain hardening cement-based composites SHCC4. V. 15. Dresden, Germany: Springer. 565–572. DOI: 10.1007/978-94-024-1194-2.

Van Zijl, G.P.A.G. & Paul, S.C. 2018. A novel link of the time scale in accelerated chloride-induced corrosion test in reinforced SHCC. *Construction and Building Materials*, 167,15–19. DOI: 10.1016/j.conbuildmat.2018.02.019.

Van Zijl, G.P.A.G., Bezuidenhout, S.R. & Van Rooyen, A.S. 2018. Chloride-induced corrosion of cracked cement-based composites. *RILEM Bookseries* - Strain hardening cement-based composites SHCC4. 15,643–650.

Vernier. 2021. Vernier CO2 gas sensor. Available: https://www.vernier.com/product/co2-gas-sensor/ [2021, August 22].

Wang, L., Tian, Z., Ma, G., & Zhang, M. 2020. Interlayer bonding improvement of 3D printed concrete with polymer modified mortar: Experiments and molecular dynamics studies. *Cement and Concrete Composites*, *110*. DOI: 10.1016/j.cemconcomp.2020.103571

Wierig, H.-J. 1984. Long-time studies on the carbonation of concrete under normal outdoor exposure. In *RILEM seminar on the durability of concrete structures under normal outdoor exposure*. Hanover: Germany.

Wolfs, R.J.M., Bos, F.P. & Salet, T.A.M. 2019. Hardened properties of 3D printed concrete: The influence of process parameters on interlayer adhesion. *Cement and Concrete Research*. 119(February),132–140. DOI: 10.1016/j.cemconres.2019.02.017.

Younsi, A., Turcry, P., Rozire, E., Aït-Mokhtar, A. & Loukili, A. 2011. Performance-based design and carbonation of concrete with high fly ash content. *Cement and Concrete Composites*. 33(10),993–1000. DOI: 10.1016/j.cemconcomp.2011.07.005.

Zareiyan, B., & Khoshnevis, B. 2017. Effects of interlocking on interlayer adhesion and strength of structures in 3D printing of concrete. *Automation in Construction*, *83*, 212–221. DOI: 10.1016/j.autcon.2017.08.019

Zhou, Y., Gencturk, B., Willam, K. & Attar, A. 2014. Carbonation-induced and chloride-induced corrosion in reinforced concrete structures. *Journal of Materials in Civil Engineering*. 27(9). DOI: 10.1061/(ASCE)MT.1943-5533.0001209.

Zivica. V. 2003. Influence of w/c ratio on rate of chloride induced corrosion of steel reinforcement and its dependence on ambient temperature. *Bulletin of. Materials Science*. 26(5),471–475.

Appendix A GECOR 10 readings

A.1 I_{corr} readings (µA/cm²)

Table A- 1: Complete I_{corr} readings

		Week																		
Variable	**Sample**	**0**	**1**	**2**	**3**	**4**	**5**	**6**	**7**	**8**	**9**	**10**	**11**	**12**	**13**	**14**	**15**	**16**	**17**	**18**
3D-0	1	0,036	0,049	0,061	0,074	0,086	0,099	0,072	0,091	0,079	0,078	0,086	0,081	0,099	0,097	0,094	0,083	0,119	0,120	0,105
	2	0,043	0,049	0,055	0,060	0,066	0,072	0,070	0,091	0,079	0,098	0,076	0,086	0,099	0,056	0,088	0,045	0,057	0,095	0,083
	3	0,041	0,044	0,047	0,050	0,053	0,056	0,051	0,061	0,058	0,074	0,066	0,054	0,051	0,063	0,072	0,079	0,063	0,091	0,091
	Average	0,040	0,047	0,054	0,061	0,069	0,076	0,064	0,081	0,072	0,083	0,076	0,074	0,083	0,072	0,085	0,069	0,080	0,102	0,093
3D-10	1	0,027	0,038	0,049	0,059	0,070	0,081	0,070	0,083	0,076	0,083	0,068	0,055	0,055	0,059	0,059	0,078	0,078	0,098	0,098
	2	0,046	0,046	0,045	0,045	0,044	0,044	0,042	0,057	0,049	0,049	0,053	0,051	0,066	0,076	0,073	0,095	0,098	0,119	0,092
	3	0,018	0,039	0,060	0,082	0,103	0,124	0,126	0,135	0,128	0,150	0,125	0,123	0,124	0,128	0,128	0,156	0,175	0,203	0,180
	Average	0,030	0,041	0,051	0,062	0,072	0,083	0,079	0,092	0,084	0,094	0,082	0,076	0,082	0,088	0,087	0,110	0,117	0,140	0,123
3D-20	1	0,039	0,056	0,073	0,089	0,106	0,123	0,132	0,132	0,132	0,121	0,111	0,093	0,160	0,151	0,145	0,110	0,113	0,140	0,168
	2	0,048	0,060	0,072	0,085	0,097	0,109	0,119	0,124	0,137	0,129	0,126	0,111	0,174	0,188	0,129	0,138	0,190	0,216	0,233
	3	0,021	0,046	0,070	0,095	0,119	0,144	0,167	0,138	0,120	0,118	0,106	0,098	0,138	0,177	0,130	0,135	0,168	0,185	0,201
	Average	0,036	0,054	0,072	0,090	0,108	0,125	0,139	0,131	0,130	0,123	0,114	0,101	0,157	0,172	0,135	0,128	0,157	0,180	0,201
3D-30	1	0,040	0,059	0,077	0,096	0,114	0,133	0,143	0,156	0,143	0,164	0,152	0,075	0,233	0,255	0,165	0,189	0,235	0,290	0,283
	2	0,047	0,061	0,075	0,090	0,104	0,118	0,139	0,145	0,159	0,158	0,072	0,056	0,193	0,243	0,244	0,195	0,174	0,260	0,245
	3	0,038	0,056	0,075	0,093	0,112	0,130	0,150	0,131	0,146	0,139	0,135	0,114	0,202	0,174	0,130	0,139	0,159	0,185	0,181
	Average	0,042	0,059	0,076	0,093	0,110	0,127	0,144	0,144	0,149	0,154	0,120	0,082	0,209	0,224	0,180	0,174	0,189	0,245	0,236
C-V	1	0,029	0,030	0,038	0,027	0,031	0,028	0,041	0,038	0,051	0,050	0,032	0,037	0,033	0,035	0,029	0,026	0,029	0,029	0,028
	2	0,024	0,031	0,039	0,032	0,030	0,030	0,037	0,050	0,048	0,050	0,033	0,042	0,037	0,040	0,041	0,035	0,033	0,030	0,035
	3	0,019	0,031	0,029	0,024	0,028	0,028	0,040	0,048	0,041	0,036	0,029	0,033	0,033	0,034	0,030	0,030	0,031	0,029	0,029
	Average	0,024	0,031	0,035	0,028	0,030	0,029	0,039	0,045	0,047	0,045	0,031	0,037	0,034	0,036	0,033	0,030	0,031	0,029	0,031

A.2 E_{corr} readings (-mV)

Table A- 2: Complete E_{corr} readings

		Week																		
Variable	**Sample**	**0**	**1**	**2**	**3**	**4**	**5**	**6**	**7**	**8**	**9**	**10**	**11**	**12**	**13**	**14**	**15**	**16**	**17**	**18**
3D-0	1	127,5	405,5	337,6	360,5	327,1	358,1	319,3	320,6	269,4	289,1	271,0	319,6	319,7	321,9	312,3	306,0	290,9	353,8	305,6
	2	127,2	309,3	284,8	297,1	252,9	356,5	358,0	362,0	351,0	339,8	319,8	330,3	310,6	276,4	274,4	301,8	251,7	245,0	207,5
	3	122,7	382,1	235,4	269,9	269,8	273,6	244,1	253,2	235,7	295,2	290,9	299,7	255,8	291,5	237,6	238,7	187,8	245,2	236,3
	Average	125,8	365,6	285,9	309,2	283,3	329,4	307,1	311,9	285,4	308,0	293,9	316,5	295,4	296,6	274,8	282,2	243,5	281,3	249,8
3D-10	1	261,3	360,4	273,5	313,7	258,2	358,3	320,2	335,5	275,3	300,8	224,4	174,3	199,3	175,0	157,8	178,9	194,9	206,1	163,9
	2	113,3	274,2	162,2	135,6	115,5	111,4	137,2	175,0	143,7	119,3	89,1	72,1	76,4	249,8	245,0	250,3	220,9	198,3	130,9
	3	241,3	455,2	390,4	380,2	359,4	358,6	321,1	296,0	303,7	367,7	306,5	317,6	303,2	294,1	308,7	269,5	233,6	290,5	220,2
	Average	205,3	363,3	275,4	276,5	244,4	276,1	259,5	268,8	240,9	262,6	206,7	188,0	193,0	239,6	237,2	232,9	216,5	231,6	171,7
3D-20	1	118,0	424,2	365,7	396,8	377,4	367,1	378,6	384,9	395,2	350,7	351,9	288,1	256,3	316,1	299,9	307,7	326,9	307,2	319,0
	2	206,1	457,5	341,4	387,2	366,9	413,3	406,8	389,1	327,0	310,4	280,9	266,2	269,8	300,7	307,1	305,4	312,3	296,7	243,8
	3	150,8	437,7	365,2	392,4	374,0	368,4	378,7	371,7	355,2	313,4	295,1	269,5	247,9	277,0	288,0	281,4	279,3	275,5	260,3
	Average	158,3	439,8	357,4	392,1	372,8	382,9	388,0	381,9	359,1	324,8	309,3	274,6	258,0	297,9	298,3	298,2	306,2	293,1	274,4
3D-30	1	127,8	418,5	385,0	402,8	404,0	388,9	417,4	431,7	390,6	407,6	363,8	358,4	338,0	375,8	354,6	375,1	355,7	376,9	310,0
	2	118,7	440,5	406,7	415,3	398,7	361,4	398,0	388,0	406,7	404,7	370,8	395,1	363,7	355,4	348,5	412,0	389,6	417,5	323,3
	3	131,9	462,1	384,0	420,9	391,4	376,7	387,4	310,2	331,1	304,4	292,7	319,9	313,7	289,5	270,7	258,9	245,0	247,5	209,1
	Average	126,1	440,4	391,9	413,0	398,0	375,7	400,9	376,6	376,1	372,2	342,4	357,8	338,5	340,2	324,6	348,7	330,1	347,3	280,8
C-V	1	130,9	132,7	129,0	124,3	121,2	107,6	104,7	114,0	92,5	69,3	69,9	66,2	63,2	37,8	24,3	16,7	25,8	14,2	20,2
	2	131,4	135,5	131,0	123,8	125,3	105,3	110,3	92,8	86,3	74,2	73,0	168,6	128,3	104,1	103,2	94,1	59,7	51,5	60,2
	3	194,7	164,2	168,7	171,2	137,0	111,7	107,8	96,8	99,2	80,1	83,0	66,7	53,4	42,2	33,6	24,3	20,7	8,1	8,5
	Average	152,3	144,1	142,9	139,8	127,8	108,2	107,6	101,2	92,7	74,5	75,3	100,5	81,6	61,4	53,7	45,0	35,4	24,6	29,6

A.3 R_{ohm} readings (kΩ)

Table A- 3: Complete R_{ohm} readings

		Week																		
Variable	**Sample**	**0**	**1**	**2**	**3**	**4**	**5**	**6**	**7**	**8**	**9**	**10**	**11**	**12**	**13**	**14**	**15**	**16**	**17**	**18**
3D-0	1	0,96	1,92	2,88	3,83	4,79	5,75	11,06	9,80	7,32	7,42	6,00	7,98	5,96	3,40	7,12	6,74	5,69	3,98	4,04
	2	0,21	1,56	2,90	4,25	5,59	6,94	7,15	6,47	6,85	5,44	6,29	7,18	4,42	11,40	3,51	12,72	8,58	5,11	5,80
	3	0,70	1,74	2,78	3,82	4,86	5,90	6,24	5,28	5,57	5,23	6,30	9,32	9,29	6,94	5,78	5,05	6,11	4,66	4,18
	Average	0,62	1,74	2,85	3,97	5,08	6,20	8,15	7,18	6,58	6,03	6,20	8,16	6,56	7,25	5,47	8,17	6,79	4,58	4,67
3D-10	1	5,07	5,22	5,36	5,51	5,65	5,80	6,49	5,76	5,97	5,81	6,42	8,73	8,14	7,27	6,37	4,77	5,11	4,60	3,93
	2	2,87	3,45	4,02	4,60	5,17	5,75	7,14	5,98	7,20	6,42	6,00	6,29	3,43	7,61	7,52	5,64	5,68	4,44	7,47
	3	2,81	3,49	4,17	4,86	5,54	6,22	6,05	5,17	5,57	5,70	6,39	6,74	6,76	6,32	13,72	4,73	4,39	3,51	3,34
	Average	3,58	4,05	4,52	4,99	5,46	5,92	6,56	5,64	6,25	5,98	6,27	7,25	6,11	7,07	9,20	5,05	5,06	4,18	4,91
3D-20	1	1,31	2,44	3,57	4,71	5,84	6,97	6,48	6,54	7,26	7,90	7,56	9,43	4,49	4,63	5,04	6,63	6,80	4,90	4,18
	2	0,13	1,51	2,89	4,28	5,66	7,04	6,55	6,73	6,82	6,43	6,98	7,53	4,59	4,22	6,30	6,00	4,92	4,02	4,13
	3	3,08	3,59	4,10	4,61	5,12	5,63	4,98	6,08	6,38	5,85	7,05	7,44	5,19	3,92	7,07	5,42	5,10	4,32	3,91
	Average	1,51	2,51	3,52	4,53	5,54	6,55	6,00	6,45	6,82	6,73	7,20	8,13	4,76	4,26	6,14	6,02	5,61	4,41	4,07
3D-30	1	1,25	2,22	3,20	4,17	5,15	6,12	5,75	5,36	5,93	6,42	6,74	17,35	4,45	3,83	6,64	7,82	5,34	4,08	4,36
	2	1,38	2,45	3,53	4,60	5,68	6,75	6,45	5,82	4,91	5,99	18,77	23,04	5,55	6,05	5,59	7,43	6,60	4,65	5,51
	3	1,02	2,50	3,98	5,45	6,93	8,41	7,20	7,24	6,87	6,54	6,89	8,76	4,85	4,55	7,42	7,58	5,76	4,42	4,99
	Average	1,22	2,39	3,57	4,74	5,92	7,09	6,47	6,14	5,90	6,32	10,80	16,38	4,95	4,81	6,55	7,61	5,90	4,38	4,95
C-V	1	3,28	2,23	1,75	4,19	4,16	4,83	4,06	2,46	1,20	2,09	5,72	13,93	9,03	8,45	10,43	11,14	10,51	14,16	11,03
	2	3,61	2,76	3,50	3,90	5,13	5,92	3,61	1,75	1,72	5,87	5,76	7,32	8,79	8,13	8,41	9,08	10,18	10,66	10,01
	3	6,06	4,16	4,35	7,07	5,40	6,76	3,14	0,88	1,92	1,83	6,98	7,85	8,60	8,50	9,63	9,30	9,49	9,67	10,25
	Average	4,32	3,05	3,20	5,05	4,90	5,84	3,60	1,70	1,61	3,26	6,15	9,70	8,81	8,36	9,49	9,84	10,06	11,50	10,43

Appendix B Carbonation model inputs

B.1 Binder composition

Table B- 1: Binder composition

	CEM II	SF	FA	Source
Binder				
Clinker/SCM	96,5%	100%	100%	Supplier
Gypsum	3,5%	0%	0%	
Oxides				
SiO_2	22,1%	84,40%	54,80%	(Papadakis, 1999a;b;
Al_2O_3	4,2%	0,60%	33,10%	Moelich et al., 2021b)
Fe_2O_3	3,3%	3,30%	3,20%	
CaO (free)	66,9%	0,70%	4,30%	
	(1,5%)	(0.02%)	(0.36%)	
Compounds				
C_3S	65,3%	-	-	Bogue model
C_2S	14,2%	-	-	
C_3A	5,5%	-	-	
C_4AF	10,0%	-	-	
other				
Mean diameter	20 µm	0.5 µm	20 µm	Supplier
Crystalline phase	-	0,05%	11,9%	(Salvoldi et al, 2015)

B.2 Constants applicable for this study

Table B- 2: Carbonation model constants

Constant	**Value**
RH	65%
ToW	0
T	23 ℃ (296.15 K)
t	42 days